National Central University

Department of Physics

Searches for Higgs pair production and probing the Higgs self couplings in the HH$\rightarrow$bb$\tau\tau$ decay channel at the ATLAS Experiment and performance studies for the High-Granularity Timing Detector for ATLAS phase-2 upgrade

SHAHZAD ALI

ADVISORS: PROF. SHIH-CHANG LEE & PROF YUAN-HANN CHANG
CO-ADVISOR: PROF. SONG-MING WANG.

JANUARY-2024

National Central University
Department of Physics

Searches for Higgs pair production and probing the Higgs self couplings in the HH$\rightarrow$bb$\tau\tau$ decay channel at the ATLAS Experiment and performance studies for the High-Granularity Timing Detector for ATLAS phase-2 upgrade

A dissertation submitted to the National Central University
in partial fulfilment of the requirements for the degree of
Doctor of Philosophy

Shahzad Ali

Advisors: Prof. Shih-Chang Lee & Prof Yuan-Hann Chang
Co-Advisor: Prof. Song-Ming Wang.

January-2024

National Central University Library
Authorization for Thesis/ Dissertation

Application Date：28/12/2023

The latest version since Sep. 2019

Applicant Name	Shahzad Ali	Student Number	106282602
Schools / Departments	Physics	Graduate Degree	☐Master ☑ Doctor
Thesis/Dissertation Title	Searches for Higgs pair production and probing the Higgs self-couplings in the $HH \rightarrow bb\tau\tau$ decay channel at the ATLAS Experiment and performance studies for the High-Granularity Timing Detector for ATLAS phase-2 upgrade	Advisor Name	Shih-Chang Lee

Authorization for Internet Access of Thesis/ Dissertation

This license authorizes my complete electronic thesis to be archived and read in the

- National Central University Library Electronic Theses & Dissertations System .
  - (✓) Released for Internet access immediately
  - ( ) Released for Internet access starting from: _______ /_______ /________ (YYYY / MM / DD)
  - ( ) Disagree, because:___________________________________
- NDLTD(National Digital Library of Theses and Dissertations in Taiwan).
  - (✓) Released for Internet access immediately
  - ( ) Released for Internet access starting from: _______ /_______ /________ (YYYY / MM / DD)
  - ( ) Disagree, because:___________________________________

I hereby agree to authorize the electronic versions of my thesis/dissertation and work to National Central University, University System of Taiwan(UST) and National Central Library(National Digital Library of Theses and Dissertations in Taiwan), in a non-exclusive way and without reimbursement, in accordance with the Copyright Act. The fore-mentioned authorized items can be reproduced by the authorized institution in the form of text, video tape, audio tape, disc and microfilm, or converted into other digital formats, without the limitation of time, places, and frequency for non-commercial uses.

Delayed Public Release for Paper Copy of Thesis/Dissertation

(You do not need to fill out this section if you make the paper copy of your thesis/dissertation available to the public immediately.)

- Reasons for the delayed release (choose one)
  - ( ) Filing for patent registration. Registration number: ________________________
  - ( ) Submission for publication
  - ( ) Your research contains information pertaining to national non-disclosure agreements.
  - ( ) Contents withheld according to the law. Please specify________________________
- Delayed Until：___________/_______/_________ (YYYY / MM / DD)

You should submit another paper copy to National Central Library (NCL) through the NCU Division of Registrar. If you would like to delay the release of this paper copy in NCL, please fill out the "Application for Embargo of thesis/dissertation" of NCL.

Signature of the Applicant：____________________ Signature of the Advisor：____________________

*Please attach this form after the thesis/dissertation cover when submitting your thesis/dissertation.

國立中央大學博士班研究生

論文指導教授推薦書

物理 學系/研究所 李杉拉 研究生所提之論文

Searches for Higgs pair production and probing the Higgs self-couplings in the HH→bbττ decay channel at the ATLAS Experiment and performance studies for the High-Granularity Timing Detector for ATLAS phase-2 upgrade, 係由本人指導撰述，同意提付審查。

（題 目）

指導教授 李世昌 (簽章)

2023 年 11 月 29 日

National Central University

Advisor’s Recommendation for Doctoral Students

This thesis is by ***Shahzad Ali*** (Author) of the graduate program in Physics, entitled: ***Searches for Higgs pair production and probing the Higgs self-couplings in the HH→bbττ decay channel at the ATLAS Experiment and performance studies for the High-Granularity Timing Detector for ATLAS phase-2 upgrade***,
which is written under my supervision, and I agree to propose it for examination.

Advisor ______________________

2023/11/29（YYYY/MM/DD）

National Central University
Verification Letter from the Oral Examination Committee for Doctoral Students

This thesis titled Searches for Higgs pair production and probing the Higgs self-couplings in the HH→bbττ decay channel at the ATLAS Experiment and performance studies for the High-Granularity Timing Detector for ATLAS phase-2 upgrade is written by Shahzad Ali studying in the graduate program in Ph.D. Program, Department of Physics.
The author of this thesis is qualified for a Doctoral degree through the verification of the committee.

Convener of the Degree Examination Committee Kai-Feng Chen

Members 張元翰 徐百嫻
李世昌 楊毅
(Song-Ming Wang)
郭家銘

Date (YYYY/MM/DD) 2023/12/11

1121211

摘要

這項研究聚焦於在 CERN 大型強子對撞機（LHC）由 ATLAS 探測器記錄的質心能量為 13 TeV 的質子-質子碰撞中，使用 140 fb^{-1} 數據尋找 $HH \to b\bar{b}\tau^+\tau^-$ 非共振希格斯玻色子對產生的信號。分析策略旨在探測希格斯玻色子（H）的自相交互作用強度 κ_λ 和四重 $HHVV(V = W, Z)$ 交互作用強度 κ_{2V} 的異常值。然而，在標準模型 (SM) 預期的背景中未觀察到顯著超出的訊號。在 95 % 的信心水準下，觀測到的 (期望的) 雙希格斯玻色子的產生率上限為標準模型預測的 5.9 (3.1) 倍。在假設所有其他希格斯玻色子交互作用固定為標準模型預測的情況下，交互作用強度被限制在觀測到的 (期望的) 95 % 信賴區間 $-3.2 < \kappa_\lambda < 9.1$ $(-2.4 < \kappa_\lambda < 9.2)$ 和 $-0.5 < \kappa_{2V} < 2.7(-0.2 < \kappa_{2V} < 2.4)$ 內。該研究還包括使用在 2018 年至 2019 年在 CERN SPS 和 DESY 收集的測試數據，對具有 50 μm 有效厚度的低增益雪崩探測器 (LGADs) 進行性能評估，重點關注 ATLAS 第二階段升級的高粒度定時探測器 (HGTD)。HGTD 旨在通過精確測量軌跡時間，分辨率約為 30 ps 到 50 ps，提高粒子-頂點分配的精度，從而減輕 LHC 高亮度運行期間的堆積效應。

Abstract

This study focuses on searches for non-resonant Higgs boson pair production in the $HH \to b\bar{b}\tau^+\tau^-$ channel using 140 fb^{-1} of proton-proton collisions at a centre-of-mass energy of 13 TeV recorded by the ATLAS detector at the CERN Large Hadron Collider (LHC). The analysis strategy aims to probe anomalous values of the Higgs boson (H) self-coupling modifier κ_λ and quartic $HHVV(V = W, Z)$ coupling modifier κ_{2V}. However, No significant excess above the expected background from Standard Model (SM) processes is observed. Observed (expected) upper limit at 95% confidence-level on the di-Higgs boson production rate is set at 5.9 (3.1) times the SM prediction. The coupling modifiers are constrained within an observed (expected) 95% confidence interval of $-3.2 < \kappa_\lambda < 9.1$ ($-2.4 < \kappa_\lambda < 9.2$) and $-0.5 < \kappa_{2V} < 2.7$ ($-0.2 < \kappa_{2V} < 2.4$), assuming all other Higgs boson couplings are fixed to the Standard Model prediction. The study also includes performance evaluations of Low Gain Avalanche Detectors (LGADs) with a 50 μm active thickness using testbeam data collected at CERN SPS and DESY between 2018 and 2019, focusing on the High-Granularity Timing Detector (HGTD) for the ATLAS phase-2 upgrade. The HGTD aims to enhance particle-vertex assignments by precisely measuring track time with resolutions ranging from approximately 30 ps to 50 ps, thereby mitigating pile-up effects during the High-Luminosity phase of the LHC operations.

Acknowledgments

I extend my deepest gratitude to my family, including my brothers and sisters, for their unwavering support and encouragement throughout my academic journey. Their love, understanding, and encouragement have been invaluable to me, especially during challenging times.

I am forever indebted to my late mother, whose unwavering belief in my abilities continues to inspire me every day. Her unconditional love and guidance have shaped me into the person I am today. Though she is no longer with us, her spirit remains a guiding light in my life.

I am profoundly grateful to my wife Shah Rukh Laleen for her endless patience, support, and understanding during the demanding phases of my doctoral studies. Her encouragement and belief in my capabilities have been a source of strength and motivation.

I am immensely grateful to my son, Alber Ali Khan, whose presence in the last two years of my PhD journey brought immeasurable joy, support, and motivation. His infectious enthusiasm and unwavering positivity were a constant reminder of the importance of balance and joy in life, inspiring me to persevere through challenges and cherish every moment of this academic pursuit.

I extend my heartfelt appreciation to my esteemed supervisors, Professor Lee Shih Chang, Song-Ming Wang, and Yuan Hann Chang, for their invaluable guidance, mentorship, and trust in my abilities. Their support provided me with the incredible opportunity to work at CERN, a pivotal moment in my academic and professional growth. Their wisdom and encouragement have been instrumental in shaping my research and academic pursuits.

I am immensely grateful to Academia Sinica, Taipei, Taiwan, and National Central University Taiwan, for their financial support throughout my doctoral studies. Their funding made my research endeavors possible and greatly contributed to the success of my academic pursuits.

I extend my heartfelt gratitude to CERN (European Organization for Nuclear Research) and The ATLAS Experiment for providing an exceptional research environment and facilitating access to invaluable resources. The world-class laboratory and collaborative efforts of the ATLAS experiment have significantly contributed to my research, enabling the analysis of high-quality data and fostering an intellectually stimulating environment for academic exploration.

At last but not the least, I wish to thank all the teachers, colleagues, and friends who have contributed to my academic and personal development. Their advice, discussions, and collaborations have enriched my experience and helped me overcome various challenges.

Contents

List of Figures

List of Tables

Introduction

The Higgs boson discovery back in 2012 by both the Large Hadron Collider (LHC)'s experiments ATLAS and CMS[1, 2] marked a significant milestone in particle physics. The Higgs boson's existence, proposed almost half a century earlier, was fundamental in validating the Higgs mechanism [3]. This mechanism, embedded in the Standard Model (SM) [3–5], elucidates the origin of particle mass through electroweak symmetry breaking.

While the observed Higgs boson aligns with many SM predictions regarding its interactions and decays, certain critical characteristics remain untested. The SM anticipates a unique aspect of the Higgs boson - its ability to self-couple. This coupling's strength directly correlates with the Higgs potential's shape, crucial in exploring electroweak symmetry breaking's precise nature. Though experimental validation of the Higgs boson self-coupling is pending, the quest for Higgs boson pair production, examined in this thesis within the ATLAS experiment at the LHC, holds promise in this pursuit.

At the LHC, the production of Higgs boson pairs (HH) primarily hinges on the Higgs boson self-coupling's potency and the top-quark Yukawa coupling. Predicted HH production cross-sections are significantly low - three orders of magnitude less than single Higgs boson production - posing challenges for current LHC datasets to observe this process. Modulations in the Higgs boson self-coupling or top-quark Yukawa coupling could notably amplify the cross-section, potentially enabling HH production's detection.

Furthermore, diverse theories extending beyond the SM aim to address its limitations. Models like the two-Higgs-doublet models [6] and the Randall-Sundrum model [7] envisage heavy resonances decaying into Higgs boson pairs. Detecting resonant pair production of Higgs bosons could directly illuminate physics beyond the SM.

This thesis explores searches for non-resonant Higgs boson pair production in the final state with two bottom quarks and two τ leptons ($b\bar{b}\tau^+\tau^-$ final state). Findings derive from proton-proton (pp) collision data collected by the ATLAS detector at 13 TeV between 2015 and 2018. The study delves into non-resonant pair production, encompassing both the SM Higgs boson couplings and the anomalous Higgs boson self-coupling.

Chapter 1 provides an overview of theoretical concepts pertinent to this thesis. Chapter 2 elucidates the LHC and the ATLAS detector's key features. It also outlines Monte Carlo simulations' role in collider physics experiments. Algorithms for reconstructing and identifying different physics objects, crucial for data analysis, are detailed in Chapter 3.

Chapters 4 and 5 outline the search for resonant Higgs boson pair production and containing the limits for the (anomalous) Higgs boson self-coupling in the $b\bar{b}\tau^+\tau^-$ final state, utilizing 140 fb^{-1} of 13 TeV pp collision data collected by the ATLAS detector from 2015 to 2018.

Finally, Chapter 6 discusses results from testbeam data on the Low Gain Avalanche Detectors (LGADs), technology slated for use in the ATLAS phase-2 upgrade project High Granularity Timing Detector (HGTD) [8] for the High Luminosity LHC [9]. Notably, these results have been previously published [10].

Author's contribution

The work detailed in this thesis was a part of the ATLAS collaboration, comprising over 3000 members. Given the complexity of the experiment and the joint efforts needed to operate the detector and its infrastructure, the outcomes from this collaboration reflect collective work. Below are the author's personal contributions to the studies and findings in this thesis.

This thesis investigates the production of pairs of Higgs bosons in the $b\bar{b}\tau^+\tau^-$ channel, to which the author has significantly contributed over the past four years. Although not included in this thesis, the author played a substantial role in a previously published paper focusing on the same channel [11]. The search included both resonant and non-resonant HH production, with the author's primary involvement centered around estimating fake backgrounds and validating input data. Additionally, the author explored methods to improve signal acceptance, introducing new trigger strategies, and conducting Multivariate Analysis (MVA) studies.

For the analyses in this thesis, the author participated in establishing a new analysis framework and implemented a data-driven method for estimating fake-tau backgrounds, described in Section 4.8.2. Additionally, the author meticulously estimated the systematic uncertainties related to the fake-tau estimation method. Leading the MVA optimization studies detailed in Section 4.11 for the semi-leptonic decay channels, the author significantly contributed to refining the analysis.

Regarding the results in Chapter 6, the author played a pivotal role in developing the framework for analyzing testbeam data. The author introduced a method to remove background noise, discussed in Section 6.7, to enhance signal extraction as well as conducted the study of analysing sensor performance by obtaining the uniformity results detailed in Section 6.7.2. Actively participating in testbeam data taking at both CERN and DESY during 2018 and 2019, the author made significant contributions to record substantial amount of data for the analysis.

Outside the scope of this thesis, the author is actively involved in the ongoing LHC Run3 data taking as the Online Data Quality Coordinator in the ATLAS data preparation team. Additionally, the author contributes expertise in Global Monitoring, emphasizing the importance of data quality in physics analysis.

Chapter 1

The Standard Model and the Higgs boson

The Standard Model (SM) of particle physics stands as one of the most remarkable achievements in our understanding of the fundamental building blocks of the universe. Developed over several decades, this theoretical framework successfully describes the interactions between elementary particles and the forces that govern their behavior. Central to the Standard Model is the discovery and subsequent confirmation of the Higgs boson, a particle that provides crucial insights into the origin of mass.

At the heart of the Standard Model lies the concept of symmetry and the fundamental particles it encompasses. These particles are classified into two categories: fermions and bosons. Fermions, including quarks and leptons, make up matter, while bosons mediate the forces between particles, such as photons, gluons, and the W and Z bosons.

However, the question of how particles acquire mass remained a puzzle until the proposal of the Higgs mechanism [3]. The Higgs boson, named after physicist Peter Higgs, is an essential component of this mechanism. It arises from a field permeating the universe known as the Higgs field, which endows particles with mass as they interact with it.

The Higgs boson discovery in 2012 claimed by both CMS [1] and ATLAS[2] experiments at the LHC was a monumental achievement for particle physics.

The experiments conducted at CERN confirmed the existence of this elusive particle, validating the predictions of the Standard Model and providing a crucial piece of the puzzle to understand the nature of mass and the underlying symmetries of the universe.

The Higgs boson's discovery has opened up new avenues for research, enabling scientists to probe deeper into the mysteries of the cosmos. It has shed light on the nature of the electroweak symmetry breaking and serves as a cornerstone in our quest to unify the fundamental forces of nature.

In this chapter, we will delve into the intricacies of the Standard Model, exploring the fundamental particles, their interactions, and the theoretical framework that underpins our current understanding of the universe. We will also examine the experimental techniques employed in the search for the Higgs boson and the significance of its discovery.

1.1 Particles in the Standard Model

The Standard Model of particle physics provides a comprehensive framework for understanding the fundamental particles and their interactions. It has been remarkably successful in describing the known particles and their behaviour within the realm of high-energy physics. In this section, we will discuss the particle content of the SM, which consists of spin-$\frac{1}{2}$ fermions (matter particles), the force careers i.e gauge bosons having spin-1, and the Higgs boson having spin-0.

1.1.1 Matter Particles

The matter particles in the Standard Model can be further divided into two categories: leptons and quarks.

Leptons

Leptons are fundamental particles that do not experience a strong force. There are three generations of leptons, each containing a charged lepton and a corresponding neutral lepton, called a neutrino. The charged leptons are the electron (e^-), the muon (μ^-), and the tau (τ^-). The neutrinos associated to the leptons are electron neutrino (ν_e), the muon neutrino (ν_μ), and the tau neutrino (ν_τ). The leptons in the standard model are briefed into three generations having six flavours.

$$\begin{pmatrix} e^- \\ \nu_e \end{pmatrix} \begin{pmatrix} \mu^- \\ \nu_\mu \end{pmatrix} \begin{pmatrix} \tau^- \\ \nu_\tau \end{pmatrix} \tag{1.1}$$

Each charged lepton has an associated antiparticle with opposite charge. The electron antiparticle is denoted as e^+ (positron), the muon antiparticle as μ^+, and the tau antiparticle as τ^+. Similarly, there are antineutrinos corresponding to each neutrino.

Quarks

Quarks are elementary particles that do experience strong nuclear force and carry electrical charge. There are six types of quarks in the standard model which exist in six flavours: up (u), down (d), charm (c), strange (s), top (t), and bottom (b). Each quark flavour has an associated antiparticle called an antiquark. Likewise leptons in standard model the quarks are also grouped in to three generations as shown as follow.

$$\begin{pmatrix} u \\ d \end{pmatrix} \begin{pmatrix} c \\ s \end{pmatrix} \begin{pmatrix} t \\ b \end{pmatrix} \tag{1.2}$$

Quarks are never found as isolated particles due to a property known as color confinement. They are always observed bound together in composite particles called hadrons. Hadrons can be either mesons, which consist of a quark-antiquark pair, or baryons, which consist of three quarks. Protons (uud) and neutrons (udd), which are the building blocks of atomic nuclei, are examples of baryons.

1.1.2 Gauge Bosons

The Standard Model includes four fundamental forces: electromagnetism, the weak force, the strong nuclear force, and gravity (which is not described within the framework of the SM). The interactions between particles mediated by these forces are carried out by gauge bosons.

The electromagnetic force is mediated by photon particle, which is a massless, spin-1 gauge boson. The weak force is mediated by three massive gauge bosons: the W^+, W^-, and Z^0 bosons. These gauge bosons have spin-1 and are responsible for processes such as radioactive decay and neutrino interactions.

The strong force, which binds quarks together to form hadrons, is mediated by massless spin-1 gauge bosons called gluons. Gluons carry the color charge and are unique to the strong interaction.

1.1.3 Higgs Boson

The Higgs boson (H) is a spin-0 particle that was discovered at the LHC in 2012 CMS [1, 2]. It is associated with the Higgs field, which gives mass to other particles through a process known as electroweak symmetry breaking [3]. The discovery of the Higgs boson was a significant milestone in confirming the mechanism by which particles acquire mass in the Standard Model.

To summaries the section 1.1, the particle content of the Standard Model includes spin-$\frac{1}{2}$ fermions (leptons and quarks), spin-1 gauge bosons (photon, W and Z bosons, gluons), and the spin-0 Higgs boson. These particles and their interactions form the foundation of our current understanding of the fundamental constituents of matter and the forces that govern them.

All the particles content of the Standard Model is briefed in Figure 1.1

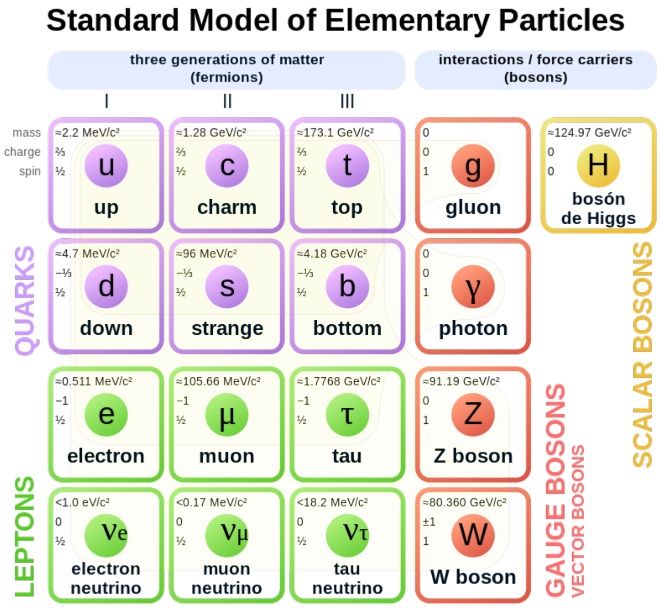

FIGURE 1.1: Standard model of elementary particles and interactions [12]

1.2 Gauge Theories in the Standard Model

Gauge theories form a fundamental framework in the description of particle physics, and they play a crucial role in the Standard Model. These theories are based on the principle of local gauge invariance, which introduces symmetries to account for the fundamental forces and interactions between elementary particles.

The Standard Model incorporates three gauge theories: Quantum Electrodynamics (QED), Quantum Chromodynamics (QCD), and the Electroweak Theory. Each of these theories describes a specific force and has its own gauge bosons, which are the force-carrying particles.

Gauge theories in the Standard Model rely on the concept of gauge fields, which mediate the interactions between particles. These gauge fields transform under specific symmetry groups, such as U(1) for electromagnetism, SU(2) for the weak interaction, and SU(3) for the strong interaction.

The gauge fields in the Standard Model are coupled to matter fields, such as quarks and leptons, through covariant derivatives. The covariant derivatives ensure that the gauge fields transform properly under the corresponding symmetry groups. In this section, we will explore three prominent gauge theories in the Standard Model: Quantum Electrodynamics (QED), Quantum Chromodynamics (QCD), and Electroweak theory.

1.2.1 Quantum Electrodynamics (QED)

The QED is a gauge theory that describes the electromagnetic interaction between charged particles. It is a fundamental part of the Standard Model of particle physics.

In QED, the electromagnetic field is quantized, and the interaction between charged particles and the electromagnetic field is described by the following Lagrangian density:

$$\mathcal{L}_{\text{QED}} = \bar{\psi}(i\gamma^{\mu}D_{\mu} - m)\psi - \frac{1}{4}F^{\mu\nu}F_{\mu\nu} \tag{1.3}$$

where:

- ψ represents a Dirac spinor field, describing charged leptons such as electrons, muons (μ), taus (τ), and other fundamental particles with half-integer spin (fermions) in QED,
- m is the mass of the electron,
- γ^μ are the Dirac gamma matrices,
- $D_\mu = \partial_\mu - ieA_\mu$ is the covariant derivative with A_μ being the electromagnetic potential,
- $F^{\mu\nu} = \partial^\mu A^\nu - \partial^\nu A^\mu$ is the electromagnetic field strength tensor.

The Euler-Lagrange equation for the electron field yields the Dirac equation in the presence of the electromagnetic field:

$$(i\gamma^\mu D_\mu - m)\psi = 0 \tag{1.4}$$

The electromagnetic field is described by Maxwell's equations, which are obtained from the variation of the electromagnetic field Lagrangian density:

$$\partial_\mu F^{\mu\nu} = -e\bar{\psi}\gamma^\nu\psi \tag{1.5}$$

QED predicts phenomena such as the scattering of electrons and photons, as well as the emission and absorption of photons by charged particles. It has been extensively tested and verified through various experiments.

Feynman Rules

In QED, the interaction between particles is represented using Feynman diagrams [1]. Feynman rules can be derived from the QED Lagrangian and are used to calculate scattering amplitudes.

---

[1] Of course, the Feynman diagram is not limited to representing QED interactions alone. It finds application across various contexts within particle physics, including other fundamental forces such as Quantum Chromodynamics and weak nuclear interactions. However, in this context, our discussion specifically emphasizes its role in elucidating QED interactions.

One important Feynman rule in QED is the vertex factor, which describes the interaction between an electron, a positron, and a photon. The vertex factor is given by:

$$-ie\gamma^{\mu}$$

where e is the electron charge and γ^{μ} is the photon vertex. Other Feynman rules involve the propagators for electrons, positrons, and photons.

These Feynman rules allow us to compute probabilities for different scattering processes in QED.

Renormalization

QED is a perturbative theory, but it suffers from ultraviolet divergences in higher-order calculations. To address these divergences, a process called renormalization is used. Renormalization involves introducing counterterms to absorb the infinities that arise in calculations.

By using renormalization, QED becomes a predictive and well-defined theory, capable of providing accurate predictions for experimental observables.

1.2.2 Quantum Chromodynamics (QCD)

QCD is the gauge theory that describes the strong interaction, which is responsible for the binding of quarks inside hadrons, such as protons and neutrons. It is a fundamental component of the Standard Model.

The Lagrangian density for QCD is given by:

$$\mathcal{L}_{\text{QCD}} = \sum_{f} \bar{q}_f (i\gamma^{\mu} D_{\mu} - m_f) q_f - \frac{1}{4} G^{a}_{\mu\nu} G^{\mu\nu}_{a} \tag{1.6}$$

where $\bar{q}_f$ represents the quark fields, m_f is the mass of the quark, γ^{μ} are the Dirac gamma matrices, and D_{μ} is the covariant derivative.

The covariant derivative in QCD accounts for the interaction between quarks and gluons, which are the gauge bosons associated with the strong force. It is defined as:

$$D_\mu = \partial_\mu - i g_s G^a_\mu t^a \tag{1.7}$$

Here, g_s represents the strong coupling constant, G^a_μ is the gluon field, and t^a are the generators of the SU(3) color group, which describes the symmetry of the strong force.

The field strength tensor $G^a_{\mu\nu}$ in QCD is defined as:

$$G^a_{\mu\nu} = \partial_\mu G^a_\nu - \partial_\nu G^a_\mu - g_s f^{abc} G^b_\mu G^c_\nu \tag{1.8}$$

where f^{abc} are the structure constants of the SU(3) color group.

One of the remarkable aspects of QCD is asymptotic freedom. At high energies or short distances, the strong coupling constant becomes small, allowing for perturbative calculations. Conversely, at low energies or large distances, the strong force becomes strong, preventing the direct observation of free quarks (confinement).

QCD predicts the existence of color-neutral composite particles called hadrons, which include mesons (quark-antiquark pairs) and baryons (three-quark combinations).

Feynman diagrams are essential tools in QCD calculations. They represent the interaction vertices involving quarks and gluons, enabling the computation of scattering amplitudes and decay rates.

QCD has been extensively tested through experiments, such as deep inelastic scattering and hadron colliders. It has proven to be a successful theory for describing the strong interaction and has contributed significantly to our understanding of the subatomic world.

The study of QCD continues to be an active area of research, exploring phenomena such as quark-gluon plasma and the dynamics of strong interactions in extreme conditions, such as those found in particle collisions at high energies.

1.2.3 Electroweak Theory

The Electroweak Theory is a gauge theory that unifies the electromagnetic and weak interactions, incorporating both the electromagnetic force and the weak nuclear force into a single framework. It is a crucial component of the Standard Model.

The Lagrangian density for the Electroweak Theory can be written as:

$$\begin{aligned}\mathcal{L}_{\text{EW}} = \bar{L}_L i\gamma^\mu D_\mu L_L + \bar{e}_R i\gamma^\mu D_\mu e_R + \bar{Q}_L i\gamma^\mu D_\mu Q_L \\ + \bar{u}_R i\gamma^\mu D_\mu u_R + \bar{d}_R i\gamma^\mu D_\mu d_R - \frac{1}{4} W^a_{\mu\nu} W^{\mu\nu}_a - \frac{1}{4} B_{\mu\nu} B^{\mu\nu}\end{aligned} \tag{1.9}$$

where L_L and Q_L are the left-handed lepton and quark doublets, e_R, u_R, and d_R are the right-handed singlets, γ^μ are the Dirac gamma matrices, D_μ is the covariant derivative, $W^a_{\mu\nu}$ are the gauge bosons associated with the weak force, and $B_{\mu\nu}$ is the gauge boson associated with the electromagnetic force.

The Electroweak Theory incorporates the Higgs mechanism, which is responsible for giving masses to the W and Z bosons while leaving the photon massless. The Higgs field acquires a vacuum expectation value, breaking the electroweak symmetry and giving rise to the masses of the particles.

The Electroweak Theory predicts various phenomena, including weak decays, electroweak interactions, and processes involving W and Z bosons. It has been experimentally verified with remarkable precision, particularly through high-energy collider experiments.

Feynman diagrams are employed to calculate amplitudes and interpret the interactions within the Electroweak Theory. These diagrams depict the exchange of gauge bosons and provide a visual representation of the underlying physics.

The successful unification of the electromagnetic and weak interactions in the Electroweak Theory represents a significant achievement in particle physics. It serves as a cornerstone in our understanding of the fundamental forces and particle interactions in the subatomic realm.

Further investigations and experiments continue to refine our knowledge of the Electroweak Theory, shedding light on phenomena such as neutrino oscillations and the properties of the Higgs boson.

1.3 Spontaneous symmetry breaking and The Brout-Englert-Higgs mechanism

As stated previously for the Electro-Weak lagrangian in section 1.2.3, the theory requires both the fermions and the gauge bosons to be massless, as any explicit mass term would violate the gauge invariance itself. Because of the gauge principle, we can't just add additional mass terms to the system. We also can't put away the gauge invariance as the whole theory becomes non-renormalizable.

The mechanism needed to generate masses for Z and W bosons is called spontaneous symmetry breaking (SSB), where the $SU(2) \otimes U(1)$ symmetry gets broken. In SSB the Lagrangian is symmetric, or invariant, under a transformation, but the ground state, describing the minimum of the system, is not. We can break the symmetry by expanding the state around a minimum and we say that the breaking is spontaneous as it does not happen for external reasons.

The spontaneous electroweak symmetry breaking introduces a new scaler boson called the Higgs boson. A complex scaler field in the of a doublet of $SU(2)$ with $Y = 1$ is introduced in this model. Now we want to break the electroweak symmetry. For this, we need to introduce a new scalar SU(2) doublet:

$$\Phi = \begin{pmatrix} \phi^+ \\ \\ \phi^0 \end{pmatrix} = \frac{1}{\sqrt{2}} \begin{pmatrix} \phi_1 + i\phi_2 \\ \\ \phi_3 + i\phi_4 \end{pmatrix} \tag{1.10}$$

The BEH lagrangian can consequently be written as:

$$\mathcal{L}_{BEH} = (D_\mu \Phi)^\dagger (D_\mu \Phi) - \mu^2 \Phi^\dagger \Phi - \lambda (\Phi^\dagger \Phi)^2 \tag{1.11}$$

where $D_\mu$is the $SU(2)_L \otimes U(1)_Y$ covariant derivative from 1.11. We can separate the potential out of the Lagrangian:

$$V(\Phi) = \mu^2 \Phi^\dagger \Phi + \lambda (\Phi^\dagger \Phi)^2 \tag{1.12}$$

The extrema of the potential can be found by calculating the zeros of the derivative.

$$\frac{\partial V}{\partial \Phi^\dagger} = (\mu^2 + 2\lambda \Phi^\dagger \Phi)\Phi = 0 \tag{1.13}$$

Next, we will allow the mass (or the minimum) to be negative, $\mu^2 < 0$, which gives us the so-called Mexican hat potential, as shown on the right-hand side in Figure 1.2, where a maximum appears at $\Phi = 0$. The minimum is now shifted to a specific non-zero value of $\Phi = \sqrt{-\frac{\mu^2}{2\lambda}}$, which breaks the symmetry spontaneously. This non-zero vacuum expectation value generates mass terms for the electroweak gauge bosons ($W^\pm$ and Z^0) while leaving the photon massless.

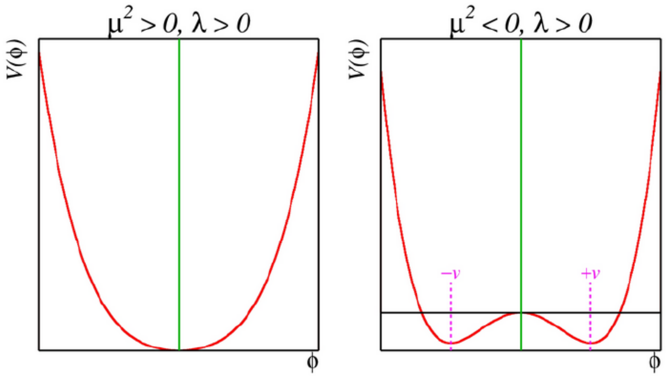

FIGURE 1.2: Potential of the scalar field for different parameters

Symmetries of the vacuum state

We are free to choose the minimum. From Eq. (1.13) we may write the vacuum state (minimum) now as,

$$\Phi^\dagger\Phi = \begin{pmatrix} \phi^{+\dagger} & \phi^{0\dagger} \end{pmatrix} \begin{pmatrix} \phi^+ \\ \\ \phi^0 \end{pmatrix} \tag{1.14}$$

from where

$$< \Phi^\dagger\Phi >= \phi^{+\dagger}\phi^+ + \phi^{-\dagger}\phi^- = -\frac{\mu^2}{2\lambda} \tag{1.15}$$

It follows that

$$\phi^- = 0 \quad \text{and} \quad \phi^+ = \sqrt{\frac{-\mu^2}{2\lambda}} = \frac{v}{\sqrt{2}} \tag{1.16}$$

This corresponds to choosing the so-called unitary gauge. We can explicitly check how this ground state responds to the symmetries of $SU(2)_L \otimes U(1)_Y$. If it was invariant, we would get:

$$e^{ia\Lambda}\Phi_{ground} = \Phi_{ground} \Rightarrow \Lambda\Phi_{ground} = 0$$

where Λ is one of the generators of $SU(2)_L \otimes U(1)_Y$, namely $\Lambda = T^{1,2,3}$ or $\Lambda = Y/2 = 1$. However, we have:

$$T^1\Phi_{ground} = \frac{1}{2}\begin{pmatrix} 0 & +1 \\ 1 & 0 \end{pmatrix}\begin{pmatrix} 0 \\ v/\sqrt{2} \end{pmatrix} = \frac{+1}{2}\begin{pmatrix} v/\sqrt{2} \\ 0 \end{pmatrix} \neq 0 \tag{1.17a}$$

$$T^2\Phi_{ground} = \frac{1}{2}\begin{pmatrix} 0 & -i \\ i & 0 \end{pmatrix}\begin{pmatrix} 0 \\ v/\sqrt{2} \end{pmatrix} = \frac{-i}{2}\begin{pmatrix} v/\sqrt{2} \\ 0 \end{pmatrix} \neq 0 \tag{1.17b}$$

$$T^3\Phi_{ground} = \frac{1}{2}\begin{pmatrix} 1 & 0 \\ 0 & -1 \end{pmatrix}\begin{pmatrix} 0 \\ v/\sqrt{2} \end{pmatrix} = \frac{-1}{2}\begin{pmatrix} 0 \\ v/\sqrt{2} \end{pmatrix} \neq 0 \tag{1.17c}$$

$$Y\Phi_{ground} = \frac{1}{2}\begin{pmatrix} 1 & 0 \\ 0 & +1 \end{pmatrix}\begin{pmatrix} 0 \\ v/\sqrt{2} \end{pmatrix} = \frac{+1}{2}\begin{pmatrix} 0 \\ v/\sqrt{2} \end{pmatrix} \neq 0 \tag{1.17d}$$

The ground state does not respect any of these symmetries. But we can find one symmetry that is still there. The electric charge Q can be written as $Q = T^3 + Y/2$. We can operate Φ_{ground} by Q:

$$Q\Phi_{ground} = (T^3 + Y/2)\Phi_{ground} = \frac{1}{2}\left[\begin{pmatrix} 1 & 0 \\ 0 & -1 \end{pmatrix} + \begin{pmatrix} 1 & 0 \\ 0 & 1 \end{pmatrix}\right]\begin{pmatrix} 0 \\ v/\sqrt{2} \end{pmatrix} = 0 \tag{1.18}$$

With the pattern $SU(2)_L \otimes U(1)_Y \rightarrow U(1)_{em}$ electroweak symmetry group is thus broken and is therefore still a symmetry of the Lagrangian around this minimum. Hence we have broken three generators out of the original four. According to Goldstone's theorem [13], the spontaneous symmetry breaking in the electroweak theory initially suggests the emergence of three massless Nambu-Goldstone bosons. However, in the Brout-Englert-Higgs mechanism, these bosons are absorbed by the $W^{\pm}$ and Z^0 gauge bosons, endowing them with mass while leaving the photon massless. Therefore, the originally anticipated massless particles get assimilated into the massive vector bosons, elucidating that after symmetry breaking, the observed massless particles no longer exist as separate entities.

Gauge boson masses and the Higgs boson

The field $\Phi(x)$ may be expressed using S $U(2)$ transformations by incorporating four scalar fields θ_1, θ_2, θ_3, and h. These fields serve as parameters that describe fluctuations around the minimum state:

$$\Phi(x) = \exp^{iT^a\theta_a/v} \begin{pmatrix} 0 \\ \frac{v+h}{\sqrt{2}} \end{pmatrix} \simeq \frac{1}{2} \begin{pmatrix} \theta_2 + i\theta_1 \\ v + h - i\theta_3 \end{pmatrix} \tag{1.19}$$

The fields θ_1, θ_2, and θ_3 represent the massless Goldstone bosons resulting from the electroweak symmetry breaking. They are removable from the Lagrangian through an SU(2) gauge transformation, leading to the resulting field expressed in what is commonly known as the unitary gauge:

$$\Phi(x) = \begin{pmatrix} 0 \\ \frac{v+h}{\sqrt{2}} \end{pmatrix} \tag{1.20}$$

Where $h(x)$is the scalar Higgs field. We'll drop the explicit dependence of the field h on the space-time coordinate and use the gauge principle as before. By using the covariant derivative, we wish to examine the first term of the Lagrangian: $|D_\mu\Phi|^2$, as it holds all the interesting kinematic contributions of the system. By inserting the covariant derivative to the term 1.11.

$$\mathcal{D}\Phi = \frac{1}{\sqrt{2}} \begin{pmatrix} \partial_\mu + i\frac{g}{2}W_\mu^3 + i\frac{g^{'}}{2}B_\mu & \frac{ig}{2}\big(W_\mu^1 - iW_\mu^2\big) \\ \frac{ig}{2}\big(W_\mu^1 + iW_\mu^2\big) & \partial_\mu - i\frac{g}{2}W_\mu^3 + i\frac{g^{'}}{2}B_\mu \end{pmatrix} \begin{pmatrix} 0 \\ v+h \end{pmatrix}$$

$$= \frac{1}{\sqrt{2}} \begin{pmatrix} \frac{ig}{2}\big(W_\mu^1 - iW_\mu^2\big)\big(v+h\big) \\ \partial_\mu h - i\big(v+h\big)\big(\frac{g}{2}W_\mu^3 - \frac{g^{'}}{2}B_\mu\big) \end{pmatrix}$$

And the conjugate is:

$$\mathcal{D}\Phi^\dagger = \frac{1}{\sqrt{2}} \Big(\tfrac{-ig}{2}\big(W_\mu^1 + iW_\mu^2\big)\big(v+h\big), \partial_\mu h + i\big(v+h\big)\big(\tfrac{g}{2}W_\mu^3 - \tfrac{g^{'}}{2}B_\mu\big)\Big)$$

Using the fields for the physical particles for the photon(A_μ or γ^μ), $W^\pm$ and Z^0 bosons in the above equation. Thus the kinetic term can be then written as:

$$|\mathcal{D}\Phi|^2 = \frac{1}{2}(v+h)^2 \begin{pmatrix} 0 & 1 \end{pmatrix} \begin{pmatrix} \partial_\mu + i\frac{g}{2}W_\mu^3 + i\frac{g^{'}}{2}B_\mu & \frac{ig}{2}\big(W_\mu^1 - iW_\mu^2\big) \\ \frac{ig}{2}\big(W_\mu^1 + iW_\mu^2\big) & \partial_\mu - i\frac{g}{2}W_\mu^3 + i\frac{g^{'}}{2}B_\mu \end{pmatrix}^2 \begin{pmatrix} 0 \\ 1 \end{pmatrix} \tag{1.21}$$

This equals to

$$|\mathcal{D}\Phi|^2 = \frac{1}{2}\partial_\mu h \partial^\mu h + \frac{1}{2}(v+h)^2 \big(\frac{g^2}{4}W_\mu^- W^{+\mu} + \frac{1}{4}(g^2 + g^{'2})Z_\mu Z^\mu\big) \tag{1.22}$$

Mass terms have appeared in the Lagrangian. The masses for W± and Z can be read from the Lagrangian and are:

$$m_W = \frac{vg}{2} \qquad\qquad m_Z = \frac{v\sqrt{g^2 + g^{'2}}}{2} \tag{1.23}$$

It's also worth noting that the photon is still massless. Also, the Weinberg angle introduced previously can be written as the ratio between the weak gauge boson masses:

$$\cos\theta_W = \frac{m_W}{m_Z} \tag{1.24}$$

This angle is a phenomenologically interesting factor. It states that by measuring the Weinberg angle and the masses, the relation is a great consistency check of the SM. Indeed, the factor

$$\rho = \frac{m_W}{m_Z \cos\theta_W} \tag{1.25}$$

has been experimentally measured to be really close to one [14]

Because the photon field doesn't appear in this mass term means that the photons stay massless after the SSB as they should. The potential part 1.11 of the scalar Lagrangian 2.58 is easy to calculate using the fact that $\Phi^\dagger\Phi = 1/22(v+h)^2$ and that $\lambda = -(\mu v)^2$ (as defined in 1.16)

$$\begin{aligned}
V(\Phi) &= \mu^2\Phi^\dagger\Phi + \lambda(\Phi^\dagger\Phi)^2 && (1.26)\\
&= \frac{1}{2}(v+h)^2(\mu^2 + \lambda\frac{1}{2}(v+h)^2) && (1.27)\\
&= \frac{1}{2}(v+h)^2(\mu^2 - (\frac{\mu}{v})^2\frac{1}{2}(v+h)2) && (1.28)\\
&= \frac{\mu^2 v^2}{2} - \mu^2 h^2 - \frac{\mu^2}{v}h^2 - \frac{\mu^4}{v^4}h^4 && (1.29)
\end{aligned}$$

The first term does not depend on any fields and therefore it does not affect the physics of the system and can be dropped. The entire Lagrangian is:

$$\mathcal{L}_{BHE} = \frac{1}{2}\partial_\mu h \partial^\mu h - \frac{1}{2}(2\lambda)h^2 \tag{1.30}$$

$$+ \Big[(\frac{gv}{2})^2 W^{\mu +}W^-_\mu + \frac{1}{2}\frac{v^2(g^2 + g^{'2})}{4} Z^\mu Z_\mu\Big]\Big(1 + \frac{h}{v}\Big)^2 \tag{1.31}$$

$$- \lambda v h^3 - \frac{\lambda}{4}h^4 + \frac{\lambda}{4}v^4 \tag{1.32}$$

The massless Goldstone bosons transfer their degrees of freedom to the $W^\pm$ and Z bosons, resulting in the acquisition of mass by these massive gauge bosons. It can be observed that the Goldstone bosons, removed with the unitary transformation, are absorbed as additional degrees of freedom of the $W^\pm$ and Z bosons, corresponding to their longitudinal polarizations: the mechanism gives mass to the weak bosons. Here are also the termns hWW and a hZZ interactions from the $2h/v$ term and a $hhWW$ and a $hhZZ$ interaction from the h^2/v^2 term. In addition, these terms have triple and quartic coupling terms of the field h with the two heavy gauge bosons $W^\pm$ and Z, which are proportional to the mass squared of the gauge boson, $\lambda_{VVh} = 2m_v^2/v^2$ and $\lambda_{VVhh} = m_v^2/v^2$respectively.

These boson masses terms can now be identified by looking at the terms in the equations 1.23 and the Higgs boson has mass m_h, given by

$$m_h = \sqrt{-2\mu^2} = v\sqrt{2\lambda} \tag{1.33}$$

The remaining terms in Equation 1.32 represent the interactions of the weak bosons with the Higgs field and the trilinear and quadlinear Higgs self-interactions, h^3 and h^4.

The third line in 1.32 that cubic and quartic self-interactions of the Higgs boson are predicted. The BEH potential can be rewritten in terms of a trilinear and a quadrilinear coupling as:

$$V(H) = \frac{1}{2} m_v^2 h^2 + \lambda_{hhh} v h^3 + \lambda_{hhhh} h^4 - v^4 \tag{1.34}$$

with the trilinear and quartic self-coupling constants for the Higgs boson are defined as:

$$\lambda_{hhh} = \frac{m_H^2}{2v^2} \tag{1.35}$$

and

$$\lambda_{hhhh} = \frac{m_H^2}{8v^2} \tag{1.36}$$

Figure 1.3 illustrates the Feynman vertices that represent the trilinear interaction of Higgs bosons (depicted in (a)) and the quartic self-interaction of Higgs bosons (shown in (b))

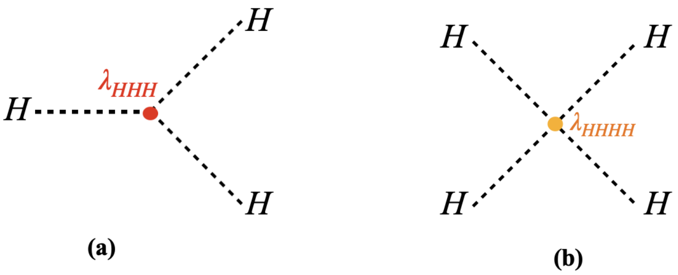

FIGURE 1.3: (a) Depicts the Feynman vertices representing the trilinear interaction among Higgs bosons, while (b) illustrates the Feynman vertices corresponding to the quartic self-interaction of Higgs bosons.

An important remark is that both Higgs boson self-couplings and the scale of the weak boson masses are closely associated with to the parameters of the scalar potential and are entirely determined from the mass of the Higgs boson and the VEV (vacuum expectation value) v. Their measurement thus represents a test of the validity and coherence of the SM. This can be evaluated by using the

Fermi constant G_F empirical value from the decay of the muon or expectation value of the Higgs field, given by $v = (\sqrt{2}G_F)^{-1/2} \sim 246$ GeV.

In a wider perspective, the Higgs boson self-couplings have no equal in the SM: in contrast to the weak boson self-interactions, which have a gauge nature, the Higgs boson self-interactions are purely related to the scalar sector of the theory and they are responsible for the mass of the Higgs boson itself.

Their experimental determination is thus crucial to reconstruct the Higgs boson potential and exploring the nature of the Electro-Weak symmetry breaking. Finally, there is a constant term in the Lagrangian density of BEH . While this is irrelevant in the SM, it contributes to the vacuum energy, which is related to the cosmological constant that determines the curvature of the Universe. The value of this constant predicted in the SM is not compatible with astronomical observations. This is a puzzle that requires either a proper quantum theory of gravity with additional interactions or a mechanism to reduce the Higgs field vacuum energy density.

However, while the masses of the Higgs boson (m_h) and vector bosons cannot be precisely predicted due to λ, g, and g' being free parameters within the theory, their accurate measurements are crucial. These measurements include both the boson masses and their interactions with the Higgs boson, essential for scrutinizing the BEH mechanism, the electroweak theory, and the Standard Model itself. The primary objective of this thesis is to enhance the measurement precision and refine calculations pertaining to fake factors. Additionally, it aims to visualize and analyze model improvements in the investigation of di-Higgs production. This pursuit intends to probe the triple Higgs self-coupling (λ_{hhh}) and, consequently, gain insights into the structure of the Higgs potential.

1.4 Fermion Masses and Yukawa Coupling

The Higgs mechanism, presented in the preceding section, adequately explains the masses of vector bosons; however, it does not account for fermion masses. Incorporating direct mass terms for fermions would violate the gauge invariance of the Lagrangian. However, by introducing a new gauge-invariant interaction term known as the Yukawa term, fermions can acquire their masses through interactions with the Higgs field, similar to the mechanism through which vector bosons obtain their masses.

In the Standard Model of particle physics, each fermion type, such as electrons, quarks, and neutrinos, is associated with a corresponding Yukawa coupling. The Yukawa coupling term is given by:

$$\mathcal{L}_{\text{Yukawa}} = -\sum_f \left[y_f \bar{\psi}_f \phi \psi_f + y'_f \bar{\psi}'_f \phi^\dagger \psi'_f \right], \tag{1.37}$$

where $\mathcal{L}_{\text{Yukawa}}$ represents the Yukawa Lagrangian term, y_f and y'_f are the Yukawa coupling constants specific to fermions f and f' respectively, $\bar{\psi}_f$ and $\bar{\psi}'_f$ are the Dirac conjugates of the fermion fields, ϕ denotes the Higgs field, and ψ_f and ψ'_f represent the fermion fields.

For leptons, the Yukawa coupling term can be written as:

$$\mathcal{L}_{\text{Yukawa, lepton}} = -\sum_\ell \left[y_\ell \bar{L}_\ell \phi E_\ell + y'_\ell \bar{E}_\ell \phi^\dagger L_\ell \right], \tag{1.38}$$

where ℓ represents the lepton generation, y_ℓ and y'_ℓ are the Yukawa coupling constants for leptons, L_ℓ denotes the lepton doublet field, and E_ℓ represents the lepton singlet field.

For quarks, the Yukawa coupling term can be written as:

$$\mathcal{L}_{\text{Yukawa, quark}} = -\sum_q \left[y_q \bar{Q}_q \phi q + y'_q \bar{q} \phi^\dagger Q_q \right], \tag{1.39}$$

where q represents the quark generation, y_q and y'_q are the Yukawa coupling constants for quarks, Q_q denotes the quark doublet field, and q represents the quark singlet field.

The Yukawa terms allow for the interaction between fermions and the Higgs field, resulting in the generation of fermion masses. When the Higgs field acquires a vacuum expectation value (VEV), denoted as $\langle \phi \rangle$, it breaks the electroweak symmetry and generates the masses of the fermions. The magnitude of the fermion mass is proportional to the product of the corresponding Yukawa coupling constant and the VEV.

The Yukawa coupling terms introduce interactions between the Higgs boson and fermions, which can be observed experimentally through processes such as Higgs boson decays into fermion-antifermion pairs. The discovery of the Higgs boson at the LHC in 2012 by both CMS [1] and ATLAS[2] provided strong evidence for the existence of Yukawa couplings and the mechanism through which fermions acquire their masses.

In summary, the Yukawa coupling and the associated Yukawa terms in the Lagrangian provide a gauge invariant way to explain the masses of fermions within the framework of the Standard Model. The coupling constants determine the strength of the fermion-Higgs interaction and play a crucial role in shaping the fermion mass spectrum.

1.5 The Higgs Boson

The Higgs boson is associated with the Higgs field, a scalar field that permeates the entire universe. It interacts with other particles and provides them with mass through the Higgs mechanism section 1.3. The Higgs boson's discovery confirmed the existence of the Higgs field and validated the mechanism through which particles acquire mass.

The properties of the Higgs boson, such as its mass and its couplings to other particles, are of great interest to physicists. Further studies of the Higgs boson at the LHC and future colliders aim to explore its properties in detail and shed light on unresolved questions in particle physics, such as the nature of dark matter and the possible existence of new physics beyond the Standard Model.

1.5.1 Higgs Production Modes

The Higgs boson can be produced through several processes in pp collision. The dominant production modes are:

1. **Gluon-Gluon Fusion ($gg \to H$):** This is the most common production mechanism at the LHC, where two gluons from the colliding protons fuse to form a Higgs boson through a quark loop. The theoretical prediction for the cross-section of Higgs production through ggF at $\sqrt{s} = 13$ TeV is $\sigma_H^{ggF} = 48.58$ at next-to-next-to-next-to-leading order (N3LO) in QCD and next-to-leading order (NLO) in the electroweak theory, for mH =125 GeV [15].

2. **Vector Boson Fusion ($qq \to qqH$):** In this mode, two quarks from the colliding protons emit electroweak vector bosons (W or Z) that subsequently fuse to produce a Higgs boson. The presence of the scattered quarks in the final state allows for efficient background rejection.

3. **Higgs-Strahlung ($q\bar{q} \to V^*H$):** The subsequent significant production mode of the Higgs boson at the LHC involves its association with a W or Z vector boson. The majority of the cross-section for VH primarily originates from $q\bar{q}$ annihilation, resulting in an off-shell W or Z boson that subsequently emits a Higgs boson. This process is commonly referred to as "Higgsstrahlung". In ZH production, there are contributions induced by gluon-gluon interactions that don't entail a virtual Z boson but produce H

and Z via a top quark loop. The $gg \to ZH$ production stands alone as a process whose contribution begins at $O\left(\alpha_S^2\right)$.

Figure 1.4 shows the leading-order (LO) Feynman diagrams corresponding to the above-mentioned process. Figure 1.5 summarizes the single Higgs boson production cross-sections for production modes. Other minor production modes include associated production with a top quark pair annihilation ($t\bar{t}H$), and Higgs radiation off a top quark (tH).

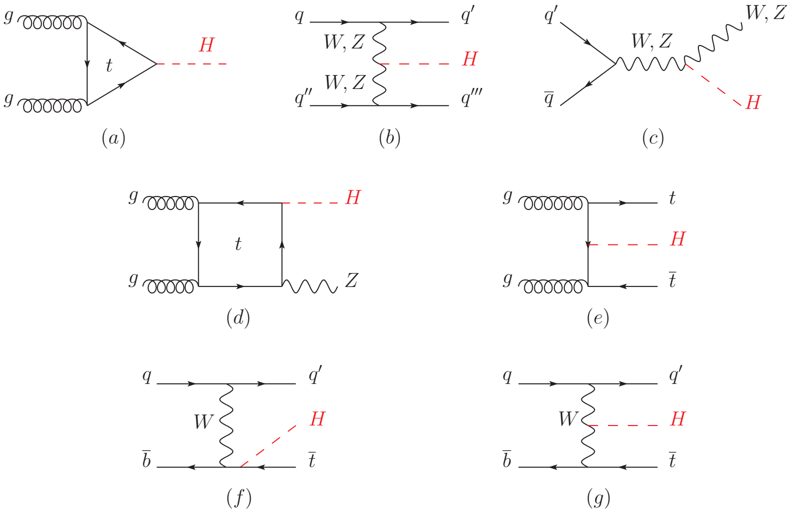

FIGURE 1.4: Examples of leading-order Feynman diagrams corresponding to the dominant mechanisms for producing the Higgs boson at the LHC.

1.5.2 Higgs Decay Modes

The Higgs boson has a relatively short lifetime and decays almost immediately after its production. The decay modes of the Higgs boson are classified based on the particles it decays into. The most common decay modes are:

1. **$H \to b\bar{b}$:** The decay into a pair of bottom quarks is the dominant mode for the Higgs boson, accounting for about 58% of its total decays. This decay channel is experimentally challenging due to the overwhelming background from other processes involving bottom quarks.

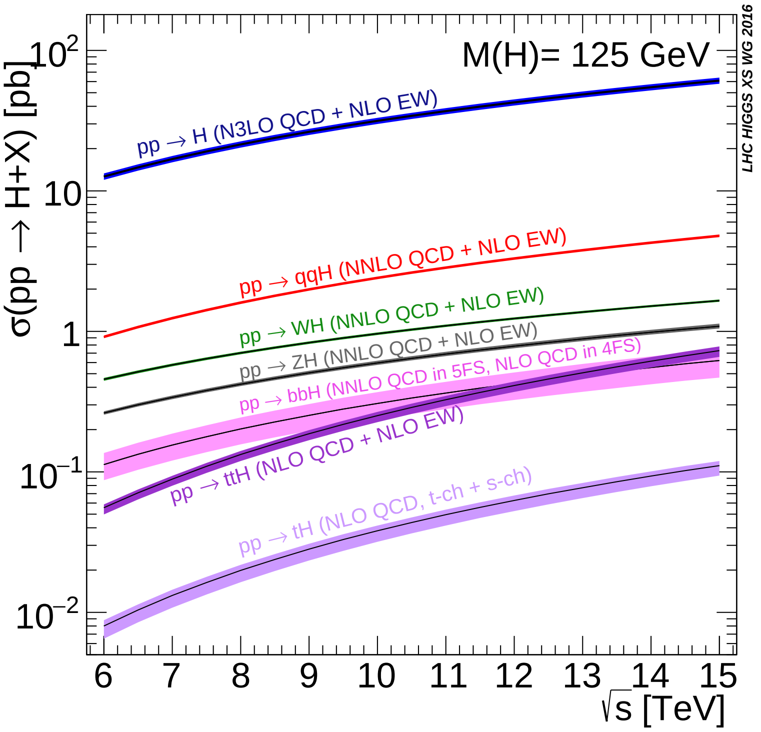

FIGURE 1.5: The cross-section for single Higgs production is depicted as a function of the center-of-mass energy ($\sqrt{s}$) for pp collisions. Each result presented here specifies the perturbation theory order from which it is derived. These outcomes have been achieved at N3LO in QCD and at NLO in the EW theory for the process $pp \to H$ [16].

2. $H \to WW^*$**:** The Higgs boson can decay into a pair of W bosons, either real or virtual. This mode accounts for approximately 21% of the Higgs decays and provides crucial information about the Higgs-W boson coupling.

3. $H \to ZZ^*$**:** Similarly, the Higgs boson can decay into a pair of Z bosons, real or virtual. This mode has a branching fraction of around 2.6% and is used to study the Higgs-Z boson coupling and properties of the Z boson.

4. $H \to \gamma\gamma$**:** This rare decay channel, with a branching fraction of about 0.23%, involves the Higgs boson decaying into a photon pair. It offers an excellent signature due to the clean experimental signature of high-energy photons.

5. $H \to \tau^+\tau^-$**:** The Higgs boson can also decay into a pair of tau leptons with a branching fraction of 6.3%. This mode is challenging to observe due to

the difficulty in distinguishing tau leptons from background processes, but it provides insights into the Higgs-lepton couplings.

Other less significant decay modes include decays to charm quark pairs ($H \rightarrow c\bar{c}$), gluon pairs ($H \rightarrow gg$), and other exotic particles.

Table 1.1 summaries the single Higgs decays with their corresponding branching ratios.

TABLE 1.1: Decay channels and branching ratios of the Higgs boson [17]

Decay Channel	Branching Ratio	Relative Uncertainty
$H \rightarrow \gamma\gamma$	2.27×10^{-3}	2.1%
$H \rightarrow ZZ$	2.62×10^{-2}	$\pm 1.5\%$
$H \rightarrow W^+W^-$	2.14×10^{-1}	$\pm 1.5\%$
$H \rightarrow \tau^+\tau^-$	6.27×10^{-2}	$\pm 1.6\%$
$H \rightarrow b\bar{b}$	5.82×10^{-1}	$+1.2\% \ -1.3\%$
$H \rightarrow c\bar{c}$	2.89×10^{-2}	$+5.5\% \ -2.0\%$
$H \rightarrow Z\gamma$	1.53×10^{-3}	$\pm 5.8\%$
$H \rightarrow \mu^+\mu^-$	2.18×10^{-4}	$\pm 1.7\%$

Figure 1.6 illustrates the branching ratios for Higgs boson decay as a function of its mass m_H. The corresponding values for a mass of $m_H = 125.09\text{GeV}$ are presented in Table 2.1. It's important to note that due to the Higgs boson's lack of coupling to massless particles such as gluons and photons, its decay into a pair of such particles occurs exclusively through quark triangle-loops. This phenomenon mirrors the process seen in ggF production, where top-quark loops, mainly attributed to their high mass and resulting large top-quark Yukawa coupling, dominate the interaction.

1.5.3 SM Higgs boson pair production at the LHC

In the Standard Model, di-Higgs (HH) events are dominantly produced via the gluon-gluon Fusion (ggF) processes at the LHC, involving both the Yukawa coupling to top quarks and the Higgs boson self-coupling. Figure 1.7 shows the

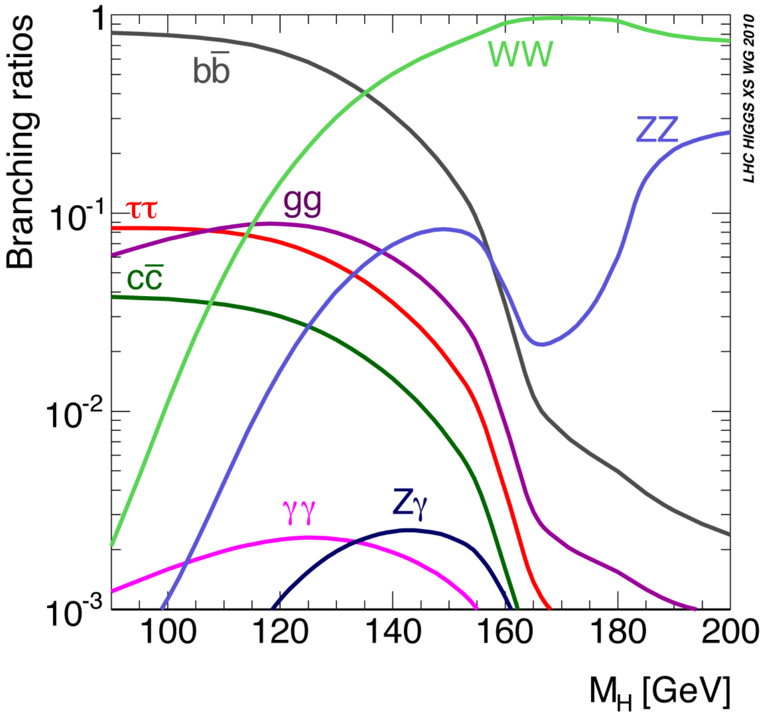

FIGURE 1.6: Decay branching ratios for standard model Higgs boson as a function of the Higgs mass m_H [16].

leading-order (LO) ggF HH production Feynman diagrams, i.e., the so-called box and triangle diagrams. These two diagrams interfere destructively, leading to a very small HH production cross-section, namely $\sigma^{SM}_{\text{ggF},HH} = 31.05 \pm 3\%$ (PDF+α_s) $^{+6\%}_{-23\%}$ (Scale + m_{top}) fb, calculated at next-to-next-to-leading-order (NNLO) accuracy in the finite top-quark mass approximation for $m_H = 125$ GeV and $\sqrt{s} = 13$ TeV [18, 19]. The HH production cross-section is about three orders of magnitude smaller than the dominant single Higgs boson production [17].

The second most dominant mode to produce a Higgs boson pair in the SM is the vector-boson fusion (VBF) process, with an even smaller production cross-section of $\sigma^{SM}_{\text{VBF},HH} = 1.726 \pm 2.1\%$ (PDF+α_s) $^{+0.03\%}_{-0.04\%}$(Scale) fb for $m_H = 125$ GeV at $\sqrt{s} = 13$ TeV [18]. The three tree-level diagrams for VBF HH production are shown in Figure 1.8.

Figure 1.9 highlighted the possible decay channels for a pair of Higgs bosons. The $b\bar{b}b\bar{b}$ channel has the highest branching ratio, however this channel is being suffered by the large QCD backgrounds. The $b\bar{b}\gamma\gamma$ channel branching ratio is

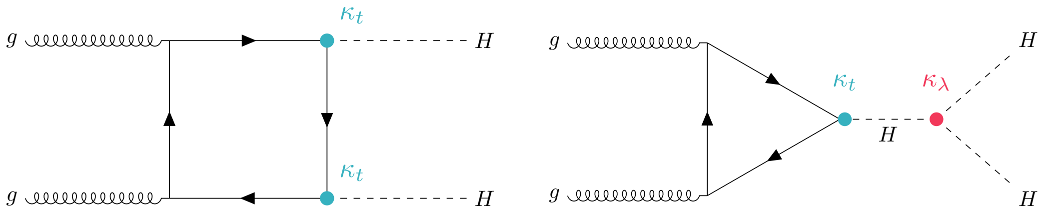

(A) Box Diagram

(B) Triangle Diagram

FIGURE 1.7: Feynman diagrams at the leading order illustrate the non-resonant ggF Higgs boson pair production in the Standard Model via (a) the involvement of the top-quark loop and (b) the triple self-coupling of the Higgs boson. The parameters κ_t and κ_λ denote the effective Higgs boson couplings. The κ_t is defined as $\kappa_t \equiv y_t/y_t^{\mathrm{SM}}$ while κ_λ defined as $\kappa_\lambda \equiv \lambda_{HHH}/\lambda_{HHH}^{\mathrm{SM}}$.

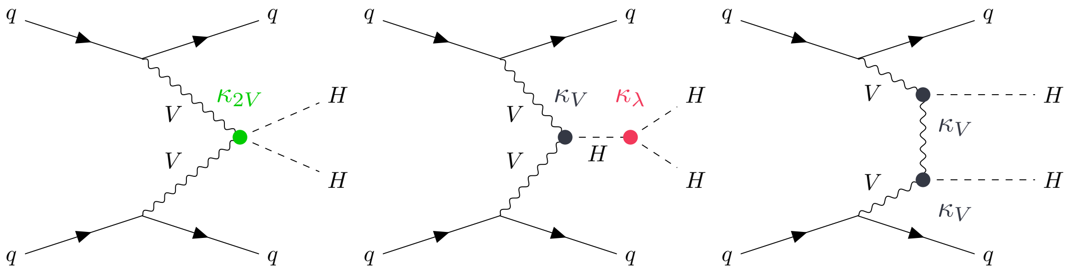

FIGURE 1.8: Tree-level Feynman diagrams for the non-resonant VBF HH production mode. The vertices denoted by κ_{2V}, κ_V and κ_λ, represent the $VVHH$, VVH, and HHH coupling modifiers, respectively.

significantly smaller compare to $b\bar{b}b\bar{b}$ channel however, it can take the advantage of excellent detector resolution in reconstructing the di-photon invariant mass. The $b\bar{b}\tau^+\tau^-$ final state of the Higgs pair decay has reasonable branching fraction of 7.3%. Due to its relatively high branching ratio and moderate background rates, this channel stands out as one of the most promising avenues to explore for the search of Higgs boson pair production.

The focus of this thesis revolves around the investigation of the $HH \rightarrow b\bar{b}\tau^+\tau^-$ decay channel. The pursuit of Higgs pair production searches holds paramount significance as it delves into one of the unmeasured property of the Higgs boson, the Higgs self-interaction. These searches are instrumental not only in exploring the Higgs self interaction but also in directly probing the Higgs potential, ultimately validating the fundamental physics principles outlined in the Standard Model.

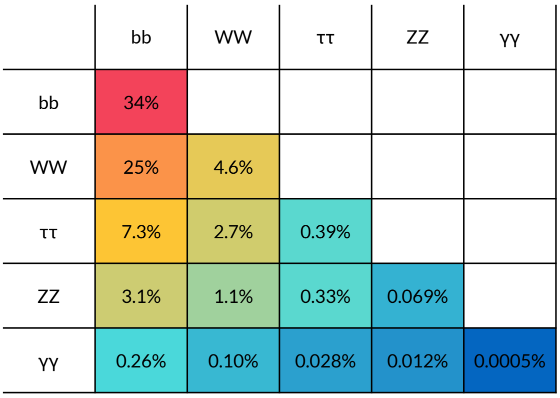

	bb	WW	ττ	ZZ	γγ
bb	34%				
WW	25%	4.6%			
ττ	7.3%	2.7%	0.39%		
ZZ	3.1%	1.1%	0.33%	0.069%	
γγ	0.26%	0.10%	0.028%	0.012%	0.0005%

FIGURE 1.9: The table presents the branching fractions for different decay channels of a pair of Higgs bosons, considering a Higgs boson mass of $m_H = 125.09$ GeV [18]

1.6 Limitations of the Standard Model

Over the past decades, the Standard Model (SM) has enjoyed remarkable success, accurately predicting the existence of various elementary particles, including the Higgs boson. Despite these achievements, the SM falls short in explaining numerous observed phenomena. As a result, scientists believe that the SM is merely an effective representation of a more fundamental theory, yet to be discovered at energies beyond our current reach.

One significant drawback of the SM is its failure to incorporate gravity. At distances smaller than the Planck length [2], the SM and general relativity become incompatible, and quantum effects of gravity are expected to dominate.

Numerous Grand Unified Theory (GUT) models propose the unification of electromagnetic, weak, and strong forces into a single force at high energies approaching the Planck scale. These models possess a more elegant structure than the SM, which relies on 19 somewhat ad hoc independent parameters (excluding

---

[2] The Planck length is defined as $l_p = \sqrt{\frac{\hbar G_N}{c^3}} = 1.616229(38) \times 10^{-35}$ meters, where G_N represents the Newtonian constant of gravitation, corresponding to the Planck mass $M_{pl} = 1.2208090(14) \times 10^{19}$ GeV [12]. These values are commonly known as the Planck scale.

neutrinos as massive particles). Though the SM can be extended to accommodate massive neutrinos, it cannot predict their masses accurately. Additionally, the SM faces the challenge of fine-tuning loop corrections to the Higgs boson mass to explain its value, which deviates significantly from the Planck energy scale. This issue is known as the SM fine-tuning problem.

Another perplexing puzzle within the SM arises from the disparity between theoretical predictions and experimental measurements of the anomalous magnetic moment of the muon. Despite its precise prediction and measurement, a notable discrepancy remains [20].

The Standard Model faces challenges in elucidating the dominance of matter compared to antimatter in the Universe. Despite demonstrating CP symmetry violation in quark and neutrino sectors, the Standard Model's explanation falls short in addressing the observed matter-antimatter asymmetry. Notably, the lack of substantial electromagnetic radiation resulting from matter-antimatter annihilation suggests a scarcity of antimatter in extensive regions. The existing imbalance is attributed to a theoretical concept known as baryogenesis; however, its compatibility with the Standard Model remains uncertain.

Additionally, the SM assumes the conservation of lepton flavor universality. Nevertheless, recent reports from the BaBar [21, 22], Belle [23, 24], and LHCb [25, 26] collaborations have indicated signs of lepton flavor universality violation over the past decade. These findings reveal anomalies in B-meson decay and persistent deviations from SM predictions.

One of the most significant limitations of both the SM and general relativity is their inability to explain astrophysical and cosmological observations that point to the existence of dark matter and dark energy. Various observations, such as the rotational curves of nearby galaxies, suggest the presence of significantly more gravitational matter than what is observable. Approximately 5% of the total energy density of the Universe is accounted for by visible matter, while dark matter constitutes another 27%, leaving the remaining portion attributed to dark energy. However, the SM lacks suitable particle candidates to explain the properties of dark matter, necessitating the introduction of new physics to address these phenomena. Dark energy remains an even greater mystery, believed to be uniformly distributed throughout the Universe, causing its accelerated expansion [27].

Beyond the SM (BSM) theories have been proposed to address the aforementioned limitations of the SM. Some of these theories predict heavy resonances that could decay into pairs of Higgs bosons, such as scalar resonances from two-Higgs-doublet models [6] or spin-2 Kaluza-Klein excitations of the graviton.

Chapter 2

The ATLAS detector at the LHC

CERN, the European Organisation for Nuclear Research, stands as a prominent hub of scientific investigation globally. Situated near Geneva on the French-Swiss border, it houses the largest and most intricate scientific instruments known to mankind. These instruments serve the purpose of delving into the fundamental building blocks of matter and exploring the fundamental structure of the universe. Established in 1954, CERN aimed to establish a center of scientific excellence in Europe, becoming one of the earliest collaborative endeavors on the continent. Presently, it boasts 22 member states. Central to CERN's operations are its particle accelerators and detectors. A series of accelerators propel beams of particles, such as protons and ions, to exceedingly high energies, ultimately causing them to collide within the LHC. Detectors meticulously observe and record the aftermath of these collisions, with one notable example being the ATLAS experiment, whose data are instrumental in the context of this thesis.

In this chapter, we embark on an exploration of the Large Hadron Collider accelerator, offering a concise explanation of the physics behind pp collisions. Additionally, we delve into the realm of Monte Carlo simulations employed within the ATLAS framework. A focal point of this chapter is an introduction to the ATLAS experiment, wherein we discuss the crucial detector components responsible for triggering and capturing data events essential for physics analyses. For more comprehensive insights into the structure and functionalities of each ATLAS subsystem, we refer readers to References [28–30].

2.1 The Large Hadron Collider

The LHC [31] at CERN is an extraordinary particle accelerator, renowned for its unprecedented energy levels. This machine is purpose-built to accelerate and collide both protons and ions. Specifically, it is engineered to facilitate pp collisions, yielding a center-of-mass energy of 14 TeV and an instantaneous luminosity of 10^{34} cm^{-2}s^{-1}. Additionally, the LHC orchestrates lead ion collisions, generating a center-of-mass energy of 2.76 TeV per nucleon and an instantaneous luminosity of 10^{27} cm^{-2}s^{-1}.

To achieve the high energies required for experiments, a series of accelerators form an injector chain leading to the LHC, as depicted in Figure 2.1. Protons are extracted from a hydrogen bottle using electric fields and then fed into the first accelerator. Each accelerator increases the protons' energy before passing them on to the next, ultimately reaching the LHC with an initial energy of 450 GeV. Upon reaching the designed energy, the rotating proton beams in the LHC collide at four interaction points (depicted as yellow dots in Figure 2.1), where specialized particle detectors analyze the products of these high-energy collisions.

Within the LHC, there are four beam-crossing points where seven [1] experiments are situated, with four main ones being ATLAS [30], CMS [32], ALICE [33], and LHCb[34]. ATLAS and CMS are considered general-purpose particle detectors and play a crucial role in verifying the SM through precise parameter measurements and the search for new physics. Among their achievements is the discovery of the Higgs boson, solidifying their status as leading TeV-scale particle physics projects. The ALICE experiment focuses on studying the strong-interaction sector of the SM, exploring quark-gluon plasma in Pb-Pb collisions at extreme energy densities and temperatures. LHCb, on the other

---

[1] The FASER experiment received approval in 2019 and is scheduled to commence operations in 2022. It aims to explore new domains related to light and weakly-coupled particles while also investigating the interactions of high-energy neutrinos.

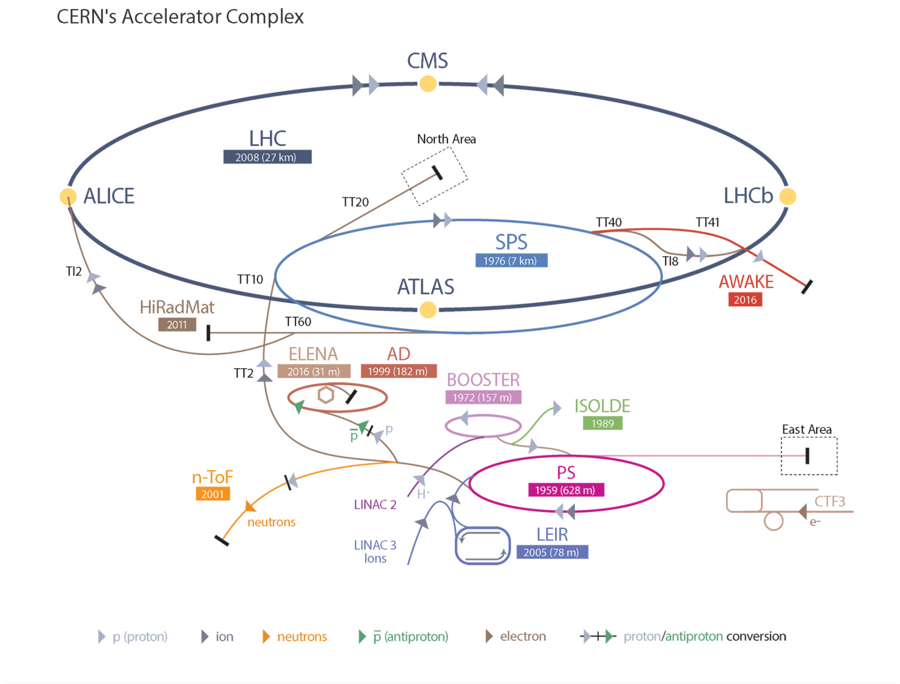

FIGURE 2.1: The configuration of the LHC and the CERN accelerator complex, which serves as the injector chain for the LHC [31]

hand, specializes in precise measurements of CP violation and rare B-hadron decays, investigating lepton universality and flavor physics. The other three experiments, TOTEM [35], LHCf, and MoEDAL[36], have smaller footprints. TOTEM measures total pp cross-sections and elastic and diffractive scattering processes. LHCf[37] studies properties of neutral particles emitted in the forward region of LHC collisions. Lastly, MoEDAL is designed to search for magnetic monopoles predicted by certain Grand Unified Theories (GUT) and superstring theories.

2.1.1 LHC Machine Overview

The LHC is a circular particle accelerator spanning a 27 km circumference, situated within a tunnel originally constructed for the Large Electron-Positron (LEP) collider between 1984 and 1989. This tunnel, positioned between the Jura mountains and Geneva airport, lies at depths ranging from 45m to 170m below the ground surface.

Proton beams are introduced into the LHC in groups, or bunches, each carrying 1.15×10^{11} protons. These bunches, totaling 2808, are organized into "trains" consisting of 72 bunches each. Within a train, the spacing between bunches is 25 ns, while 12 empty bunches separate consecutive trains. The acceleration of proton beams is facilitated through radio frequency (RF) cavities, while powerful magnetic fields, generated by dipoles reaching 8.33 T, guide the beams along the LHC ring. Additional quadrupoles and higher-order magnets serve to focus and adjust the beam trajectory. To accommodate two counter-rotating proton beams within the same circumference, a single cryogenic structure employing a complex twin-bore design houses both proton rings.

Collisions between circulating beams occur at "bunch crossings," yielding a peak collision rate of 40 MHz. In order to maximize the collision rate, the transverse size of the beams is reduced to 17 μm at the IP. Over an approximate distance of 140 m in each direction at the IP, both beams are confined within a single beam pipe to prevent unintended collisions. When beams are brought together at the interaction point, the separation between them is eliminated.

The collision rate is influenced by the instantaneous luminosity $\mathcal{L}$ and the collision cross section σ, linked through the relationship:

$$\frac{dN}{dt} = \mathcal{L} \cdot \sigma \tag{2.1}$$

The expression for instantaneous luminosity is defined as:

$$\mathcal{L} = \frac{N_b^2 n_b f_{\text{rev}} F \gamma}{4\pi \epsilon \beta^*} \tag{2.2}$$

Here, N_b denotes the number of particles per bunch, n_b signifies the number of bunches per beam, and f_{rev} represents the revolution frequency. Additionally, F is a geometric function accounting for the beam crossing angle, γ refers to the relativistic Lorentz factor, ϵ quantifies the beam emittance, and β^* characterizes the beam's size at the interaction point.

The integrated luminosity $L = \int \mathcal{L}, dt$ signifies the cumulative number of collisions. For a specific process with cross section σ_{process}, the corresponding number of events N_{process} is given by $N_{\text{process}} = L \cdot \sigma_{\text{process}}$. Given the small cross sections of many intriguing physics phenomena at the LHC, maximizing luminosity is imperative to capture as many relevant events as possible.

2.1.2 The Operational Timetable of the LHC

The LHC started its operations in November 2009, initiating pp collisions at an initial center-of-mass energy of 900 GeV. During the initial year, the centre-of-mass energy progressively increased, and by 2010, it was successfully raised to 7 TeV. Continuing its operations from 2010 to 2011, the LHC operated at a center-of-mass energy level of 7 TeV, which was later enhanced to 8 TeV in 2012. At the conclusion of its first operational phase, known as Run 1, the LHC delivered 5.5 fb^{-1} and 22.8 fb^{-1} at 7 TeV and 8 TeV, respectively.

After an extensive shutdown the LHC started operation for the second phase known as Run 2 in 2015, and performed the collisions at 13 TeV. The 1.38×10^{34} cm^{-2}s^{-1} peak of the instantaneous luminosity was achieved at 25 ns bunch crossing. Throughout Run 2, which concluded in December 2018, a total luminosity of 158 fb^{-1} was delivered, while the ATLAS experiment recorded 149 fb^{-1}. Figure 2.2 illustrates the delivered LHC-integrated luminosity and ATLAS recorded during this period (Run2).

The thesis analyzes data obtained from the ATLAS experiment during Run 2, covering the period from 2015 to 2018. This dataset corresponds to an integrated luminosity of 140 fb^{-1}, following the application of the Good-Run-List requirement. This requirement ensures the full operational functionality of essential components within the ATLAS detector during data acquisition. Figure 2.3 illustrates the yearly integrated luminosity delivered by the LHC and recorded by the ATLAS experiment throughout 2015 to 2018, depicted over time.

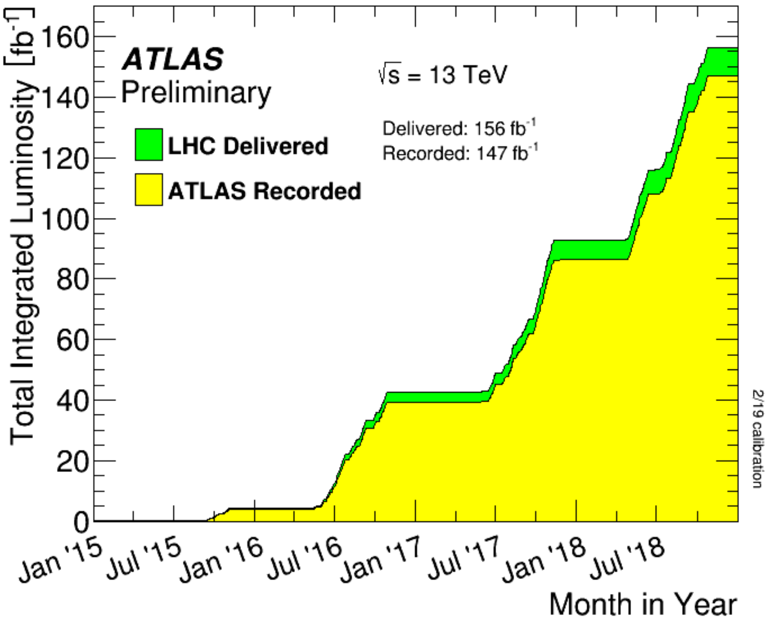

FIGURE 2.2: The integrated luminosity as function of time delivered by the LHC and recorded by the ATLAS during Run2 [38].

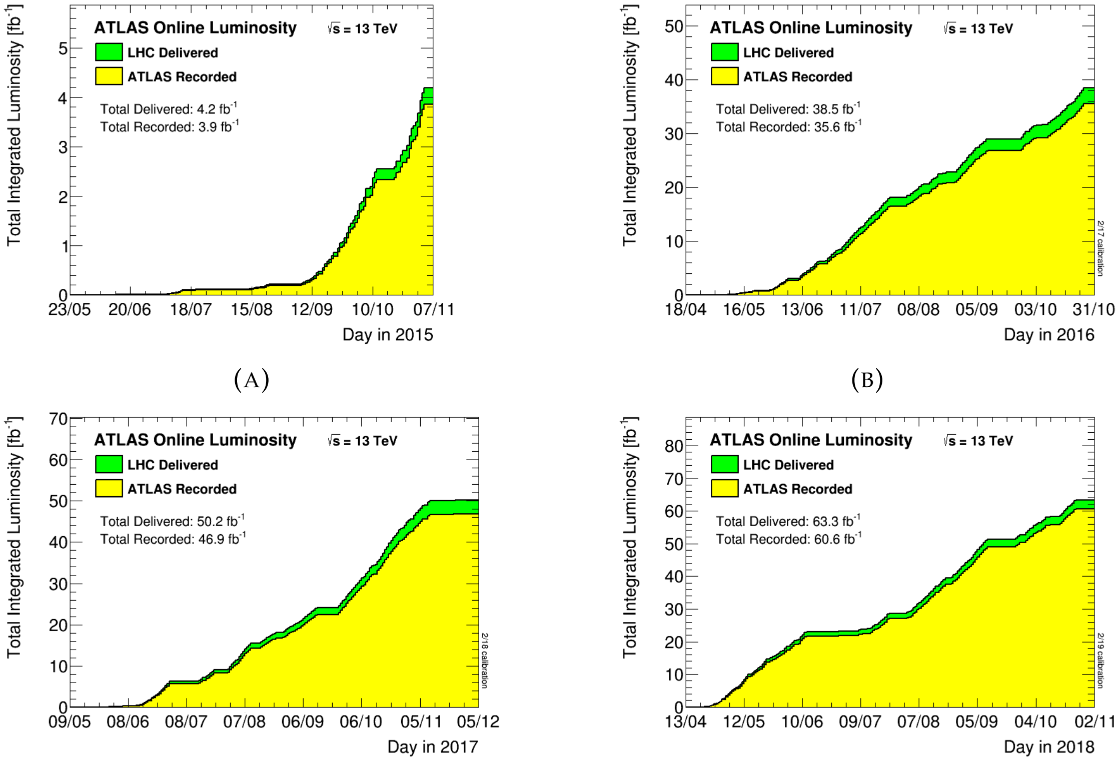

(A) (B)

(C) (D)

FIGURE 2.3: The cumulative luminosity over time, where the green line represents the delivered luminosity to ATLAS during stable beams for *pp* collisions at 13 TeV, while the yellow line represents the luminosity recorded by ATLAS in 2015 (2.3a), 2016(2.3b), 2017(2.3c) and 2018(2.3d) respectively [38].

2.2 Simulations and proton-proton process in physics

Proton-proton collisions pose significant complexities arising from the internal composition of protons collisions and the intricate interplay of QCD processes. In this section, we elucidate the phenomena inherent in pp collisions and outline the simulation for the physics processes occurring within the collisions and the ATLAS detector.

2.2.1 Physics of pp collisions

In pp collisions, fundamental interactions take place among constituents known as partons, encompassing quarks and gluons residing within the protons. These constituents exhibit behavior akin to free particles due to the principle of QCD asymptotic freedom. A proton consists of three 'valence quarks'—specifically, two up quarks and one down quark—defining the fundamental quantum properties of the proton. Gluons facilitate the binding of these quarks and also engage in interactions among the partons. Additionally, gluons can transiently fragment into quark-antiquark pairs, known as 'sea quarks,' contributing to the overall parton interactions. Each parton carries a fraction of the proton's momentum, represented as x_i, influencing the effective center-of-mass energy of the partonic collision.

The expression for the center-of-mass energy in a partonic collision is given by Equation 2.3:

$$\sqrt{\hat{s}} = \sqrt{x_1 x_2 s} \tag{2.3}$$

Here, x_1 and x_2 represent the momentum fractions carried by the interacting partons from their respective protons. Parton Distribution Functions (PDFs) [39, 40] describe the likelihood of locating a parton within a proton possessing a specific momentum fraction x_i (where $i \in (1, 2)$). These functions rely on the parton's nature and the collision's momentum transfer scale Q^2. The evolution of PDFs in (x; Q^2) is governed by the DGLAP equation [41]. In Figure 2.4, the proton's PDFs are depicted at two distinct Q^2 scales: Q^2 = 10 GeV^2 and Q^2 = 10^4 GeV^2. The figure illustrates that gluons dominate among the partons, indicating a notably high 'parton luminosity' for gluons at the LHC. Consequently, the LHC is often referred to as a 'gluon collider' due to the substantial cross-sections observed in processes initiated by gluon-gluon interactions compared to other partonic processes.

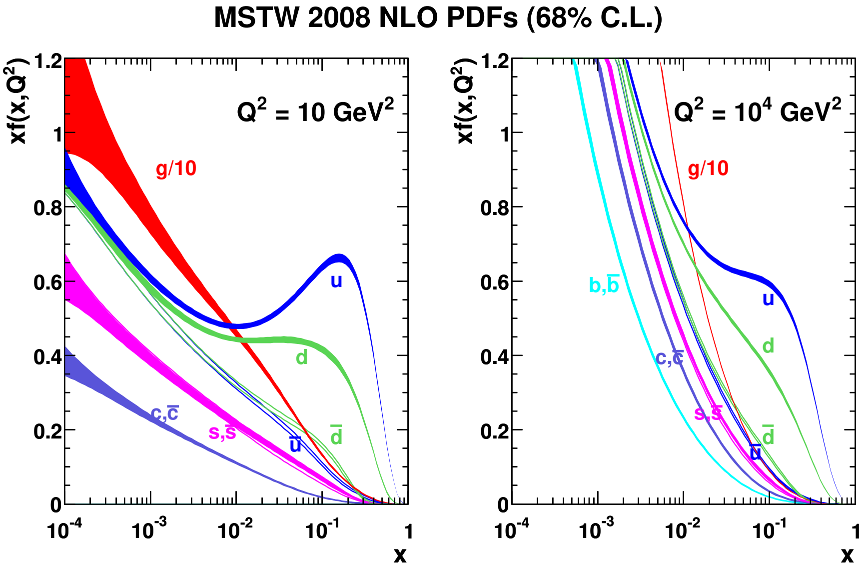

FIGURE 2.4: Parton distribution functions (PDFs) for protons at Q^2 = 10 GeV^2 (left) and at Q^2 = 104 GeV^2 (right) [40].

In pp collisions, the phenomena can be analyzed using the "factorization theorem," enabling a breakdown of the collision's dynamics into distinct components. These components comprise the initial protons and their parton distributions detailed by the Parton Distribution Functions (PDFs), the primary interaction (hard scattering) among the partons represented by the matrix element (ME), subsequent parton showering (PS), and the conversion of final-state partons into color-neutral hadrons through hadronization. Figure 2.5 presents a schematic depiction illustrating these successive stages. Consequently, the expression for the cross section of the $pp \to X$ process can be articulated as follows:

$$\sigma(pp \rightarrow X) = \sum_{i,j} \int dx_i dx_j \int dz_k dz_m f_i(x_i, \mu_F^2) f_j(x_j, \mu_F^2) \\ \times \hat{\sigma}_{i,j\rightarrow k,m}\left(\sqrt{\hat{s}}, \alpha_s(\mu_R^2)\right) D_k(z_k, \mu_F^2) D_m(z_m, \mu_F^2) \tag{2.4}$$

The given equation involves various terms and factors to describe the interactions in proton-proton (pp) collisions. Let's break down the components of the equation:

- i and j represent the interacting partons within the protons.
- x_i and x_j are their respective momentum fractions within the proton.
- f_i and f_j are the PDFs that describe the probability of finding a specific parton for a given fraction of momentum inside the proton.
- $\hat{\sigma}_{i,j\rightarrow k,m}$ represents the partonic cross section for the process whereas k and m are partons of the final state .
- D_k & D_m are their respective fragmentation functions, that describes the partonic showers and hadronization processes.

The equation is decomposed into three distinct components: the perturbative segment (ME), and the non-perturbative elements (PDFs and PS). For the computations, two energy scales, namely the factorization scale μ_F and the renormalization scale μ_R, are established. The factorization scale delineates the boundary between the perturbative computation of the partonic cross-section and the non-perturbative evaluations of the parton density functions and fragmentation functions. Conversely, the renormalization scale serves as a cutoff in the calculation of the partonic cross-section, managing divergences and influencing the behavior of the running coupling constant α_s, which acquires dependence on μ_R.

It's important to note that the factorization and renormalization scales are artifacts of perturbation theories with divergences. In a complete calculation including all orders in perturbation theory, the cross section would not depend on the chosen scales. However, in perturbation theory the cross sections are often computed at a fixed order that lead to some scale dependence in the calculation.

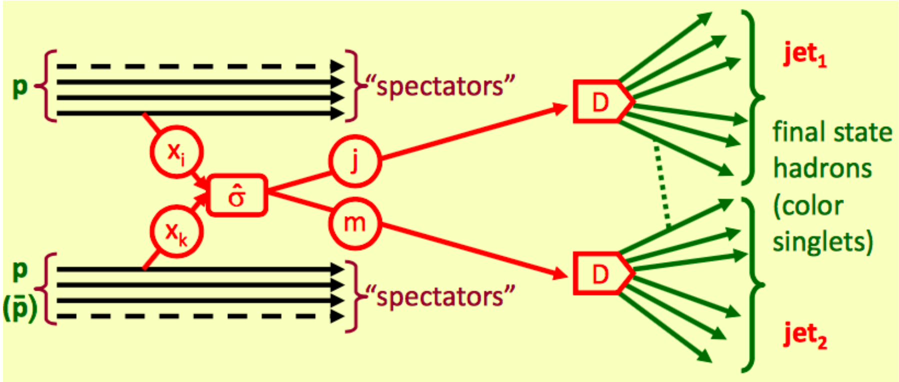

FIGURE 2.5: View of the various steps involved in the simulation of a *pp* collision

2.3 The ATLAS detector

ATLAS serves as one of the two general-purpose particle physics detectors that is installed at the LHC. Its main purpose of designing is to detect particles produced in both *pp* and ion-ion interactions. The exceptional capabilities of the LHC *pp* collisions, with their high centre-of-mass energy and luminosity, enable groundbreaking physics studies at the TeV scale. The detector is equipped to facilitate various research objectives, including:

- Exploring the *Standard Model Higgs boson* and precisely measuring its properties.
- Conducting *Supersymmetry* searches.
- Performing precision tests of electroweak interactions, flavor physics, and QCD.

- Measuring the properties of the top quark.
- Conducting generic searches for new particles and interactions, often referred to as exotic searches.

To address these multifaceted challenges, *ATLAS* was meticulously designed with the following features:

- Complete coverage in azimuthal angle, enabling accurate measurements of missing transverse energy and wide acceptance in pseudo-rapidity.
- Utilization of high granularity to function effectively in environments with substantial particle flux and overlapping events.
- Implementation of precision tracking to achieve high-resolution momentum measurements and facilitate the detection of secondary vertices related to b-hadrons and l-leptons.
- Deployment of precise electromagnetic calorimetry for the precise identification and energy measurement of electrons and photons.
- Incorporation of full-coverage hadronic calorimetry to ensure accurate measurements of jets and missing transverse energy.
- Ensuring high efficiency in muon identification, momentum resolution, and charge determination across a wide momentum range.
- Implementation of an efficient triggering system for detecting low transverse-momentum objects.

Table 2.1 presents the key performance objectives of the ATLAS detector, showcasing its capabilities. In Figure 2.6, we can observe a schematic representation of the ATLAS detector, which stands as the largest volume detector ever constructed for a particle collider. With dimensions of 44m in length and

Detector Component	Design Resolution	η Coverage	
		Measurement	Level 1 Trigger
Tracking	$\sigma_{p_T}/p_T = 0.05\% p_T \oplus 1\%$	± 2.5	None
EM Calorimetry	$\sigma_E/E = 10\%/\sqrt{E} \oplus 0.7\%$	± 3.2	± 2.5
Hadronic Calorimetry			
Barrel and End-Cap	$\sigma_E/E = 50\%/\sqrt{E} \oplus 3\%$	± 3.2	± 3.2
Forward	$\sigma_E/E = 100\%/\sqrt{E} \oplus 10\%$	$3.1 < \lvert\eta\rvert < 4.9$	$3.1 < \lvert\eta\rvert < 4.9$
Muon Spectrometer	σ_{p_T}/p_T = 10% at $p_T = 1$ TeV	± 2.7	± 2.4

TABLE 2.1: Performance goals of the ATLAS detector. Units of p_T and E are GeV [28].

25m in diameter, it takes the form of a cylinder. The detector is longitudinally divided into three regions: the central "barrel" and the two outer "end-caps."

The ATLAS detector is a complex system, comprising an inner tracking detector (ID) encircled by electromagnetic calorimeters, hadronic calorimeters, and a muon spectrometer. To enable precise momentum measurements, the inner detector operates within an axial magnetic field of 2 T, generated by a solenoid. Similarly, the muon spectrometer operates within its magnetic field, facilitated by an air-core toroid system. To manage data collection effectively, a two-level trigger system is implemented for event selection. Further insights into the various sub-systems of the ATLAS detector will be provided in subsequent sections.

2.4 ATLAS Coordinate Framework

The ATLAS experiment uses a Cartesian coordinate system with the origin located at the nominal interaction point, as depicted in Figure 2.7. The z-axis coincides with the beam line, while the x-y plane lies perpendicular to the beam line, where positive x points towards the center of the LHC ring, and positive y points upward.

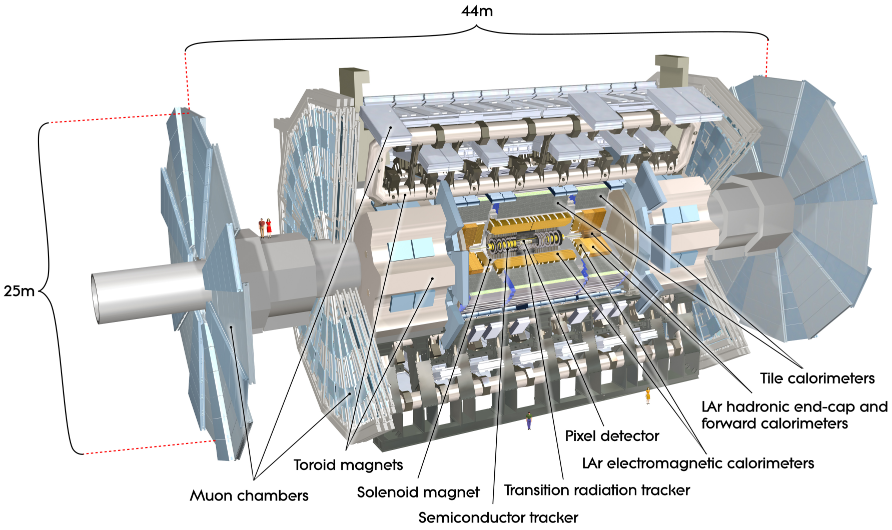

FIGURE 2.6: ATLAS detector overview with the labelling of various detector sub-systems[42].

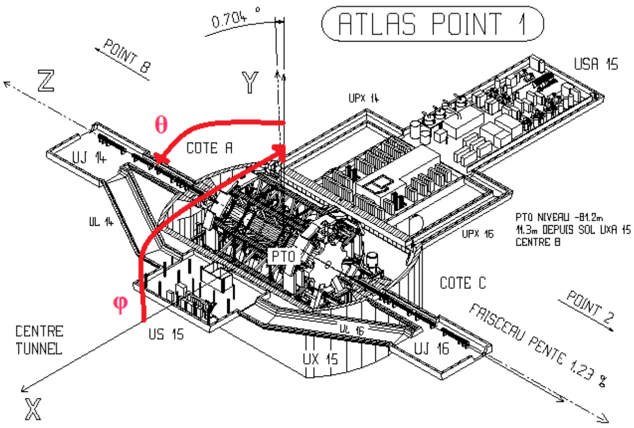

FIGURE 2.7: Illustration of the ATLAS coordinate system [29].

When describing the position of a physical object within the detector, a cylindrical coordinate system is used. In this system, θ represents the polar angle, r and ϕ signify the radius and the azimuthal angle in the x-y plane (transverse plane), respectively. These angles, θ and ϕ, are measured from the positive z-axis and the positive x-axis, respectively.

The energy (E) and momentum (p) of outgoing particles are projected onto the transverse plane, enabling the application of conservation laws due to known energy and momentum of the initial state, whereas the initial component along the z-axis is unknown. Consequently, transverse momentum is defined as $p_T = \sqrt{p_x^2 + p_y^2}$ and transverse energy as $E_T = E\sin(\theta)$.

The polar angle θ is often converted to pseudo-rapidity, given by

$$\eta = -\ln\left(\frac{\theta}{2}\right) \tag{2.5}$$

which approximates the rapidity

$$y = \frac{1}{2}\ln\frac{E + P_z}{E - P_z} \tag{2.6}$$

In situations where the particle's energy (E) far exceeds its mass ($E \gg m$) and the longitudinal momentum component (P_z), the pseudo-rapidity (η) tends toward 0 in the transverse plane and approaches infinity along the z-axis. Specifically, at 45° from the axis, η equals 1. Pseudo-rapidity and rapidity prove advantageous in describing angles when the initial z-momentum is unknown, as in hadron colliders involving parton interactions from protons. Notably, the difference in rapidity between two particles remains invariant under boosts along the z-axis. An extensively used metric is the angular distance between objects in the $\eta - \phi$ plane, defined as $\Delta R = \sqrt{\Delta\eta^2 + \Delta\phi^2}$.

2.4.1 The ATLAS Magnetic System

The ATLAS detector employs a superconducting magnet system that encompasses a volume of approximately $12,000\,\mathrm{m}^3$. In contrast to CMS, which utilizes a single solenoid magnet to generate a $4\,\mathrm{T}$ magnetic field, the design of ATLAS includes two distinct magnetic systems: a central solenoid [43], situated between the Inner Detector and the Electromagnetic Calorimeter, responsible for creating an axial magnetic field within the ID volume, and a barrel toroid along with two end-cap toroids, which generate a toroidal magnetic field within the Muon Spectrometer volume.

The **solenoidal** magnet is a coil made of superconducting material that generates an axial magnetic field of $2\,\mathrm{T}$ for the Inner Detector, achieved through an $8\,\mathrm{kA}$ electric current and cooled to a temperature of $4.5\,\mathrm{K}$. It measures $5.8\,\mathrm{m}$ in length, with an inner radius of $1.23\,\mathrm{m}$ and an outer radius of $1.28\,\mathrm{m}$, corresponding to only 0.66 radiation lengths. To optimize the material budget, the coil is positioned inside the calorimeter cryostat.

The ATLAS **toroidal** magnet system, shown in Figure 2.8, consists of a barrel toroid comprising eight separate coils with an electric current of $20\,\mathrm{kA}$ and two end-cap toroids that produce magnetic fields of $0.5\,\mathrm{T}$ and $1\,\mathrm{T}$ in the central and end-cap regions, respectively. These magnets are situated outside the calorimeters. The barrel has an inner diameter of $9.4\,\mathrm{m}$, an outer diameter of $20.1\,\mathrm{m}$, and a length of $25.3\,\mathrm{m}$. The end-cap toroids are designed to generate a magnetic field near the beam axis to deflect particles with small polar angles. Each of the toroids comprises eight superconducting coils housed within an insulating vacuum vessel with a diameter of $10.7\,\mathrm{m}$ and a width of $5\,\mathrm{m}$. Together with the barrel toroid, they ensure almost complete geometric coverage of the magnetic field.

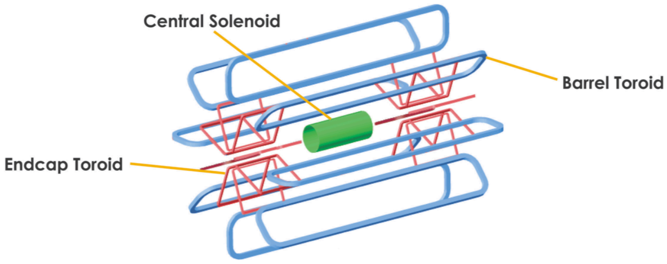

FIGURE 2.8: Layout of the ATLAS magnetic system.

2.4.2 Inner detector

The Inner Detector (ID) [43, 44] is the most closest apparatus to the interaction point in the ATLAS detector. It is specifically designed for reconstructing the paths traversed by the charged particles results of the collisions of either protons or heavy ions. The paths are referred to as tracks helping in identifying the primary vertices of the interactions and possible secondary vertices resulting from the decay of long-lived particles. With a cylindrical shape and dimensions of 1.1m in radius and 6.2m in length, the ID surrounds the interaction point. The hits in the ID are used to reconstruct charged particles trajectories. The entire ID operates within the solenoidal magnetic field of strenght 2 T, enabling the measurement of particle momentum and charge from the curvature of their trajectories. Detailed information on track and vertex reconstruction, crucial for identifying jets from b-quarks and the hadronic decay of the τ-leptons in the final state of analysis presented in this thesis, it will be described in Chapter 3.

The ID ensures the sophisticated and coherence tracking of charged particles having $p_T > 0.5\,\text{GeV}$ within the range of $|\eta| < 2.5$. It provides a transverse momentum resolution given by:

$$\frac{\sigma_{p_T}}{p_T} = 0.05\% p_T \oplus 1\% \tag{2.7}$$

as sumarised in Table 2.1.

The three utilized technologies for measuring hits of the tracks are an innermost pixel detector which is composed of silicon pixels technology , an intermediate silicon strip detector (SCT), and the outermost transition radiation tracker (TRT). A three-dimensional illustration of the ID layout is shown in Figure 2.9a, while Figure 2.9b provides a detailed layout.

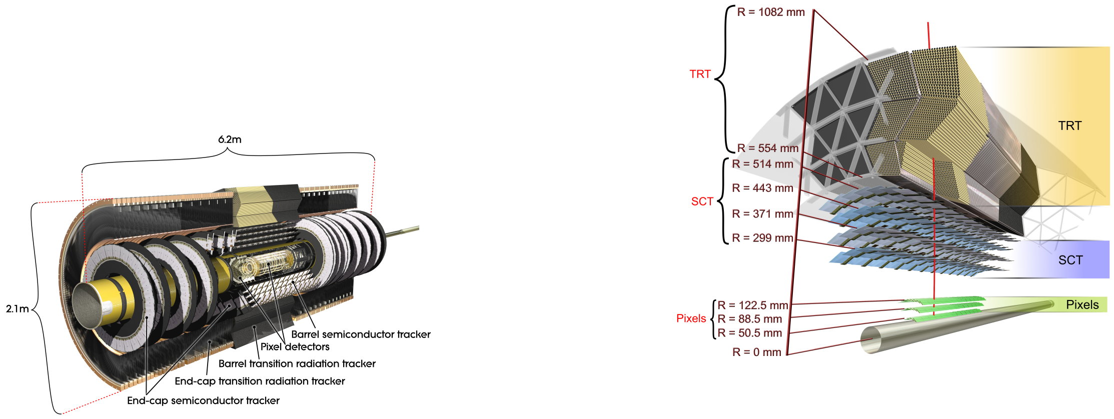

(A) (B)

FIGURE 2.9: 2.9a The ATLAS Inner detector's layout. 2.9b a zoomed-in glimpse at the three subdetectors that make up the ATLAS Inner detector: the pixel detector and Insertable B-layer, the semiconductor tracker, and the transition radiation tracker [45].

Pixel detector and the insertable B-Layer (IBL)

The silicon based pixel detector is located very close to the beam in the ATLAS detector. It is constructed with layers of silicon pixels to achieve high granularity for precise resolution of primary and secondary interaction vertices. The detector comprises three cylindrical layers in the barrel region, situated at radial distances of 50.5 mm, 88.5 mm, and 122.5 mm. Additionally, in the end-caps there are disks perpendicular to the beams. They are positioned longitudinally with distances of 49.5 mm, 58.0 mm, and 65.0 mm. The B-layer which is positioned at a radius of 50.5 mm, plays a significant role in the detection of secondary vertices. Which enables the jets identification that are originating from b-quark hadronization. During the LHC first long shutdown back in 2014 the insertable

B-Layer (IBL) a fourth pixel layer was installed inside the existing detector at a radius of 33 mm from the beam axis [46]. The IBL significantly improves b-jet identification by offering an additional space point in close proximity to the interaction point. The detector is composed of silicon based sensor modules, resulting in approximately 92 million pixels (and readout channels) in total.

Particles with $|\eta| < 2.5$ typically traverse the four layers of the detector, yielding four space points. The pixel detector achieves a resolution of $\sigma_\phi = 10\mu$m in the bending direction (R - ϕ) and $\sigma_{Z,R} = 115\mu$m in the z (R) direction for the barrel (end-caps), respectively. The high precision in the hit positions measurements allows us for the accurate reconstruction of tracks and secondary vertices of short-lived particles, as well as the measurement of the impact parameter of the tracks. This measurement is importantl for identifying jets originating from b-quarks and the hadronic decay of τ-leptons.

SCT: SemiConductor Tracker

The SCT is a silicon strip based detector comprising four layers of strips positioned along the beam-pipe axis in the barrel region and aligned along the R direction in the end-caps. Identical silicon-strip sensors are placed back-to-back with the first layer, forming a stereo angle of 40 milliradians. This configuration allows for a two-sided module, enabling measurement of the second coordinate. Across both the barrel region and the end-caps, the SCT incorporates more than 6 million channels. The spatial resolution of the detector is σ_ϕ = 17 μm in the bending direction (R - ϕ) and $\sigma_{z,R}$ = 580 μm in the z direction for the barrel or R direction for the end-cap.

TRT: Transition Radiation Tracker

The TRT comprises the outermost segment of the ATLAS inner detector. It functions as a straw drift tube tracker while providing additional capabilities for particle identification through transition radiation. Each TRT module consists of bundles of 4mm diameter straws filled with a gas mixture primarily containing 70% Xenon (Xe), 27% Carbon Dioxide (CO_2), and 3% Oxygen (O_2), all immersed in a propylene radiator. In the barrel region, these straws align parallel to the beam axis, whereas in the end-caps, they adopt a radial arrangement.

Particles with a transverse momentum (p_T) greater than 0.5 GeV and an absolute pseudorapidity ($|\eta|$) below 2.0 traverse at least 36 straws, except within the transition zone between the barrel and end-caps (0.8 < $|\eta|$ < 1.0), where only 22 straws are encountered.

Primarily providing measurements in the bending direction $(R - \phi)$, the TRT has a spatial resolution of σ_ϕ = 130 μm. Despite its lower resolution compared to silicon trackers and its limitations in the z direction, the TRT significantly contributes to pattern recognition and momentum resolution due to the multitude of measurements and the extended track length.

When charged particles transition between the straw and the propylene fibers (foils) in the barrel (end-caps), they emit transition radiation photons, absorbed by the Xenon gas mixture. The intensity of emitted transition radiation relies on the Lorentz γ-factor of incoming particles, linked to the particle mass at a specific energy. This information aids in particle identification, particularly in distinguishing electrons from pions.

The ATLAS detector's calorimeter system encompasses the electromagnetic calorimeter (ECal), covering the region $|\eta| < 3.2$, and the hadronic calorimeter (HCal), spanning $|\eta| > 4.9$. Figure 2.10 provides an overview of the calorimeter design. These vital components measure the energy and direction of motion for electrons, photons, and sufficiently long-lived hadrons.

When traversing a medium, electrons experience energy loss primarily due to Bremsstrahlung, while energetic photons undergo e^+e^- pair production. This process depends on the medium's characteristic radiation length, X_0, which varies. Passing through a suitable medium, these particles initiate a cascade of interactions known as an *electromagnetic (EM) shower*. As the particles lose energy within the shower, they eventually stop and get absorbed, producing a measurable cluster of signals calibrated to determine the initial particle's energy.

On the contrary, energetic hadrons produce *hadronic showers* through multiple inelastic interactions. The interaction length, λ, is notably greater than X_0 for the same medium, leading to the HCal's placement further away from the interaction point compared to the ECal. Moreover, hadronic showers exhibit broader transverse spread compared to EM showers due to the cascade's opening angle scaling with the interaction length. These showers are primarily dominated by pions, where around one-third of the generated pions are neutral (ϕ^0) and decay into $\phi^0 \rightarrow \gamma\gamma$, dissipating energy as EM showers.

Both the ECal and HCal employ a sampling calorimeter design, consisting of alternating layers of passive and active materials. These layers produce the particle shower and measure the deposited energy, respectively. The shower depth, measured in radiation or interaction lengths, logarithmically correlates with the initial particle's energy. Despite its finite depth, this design enables the calorimeter to accurately measure a wide range of energies.

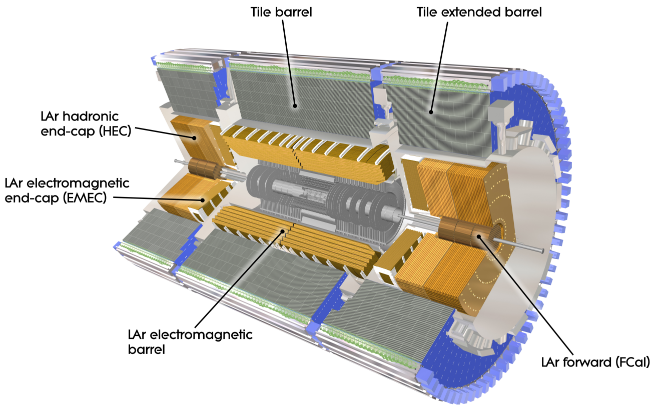

FIGURE 2.10: View of the ATLAS calorimeter system [47]

Electromagnetic Calorimeter (ECal)

The ECal serves as the innermost calorimeter within the ATLAS detector, dedicated to measuring the energy of electrons and photons. It follows a sampling calorimeter design, employing lead as the absorber material and liquid argon (LAr) as the active medium. Consisting of accordion-shaped cells filled with liquid argon interspersed with lead layers, this configuration efficiently measures particle energies.

This detector divides into several sections:

1. **EMB (Electromagnetic Barrel):** Two half-barrels covering the range up to $|\eta| < 1.475$, with a 4 mm gap at $z = 0$.

2. **EMEC (Electromagnetic End-Cap):** Two wheels; the first wheel spans $1.375 < |\eta|$, while the second encompasses $2.5 < |\eta| < 3.2$. Note: The region $1.375 < |\eta| < 1.52$ is impacted by additional instrumental and cooling material, affecting energy resolution.

In the transverse direction, the EM calorimeter comprises three layers:

1. A high granularity pre-sampler, situated closest to the interaction point, aids in reconstructing neutral pions decaying into two photons and captures particles initiating showers in the inner detector.

2. Longer towers with high granularity, following the pre-sampler, detect the majority of EM showers, allowing measurements of the particles' ϕ and θ coordinates.

3. The final layer identifies showers initiated by particles other than electrons or photons, which begin showering within the EM calorimeter before exiting.

The energy resolution of the ATLAS EM calorimeter is defined by the formula:

$$\frac{\sigma_E}{E} = \frac{10\%}{\sqrt{E}} \oplus 0.7\%$$

Specific energy resolution values are detailed in Table 2.1.

Hadronic Calorimeter (HCal)

The HCal in ATLAS surrounds the EM calorimeter and focuses on measuring the energy and directional information of hadrons resulting from quark and gluon hadronization. It comprises three distinctive components:

1. **Hadronic Tile Calorimeter:**
    - Covers the $|\eta| < 1.7$ region.
    - Utilizes steel as the absorber and plastic scintillator tiles as the active material.
    - Comprises a barrel section ($|\eta| < 0.8$) and two extended barrels ($0.8 < |\eta| < 1.7$) located immediately behind the EM calorimeter.
    - The readout photomultiplier tubes are connected to scintillators through wavelength-shifting fibers, forming projective towers in η.
2. **Hadronic End-Cap Calorimeter (HEC):**
    - Consists of two wheels per end-cap covering $1.5 < |\eta| < 3.2$.
    - Utilizes copper as the absorber and liquid argon (LAr) as the active material.
    - Located directly behind the EMEC.
3. **Forward Calorimeter (FCal):**
    - Covers the $3.1 < |\eta| < 4.9$ region.
    - Designed to accommodate relatively long showers within a compact volume due to high particle flux and energy.
    - Divided into three compartments:
        - First compartment: Intended for electromagnetic measurements, using copper and LAr.

  - Other two compartments: Designed for hadronic measurements, utilizing tungsten and LAr to contain and minimize lateral spread of hadronic showers due to tungsten's high density.

The energy resolution of the Hadronic Calorimeter:

$$\frac{\sigma_E}{E} = \frac{50\%}{\sqrt{E}} \oplus 3\%$$

in the barrel and end-caps, whereas it is

$$\frac{\sigma_E}{E} = \frac{100\%}{\sqrt{E}} \oplus 10\%$$

in the forward region, as detailed in Table 2.1.

The Muon Spectrometer (MS) stands as the largest and outermost detector within the ATLAS experiment, enveloping the entire calorimeter system and occupying a significant portion of the ATLAS cavern. Its primary function is the precise identification and momentum measurement of muons within the range of approximately 10 GeV to around 1 TeV. To accomplish this task, the Muon Spectrometer employs various detector technologies, enabling accurate momentum and directional measurements of muons alongside efficient triggering.

The layout of the Muon Spectrometer, depicted in Figure 2.11, extends over the range $|\eta| < 2.7$. Its performance objectives, outlined in Table 2.1, aim to achieve a 10% transverse momentum resolution for 1 TeV muon tracks. Comprising four subsystems, each utilizing different gas detector technologies, the Muon Spectrometer integrates Resistive Plate Chambers (RPC) in the barrel region and Thin Gap Chambers (TGC) in the end-cap region for trigger signal provision. In contrast, Monitored Drift Tubes (MDT) and Cathode Strip Chambers (CSC) facilitate precise momentum measurements. The MDT chambers excel in high-precision measurements along the bending direction across a vast portion of the detector's acceptance. Conversely, CSCs operate in the forward region, where particle flux surpasses the MDT chambers' capabilities. The arrangement of muon chambers in the barrel region ($|\eta| < 1.05$) comprises three cylindrical layers encircling the beam axis, while in the end-cap regions ($1.05 < |\eta| < 2.7$), the chambers are distributed among three wheels.

The extensive coverage and precise muon momentum measurements provided by the Muon Spectrometer play a pivotal role in the accurate reconstruction and identification of muons within the ATLAS experiment.

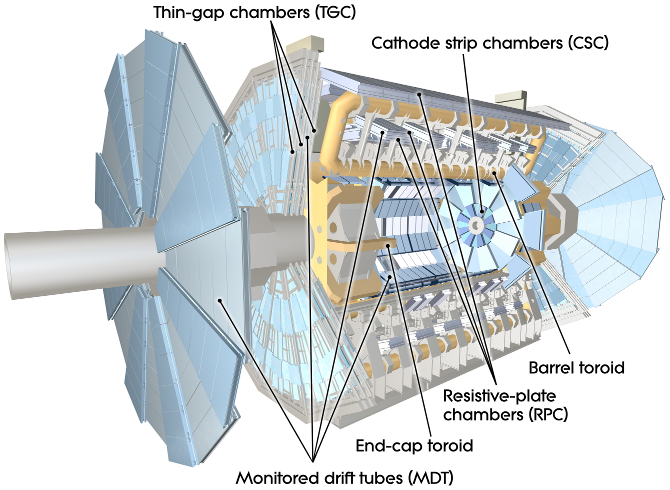

FIGURE 2.11: View of the ATLAS muon spectrometer [48]

2.4.3 Trigger System

As previously discussed in Section 2.1.1, the LHC operates at a high bunch crossing frequency of 40 MHz, equivalent to bunch crossings every 25 ns. Due to this exceedingly rapid collision rate, the ATLAS detector cannot feasibly process and record all events in real-time. Hence, the ATLAS Trigger and Data Acquisition (TDAQ) system [49] is designed to selectively identify and capture only the most relevant events.

To efficiently manage the event rate, the TDAQ system operates in two sequential stages, as depicted in Figure 2.12. Initially, the Level-1 (L1) trigger, which operates on hardware, swiftly identifies Regions of Interest (RoIs) within the calorimeters and muon spectrometer. This immediate action reduces the event rate from 40 MHz to 100 kHz, achieving an overall latency of around 2.5

µs. Subsequently, the High-Level Trigger (HLT) takes charge, incorporating aspects of the L2 and Event Filter levels employed during Run 1. The HLT utilizes rapid algorithms to access RoI data or full event information, drawing upon high-resolution data from the calorimeters, muon spectrometer, and inner detector. These algorithms mirror those used for physics object reconstruction and identification (discussed in Chapter 5) but prioritize speed over precision. The HLT's primary task is to identify events containing physics objects—electrons, muons, photons, jets, or τ-lepton candidates—critical to the ATLAS physics program. This stage substantially reduces the event rate by two orders of magnitude, maintaining an average rate of 1 kHz with a latency of 0.2 μs.

The Data Acquisition (DAQ) system plays a pivotal role in supervising data recording onto storage disks. When the L1 trigger system identifies a noteworthy event, the DAQ transfers the corresponding event data from detector electronics to detector-specific Read-Out Drivers (ROD). If the event also satisfies the HLT criteria, the event data are consolidated and then archived onto disks for subsequent analysis.

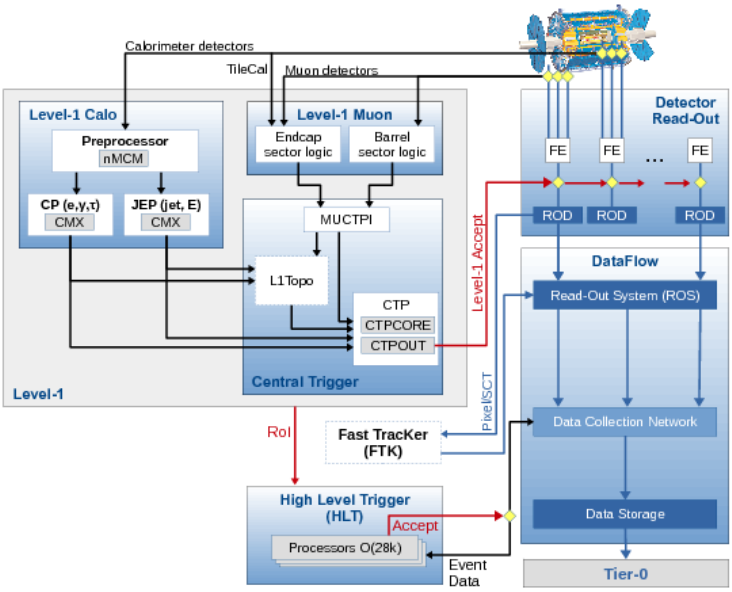

FIGURE 2.12: Illustration of the two-level trigger system in the ATLAS experiment [49] .

Chapter 3

Physics objects reconstruction in ATLAS

Following the recording of raw data, a fundamental step in every ATLAS analysis involves reconstructing and identifying the numerous physics entities found in the final state. This pivotal process initiates by tracing particle tracks within both the inner detector and the muon spectrometer, facilitating precise measurements of charged particle trajectories. Concurrently, energy deposits in the calorimeter systems are clustered to characterize particle energies.

Consequently, data from these diverse sub-detectors are amalgamated to reconstruct and identify an array of particles, including but not limited to electrons, muons, photons, jets, and leptons. Moreover, essential event properties, like missing transverse energy, are computed to infer the existence of neutrinos or other imperceptible particles. Figure 3.1 illustrates the distinct characteristics representing various particles as observed within the ATLAS detector.

This chapter provides a comprehensive insight into the intricate algorithms utilized by ATLAS for the precise reconstruction and identification of pertinent particles pertinent to this thesis. These sophisticated algorithms are finely tuned to accurately discern unique particle signatures from complex event data, facilitating precise measurements of diverse physics observables.

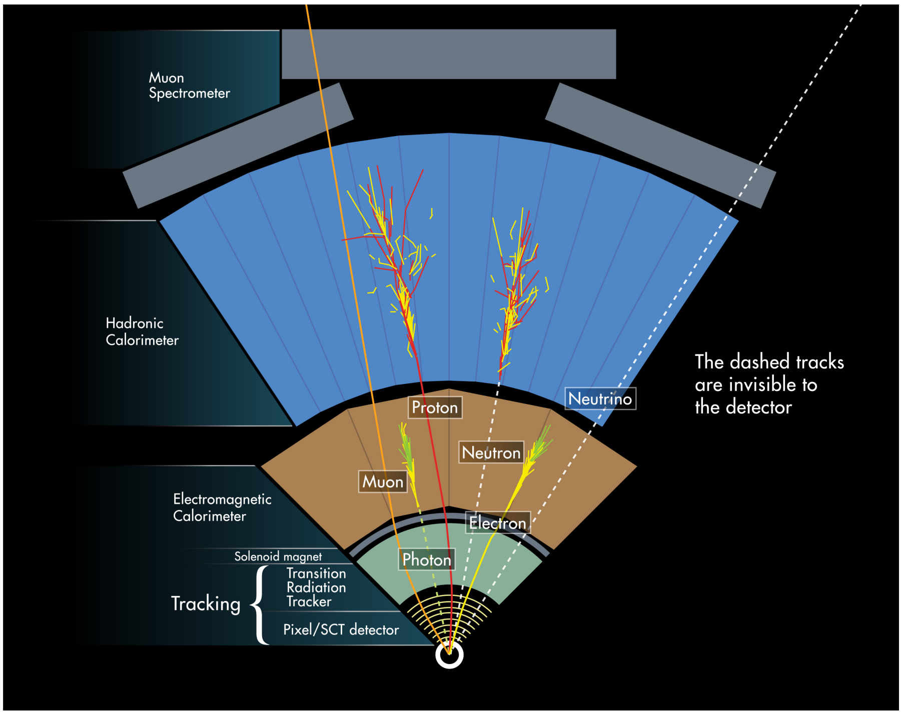

FIGURE 3.1: Illustrating the distinctive characteristics exhibited by various particles within the ATLAS detector [50]

3.1 Track and vertex reconstruction

Tracks are reconstructed [51] by analyzing the hits registered across various layers of the inner detector when charged particles traverse the responsive material. A track is defined by a collection of attributes, including transverse and longitudinal impact parameters [1] denoted as d_0 and z_0 respectively, angular coordinates ϕ and θ, as well as the charge-to-momentum ratio q/p.

Initial measurements obtained from the Pixel detector and SCT undergo a process of clustering via connected component analysis (CCA) [52]. This procedure generates three-dimensional space-points that serve as the foundation for track reconstruction. Given the high particle density within the LHC environment, numerous space-points comprise signals from multiple particles that

---

[1] The transverse impact parameter, denoted as d_0, refers to the closest distance between the track projection onto the transverse plane and the interaction point (IP). Similarly, the longitudinal impact parameter, termed z_0, is calculated as the minimal absolute disparity between Z_{track} and Z_{IP}.

have traversed through. Specialized algorithms are utilized to discern and isolate these instances. The foundation for the subsequent track reconstruction is laid by constructing seed tracks using three space-points. Following this, a stringent selection process ensues, ensuring the compatibility of these tracks with additional space-points.

The chosen seed tracks undergo processing through a combinatorial Kalman filter [53], which further constructs additional track candidates by considering available space-points across all layers of the Pixel and SCT detectors. Each track candidate is then assigned a score based on factors such as the count of incorporated space-points, any missing space-points in specific layers, the track's transverse momentum, its χ^2 value, and more. This score, representing the track's quality, plays a vital role in prioritizing tracks when resolving potential ambiguities. In the subsequent stage, the TRT measurements are also incorporated [54], followed by an accurate track fit with high resolution.

Once the process of track reconstruction and selection reaches its conclusion, a specialized algorithm for vertex finding [55, 56] is engaged. The initial seed for the vertex is determined by identifying the global maximum in the z_0 distribution of tracks in relation to the interaction point. Each track's compatibility with this vertex is examined, and if an inconsistency exceeding $d_0/\sigma(d_0)$> 7 is detected, the track remains unaffiliated. This sequence is reiterated until all tracks find an association with a vertex. The vertex with the highest total of p_T^2 for the associated tracks is established as the primary vertex (PV) of the event. Any other reconstructed vertices situated within the bunch-crossing region are categorized as pileup interactions. Vertices located outside the bunch-crossing area are denoted as secondary vertices.

3.2 Electron reconstruction and Identification

The process of reconstructing, identifying, and isolating electrons within the ATLAS experiment [57] relies on localized energy clusters in the electromagnetic calorimeter (ECal), tracks reconstructed in the inner detector (ID), and precise matching in the $\eta \times \phi$ space between these components.

ATLAS focuses on electron reconstruction within the $|\eta| < 2.47$ region. It starts by combining energy deposits in the ECal's layers and presampler to create energy towers in cells of 0.025×0.025 in $\Delta\eta \times \Delta\phi$. A scanning algorithm looks for seed clusters formed by these towers, each requiring a minimum transverse energy of 2.5 GeV. Then, tracks exceeding $p_T > 0.5$ GeV extend into the ECal volume, associating with these seed clusters. For a valid association, the track's impact point and the seed cluster's barycenter must be within $|\Delta\eta| < 0.05$ and $|\Delta\phi| < 0.1$. Seed clusters not tied to tracks are considered photon candidates.

Instances where multiple tracks link to a seed cluster choose one as the primary track. If this primary track aligns with a secondary vertex without pixel hits, it is deemed a photon converted into an e^+e^- pair. Thus, for an electron candidate, the primary track should originate from the primary vertex. Lastly, the cluster's size extends to include any energy spread, encompassing any energy deposits beyond the ECal in the total cluster energy.

The prompt electrons are those originating from decays of heavy resonances or semi-leptonic hadron decays, photon conversions, or resulting from spurious candidates. An electron identification technique [57] employs a multivariate likelihood method trained to distinguish these prompt electrons from alternative candidates. The algorithm defines three identification levels, referred to as working points: loose, medium, and tight. The loose working point prioritizes achieving the highest efficiency in identifying true prompt electrons, while the tight working point emphasizes the lowest rejection of non-prompt electrons. Figure 3.2 illustrates the efficiencies of electron identification corresponding to these working points concerning electron E_T and η.

The isolation algorithm [57] further rejects non-prompt electrons. An isolation cone, defined with a fixed or p_T-dependent radius ΔR around the electron candidate, is employed. Calorimeter- and track-based isolation variables are computed. The detailed electron energy calibration is executed using multivariate techniques [58, 59] derived from Monte Carlo simulations and data, following the final selection of electron candidates.

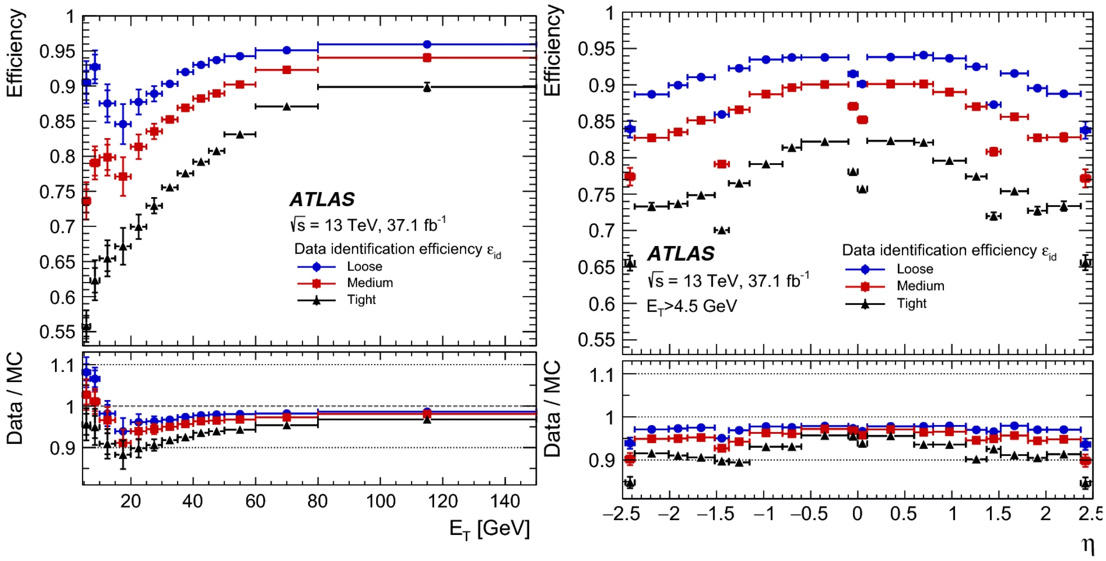

(A)

(B)

FIGURE 3.2: Electron identification efficiencies were computed using a $Z \rightarrow e^+e^-$ sample for the three working points, plotted against the **(a)** transverse energy E_T of the electron and **(b)** its pseudorapidity η [57] . The lower panels depict the ratios of data-to-simulation, considering both statistical and systematic uncertainties.

3.3 Muon reconstruction and Identification

Muon reconstruction and identification procedures leverage data from the ID, MS, and calorimeter systems. Tracking is autonomously carried out in the ID and MS.

Within the MS, the local track segments materialize through patterns of the hit within individual MS chambers. These segments, spanning diverse MS layers, are then integrated to establish complete MS tracks [60]. Roughly 96% of instances involve a global refit for muon reconstruction, amalgamating hits from both the ID and MS. These muon candidates, a product of this process, are termed combined muons. Alternative muon categories include tagged ID tracks harmonized with muon indications in the MS or the calorimeter.

Additional criteria are employed to discern non-prompt muons, often stemming from pion and kaon decays, using supplementary muon identification criteria [60]. Such non-prompt muons frequently exhibit distinctive track geometries resembling "kinks" or originate from secondary vertices. Several variables that effectively discriminate between prompt and non-prompt muons combine to establish four levels of muon identification: loose, medium, tight, and high-p_T. The efficiency of muon reconstruction under the medium criteria, depicted in Figure 3.3, is illustrated concerning muon p_T and η.

In a manner akin to electrons, different working points for muon isolation are established, grounded in varied track- and calorimeter-related parameters designed to quantify the extent of activity within an isolation cone encompassing the muon candidate. Calibrations of momentum scale, resolution, and dimuon mass resolution emanate from meticulous scrutiny of $J/\Psi \to \mu^+\mu^-$, $\Upsilon \to \mu^+\mu^-$, and $Z \to \mu^+\mu^-$ processes [61]. These analyses refine MC simulations, harmonizing them with data and minimizing associated uncertainties.

3.4 Jet reconstruction

Shortly after their creation, quarks and gluons initiate a cascade of interactions and undergo hadronization, resulting in the formation of a closely aligned cluster of particles known as a jet. Analyzing characteristics such as energy content, direction, shape, and substructure variables offers insights into the underlying

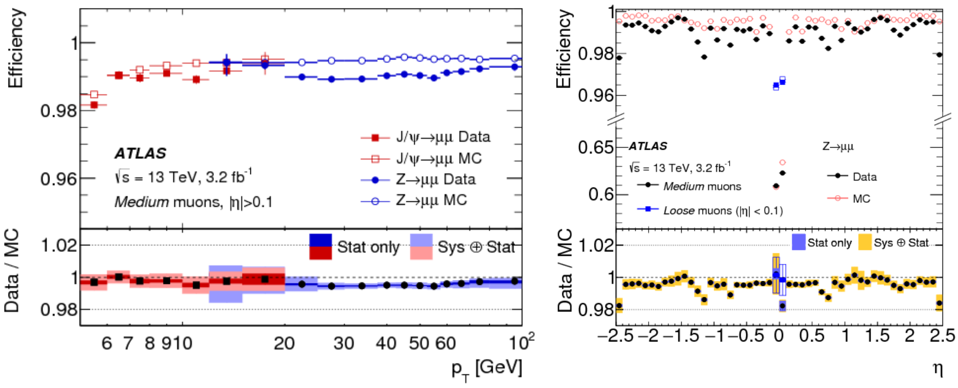

(A) (B)

FIGURE 3.3: Efficiency of muon reconstruction in events from $J/\Psi \to \mu^+\mu^-$ and $Z \to \mu^+\mu^-$ decays at the medium identification threshold, depicted as a function of **(a)** muon p_T and **(b)** muon η measured in $Z \to \mu^+\mu^-$ events. The lower panels illustrate the data-to-simulation ratios, including both statistical and systematic uncertainties.

initiating parton. Nevertheless, it's important to note that jets don't always correspond to individual partons [2]. For instance, in scenarios where a pair of quarks is generated through the decay of a resonance, these quarks can be reconstructed as a singular jet or even as multiple jets, contingent upon the degree of collimation between the quarks and their radiative products.

A jet's characterization encompasses both a *jet algorithm and a recombination scheme* [62]. The former outlines the methodology for amalgamating specific inputs into distinct jet collections, whereas the latter outlines the approach for attributing a momentum to each jet. This definition can be applied to jets simulated at the parton, hadron (particle), or detector level, as depicted in Figure 3.4. The jet identified at the particle level is commonly referred to as the "truth-jet." A robust jet algorithm ensures consistency across the variety of reconstructed jets across all these levels.

A clustering algorithm [64] is employed to delineate interconnected calorimeter cells that exhibit energy depositions surpassing the calorimeter noise level, denoted as σ_{cell}. These agglomerates are termed *topo-clusters*. Within

---

[2] In the context of jets, the term "parton" lacks a precise definition, but it generally pertains to either a quark or a gluon originating from the hard-scatter interaction or emerging from the decay of a massive resonance.

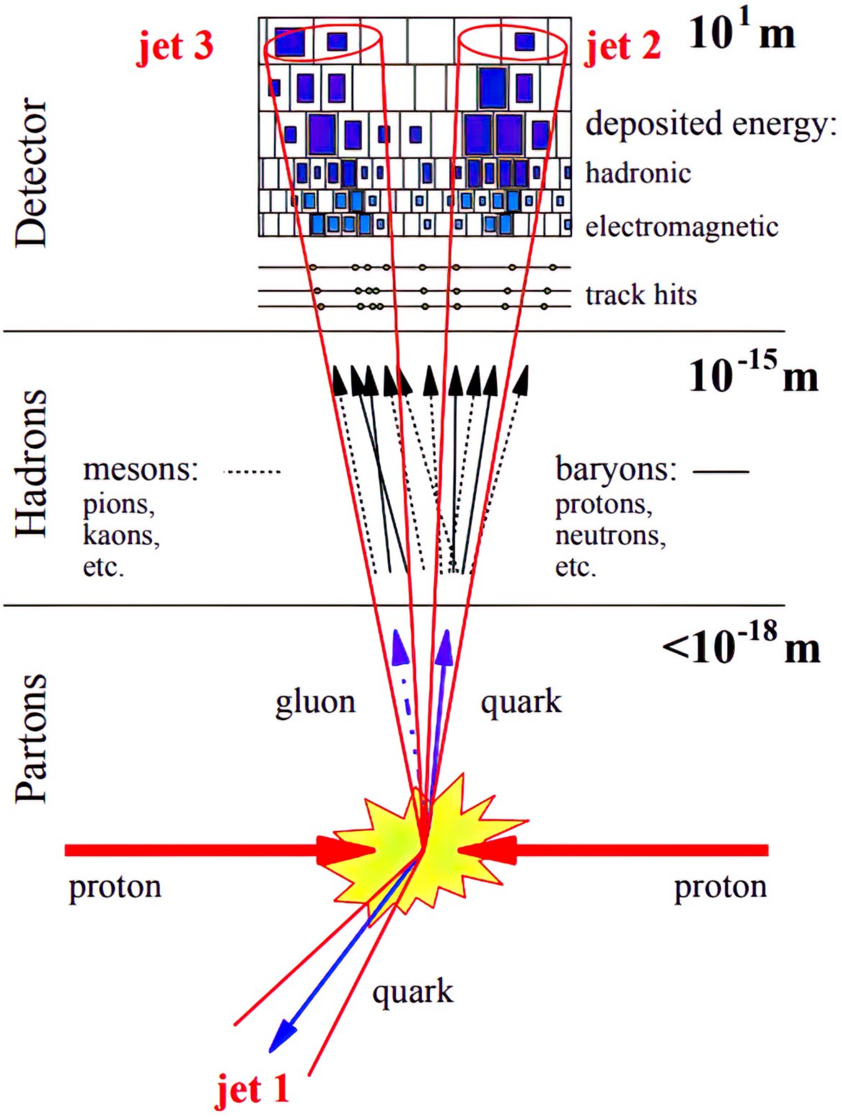

FIGURE 3.4: Illustration of a jet evolution [63].

the ATLAS framework, they originate from calorimeter cells with energy E_{cell} exceeding $4\sigma_{\text{cell}}$. Subsequently, neighboring cells satisfying $E_{\text{cell}} > 2\sigma_{\text{cell}}$ are incorporated to extend the cluster. The formation of topo-clusters culminates with the addition of a single layer of neighboring cells with $E_{\text{cell}} > 0$.

The calorimeter jets utilized in the investigations presented in this dissertation are constructed from topo-clusters using the anti-k_t jet algorithm [65]. A salient feature of this algorithm is its compliance with infrared and collinear (IRC) safety, indicating that the final ensemble of jets remains unaffected by the introduction of a collinear split among constituents or the occurrence of soft radiation.

The $anti-k_t$ algorithm starts with calculating

$$d_{ij} = \min\left(\frac{1}{p_{T,i}^2}, \frac{1}{p_{T,j}^2}\right)\frac{\Delta R_{i,j}^2}{R^2} \tag{3.1}$$

$$d_{iB} = \frac{1}{p_{T,i}^2} \tag{3.2}$$

In the algorithm, d_{ij} represents a weighted "distance" between two constituents, d_{iB} is the threshold value of this distance for constituent i, explained below. R signifies the algorithm's size parameter. The subsequent step involves determining the minimum value between d_{ij} and d_{iB}. If the minimum corresponds to d_{ij}, constituents i and j are merged. If it corresponds to d_{iB}, constituent i is deemed one of the final jets and is removed from the list. This process repeats until all constituents are clustered into jets. For ATLAS, the jet size parameter is conventionally set at $R = 0.4$.

Multiple procedures are essential to rectify and fine-tune the characteristics of jets [66, 67]. Initially determined with respect to the primary vertex, the jet direction is recalibrated, initially computed relative to the nominal interaction point. Accounting for the average pileup impact, corrections are applied to each jet based on the identified jet area [68] and the count of reconstructed primary vertices. The Absolute MC-based calibration aims to harmonize the jet energy reconstructed at the electromagnetic scale with the particle-level energy. This calibration, derived from Monte Carlo (MC) simulations, influences both the jet's energy magnitude and its directional pseudorapidity (η). Subsequently, the global sequential calibration is executed to minimize biases in jet flavor and counteract energy spillage beyond the reach of the hadronic calorimeter. Moreover, the in situ jet calibration is exclusively tailored for data analysis. These adjustments involve aligning a jet's p_T by juxtaposing it against another precisely measured object. To discriminate jets originating from pileup (pileup jets), the Jet Vertex Tagger (JVT) [69] is utilized, effectively discerning jets connected with the hard-scatter interaction.

3.4.1 Identification of b-jets: b-tagging

The identification of jets arising from the hadronization of b-quarks, commonly referred to as b-tagging, is of paramount importance in analyses aimed at processes involving one or more b-quarks in the final state. This significance is particularly evident in the HH $\rightarrow b\bar{b}\tau^+\tau^-$ analysis, as elucidated in this thesis. Numerous algorithms have been devised to discriminate jets resulting from the decay of b-hadrons. These techniques leverage distinct characteristics such as extended lifetime, substantial mass, and decay multiplicity of b-hadrons, as well as the distinctive fragmentation pattern of hard b-quarks.

B-hadrons exhibit lifetimes of approximately 1.6 picoseconds ($\tau \approx 1.6\,\text{ps}$). This allows the hadron to travel a few millimeters ($2-3\,\text{mm}$) away from the primary vertex before it undergoes decay. However, this duration is insufficient for the hadron to reach the calorimeters. Consequently, a crucial feature for identifying b-hadrons lies in the potential to detect a displaced secondary vertex within the inner detector. Characteristics such as the secondary vertex's distance from the primary vertex, the collective mass of particles associated with the vertex, and the impact parameter of the tracks prove to be valuable quantities for identification. Additionally, b-jets can be discerned by capitalizing on the high multiplicity of charged tracks and the elevated transverse momentum of decay particles stemming from b-hadrons. For visual clarity, Figure 3.5 provides an illustrative depiction of the underlying principle governing the identification of jets originating from b-hadron decays.

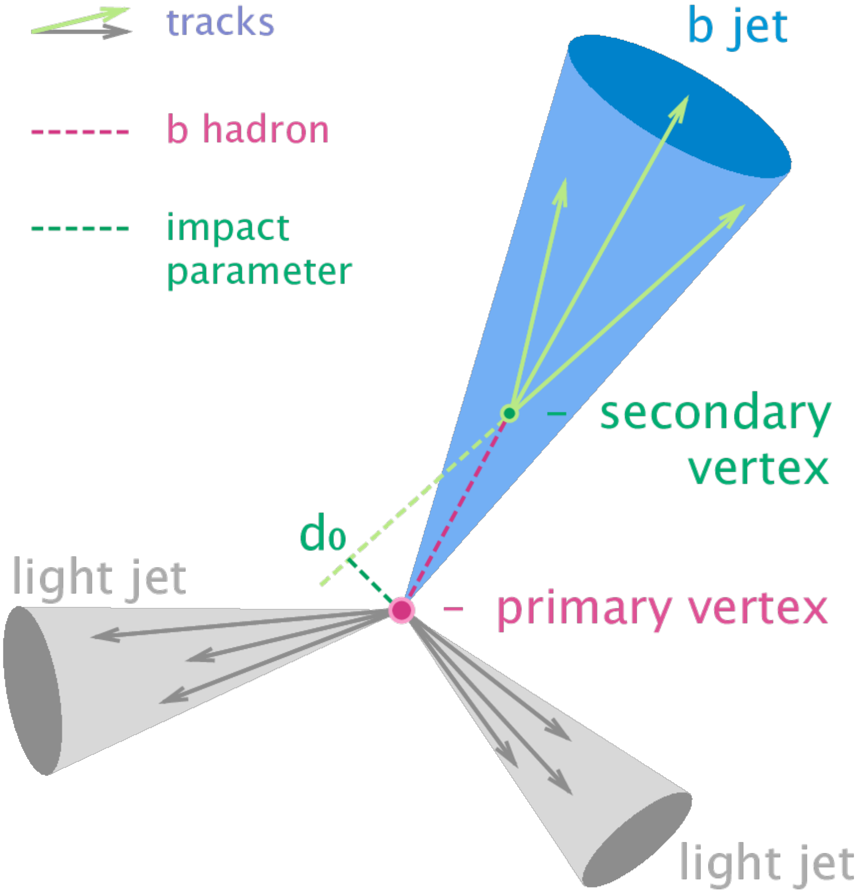

FIGURE 3.5: An illustration depicting distinctive features of a b-jet: the appearance of a secondary vertex within the jet and the presence of tracks exhibiting considerable impact parameters originating from this secondary vertex.

In the ATLAS experiment, identifying b-quark jets relies on three core b-tagging algorithms: those that hinge on impact parameters, an inclusive secondary vertex reconstruction method, and a decay chain multi-vertex reconstruction approach.

The analysis presented in this thesis utilizes a multivariate classification algorithm, the DL1r tagger [70, 71], which employs a deep neural network to distinguish b-jets from the background of light-flavour- and charm-quark-initiated jets. This process utilizes information pertaining to jet kinematics, the impact parameters of associated tracks, and the presence of displaced vertices. The inputs to the DL1r network encompass variables derived from a recurrent neural network (RNNIP) [72], designed to exploit spatial and kinematic correlations between tracks originating from the same b-hadrons.

For the analysis detailed in this thesis, the signal regions are defined by selecting exactly two b-jets passing the 77% working point, elaborated further in Chapter 4. The pseudo-continuous b-tagging information, represented by quantiles corresponding to 77%-70%, 70%-60%, and above 60% b-tagging efficiencies, is employed in MVA trainings to further leverage the discriminative capabilities of the flavour-tagging information.

The comparison plots illustrating the DL1r quantiles of the sub-leading b-tagged jet are depicted in Figure 3.6(a) for SM ggF, ggF ($\kappa_\lambda = 10.0$), and SM VBF signals along with the cumulative backgrounds. Additionally, Figure 3.6(b) demonstrates the same variable for each background component.

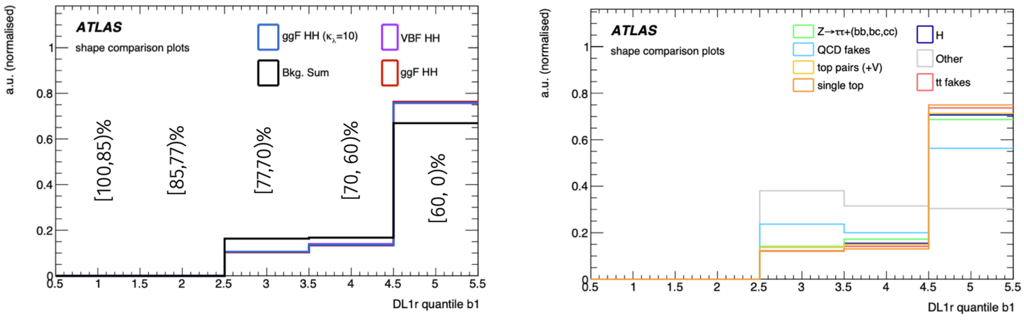

(A)

(B)

FIGURE 3.6: Sub-leading b-jet DL1r quantiles for (**a**) ggF (κ_λ=1.0, in red), ggF (κ_λ= 10.0, in blue), SM VBF (in purple) signals, together with the sum of the backgrounds (in black); and (**b**) for each background component of this analysis.

Muon-in-jet and the PtReco corrections

In addition to the standard jet calibration, two supplementary adjustments to the jet energy scale are implemented to enhance the accuracy of reconstructing the invariant mass of a resonance decaying into two bottom quarks. The muon-injet correction [73] is applied to accommodate B- and C-hadron decays into muons, as muons only deposit a portion of their energy in the calorimeter. If a muon with $p_T > 5\,\text{GeV}$ and meeting the medium identification criteria is identified within the jet, its four-momentum is combined with that of the jet. When multiple such muons are detected within the jet, the one closest to the jet-axis in terms of angular separation is selected, and the calorimeter energy associated with that muon is subtracted from the jet energy.

An additional adjustment, known as *PtReco* [73], is applied to mitigate the residual discrepancy between the reconstructed-jet p_T and the p_T of the corresponding truth-jet[3]. The impact of both corrections on the distribution of di-b-jet invariant mass (m_{bb}) is demonstrated in Figure 3.7, using simulated ZH $\rightarrow l^+l^-b\bar{b}$ samples, where l represents an electron or muon. Additionally, the *PtReco* correction method could be replaced by the Kinematic Likelihood Fit [73]. However, the results presented in this thesis do not employ the latter method.

3.5 Missing transverse energy

The LHC experiences collisions primarily along the longitudinal axis, which enables the application of momentum conservation in the transverse plane. Neutrinos and other weakly-interacting particles traverse through the detector unnoticed. In an ideal detector, the transverse momentum sum of these particles ($\vec{p}_T^{\,miss}$) can be derived from the transverse momenta of the observed detector entities, as follows:

---

[3] Matching between the reconstructed jet and the truth-jet is required in terms of geometry.

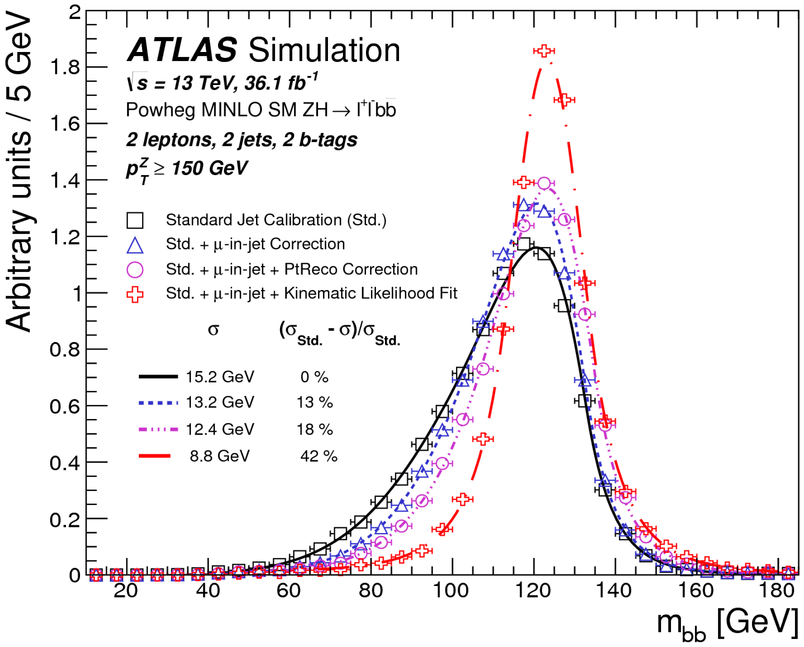

FIGURE 3.7: Comparison of the m_{bb} distributions with additional corrections applied to the jet energy scale. These distributions are shown for simulated events in the 2-lepton channel within the 2-jet and $p_T^Z > 150$ GeV region. Each distribution is fitted with a Bukin function, and the resolution values along with improvements are indicated in the legend [73].

$$\vec{p}_T^{\,\text{miss}} = -\sum_i \vec{p}_{T,i}^{\,\text{visible}} \tag{3.3}$$

The missing transverse momentum ($\vec{p}_T^{miss}$) is computed as the negative sum of the transverse momenta of all visible particles in the detector:

However, due to inherent limitations in detector precision, certain physics entities might be reconstructed with reduced accuracy or potentially not reconstructed at all. These considerations must be factored in when calculating $\vec{p}_T^{miss}$. Furthermore, some objects could fall beyond the detector's measurable range.

Every component used to compute $\vec{p}_T^{miss}$ (namely: electrons, muons, photons, hadronically-decaying τ leptons, jets derived from energy deposits in the calorimeter, and charged-particle tracks) undergo calibration to enhance the $\vec{p}_T^{miss}$ resolution. The measured momentum not assigned to any of the aforementioned physics entities is known as the 'soft-term' [74]. It's derived from reconstructed charged-particle tracks not linked to other reconstructed entities. These tracks are cross-referenced with the PV to exclude contributions from pileup.

Information pertaining to the contribution of neutral particles to the track-based soft-term is omitted due to its sensitivity to pileup contributions and its anticipated symmetry in ϕ. The magnitude of $\vec{p}_T^{miss}$ is commonly referred to as 'missing transverse energy', denoted by E_T^{miss}.

3.6 Reconstruction and identification of τ leptons

The mean lifetime of τ leptons is very short, approximately 0.29 ps, which means their decay occurs predominantly within the beam pipe. They decay through the emission of an off-mass-shell W boson, which then decays either leptonically or hadronically, as shown in the Feynman diagram in Figure 3.8.

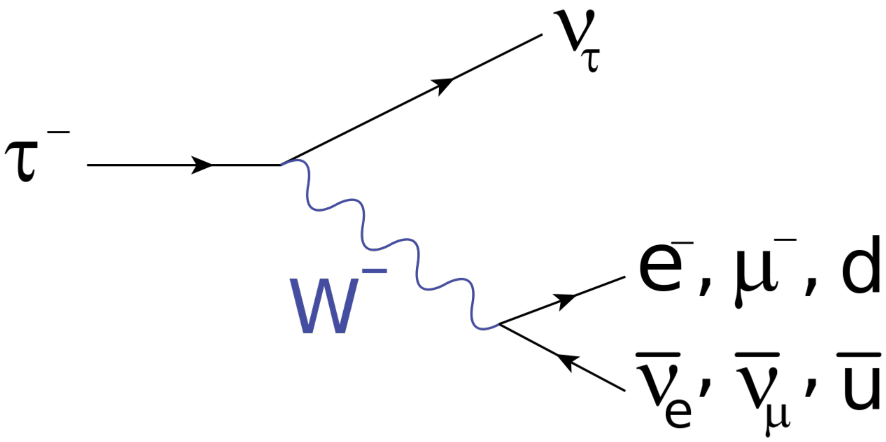

FIGURE 3.8: Feynman diagram of the τ lepton decay by emission of an off-mass shell W boson.

3.6.1 τ leptonic decay

The branching fraction of τ leptons decaying into electrons (muons) is 17.8 ± 0.4 % (17.4 ± 0.4 %) [12]. These electrons and muons, in isolation, cannot be distinguished from other promptly-produced electron and muon candidates. Moreover, the two neutrinos produced in the leptonic τ-lepton decay cannot be directly identified, as discussed in Section 3.5. Consequently, a τ lepton decaying leptonically, denoted as τ_{lep} in this thesis, is reconstructed as a charged electron or muon, contributing to the E_T^{miss}.

3.6.2 Hadronic Decays of τ Leptons

Given its relatively substantial mass of about 1.777 GeV [12], the τ lepton stands as the sole lepton with adequate mass to engage in hadronic decays, which occur in roughly 64.8% of instances. When a τ lepton decays hadronically, denoted as τ_{had} in this work, it results in either one or three charged pions or kaons, occasionally involving up to two neutral pions along with a ν_τ. These decays are classified into "1-prong" decay, involving one charged hadron, and "3-prong" decay, involving three charged hadrons. Table 3.1 presents a summary of the most prevalent hadronic decay modes of the τ lepton and their corresponding branching ratios.

Decay mode	Intermediate resonance	Branching ratio [%]
$\tau^- \to h^- \nu_\tau$	-	11.5
$\tau^- \to h^- \pi^0 \nu_\tau$	$\rho(770)$	26.0
$\tau^- \to h^- \pi^0 \pi^0 \nu_\tau$	$a_1(1260)$	9.5
$\tau^- \to h^- h^+ h^- \nu_\tau$	$a_1(1260)$	9.8
$\tau^- \to h^- h^+ h^- \pi^0 \nu_\tau$	-	4.8
Other modes with hadrons	-	3.2
All modes with hadrons	-	64.8

TABLE 3.1: Approximate branching ratios are depicted for the most prevalent hadronic decay modes of the τ lepton [12]. The notation h^- denotes a charged hadron, which could be either a pion or a kaon. Certain decay modes occur through intermediary resonances, such as $\rho(770)$ or $a_1(1260)$ mesons.

In the following a brief summary is given for the reconstruction of τ_{had} candidate:[4]

Seed jets

The initial step involves identifying a τ_{had} candidate, which is initiated from a selected jet candidate [75]. This set of jets is reconstructed utilizing the anti-k_t algorithm with a radius parameter of $R = 0.4$, akin to the jet ensemble derived from topo-clusters, as detailed in Section 3.4. Notably, prior to jet formation, topo-clusters undergo a local hadronic calibration (LC) [64]. We exclusively consider jets with transverse momentum surpassing 10 GeV within the $|\eta| < 2.5$ range.

Vertex Association

The decay vertex for τ-lepton is typically displaced from the primary vertex (PV) due to the finite τ-lepton decay length. Correctly identifying this vertex allows

---

[4] It's more accurate to differentiate between two terminologies: τ_{had}, denoting a τ lepton decaying hadronically, and $\tau_{had-vis}$, indicating solely the observable component of the τ_{had} candidate, considering that the energy of neutrinos remains unmeasured. For the sake of simplicity, this thesis utilizes the former terminology, though the specific interpretation should be inferred from the context.

us to ensure that the tracks associated with the seed jet are matched to the τ-lepton decay vertex, effectively suppressing contributions from pileup events while maintaining high τ_{had} reconstruction efficiency. All tracks within a cone of 0.2 in ΔR around the seed jet axis (referred to as the core region) are utilized to select the τ-lepton decay vertex from the PV candidates. Subsequently, the direction of the τ_{had} candidate is adjusted in relation to the decay vertex, and the impact parameters are re-evaluated [75].

Track selection

The choice of tracks in the central region of the τ_{had} candidate is fine-tuned to maximize the efficiency in reconstructing 1- and 3-prong τ_{had} candidates with the accurate count of charged particles [75].

Energy calibration

In the calibration process for τ_{had} candidates, apart from constructing seed-jets derived from topo-clusters calibrated to the LC scale, two supplementary energy adjustments are applied [75]. Initially, an estimation and removal of energy contributions from pileup interactions are carried out. Following this, corrections are implemented to address emissions that either lack sufficient energy to reach the calorimeter or fail to form the topo-clusters. Additionally, adjustments are made for emissions located outside the central region of the τ_{had} candidate.

Identification

The τ_{hadvis} reconstruction algorithm alone does not differentiate against other particles that exhibit jet-like features in the detector. Thus, specialized algorithms are employed to discern hadronic tau lepton decays. In this context, a recurrent neural network (RNN) classifier is implemented, as elucidated in Ref.[76]. Given the distinctive characteristics of 1- and 3-prong τ_{hadvis} decays, the τ_{hadvis}-identification (τ_{hadvis}-ID) is divided into tailored algorithms for these cases.

The chosen τ_{hadvis} candidates in this thesis must fulfils the criteria of $p_T > 20$ GeV, $|\eta| < 2.5$. Candidates in the transition region of the calorimeter, where $1.37 < |\eta| < 1.52$, are excluded due to suboptimal detector coverage. Additionally, candidates must feature either one or three tracks, possess unit charge, and satisfy the 'loose' τ_{hadvis}-ID working point. The loose WP corresponds to an efficiency of 85% for 1-prong and 75% for 3-prong (with efficiency being constant in p_T by definition).

Furthermore, a BDT leveraging track and shower shape information is employed to further reject τ_{hadvis} candidates originating from electrons. The 'loose' working point is chosen, ensuring a selection efficiency of approximately 95% for true τ_{hadvis} candidates.

3.7 Reconstruction of Di-Tau Mass

In τ-lepton decays, one or two neutrinos are produced depending on the decay mode, causing uncertainty in the reconstructed visible four-momentum of the τ_{had} due to undetermined neutrino energies. This uncertainty broadens the reconstructed visible mass, posing challenges in distinguishing signal from background in resonance analyses involving pairs of τ leptons.

To address this issue, the $HH \rightarrow b\bar{b}\tau^+\tau^-$ analysis employs the Missing Mass Calculator (MMC) method [77] to reconstruct the invariant mass of the τ-lepton pairs. MMC, which relies on likelihood principles, significantly enhances the resolution of the invariant mass compared to using only the visible mass information. This technique involves solving a system of equations with several unknowns (ranging from six to eight, depending on the number of neutrinos in the $\tau^+\tau^-$ final state). These unknowns correspond to the momentum carried by the neutrinos for each τ lepton along the x, y, and z axes, as well as the invariant mass of the two neutrinos from any leptonic τ decays.

Since the number of unknowns surpasses the available constraints, obtaining an exact solution is not feasible. Nonetheless, the MMC method assigns probabilities to different solutions based on constraints derived from the measured x and y components of the missing transverse momentum, along with the visible masses of both τ-lepton candidates. A systematic scan is conducted over the components of the missing transverse momentum vector and the unresolved variables. Each point in this scan is assessed based on its likelihood using the E_T^{miss} resolution and characteristics specific to the decay of τ-leptons. The estimator for the $\tau^+\tau^-$ mass is determined as the most probable value among these scan points.

Figure 3.9 illustrates the comparison between the reconstructed visible invariant mass and the MMC invariant mass for $HH \rightarrow b\bar{b}\tau^+_{had}\tau^-_{had}$ simulated events. MMC demonstrates a more accurate estimation of the $\tau^+\tau^-$ mass, characterized by both peak position and relative width. In this thesis' $HH \rightarrow b\bar{b}\tau^+\tau^-$ analysis, the di-τ mass resolution is approximately $15\,\text{GeV}$ for the SM di-Higgs signal in the $b\bar{b}\tau^+_{had}\tau^-_{had}$ channel, where both τ-leptons decay hadronically.

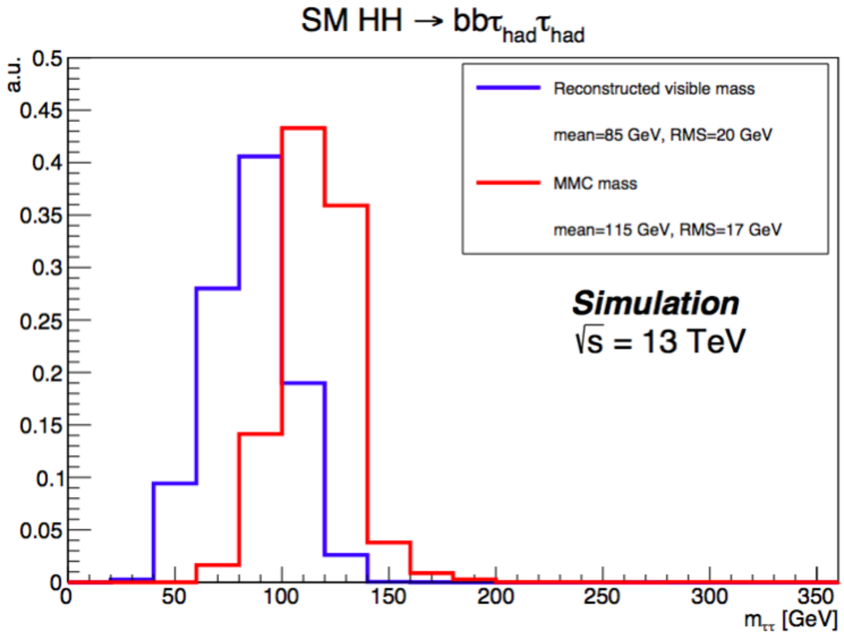

FIGURE 3.9: Comparison between the reconstructed visible invariant mass and the reconstructed MMC invariant mass for simulated $HH\rightarrow b\bar{b}\tau^{+}_{had}\tau^{-}_{had}$ events. The plots illustrate the differences in mass estimation techniques for di-τ pairs, showcasing the MMC method's ability to provide a more accurate estimation of the invariant mass compared to using the visible mass alone

Chapter 4

Searches for Higgs bosons pair production in the $b\bar{b}\tau^+\tau^-$ final state with 140 fb^{-1} of 13 TeV *pp* collision data in ATLAS

4.1 Introduction

In this chapter a search for the non-resonant Higgs pair (HH) productions in the final state with two bjets and two τ leptons using 140 fb^{-1} of pp collision data recorded by the ATLAS experiment at $\sqrt{s}$ = 13 TeV is presented. The $b\bar{b}\tau^+\tau^-$ channel has one of the largest branching fractions (7.3%) among the investigated *HH* decay channels and a relatively clean final state. Since τ leptons can decay either leptonically (τ_{lep}: into e or μ) or hadronically (τ_{had}: typically into one or three charged pions, plus some neutral pions), in this regard two sub-channels are considered, namely $b\bar{b}$ $\tau_{lep}\tau_{had}$ and $b\bar{b}$ $\tau_{had}\tau_{had}$, while the decay channel with both τ decays leptonically is not studied in the analysis presented in the thesis but instead is covered in ref [78].

The pervious search performed for the $b\bar{b}\tau^+\tau^-$ decay channel was dedicated for *HH* cross-section measurements for both resonant and non-resonant signal hypothesis [79], in which the author has also made significant contributions. The non-resonant analysis set an observed (expected) upper limit on the *HH* cross-section to 140 (110) fb at 95% CL, corresponding to 4.7 (3.9) times the SM prediction with respect to the background-only hypothesis. While for constraining the anomalous trilinear Higgs boson self-couplings λ_{HHH} the $b\bar{b}\tau^{+}\tau^{-}$ channel results were presented in a combination search with the other *HH* decay channels. In the absence of a Higgs boson pair production signal, values of the κ_{λ}[1] modifier of the trilinear Higgs boson self-coupling outside of [-2.4, 9.2] ([-2.0, 9.0]) are excluded at 95% CL [80]. Assuming SM *HH* production and couplings, κ_{λ} is constrained between observed (expected) $-2.7 < \kappa_{\lambda} < 9.5$ ($-3.1 < \kappa_{\lambda} < 10.2$) and κ_{2V}[2] between $-0.6 < \kappa_{2V} < 2.7$ ($-0.5 < \kappa_{VV} < 2.7$) at 95% CL [81]. In this case, limits are obtained using the test statistic ($-2\ln\,\Lambda$) in the asymptotic approximation.

The analysis presented in this thesis has been re-optimized for κ_{λ} constraints. This was achieved by implementing an event categorization based on the invariant mass of the HH system, m_{HH} in the ggF region. Additionally, we enhanced the κ_{VV} sensitivity (discussed in Chapter 5) by introducing a dedicated VBF category. Multivariate analysis (MVA) techniques are employed to ensure an optimal separation between the ggF/VBF signal and background processes. The MVA outputs serve as the final discriminants in the fit.

4.2 Data and Monte Carlo samples

The analysis presented in this thesis uses the proton-proton collision data at a centre-of-mass energy of $\sqrt{s}$ =13 TeV, collected by the ATLAS detector at the LHC between 2015 and 2018, corresponding to an integrated luminosity of $\mathcal{L}$ =140.1 ± 1.2 fb^{-1}[82].

---

[1] $\kappa_{\lambda}$is the modifier Higgs self coupling constant and it is defined as $\kappa_{\lambda} = \frac{\lambda_{HHH}}{\lambda_{HHH}^{SM}}$

[2] κ_{2V} is the coupling between two vector bosons and two Higgs bosons

The background and signal processes, both SM non-resonant *HH* production and Beyond the Standard Model (BSM) *HH* production, are modelled using MC simulated events. These events underwent a comprehensive simulation of the ATLAS detector based on GEANT [83], as well as the inclusion of pile-up effects from both the same and adjacent bunch crossings. The latter was achieved by overlaying each hard-scatter event with minimum-bias events, which were simulated using the soft quantum chromodynamics (QCD) processes of PYTHIA[8.186] [84] with parameters fine-tuned using the A3 tune [85], along with the use of NNPDF[2.3lo] parton distribution functions (PDFs) [86].

For the simulation of bottom and charm hadron decays, the EVTGEN program [87] was employed in all event samples, except for those generated using SHERPA [88]. In the case of samples generated with SHERPA, the decay model for bottom and charm hadrons incorporated in the generator itself was utilized. Following simulation, the events were subjected to the same reconstruction algorithms as the experimental data.

In all datasets featuring a SM Higgs boson, its mass was consistently set to $125\ \mathrm{GeV}$. This mass value was consistently employed in computing the branching fractions of the Higgs boson decay as well as in determining the cross-sections for single-Higgs-boson and SM non-resonant HH production, unless otherwise specified. When referring to cross-section calculation, it is implied to be an expansion in the strong coupling constant (α_s). For a comprehensive list of event samples utilized in simulating both signal and background processes, please refer to Table 4.1.

The analysis utilizes MC samples generated using the ATLAS simulation framework [89] for both signal and background processes. Detailed descriptions of the signal and background MC samples are provided in the subsequent sections.

Process	MC generator	MC QCD order	ME PDF	PS and hadronisation	UE model tune	Cross-section order
Signal						
$gg \to HH$ (ggF with $\kappa_\lambda = 1, 10$)	Powheg Box v2	NLO	PDF4LHC15nlo	Pythia 8.244	A14	NNLO FTApprox
$qq \to qqHH$(VBF with varied κ_λ, κ_{2V}, κ_V)	MadGraph5_aMC@NLO 2.7.3	LO	NNPDF3.0nlo	Pythia 8.244	A14	N^{3}LO(QCD)
Top-quark						
$t\bar{t}$	Powheg Box v2	NLO	NNPDF3.0nlo	Pythia 8.230	A14	NNLO+NNLL
t-channel	Powheg Box v2	NLO	NNPDF3.0nlo	Pythia 8.230	A14	NLO
s-channel	Powheg Box v2	NLO	NNPDF3.0nlo	Pythia 8.230	A14	NLO
Wt	Powheg Box v2	NLO	NNPDF3.0nlo	Pythia 8.230	A14	NLO
$t\bar{t}Z$	Sherpa 2.2.1	NLO	NNPDF3.0nnlo	Sherpa 2.2.1	Default	NLO
$t\bar{t}W$	Sherpa 2.2.8	NLO	NNPDF3.0nnlo	Sherpa 2.2.8	Default	NLO
Vector boson + jets						
W/Z+jets	Sherpa 2.2.11	NLO ($\leq$ 2 jets) LO (3,4,5 jets)	NNPDF3.0nnlo	Sherpa 2.2.11	Default	NNLO
Diboson						
WW, WZ, ZZ	Sherpa 2.2.1	NLO ($\leq$ 1 jet) LO (2,3 jets)	NNPDF3.0nnlo	Sherpa 2.2.1	Default	NLO
Single Higgs boson						
ggF	Powheg Box v2	NNLO	NNPDF3.0nlo	Pythia 8.212	AZNLO	N^{3}LO(QCD)+NLO(EW)
VBF	Powheg Box v2	NLO	NNPDF3.0nlo	Pythia 8.212	AZNLO	NNLO(QCD)+NLO(EW)
$qq \to WH$	Powheg Box v2	NLO	NNPDF3.0nlo	Pythia 8.212	AZNLO	NNLO(QCD)+NLO(EW)
$qq \to ZH$	Powheg Box v2	NLO	NNPDF3.0nlo	Pythia 8.212	AZNLO	NNLO(QCD)+NLO(EW)†
$gg \to ZH$	Powheg Box v2	NLO	NNPDF3.0nlo	Pythia 8.212	AZNLO	NLO+NLL
$t\bar{t}H$	Powheg Box v2	NLO	NNPDF3.0nlo	Pythia 8.230	A14	NLO

TABLE 4.1: Generators used to simulate the signal and background processes. If not otherwise specified, the order of the cross-section calculation refers to the expansion in the strong coupling constant (α_s). The acronyms ME, PS and UE are used for matrix element, parton shower and underlying event, respectively. Details of the simulation of the signal and background samples are described in the text. †The NNLO(QCD)+NLO(EW) cross-section calculation for the $pp \to ZH$ process already includes the $gg \to ZH$ contribution. The $qq \to ZH$ process is normalised to the NNLO(QCD)+NLO(EW) cross-section for the $pp \to ZH$ process, after subtracting the $gg \to ZH$ contribution.

4.2.1 Signal samples

Simulated *HH* signal production includes the contributions from the ggF and VBF processes.

The **ggF *HH*** signal samples for both κ_λ = 1.0 and 10.0 are simulated with **Powheg Box v2** generator [90] at next-to-leading order (NLO) with finite top-quark mass. Parton showers and hadronisation were simulated using **PYTHIA 8.244** with the A14 set of tuned parameters and the **NNPDF**2.3_{LO} PDF set. Figure 4.1 shows the m_{HH} distribution of the ggF *HH* signal samples for κ_λ = 1.0, 10.0 values produced at parton level. The plot demonstrates the interesting feature that this kinematic variable will further provide in terms of analysis categorisation as discussed in this chapter.

ggF *HH* events with different κ_λ values (in the interval $\kappa_\lambda \in [-20, 20]$) can be

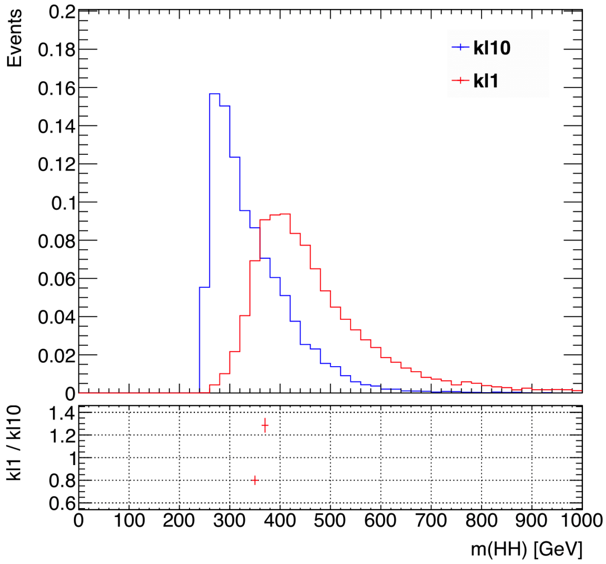

FIGURE 4.1: Parton level invariant mass distribution of the *HH* system m_{HH}, for the nominal ggF *HH* signal samples with varied κ_λ= 1.0, 10.0 values overlayed.

provided by reweighting either of the two available samples using the common *HH* κ_λ reweighting tool, which provides per-event weights, depending on the targeted κ_λ value and on the truth m_{HH}. Details on the κ_λ reweighting procedure for the ggF *HH* sample are provided in appendix A.1.

The **VBF *HH*** signal samples were generated at LO using the **MadGraph5_aMC@NLO2.7.3** [91] generator with the **NNPDF**3.0_{LO} PDF set [92]. The process of parton showering and hadronisation was modelled using **Pythia 8.244**, utilizing the A14 tune and the **NNPDF**2.3_{NLO} PDF set. For simulating the decays of *b*- and *c*-hadrons, the EvtGen v1.7.0 program was employed.

VBF samples have been produced for different values of the coupling modifiers κ_λ, κ_{2V} and κ_V [3] as shown in table 4.2,

A linear combination of (κ_λ, κ_{2V}, κ_V) = (1, 1, 1), (1, 1.5, 1), (2, 1, 1), (10, 1, 1), (1, 1, 0.5), (-5, 1, 0.5), as demonstrated in appendix A.1. These six basis samples were chosen to lie in the region where the analysis is expected to be sensitive, in order to avoid large statistical uncertainties in the interpolation resulting from the reweighting. Figures 4.2 and 4.3 show a representative set of

---

[3] κ_V is the coupling between vector boson and a Higgs boson as shown in figure 1.8.

κ_λ	κ_{2V}	κ_V
1	1	1
1	0	1
1	0.5	1
1	1.5	1
1	2	1
1	3	1
0	1	1
2	1	1
10	1	1
1	1	0.5
1	1	1.5
0	0	1
-5	1	0.5

TABLE 4.2: κ_λ, κ_{2V} and κ_V coupling modifier values considered for the nominal VBF *HH* samples generation.

relevant distributions of these nominal samples at parton level, with the highest m_{jj}[4] pair selected as a proxy for the VBF jets, for the $\tau_{had}\tau_{had}$ and $\tau_{lep}\tau_{had}$ channels, respectively. As can be seen, the invariant mass distribution of the VBF jets system is unchanged with respect to the couplings variations. Distributions of the pseudo-rapidity gap between two VBF jets also don't change for various couplings. However, given the large pseudo-rapidity gap is a distinct feature for VBF jets, this variable provides a good handle for the separation of ggF and VBF *HH* processes. Another possibility is to exploit the interesting kinematic region at large m_{HH}, in particular when κ_{2V} departs from its SM value as shown in 4.4.

---

[4] The b-tagged jets are first removed from the pair of jets used to compute the m_{jj}

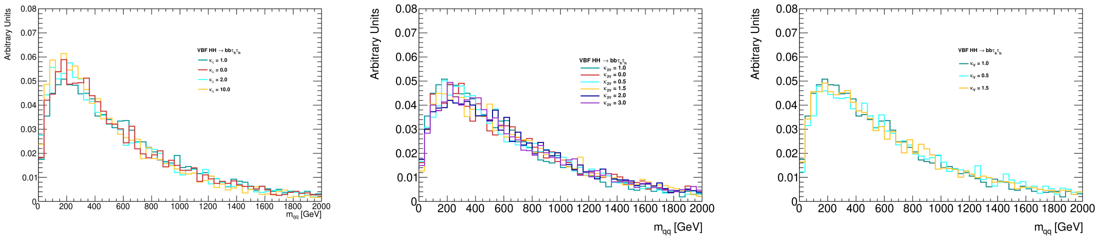

(A) $\kappa_\lambda$variation (κ_V =κ_{2V}=1) (B) κ_{2V}variation (κ_λ=κ_V =1) (C) κ_V variation (κ_λ=κ_{2V}=1)

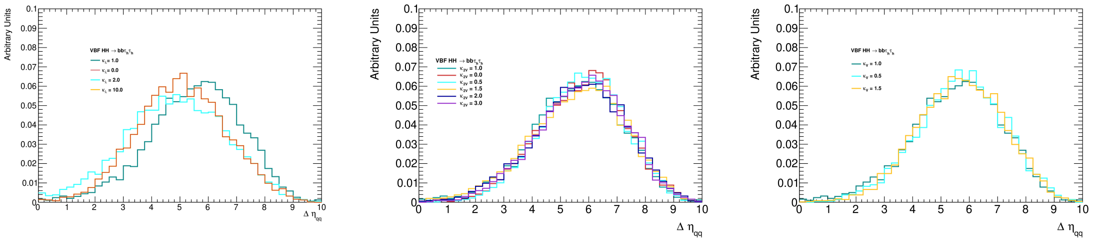

(D) $\kappa_\lambda$variation (κ_V =κ_{2V}=1) (E) κ_{2V}variation (κ_λ=κ_V =1) (F) κ_V variation (κ_λ=κ_{2V}=1)

FIGURE 4.2: Parton level plots for the VBF *HH* signal sample showing the invariant mass distribution and the pseudo-rapidity separation of the VBF jets system in the $\tau_{had}\tau_{had}$ channel. For each plot κ_λ, κ_{2V} and κ_V are varied respectively as shown in Table 4.2 while the other two couplings are set to their SM prediction. The distributions are normalised to unity.

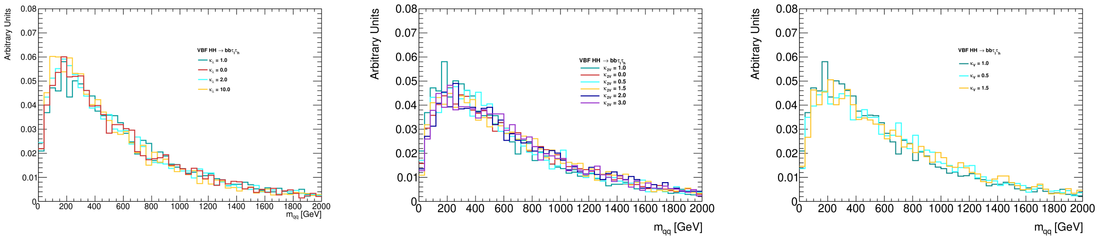

(A) $\kappa_\lambda$variation (κ_V =κ_{2V}=1) (B) κ_{2V}variation (κ_λ=κ_V =1) (C) κ_V variation (κ_λ=κ_{2V}=1)

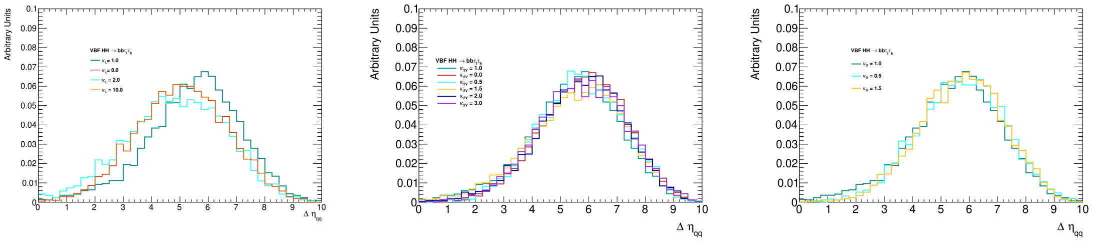

(D) $\kappa_\lambda$variation (κ_V =κ_{2V}=1) (E) κ_{2V}variation (κ_λ=κ_V =1) (F) κ_V variation (κ_λ=κ_{2V}=1)

FIGURE 4.3: Parton level plots for the VBF *HH* signal sample showing the invariant mass distribution and the pseudo-rapidity separation of the VBF jets system in the $\tau_{lep}\tau_{had}$ channel. For each plot κ_λ, κ_{2V} and κ_V are varied respectively as shown in Table 4.2 while the other two couplings are set to their SM prediction. The distributions are normalised to unity.

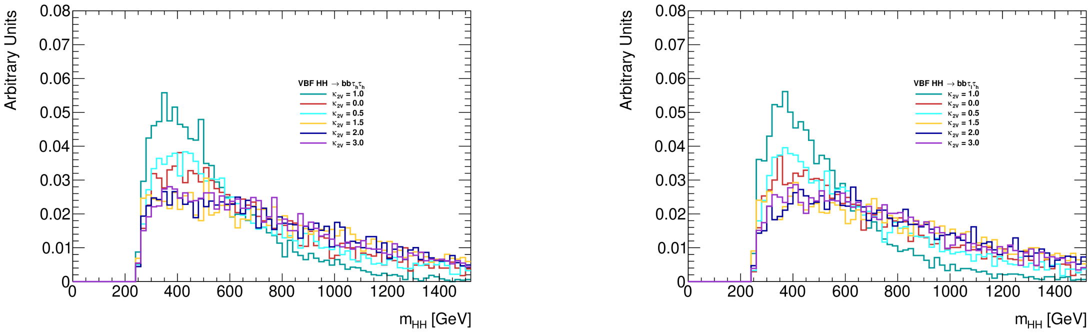

(A) HadHad Channel

(B) LepHad Channel

FIGURE 4.4: Nominal VBF *HH* signal sample plots for various κ_{2V} values at parton level. m_{HH} distributions are shown in the $\tau_{had}\tau_{had}$ (a) and $\tau_{lep}\tau_{had}$ (b) channels. For each plot κ_λ, κ_{2V} and κ_V are varied respectively as shown in Table 4.2 while the other two couplings are set to their SM prediction. The distributions are normalised to unity.

4.2.2 Background samples

Top Quarks: The generation of $t\bar{t}$ pairs and single top-quark events in the Wt, s and t channels is performed utilizing the POWHEGBOXv2 generator [93–95]. The choice of PDF set is NNPDF30NLO [96]. Subsequently, the events are linked to PYTHIA8 (version 8.230) [97] for parton showering and hadronization, employing the A14 set of tuned parameters [98, 99] along with the NNPDF23LO PDF set [100]. The properties of bottom and charm hadron decays are simulated using EvtGen v1.6.0 [101]. In all top-quark processes, spin correlations of the top quarks are conserved. For t-channel production, the decay of top quarks is handled using MadSpin [102]. The top-quark mass is fixed at 172.5 GeV. The NLO $t\bar{t}$ production cross section is adjusted to match the theory prediction computed at NNLO+NNLL. For single top-quark processes, the cross sections are adjusted to the theory predictions calculated at NLO. The interference between $t\bar{t}$ and Wt processes is managed using the diagram removal scheme.

V+ jets: Events featuring W or Z bosons produced alongside with jets are modeled using the SHERPA2.2.11 [88] generator. This employs NLO matrix elements accounting for up to two partons, and LO matrix elements for up to five partons, computed with the Comix [103] and OPENLOOPS [104–106] libraries.

These matrix elements are harmonized with the SHERPA parton shower using the MEPS@NLO prescription [107–110], employing a tailored set of parameters crafted by the SHERPA authors. The NNPDF3.0NNLO PDF set [92] is utilized. The selection of SHERPA2.2.11 configuration, in lieu of SHERPA2.1.1 employed in the prior analysis iteration, is motivated by the considerations in Ref. [111].

Drell-Yan and Diboson: Drell-Yan, ZZ, WZ and WW processes, where one of the bosons decays hadronically and the other leptonically, are simulated using the SHERPA version 2.2.1 [88] generator. The NNPDF3.0NNLO set of PDFs [92] is employed along with a dedicated parton shower tuning developed by the SHERPA authors. The generator NLO cross-sections are utilized.

ttV: Production of W and Z bosons in association with a top-quark pair, ttV, is simulated using SHERPA version 2.2.1 with multileg NLO merging for the ttZ production and SHERPA version 2.2.8 at NLO for the ttW production. The NNPDF3.0NNLO set of PDFs [92] is used along with a dedicated parton shower tuning developed by the SHERPA authors. The most accurate NLO generator cross-sections are utilized.

ttH: SM Higgs production in association with a top-quark pair ttH, is simulated using the POWHEGBOX generator [93–95]. The NNPDF30NLO PDF set is employed. The events are interfaced to PYTHIA8 version 8.230 [97] for the parton shower and hadronisation with the A14 set of tuned parameters [98, 99] and the NNPDF23LO PDF set [100]. The EvtGen program [101] is also utilized. The cross-section is set to ttH production NLO calculations [15].

ZH: The Higgs boson production in association with a Z boson, ZH, with the Higgs boson decaying to bb or $\tau\tau$, is included in the analysis using three samples. The $qqZH(Z \to ll, H \to bb)$, $ggZH(Z \to ll, H \to bb)$ (where "l" includes all leptons e, μ, τ) and $qqZH(Z \to all, H \to \tau\tau)$, $ggZH(Z \to all, H \to \tau\tau)$ are simulated using POWHEGBOXv2. The NNPDF3.0NNLO set of PDFs [92] is used. The events are interfaced with PYTHIA8 version 8.212 using the AZNLO tune [112] and the CTEQ6L1 PDF set [113]. The EvtGen program [101] is also utilized. The cross-section is set to the NNLO(QCD)+NLO(EW) calculations for $qqZH$ and to the NLO+NLL in QCD for $ggZH$.

WH: The associative production of Higgs boson with a W boson, WH, with the Higgs boson decaying to bb or $\tau\tau$, is included in the analysis using four samples. The $W^{\pm}H(W \rightarrow l\nu, H \rightarrow bb)$ where "l" includes all leptons e, μ, τ, $W^{\pm}H(W \rightarrow all, H \rightarrow \tau\tau)$ are simulated using POWHEGBOXv2. The NNPDF3.0NNLO set of PDFs [92] is used. The events are interfaced with PYTHIA8 version 8.212 using the AZNLO tune [112] and the CTEQ6L1 PDF set [113]. The EvtGen program [101] is also utilized. The cross-section is set to the NNLO(QCD)+NLO(EW) calculations.

ggF $H \rightarrow \tau\tau$: The gluon-fusion Higgs boson production with the Higgs boson decaying to $\tau\tau$ is simulated using POWHEGBOXv2. The NNPDF3.0NNLO set of PDFs [92] is used. The events are interfaced with PYTHIA8 version 8.212 using the AZNLO tune [112] and the CTEQ6L1 PDF set [113]. The EvtGen program [101] is also utilized. The cross-section is set to the N3LO(QCD)+NLO(EW) calculations [15].

VBF $H \rightarrow \tau\tau$: The VBF Higgs boson production with the Higgs boson decaying to $\tau\tau$ is simulated using POWHEGBOXv2. The NNPDF3.0NNLO set of PDFs [92]. The events are interfaced with PYTHIA8 version 8.212 using the AZNLO tune [112] and the CTEQ6L1 PDF set [113]. The EvtGen program [101] is also utilized. The cross section is set to the NNLO(QCD)+NLO(EW) calculations [15].

4.3 Object selection

The objects resulting from the *pp* collisions are reconstructed in the ATLAS detector, as detailed in Chapter 3. The analysis employs the following criteria for reconstruction and identification:

- Electrons: are required to satisfy $p_T > 7\,\text{GeV}$ and $|\eta| < 2.47$, with a veto in the transition region between the barrel and endcap of the calorimeter ($1.37 < |\eta| < 1.52$). Additionally, electrons must pass the tight identification and loose isolation criteria.

- Muons: are required to satisfy $p_T > 7\,\text{GeV}$ and $|\eta| < 2.7$. Muons must also pass the medium and loose identification isolation requirments.

- Jets: Reconstructed by utilising the anti-k_t algorithm[65] and the Particle-Flow algorithm [114] with required radius parameter of $R = 0.4$, and also have $p_T > 20\,\text{GeV}$ and $|\eta| < 2.5$. The analysis also makes use of forward jets, in particular for the definition of VBF *HH* enriched signal region. These forward jets are required to fall within 2.5 ≤ $|\eta|$ < 4.5 and have $p_T > 30\,\text{GeV}$.

- b-Jets: Identified using a multivariate classification algorithm based on a deep neural network, the DL1r tagger [70, 71], is used to distinguish b-jets from the background of light-flavour- and charm-quark-initiated jets using information about the jet kinematics, the impact parameters of tracks associated with the jet, and the presence of displaced vertices. The inputs to the DL1r network include variables based on a recurrent neural network (RNNIP) [72], which can exploit the spatial and kinematic correlations between tracks that are initiated from the same b-hadrons. In this analysis, the signal regions are defined by selecting exactly 2 b-jets passing the 77% working point.

- τ_{had}: are required to have $p_T > 20\,\text{GeV}$ and $|\eta| < 2.5$, with a veto in the transition region between the barrel and endcap of the calorimeter ($1.37 < |\eta| < 1.52$). Additionally, it should have either at least one or three tracks and have passed the medium identification criteria.

- Anti-τ_{had}: In order to provide fake-τ_{had}-enriched regions used for background estimation, an anti-τ_{had} selection is defined. Those $\tau_{had-vis}$ objects that fail the RNN loose τ_{had}-ID and have the RNN score greater than 0.01 are labelled as anti-τ_{had} candidates[5]. For channels where τ_{had}-ID is applied at the trigger level, anti-τ_{had} candidates are also required to be matched to the trigger τ_{had} in the same way as is required for signal τ_{had}. This definition selects objects that are predominantly jets faking hadronic τ decays. The minimum RNN score requirement ensures that the jets still have some τ_{had}-like properties and ensures that the composition of quark- and gluon-initiated jets is closer to that of the signal region. Anti-τ_{had} objects are selected only in events in which there are fewer τ_{had} that pass the offline τ_{had}-ID than required for a given channel (one for the $\tau_{lep}\tau_{had}$ and two for the $\tau_{had}\tau_{had}$ selection). In that case, additional anti-τ_{had} candidates are selected so that the total number of selected τ_{had} (loose, which always has priority, and anti-τ_{had}) corresponds to the required multiplicity in each channel.

4.4 Overlap Removal

Following event reconstruction, an overlap-removal procedure is applied to resolve ambiguities that may arise when a physical object is detected as multiple types of particles in the ATLAS detector. The angular distance $\Delta R_y = \sqrt{\Delta y^2 + \Delta\phi^2}$ is utilized to quantify the overlap of two reconstructed objects.

Most overlaps between detector objects employed in this analysis are resolved using the standard overlap removal tools `AssociationUtils` [115]. An exception arises when addressing overlaps between the reconstructed $\tau_{had-vis}$,

---

[5] The defined cut, RNN score > 0.01, has per definition an efficiency of approximately 99% for true-τ_{had} in $\gamma^* \to \tau\tau$ events, which is independent of the $\tau_{had-vis}$ p_T due to a flattening of the RNN score, and a fake-τ_{had} rejection in multijet MC of about 5 (8) for 1-prong (3-prong) candidates.

anti-$\tau_{had-vis}$ objects, and jets. In these cases, a procedure tailored for this analysis is implemented, as detailed below. The analysis adopts the *Standard* recommended working point of the `AssociationUtils` tool [116].

The step-by-step procedure for resolving ambiguities in the reconstructed objects is outlined as follows:

- e_1 - e_2: Reject e_1 if both electrons share the track and $p_{T1} < p_{T2}$
- $\tau_{had-vis}$- e: Reject $\tau_{had-vis}$ if ΔR_y < 0.2 and e passes `DFCommonElectronsLHLoose`
- $\tau_{had-vis}$- μ: Reject $\tau_{\text{had-vis}}$ if ΔR_y < 0.2:
  - Case 1 ($\tau_{\text{had-vis}}$ p_T > 50 GeV): $p_{T,\mu}$ > 2 GeV and combined muon
  - Case 2 ($\tau_{\text{had-vis}}$ $p_T \leq$ 50 GeV): $p_{T,\mu}$ > 2 GeV
- μ - e: Reject μ if calo-muon and shared ID track
- e - μ: Reject e if shared ID track
- jet - e: Reject jet if ΔR_y < 0.2
- e - jet: Reject e if 0.2< ΔR_y < 0.4
- jet - μ: Reject μ if ΔR_y < 0.2
- μ - jet: Reject μ if ΔR_y < 0.4

Additionally, an analysis-specific overlap-removal procedure for $\tau_{had-vis}$, anti-$\tau_{had-vis}$, and jets is implemented:

- jet - $\tau_{had-vis}$: Reject jet if ΔR_y < 0.2
- anti-$\tau_{had-vis}$- jet: Reject anti-τ_{had} if jet is b-tagged and ΔR_y < 0.2
- jet - anti-$\tau_{had-vis}$: Reject jet if ΔR_y < 0.2

This establishes the following priority: $\tau_{had-vis}$> b-tagged jet > anti-$\tau_{had-vis}$> un-tagged jet.

An alternative priority of b-tagged jet > $\tau_{had-vis}$ > anti-$\tau_{had-vis}$ > b-tagged jet was considered but found to significantly reduce signal acceptance in the 2-tag region due to limited τ_{had} rejection of the DL1r b-tagging algorithm at the 77% working point[6]. With the alternative priority, the signal acceptance is reduced by approximately 8% (13%) in $\tau_{lep}\tau_{had}$ ($\tau_{had}\tau_{had}$).

4.5 Event selection

As outlined in Section 4.1, the analysis is divided into two sub-channels based on the di-τ decay mode, as summarised in table 4.3.

The $b\bar{b}$ $\tau_{had}\tau_{had}$ sub-channel is designed for events featuring two oppositely charged $\tau_{\text{had-vis}}$ and two b-jets. In contrast, the $b\bar{b}$ $\tau_{lep}\tau_{had}$ sub-channel, further divided into two categories based on trigger choice, focuses on events with either an electron or muon, an oppositely charged $\tau_{\text{had-vis}}$, and two b-jets. In both sub-channels, the two b-jets are required to pass the 77% efficiency working point. Details regarding the trigger configuration for the $b\bar{b}$ $\tau_{lep}\tau_{had}$ sub-channel, encompassing single-lepton triggers (SLT) and lepton-plus-$\tau_{\text{had-vis}}$ triggers (LTT), and for the $b\bar{b}$ $\tau_{had}\tau_{had}$ sub-channel, involving a combination of single-$\tau_{\text{had-vis}}$ triggers (STT) and di-$\tau_{\text{had-vis}}$ triggers (DTT), are provided in Sections 4.5.1 and 4.5.2 respectively.

4.5.1 $\tau_{lep}\tau_{had}$ event selection

In the $\tau_{lep}\tau_{had}$ sub-channel, events were recorded using a combination of two types of triggers: single-lepton triggers (SLTs) and lepton-plus-$\tau_{\text{had-vis}}$ triggers (LTTs). The SLTs necessitate the reconstruction of either an electron or a muon

---

[6] Furthermore, the adopted priority ensures consistent treatment of electrons, muons, and $\tau_{had-vis}$ candidates in relation to b-jets in the signal regions of the analysis, facilitating the use of an $\ell\ell bb$ control region, as will be discussed.

at the HLT. The required thresholds are determined by the data-taking period, ranging from 24 GeV to 26 GeV for electrons and from 20 GeV to 26 GeV for muons.

On the other hand, the LTTs mandate the presence of an electron with $p_{\mathrm{T}} >$ 17 GeV or a muon with $p_{\mathrm{T}} > 14$ GeV in addition to a $\tau_{\text{had-vis}}$ with $p_{\mathrm{T}} > 25$ GeV, reconstructed at the HLT. For LTTs collecting lepton-plus-$\tau_{\text{had-vis}}$ events with $\tau_{\text{had-vis}}$ $p_{\mathrm{T}} < 35\ GeV$, extra criteria at the L1 trigger was applied. This required either an additional jet with $E_{\mathrm{T}} > 25\ GeV$, or two additional jets with $E_{\mathrm{T}} > 12\ GeV$. In cases where the electron-plus-$\tau_{\text{had-vis}}$ triggers necessitating an additional jet with $E_{\mathrm{T}} > 25\ GeV$ did not select the event, the triggers requiring two additional jets with $E_{\mathrm{T}} > 12\ GeV$ were utilized.

For events to be selected based on the presence of a muon, the muon must have $|\eta| < 2.5$. To ensure a well-modeled representation of trigger efficiencies, the offline electrons, muons, and $\tau_{\text{had-vis}}$ objects were required to be within $\Delta R = 0.07$, $\Delta R = 0.1$, and $\Delta R = 0.2$ of the corresponding objects at the HLT, respectively. Minimum p_{T} requirements were imposed on the offline objects. Specifically, these requirements were 1 GeV above the thresholds set for electrons and muons at the HLT, 5 GeV above the thresholds for $\tau_{\text{had-vis}}$ at the HLT, and 80 GeV (45 GeV) for jets, corresponding to an L1-trigger E_{T} threshold of 25 GeV (12 GeV). Events that satisfied the offline SLT lepton p_{T} requirements were excluded from consideration for the LTT. This measure was implemented to ensure no overlap between the SLT and LTT categories. Consequently, these two categories were analyzed separately.

4.5.2 $\tau_{had}\tau_{had}$ event selection

Events in the $\tau_{had}\tau_{had}$ sub-channel are captured using a combination of single-$\tau_{\text{had-vis}}$ triggers (STTs) and di-$\tau_{\text{had-vis}}$ triggers (DTTs).

The STTs admit events with at least one $\tau_{\text{had-vis}}$ at the HLT, with a minimum p_{T} threshold ranging from 80 GeV to 160 GeV, dependent on the data-taking period.

The DTTs select events with a pair of $\tau_{\text{had-vis}}$ reconstructed at the HLT. The leading $\tau_{\text{had-vis}}$ is required to have a minimum p_{T} of 35 GeV (25 GeV for the sub-leading $\tau_{\text{had-vis}}$), where the leading (sub-leading) $\tau_{\text{had-vis}}$ is defined as the one with the highest (second-highest) p_{T} in the event.

Starting from the 2016 data-taking period, additional criteria were implemented in the L1 trigger to reduce the DTT rates. In 2016, an extra jet with $E_{\text{T}} > 25\ GeV$ was mandated. For 2017 and 2018, if two offline jets with $p_{\text{T}} > 45\ GeV$ are found, a trigger requiring two additional jets with $E_{\text{T}} > 12\ GeV$ (and $|\eta| < 2.3$) at L1 is employed. Otherwise, another trigger is used, requiring one additional jet with $E_{\text{T}} > 25\ GeV$ and the $\tau_{\text{had-vis}}$ to be reconstructed within $\Delta R = 2.8$ of each other.

To ensure the events are near the trigger efficiency plateaus where the efficiencies are accurately modeled, the offline $\tau_{\text{had-vis}}$ must be within $\Delta R = 0.2$ of the corresponding HLT $\tau_{\text{had-vis}}$ objects. Additionally, minimum offline p_{T} requirements are applied to $\tau_{\text{had-vis}}$ and the jets. The offline p_{T} thresholds for the $\tau_{\text{had-vis}}$ range between 100 GeV and 180 GeV for the STTs. For the DTTs, the thresholds are 40 GeV (30 GeV for the sub-leading $\tau_{\text{had-vis}}$).

Additional offline requirements for the DTTs are either that two additional jets with $p_{\text{T}} > 45$ GeV are present in the event, or that a jet with $p_{\text{T}} > 80\ GeV$ is present in the event and the $\tau_{\text{had-vis}}$ are reconstructed within $\Delta R = 2.5$ of each other.

For events that satisfy both the STTs and DTTs, the offline requirements used for the STTs are applied. Events that meet the $\tau_{\text{had}}\tau_{\text{had}}$ event selection criteria are analyzed together.

$\tau_{\text{had}}\tau_{\text{had}}$ category		$\tau_{\text{lep}}\tau_{\text{had}}$ categories	
STT	DTT	SLT	LTT
e/μ selection			
No loose e/μ		Exactly one loose e/μ	
		e (μ) must be tight (medium and have $\lvert\eta\rvert < 2.5$)	
		$p_{\text{T}}^{e} > 25, 27$ GeV	18 GeV $<$ p_{T}^{e} $<$ SLT cut
		$p_{\text{T}}^{\mu} > 21, 27$ GeV	15 GeV $<$ p_{T}^{μ} $<$ SLT cut
$\tau_{\text{had-vis}}$ selection			
Two loose $\tau_{\text{had-vis}}$		One loose $\tau_{\text{had-vis}}$	
		$\lvert\eta\rvert < 2.3$	
$p_{\text{T}} > 100, 140, 180$ (25) GeV	$p_{\text{T}} > 40$ (30) GeV		$p_{\text{T}} > 30$ GeV
Jet selection			
≥ 2 jets with $\lvert\eta\rvert < 2.5$			
Leading jet $p_{\text{T}} >$ 45 GeV	Trigger dependent	Leading jet $p_{\text{T}} >$ 45 GeV	Trigger dependent
Event-level selection			
Trigger requirements passed			
Collision vertex reconstructed			
$m_{\tau\tau}^{\text{MMC}} > 60$ GeV			
Opposite-sign electric charges of $e/\mu/\tau_{\text{had-vis}}$ and $\tau_{\text{had-vis}}$			
Exactly two b-tagged jets			
		$m_{bb} < 150$ GeV	

TABLE 4.3: Summary of the event selections, shown separately for events that are selected by different triggers. In cases where pairs of reconstructed objects of the same type are required, thresholds for the (sub-)leading p_{T} object are given outside (within) parentheses where different event selection thresholds are applied. When the selection depends on the year of data-taking, the possible values of the requirements are separated by commas, except for the jet selection in the LTT and DTT triggers, which use multiple selection criteria as described in Section 4.5.2. The trigger p_{T} thresholds shown are applied to the offline physics objects that are matched to the corresponding trigger objects.

4.6 Event Categorization

Events within each sub-channel, as discussed in Section 4.5, are classified into ggF and VBF signal regions (SRs) using BDTs detailed in Section 4.9. The ggF regions are further divided into low- and high-mass SRs based on the invariant mass of the HH system in each event, with a mass cut set at 350 GeV, as illustrated in Figure 4.5. Additionally, a control region ($Z+$ HF CR) is defined for background normalization. This region involves the production of a Z boson associated with one or more jets initiated by heavy-flavour quarks ($Z+$ HF background). It is established using $bb\ell\ell$ triggers and specific event selection criteria. The parameter of interest in this region is the $m_{\ell\ell}$ shape, with further details provided in Section 4.7.

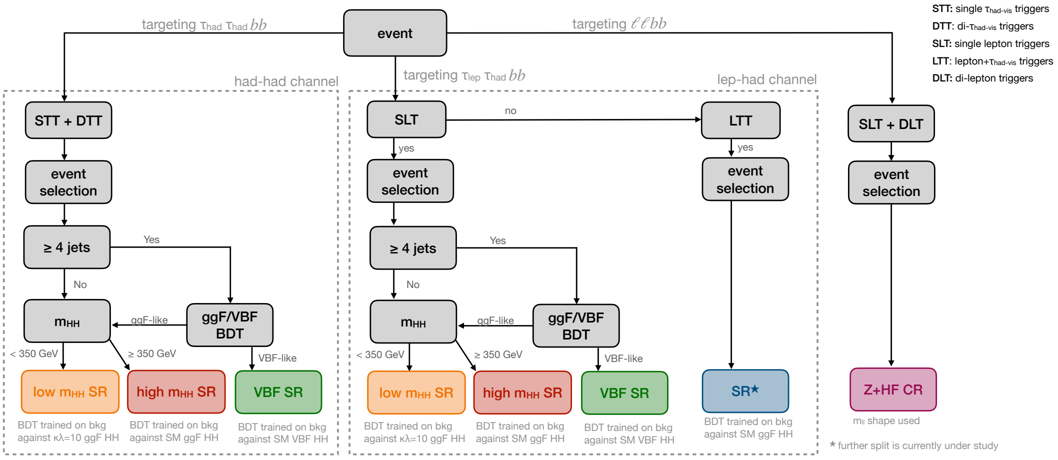

FIGURE 4.5: Schematic representation of the analysis strategy, starting with triggers and event selection for the $b\bar{b}\ \tau_{had}\tau_{had}$ and $b\bar{b}\ \tau_{lep}\tau_{had}$ sub-channels. This is followed by a BDT-based approach to define the orthogonality between ggF and VBF signal regions. The ggF signal region is then divided based on a m_{HH} cut of 350 GeV to enhance sensitivity to modified couplings. Furthermore, a control region ($Z+$ HF) is defined based on the $bb\ell\ell$ trigger and event selection, with $m_{\ell\ell}$ shape serving as the parameter of interest.

For events with at least four jets, a ggF/VBF BDT classifier is applied to optimally distinguish events originating from ggF and VBF production modes. If the event passes a certain ggF/VBF BDT working point, it is considered VBF-like and is placed in the dedicated VBF signal region.

Conversely, if an event has less than four jets or fails the ggF/VBF BDT cut, it is considered ggF-like and is further categorized based on the invariant mass of the di-Higgs system, m_{HH}. A low-mass ggF signal region is defined by $m_{HH}<$ 350 GeV and targets BSM signals with $\kappa_\lambda \neq 1$ values that are enhanced in that region.

Finally, events with m_{HH} > 350 GeV are categorized in a high-mass ggF region, targeting SM-like scenarios. The threshold of 350 GeV is chosen to achieve stringent constraints on κ_λ while maintaining a sufficiently large sample size in the low-mass region and retaining sensitivity to the SM-like *HH* signal. Additionally, at this value, the destructive interference between the two ggF LO Feynman diagrams becomes maximal.

A separate BDT classifier is trained in each signal region, utilizing different *HH* signal hypotheses each time to distinguish *HH* signal events from background processes. In the VBF region, a BDT is trained using the SM VBF *HH* signal. In the high-mass BDT training, the SM ggF *HH* signal is used, while in the low-mass region, the BDT is trained on the ggF κ_λ =10 signal, which is enhanced there, as demonstrated in Figure 4.1.

4.7 Z+HF

The SHERPA MC simulation poorly predicts the cross-section of Z boson production when associated with heavy flavor (b, c) jets. Therefore, these specific processes are normalized concerning the observed data within a defined control region. As the production of jets is unrelated to the decay mode of the Z boson, the selection of $Z \to \mu\mu/ee$ + heavy flavor jets is made due to its high purity, making it orthogonal to the selection criteria of signal regions. This high purity sample is utilized in the final fitting procedure to derive the Z+HF normalization using data..

The events falling in the control region are selected as follows:

- Events selected with $bb\ell\ell$ trigger selection using single-lepton and di-lepton triggers;
- Exactly two muons or two electrons with opposite-sign charges;
- Exactly two b-tagged jets (using DL1r tagger and 77% working point);
- 75 GeV $<m_{\ell\ell}<$ 110 GeV (select Z mass peak);
- $m_{bb}<$ 40 GeV or $m_{bb}>$ 210 GeV (to veto Higgs mass peak and to ensure orthogonality to $bb\ell\ell$ signal region);
- leading b-jet $p_T > 45$ GeV;
- lepton $p_T > 40$ GeV.

The determination of the normalization for the background of $Z+$ heavy flavor jets is achieved using data. This involves the inclusion of this control region as a histogram in a single bin within the final fitting process, elaborated upon in Section 4.15.2.

4.8 Background estimation

The background estimations for the $b\bar{b}\tau^+\tau^-$ analysis are outlined in Table 4.4.

In the $bb\tau_{\text{had}}\tau_{\text{had}}$ and $bb\tau_{\text{lep}}\tau_{\text{had}}$ final states[7], several processes contribute significantly. These processes have much higher production cross-sections compared to the expected pair production of Higgs bosons. Therefore, the analysis faces the challenge of developing efficient techniques for extracting the signal.

The $t\bar{t}$ production process is the dominant background in the $\tau_{\text{lep}}\tau_{\text{had}}$ channel and one of the most significant backgrounds in the $\tau_{\text{had}}\tau_{\text{had}}$ channel. The top quark mainly decays into a W boson and a bottom quark. In approximately

---

[7] In some instances, for the sake of simplicity, the bar symbol, denoting the presence of an antiparticle, and the plus and minus signs indicating the electric charge of a particle may be omitted.

11.4% of the cases [25], the W boson decays into a τ lepton and the corresponding neutrino. The $t\bar{t}$ decay into the $bb\ell\tau_{\text{had}}$ final state has a significantly larger branching ratio compared to the $bb\tau_{\text{had}}\tau_{\text{had}}$ final state. Consequently, the background rates in the $\tau_{\text{lep}}\tau_{\text{had}}$ channel are almost an order of magnitude larger than in the $\tau_{\text{had}}\tau_{\text{had}}$ channel. The expected signal sensitivity in the $\tau_{\text{lep}}\tau_{\text{had}}$ channel is slightly lower as a result.

The $t\bar{t}$ background encompasses events with one (two) true-τ_{had} objects for the $\tau_{\text{lep}}\tau_{\text{had}}$ ($\tau_{\text{had}}\tau_{\text{had}}$) channel, as well as events where at least one τ_{had} candidate is misidentified, often originating from a quark-initiated jet. Figure 4.6 illustrates the corresponding Feynman diagrams. Properly modeling the τ_{had}-ID for the fake-τ_{had} candidates in simulation is challenging, and the probabilities of jet $\to \tau_{\text{had}}$ misidentifications are observed to differ between simulation and data. Consequently, backgrounds with a significant number of events featuring fake-τ_{had} candidates are estimated using data-driven or semi-data-driven techniques, as will be explained.

Apart from $t\bar{t}$, multijet events with quark- or gluon-initiated jets being misidentified as τ_{had} objects, along with $Z(\to \tau\tau)+$ jets events, are important background processes. These contribute more to the $\tau_{\text{had}}\tau_{\text{had}}$ channel. Accurately simulating multijet processes is highly challenging, hence these contributions are estimated using data-driven methods. The $Z+$ jets events are categorized into three groups: $Z+(bb, bc, cc)$ (abbreviated as $Z+$ heavy flavor jets, or simply $Z+\text{hf}$), $Z+(bq_{\text{lf}}, cq_{\text{lf}})$, where $q_{\text{lf}} = \{u, d, s\}$, and $Z+q_{\text{lf}}q_{\text{lf}}$ (abbreviated as $Z+$ light flavor jets, or simply $Z+$ lf) events.

The estimations for backgrounds where the chosen τ_{had} candidates are anticipated to be correctly identified are derived from simulations. For certain backgrounds like $t\bar{t}$ and $Z+$ HF, the overall normalization is allowed to vary in the final fitting process, as detailed in Sections 4.8.1 and 4.15.2. For major backgrounds where the selected τ_{had} candidates might be erroneous, estimations rely

Background	$\tau_{\text{had}}\tau_{\text{had}}$	$\tau_{\text{lep}}\tau_{\text{had}}$
$t\bar{t}$ & SingleTop	Simulation	
W/Z + Jets	Simulation	
Diboson (WW/WZ/ZZ)	Simulation	
Single Higgs	Simulation	
$t\bar{t}$ fake-$\tau_{\text{had-vis}}$	Scale Factor	Combined Fake Factor Method
Multi-jet fake-$\tau_{\text{had-vis}}$	Fake Factor Method	Combined Fake Factor Method

TABLE 4.4: Background estimation for $b\bar{b}\tau^{+}\tau^{-}$

on data-driven or semi-data-driven techniques, which will be discussed subsequently. Simulations are used for estimating other (minor) backgrounds in similar scenarios.

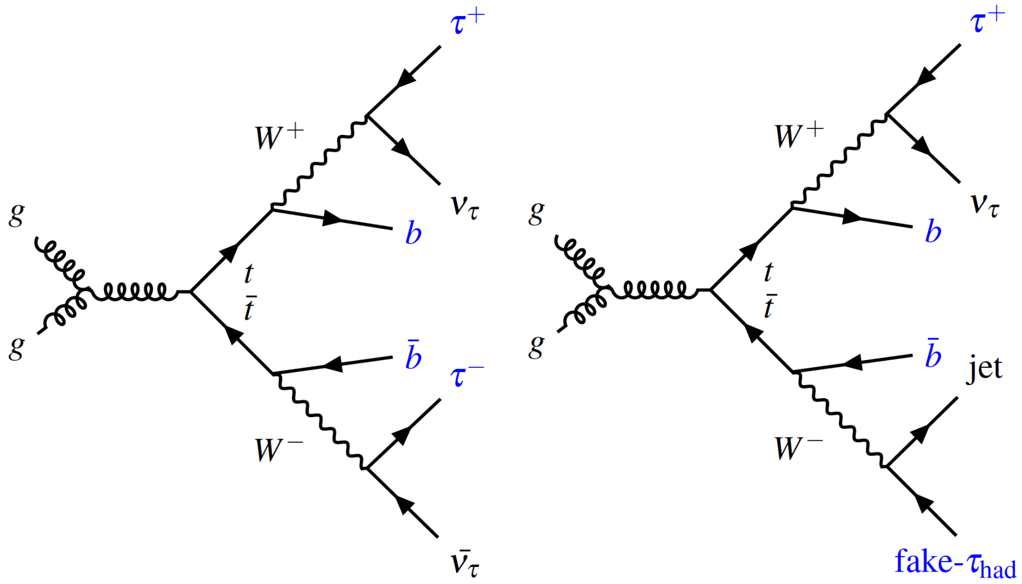

(a) **(b)**

FIGURE 4.6: Illustrates an instance of s-channel $t\bar{t}$ production, followed by decay into the (a) $bb\tau\tau$ final state and (b) $bb\tau+$ misidentified τ_{had} final state.

4.8.1 $t\bar{t}$ Background Estimations with true-τ_{had} Candidates

For both channels, the $t\bar{t}$ background with true-τ_{had} candidates is estimated using MC simulation. The normalization of this background is a flexible parameter determined from data in the final fit. This normalization factor is correlated among SRs and the $Z \to \mu\mu$ + HF Control Region (CR) discussed in Section 4.7.

The post-fit normalization is primarily influenced by the $\tau_{\text{lep}}\tau_{\text{had}}$ SRs due to the substantially higher number of selected $t\bar{t}$ events, resulting in lower relative statistical uncertainties. Additionally, the proportion of $t\bar{t}$ background in relation to the overall background is greater in the $\tau_{\text{lep}}\tau_{\text{had}}$ channel compared to the $\tau_{\text{had}}\tau_{\text{had}}$ channel.

In both the $\tau_{\text{had}}\tau_{\text{had}}$ SR and the $Z \to \mu\mu$ + HF CR, the post-fit normalization of $t\bar{t}$ is allowed to deviate from the normalization in the $\tau_{\text{lep}}\tau_{\text{had}}$ SRs, provided that the difference falls within the uncertainty range of the product of acceptance and efficiency for $t\bar{t}$ events between the respective region and the $\tau_{\text{lep}}\tau_{\text{had}}$ SRs. Further details will be discussed in the section covering modeling uncertainties.

4.8.2 Background with a jet misidentified as a τ_{had} in the $\tau_{\text{lep}}\tau_{\text{had}}$ channel

The fake- τ_{had} background can have different origins. In Figure 4.7, two Feynman diagrams are shown for the two dominant processes contributing to the fake- τ_{had} background, which are the $t\bar{t}$ and multi-jet (referred to as QCD) processes.

In the $t\bar{t}$ events, the fake- τ_{had} background typically originates from quark-initiated jets from top quark decay; in multi-jet events, jets initiated from both quarks and gluons can be misidentified as τ_{had} . In the following text, the fake background initiated by the $t\bar{t}$ (multi-jet) events is referred to as $t\bar{t}$ (multi-jet) fakes.

Fake Factor Method

The fake factor (FF) method is employed to estimate the fake-τ_{had} background events. This approach is preferred due to the imperfect simulation of these processes. The FF represents the ratio of events with τ_{had} in one region to another. In

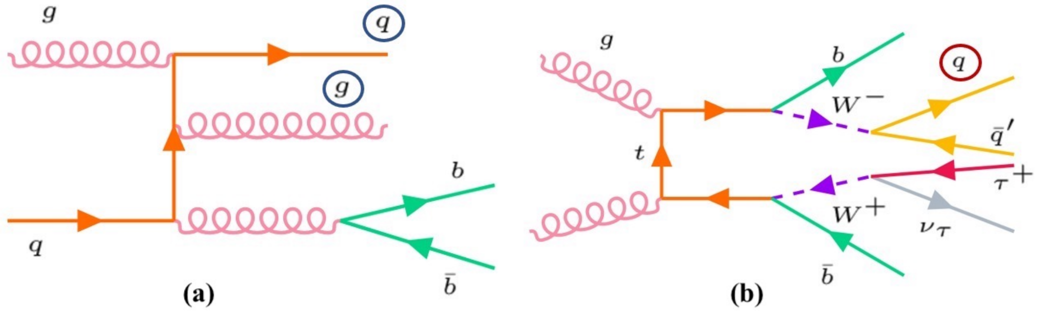

FIGURE 4.7: Feynman diagrams representing the origin of fake τ_{had} background, with the left (**a**) diagram corresponding to multi-jet events and the right (**b**) one to $t\bar{t}$ events. In the left diagram, the gluon and quark encircled in blue mimic a τ_{had} and a lepton, respectively. On the other hand, the quark encircled in red in the right diagram imitates a τ_{had}.

this context, the FF for a specific background source is defined by the equation:

$$\text{FF} = \frac{N(\text{ID selection})}{N(\text{anti-ID selection})} \tag{4.1}$$

Here, the numerator (N(ID selection)) denotes the number of fake-τ_{had} background events passing the nominal signal region τ_{had}-ID selection, while the denominator (N(anti-ID selection)) refers to the number of fake-τ_{had} background events passing the anti-τ_{had} selection (as defined in Section 4.3). To ensure an accurate estimation, events with a true τ_{had} are subtracted from the data events, i.e., $N = \text{data} - N(\text{true } \tau_{had}, \text{MC})$.

The calculation of fake factors is performed separately for the SLT and LTT channels, considering the different origins[8] of fake-τ_{had}. Specifically, FFs are computed separately for $t\bar{t}$ and multi-jet events, as well as for 1- and 3-prong τ_{had} candidates. The fake factor is parameterized in bins of p_T of the τ_{had}, while the dependence on η is also examined, though no significant trend is observed.

Each dedicated control region for a given source is referred to as FF-CR. The definitions are as follows:

- $t\bar{t}$ FF-CR: Identical to the ID/anti-ID selection but with the m_{bb} cut reversed: $m_{bb} > 150\text{GeV}$.

---

[8] In the LTT case we have the freedom to go lower in the p_T^l where $l = e, \mu$ however in addition we need to require $\tau_{had-vis}$ p_T > 25 GeV as mentioned in section 4.5.1.

- Multi-jet FF-CR: Same as the ID/anti-ID selection, except with reversed lepton isolation requirements. 'Tight' electrons and 'medium' muons are required to fail their respective 'loose' isolation working points.

The combined fake factor is determined using the factors from individual FF-CRs:

$$\mathrm{FF(comb)} = \mathrm{FF}(\text{multi-jet}) \times \mathrm{r_{QCD}} + \mathrm{FF}(t\bar{t}) \times (1 - \mathrm{r_{QCD}}) \tag{4.2}$$

Here, $\mathrm{FF}(\text{multi-jet})$ and $\mathrm{FF}(t\bar{t})$ represent the fake factors calculated in the multi-jet and $t\bar{t}$ FF-CRs respectively. The $\mathrm{r_{QCD}}$ is defined as the fraction of multi-jet events in the signal region template. It is measured as a function of the $\tau_{had}\, p_T$, split into 1-prong and 3-prong, and categorized by the type of light lepton (e or μ), given that an electron is more prone to misidentification as a jet than a muon. A schematic depiction of this method is shown in Figure 4.8. The measurement of $\mathrm{r_{QCD}}$ is performed for events passing the the signal region selection and anti-ID selection:

$$\mathrm{r_{QCD}} = \frac{N(\text{multi-jet, data})}{N(\text{data}) - N(\text{true } \tau_{had}, \mathrm{MC})} \tag{4.3}$$

where all events predicted from MC in the anti- τ_{had} region are subtracted from the number of data events, N (data), regardless of whether or not they contain a true τ_{had}. While the N (multi-jet, data) is calculated by subtracting all background contributions apart from multi-jet, regardless of whether they contain fake or true- τ_{had} candidates, from the data in the anti-ID tau region. The subtracted backgrounds are taken from the MC predictions.

$$N(multi - jet, data) = N(data) - N\left(true\tau_{\mathrm{had}}, \mathrm{MC} + fake\ \tau_{\mathrm{had}}, \mathrm{MC}\right) \tag{4.4}$$

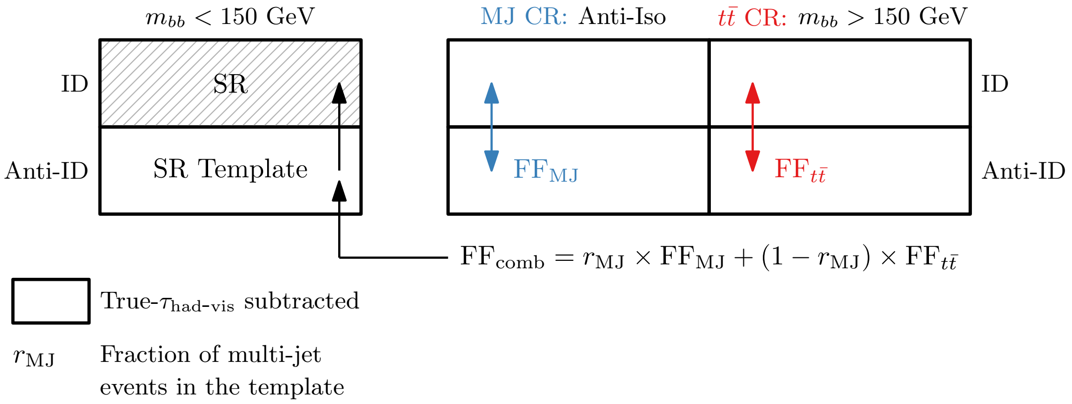

FIGURE 4.8: Illustration of the integrated fake-factor approach employed for the evaluation of multi-jet and $t\bar{t}$ background contributions involving fake-$\tau_{\text{had-vis}}$ in the $\tau_{\text{lep}}\,\tau_{\text{had}}$ channel. Backgrounds originating from genuine $\tau_{\text{had-vis}}$ in jets are derived using simulated data and subsequently subtracted from the observed data across all control regions. Additionally, events where an electron or muon is incorrectly identified as a $\tau_{\text{had-vis}}$ are also accounted for, although their impact is minimal.

$t\bar{t}$ background reweighting

The precision of the combined fake factor hinges on the accurate representation of simulated $t\bar{t}$ events featuring true-τ_{had}. This is crucial as $t\bar{t}$ constitutes the primary background subtracted from data in obtaining the fake factors and $\mathrm{r}_{\mathrm{QCD}}$. The $t\bar{t}$ modeling also directly impacts the estimation of fake background in the signal region, since the fake factor is applied to anti-ID events after the removal of the true-τ_{had} $t\bar{t}$ background. An issue was identified wherein discrepancies in the true $t\bar{t}$ background, particularly in regions of high jet count and elevated top-quark p_{T}, could lead to the calculation of FF yielding non-physical negative values in the high $\tau_{\text{had}}p_{\mathrm{T}}$ zone. To address this, events from $t\bar{t}$ production in simulation were differentially reweighted based on jet count and the scalar sum of p_T of all observable final state objects (H_T) in the event.

These reweighting factors were determined on a bin-by-bin basis in the distributions of jet count and H_T from another $t\bar{t}\mathrm{FF}-\mathrm{CR}$, $t\bar{t}\mathrm{FF}-\mathrm{CR2}$. This region shared identical selection criteria with the SR, except for the $t\bar{t}$ FF-CR m_{bb} requirements ($m_{bb} > 150\mathrm{GeV}$) and an additional $m_{\mathrm{T}}^{W} > 40\mathrm{GeV}$ constraint, with m_{T}^{W} defined as

$$m_{\mathrm{T}}^{W} = \sqrt{2p_{\mathrm{T}}^{\ell}E_{\mathrm{T}}^{\mathrm{miss}}\left(1 - \cos\Delta\phi_{\ell,E_{\mathrm{T}}^{\mathrm{miss}}}\right)}$$

is the transverse mass of the lepton and the $E_{\mathrm{T}}^{\mathrm{miss}}$, with $\Delta\phi_{\ell,E_{\mathrm{T}}^{\mathrm{miss}}}$.

The presence of a reconstructed τ_{had} candidate was mandated for events in this region, but this candidate was not required to pass any $\mathrm{RNN}\,\tau_{\mathrm{had}}$ requirements. The m_{T}^{W} constraint was introduced to mitigate potential contamination from multi-jet events. The reweighting factors are displayed in Appendix A.2, Figure A.2. The discrepancy between the reweighted and original fake-τ_{had} background estimates was taken as a systematic uncertainty attributed to $t\bar{t}$ background modeling. Further elaboration can be found in Section 4.13.1.

Fake factor calculation

In order to establish the authenticity of the intended backgrounds in both the $t\bar{t}$ Control Region ($t\bar{t}$-CR) and Multi-Jet Control Region (MJ CR), distributions depicting the p_T of the τ are presented. These distributions are categorized based on the presence of a τ_{had} or anti-τ_{had}, and further distinguished for 1-prong and 3-prong τ_{had}. Refer to Fig.4.9, Fig.4.10, Fig.4.11, and Fig.4.12 for visual representations. Notably, the contribution from fake events is solely derived from MC simulations. As a consequence, any disparity observed between the MC prediction and actual data in the MJ CR is attributed to multi-jet events, which have not been explicitly accounted for in the simulation for this analysis.

Backgrounds which are not from events with fake-$\tau_{\text{had-vis}}$ originating from jets, are estimated from simulation and are subtracted from the distribution of the data in all the control regions used for the FF measurement. After the subtraction, the FFs are derived as the ratio of the number of events in the ID region to the number of events in the anti-ID region. Figures 4.13 and 4.14 demonstrate no clear trend when FFs are parameterised in terms of η. They are parameterised only in terms of the $\tau_{\text{had-vis}}$ p_{T}, independently for 1- and 3-prong $\tau_{\text{had-vis}}$ ('1- and

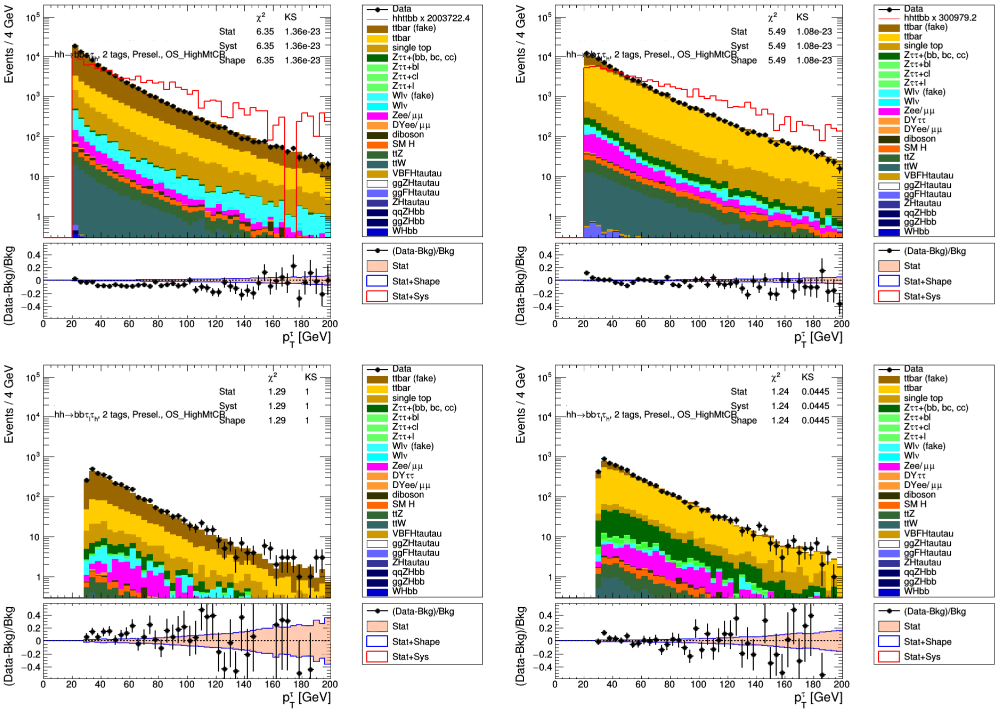

FIGURE 4.9: Plots of the τ_{had} p_T distributions for the (left) anti-τ_{had} and (right) τ_{had} selection for SLT (top) and LTT (bottom) channels in the $t\bar{t}$ control region with 1-prong τ_{had}.

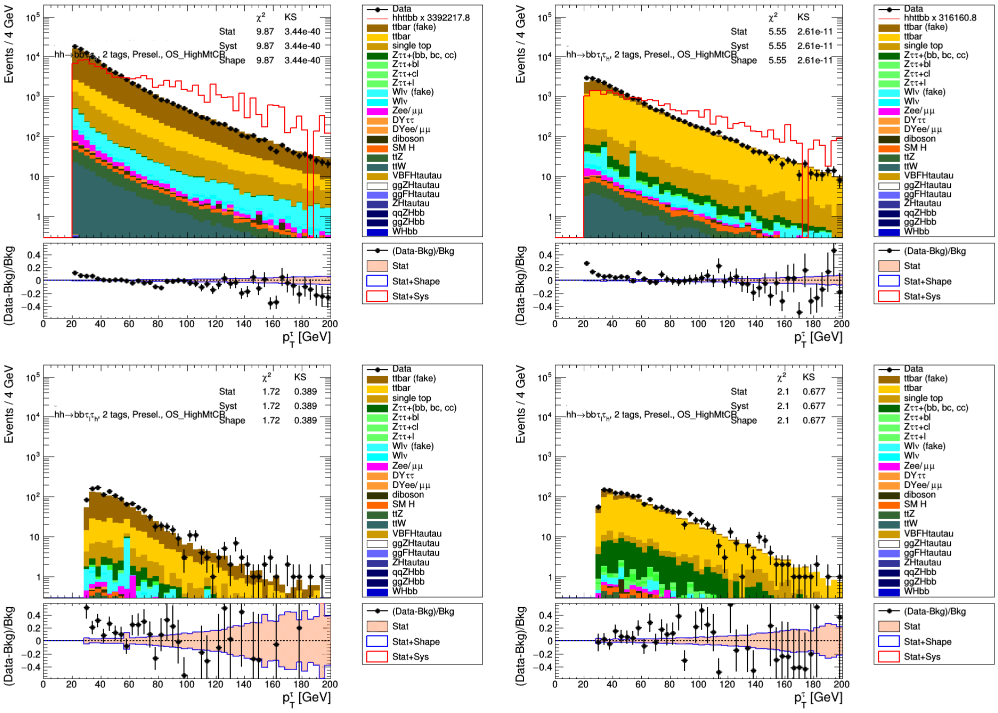

FIGURE 4.10: Plots of the τ_{had} p_T distributions for the (left) anti-τ_{had} and (right) τ_{had} selection for SLT (top) and LTT (bottom) channels in the $t\bar{t}$ control region with 3-prong τ_{had}.

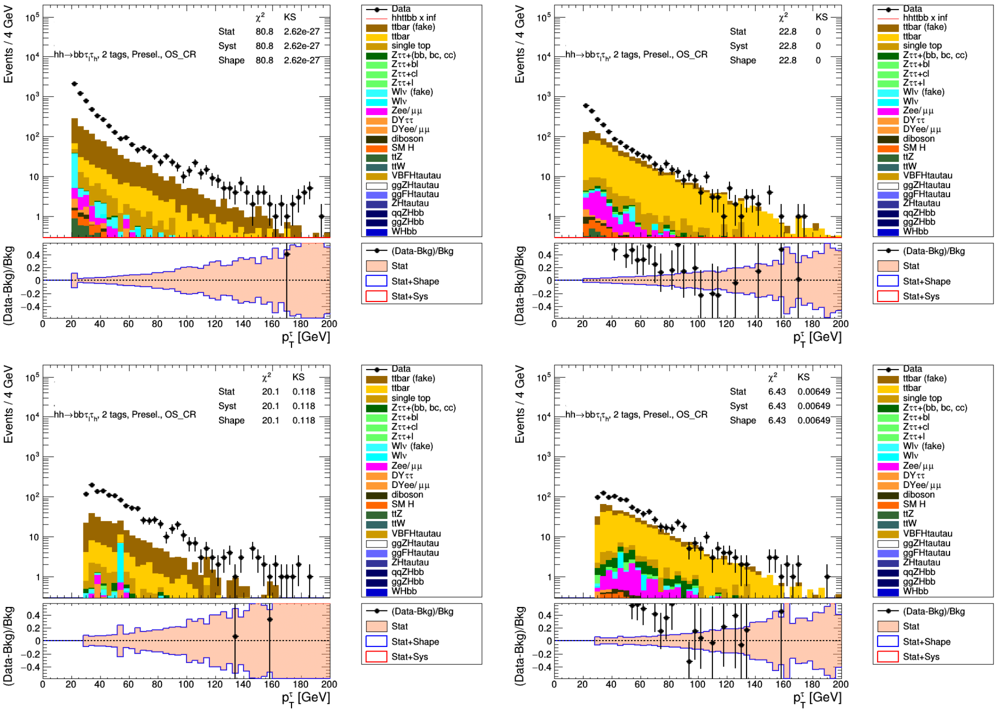

FIGURE 4.11: Plots of the τ_{had} p_T distributions for the (left) anti-τ_{had} and (right) τ_{had} selection for SLT (top) and LTT (bottom) channels in the multi-jet control region with 1-prong τ_{had}.

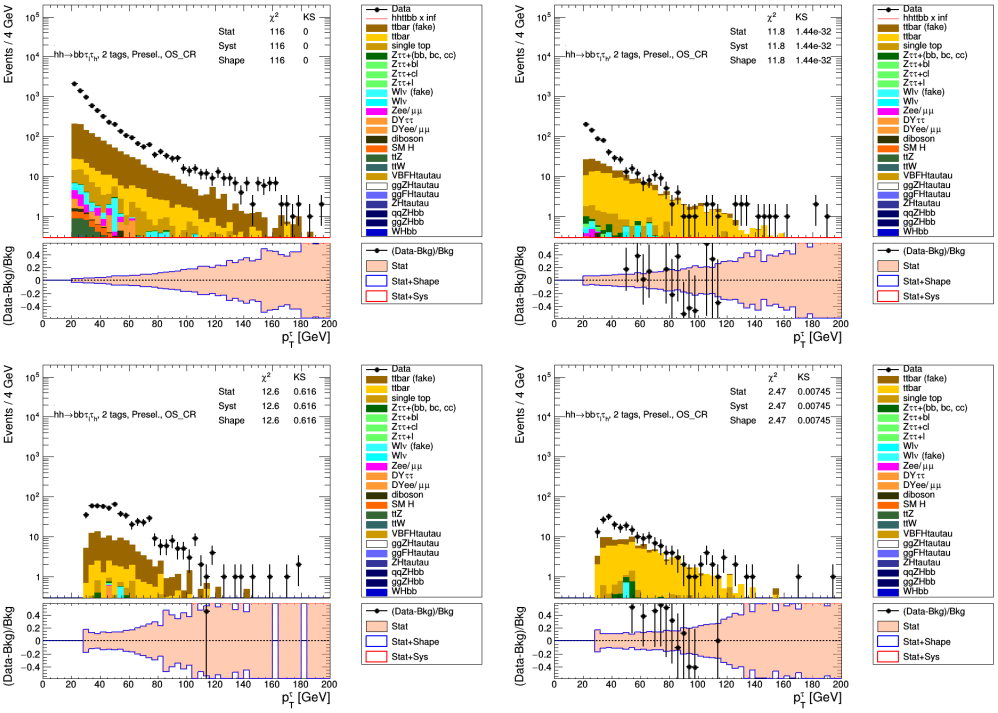

FIGURE 4.12: Plots of the τ_{had} p_T distributions for the (left) anti-τ_{had} and (right) τ_{had} selection for SLT (top) and LTT (bottom) channels in the multi-jet control region with 3-prong τ_{had}.

3-prong' refers to the number of tracks associated with a reconstructed $\tau_{\text{had-vis}}$), and separately for the SLT and LTT categories. Individual fake factors for each process (multi-jet and $t\bar{t}$) are then used to provide a combined fake factor.

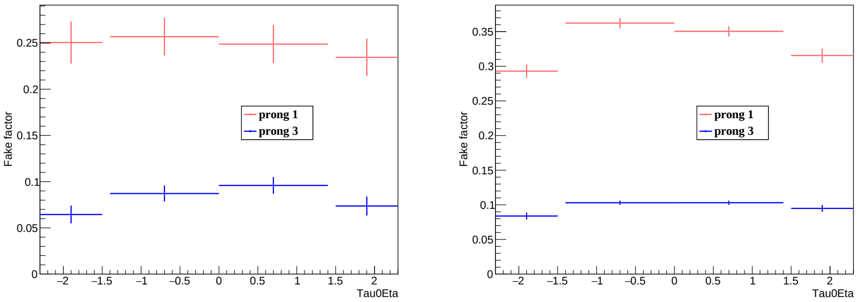

FIGURE 4.13: Fake-factors as a function of η for 1-prong and 3-prong τ_{had} candidates for multi-jet (left) and $t\bar{t}$ processes (right) for the $\tau_{lep}\tau_{had}$ SLT category. No significant trend is observed.

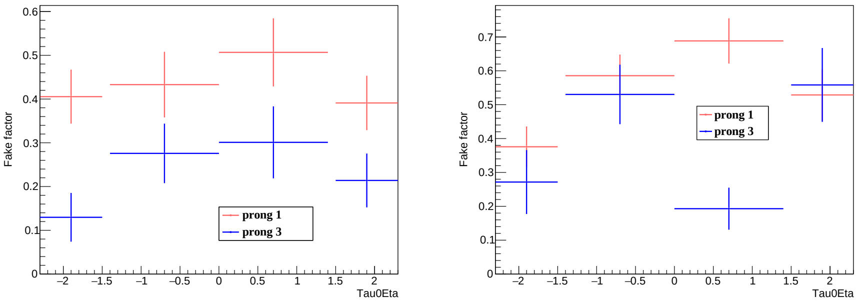

FIGURE 4.14: Fake-factors as a function of η for 1-prong and 3-prong τ_{had} candidates for multi-jet (left) and $t\bar{t}$ processes (right) for the $\tau_{lep}\tau_{had}$ LTT category. No significant trend is observed.

Figures 4.15 and 4.16 show respectively the FF for the SLT and LTT categories calculated separately for $t\bar{t}$ and multi-jet, and for 1 and 3-prong τ_{had} candidates. They are parameterised in terms of $p_T(\tau_{had})$ requiring opposite-sign lepton-tau pairs. The method is found to provide a good prediction-to-data agreement in the 1-b-tag $t\bar{t}$-CRs, the validation regions, as well as in the $\tau_{lep}\tau_{had}$-SRs, for which the figures can be found in the previous publish paper ref. [117]. The validation study performed for this paper presented in the thesis is explained in section 4.8.2.

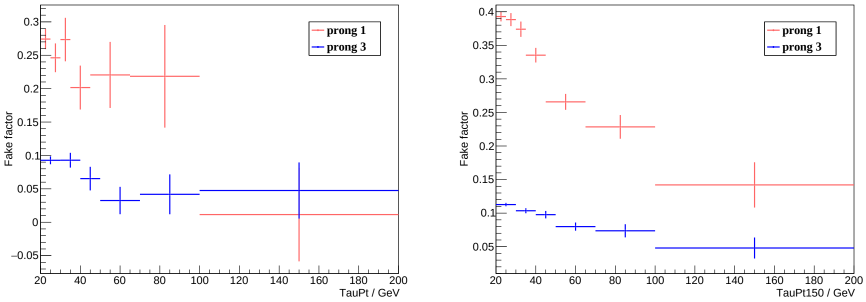

FIGURE 4.15: Fake-factors for 1-prong and 3-prong τ_{had} candidates for multi-jet (left) and $t\bar{t}$ processes (right) for the $\tau_{lep}\tau_{had}$ SLT category.

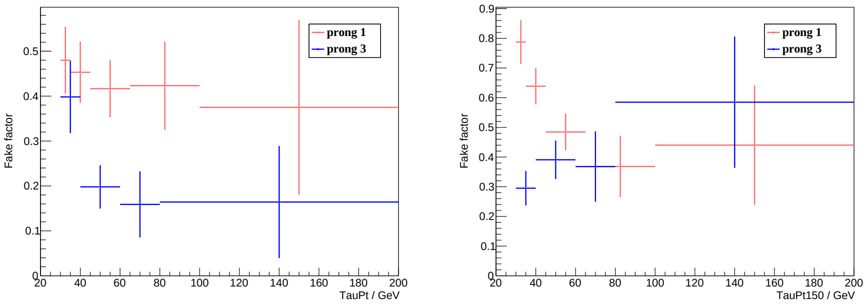

FIGURE 4.16: Fake-factors for 1-prong and 3-prong τ_{had} candidates for multi-jet (left) and $t\bar{t}$ processes (right) for the $\tau_{lep}\tau_{had}$ LTT category.

Fake factor method validation

To validate the ability of the combined fake factor method to describe the MVA BDT shape for low-m_{HH} ggF, high-m_{HH} ggF and VBF categories, plots have been made using the fake factor method to estimate the combined multi-jet and $t\bar{t}$ contribution in validation regions. The combined FF method is checked for closure in the $t\bar{t}$ CR and validated in the 1-b-tagged region, which is the same as the $\tau_{lep}\tau_{had}$ SR except for the requirement of exactly one b-tagged jet. The combined fake factor method applied directly to the $t\bar{t}$ CR can be seen in 4.17. In 4.18, the BDT distributions for low-m_{HH} ggF, high-m_{HH} ggF and VBF categories in the 1-b-tag validation region are shown respectively for SLT and LTT. The estimated background distributions agree well with the observed distributions in the SLT and LTT validation regions.

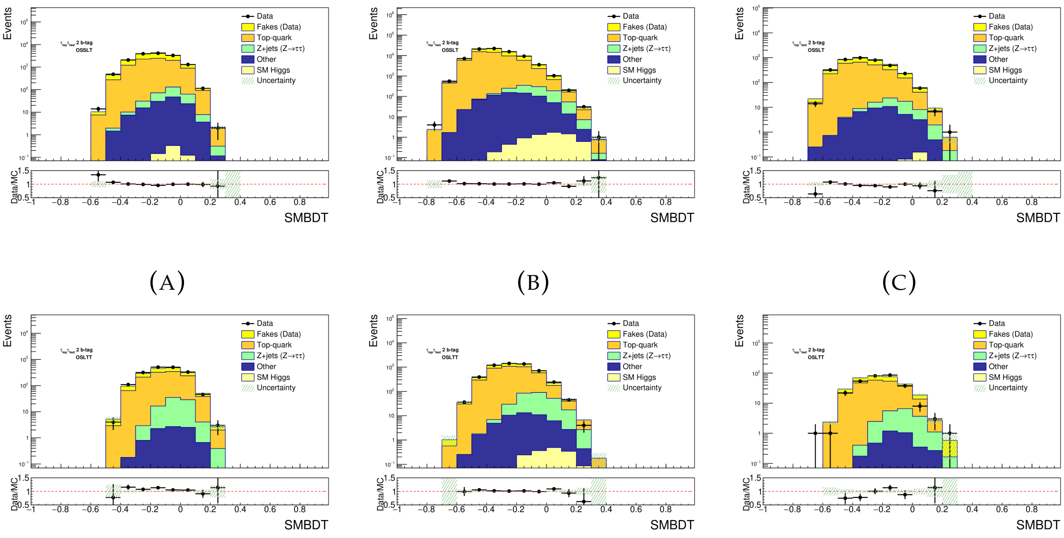

(A) (B) (C)

(D) (E) (F)

FIGURE 4.17: The top row shows the SLT BDT distributions for **(a)** low-m_{HH} ggF, **(b)** high-m_{HH} ggF, and **(c)** VBF categories. The bottom row shows the LTT BDT distributions for the same categories. These plots are in the signal-depleted $t\bar{t}$ CR where the $t\bar{t}$ FF are measured. This is a simple closure test.

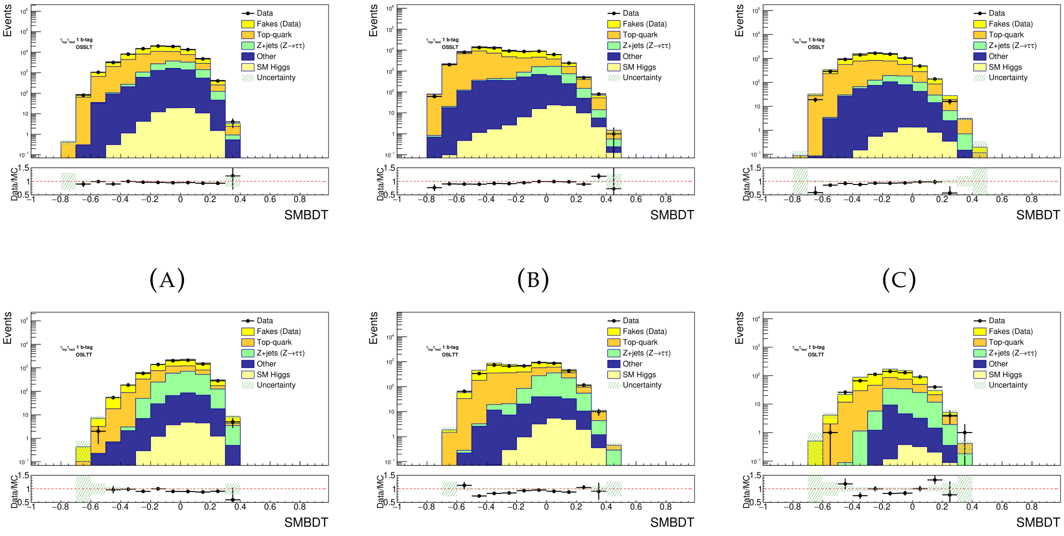

(A) (B) (C)

(D) (E) (F)

FIGURE 4.18: The top row shows the SLT BDT distributions for **(a)** low-m_{HH} ggF, **(b)** high-m_{HH} ggF, and **(c)** VBF categories. The bottom row shows the LTT BDT distributions for the same categories. These plots are in the 1-b-tag validation region.

4.8.3 Fake- $\tau_{\text{had-vis}}$ background in the $\tau_{\text{had}}\,\tau_{\text{had}}$ channel

In the $\tau_{\text{had}}\,\tau_{\text{had}}$ channel, two separate methods are used to estimate the backgrounds with fake- $\tau_{\text{had-vis}}$ from $t\bar{t}$ and multi-jet production. Multi-jet production events can only enter the signal selection when both $\tau_{\text{had-vis}}$ are fake, whereas for $t\bar{t}$ production, predominantly only one reconstructed $\tau_{\text{had-vis}}$ is fake.

Fake- $\tau_{\text{had-vis}}$ background from multi-jet production

In the $\tau_{\text{had}}\tau_{\text{had}}$ channel, we employ two distinct approaches to assess the presence of fake-$\tau_{\text{had-vis}}$ backgrounds originating from $t\bar{t}$ and multi-jet production. Multi-jet production events are only considered for the signal selection when both $\tau_{\text{had-vis}}$ are fake. In contrast, for $t\bar{t}$ production, typically only one reconstructed $\tau_{\text{had-vis}}$ is fake.

Fake-$\tau_{\text{had-vis}}$ Background from Multi-jet Production

In the $\tau_{\text{had}}\tau_{\text{had}}$ channel, we estimate the fake-$\tau_{\text{had-vis}}$ background from multi-jet production using a fake-factor method. Figure 4.19 provides a schematic representation of this method. The ID region selection pertains to events with two identified $\tau_{\text{had-vis}}$. To establish an anti-ID region selection, prior to the final step of the overlap removal procedure discussed in Section 4.4, we examine events with only one identified $\tau_{\text{had-vis}}$ to verify if there exists a reconstructed $\tau_{\text{had-vis}}$ candidate that satisfies the anti-$\tau_{\text{had-vis}}$ criteria. The chosen anti-$\tau_{\text{had-vis}}$ must be within $\Delta R < 0.2$ of an HLT $\tau_{\text{had-vis}}$ object, except in the STT category for events where the identified $\tau_{\text{had-vis}}$ is already trigger-matched. If multiple anti-$\tau_{\text{had-vis}}$ candidates meet the defined criteria, one is randomly selected.

To establish a template for the multi-jet background, an anti-ID region is defined mirroring the SR selection, featuring one identified and one anti-$\tau_{\text{had-vis}}$ instead of two identified $\tau_{\text{had-vis}}$. This template, designated as the SR Template

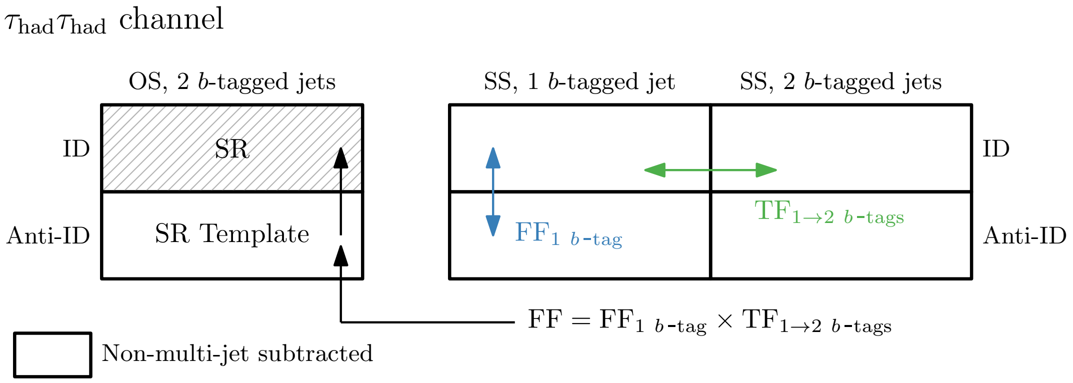

FIGURE 4.19: Schematic depiction of the combined fake-factor method to estimate the multi-jet background with fake $\tau_{\text{had-vis}}$ in the $\tau_{\text{had}}\,\tau_{\text{had}}$ channel. Backgrounds with true- $\tau_{\text{had-vis}}$ that are not from multi-jet events are simulated and subtracted from data in all the control regions. This is indicated by "Non-multi-jet subtracted" in the legend.

for estimating the multi-jet background within the SR, is constructed by deducting simulated non-multi-jet events from data in the template region. A significant portion of the subtracted non-multi-jet events originates from $t\bar{t}$ production. These simulated $t\bar{t}$ events, which involve fake-$\tau_{\text{had-vis}}$, are rectified using scale factors based on the misidentification efficiencies of the fake-$\tau_{\text{had-vis}}$ in the anti-ID region, as outlined in Section 4.8.2.

Similar to the approach employed in the $\tau_{\text{lep}}\tau_{\text{had}}$ channel, the template is additionally adjusted using FFs to estimate the multi-jet background within the SR.

A control region enriched with multi-jet events is defined within the $\tau_{\text{had}}\,\tau_{\text{had}}$ SR selection. However, in this control region, it is required that both $\tau_{\text{had-vis}}$ candidates possess the same-sign (SS) charges, in contrast to the SR selection where opposite-sign (OS) charges are mandated for the $\tau_{\text{had-vis}}$ candidates. Additionally, events in this control region must exhibit exactly one b-tagged jet per event (SS CR with $1b$-tagged jet). Both this control region and its corresponding anti-ID counterpart are utilized for FF measurements. The FFs are determined by calculating the ratio of the number of events in the ID region to the number of events in the anti-ID region after subtracting all simulated non-multi-jet backgrounds from the data. They are parameterized based on event characteristics and properties of $\tau_{\text{had-vis}}$ candidates in the event. The FFs are derived separately for the Single Tau (STT) and Double Tau (DTT) categories, and for different years of data-taking to accommodate the variations in the $\tau_{\text{had-vis}}$ identification algorithms and event selection topologies employed in the trigger. In the SS CR with $1b$-tagged jet, the FFs are determined due to the limited number of selected events and the significant $t\bar{t}$ background contamination in the SS region with 2 b-tagged jets. To address the transition from 1- to 2 - b-tagged events, transfer factors (TFs) are introduced. In the DTT category, the FFs are categorized based on the p_{T} and η of the anti-$\tau_{\text{had-vis}}$. Meanwhile, in the STT category, the FFs are measured inclusively in p_{T} and η, but they are distinguished based on whether the selected anti-$\tau_{\text{had-vis}}$ is the p_{T}-leading or sub-leading $\tau_{\text{had-vis}}$ candidate. In both categories, FFs are assessed separately for events with 1- and 3-prong anti-$\tau_{\text{had-vis}}$ candidates.

TFs are calculated as the ratios of the FFs observed in the Single STT and DTT categories, within the SS CR, where events feature either 2 or 1 b-tagged jets. These ratios are computed inclusively for both p_{T} and η of the $\tau_{\text{had-vis}}$. Moreover, the TFs are assessed separately for events with 1- and 3-prong anti-$\tau_{\text{had-vis}}$ candidates. The TFs are also stratified based on whether the chosen anti-$\tau_{\text{had-vis}}$ is the p_{T}-leading or sub-leading $\tau_{\text{had-vis}}$ candidate. This analysis is conducted independently for different years of data-taking. The results demonstrate compatibility within the statistical uncertainty.

Figure 4.20 shows a completion test of the fake factor estimation strategy in the 1-tag SS region for the low-m_{HH} ggF SR, high-m_{HH} ggF SR and VBF SR analysis categories. This region is used to estimate the fake factors and can therefore only contribute as a closure check.

Figure 4.21 shows the multi-jet fake validation region (1-tag OS) for the low-m_{HH} ggF SR, high-m_{HH} ggF SR and VBF SR analysis categories. This region is not used in the development of the method and therefore constitutes an independent validation region.

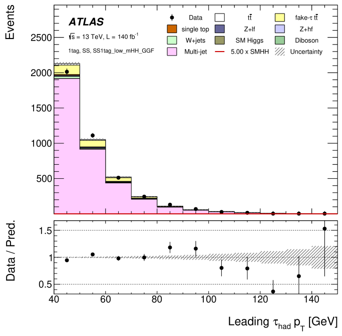

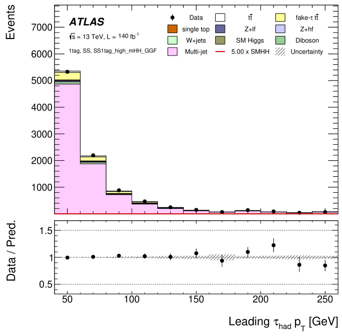

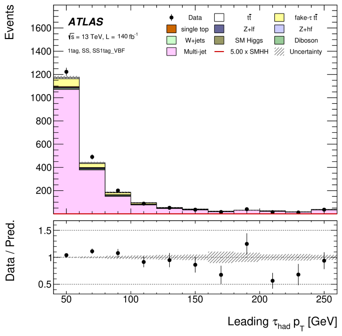

(A) (B) (C)

FIGURE 4.20: Closure check of the fake factor method in 1-tag SS ID-region showing the leading τ_{had} p_T distributions for the **(a)** low-m_{HH} ggF, **(b)** high-m_{HH} ggF and **(c)** VBF categories in the $\tau_{had}\tau_{had}$ channel.

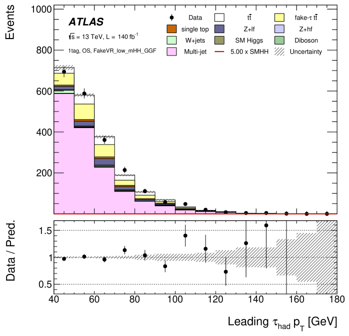

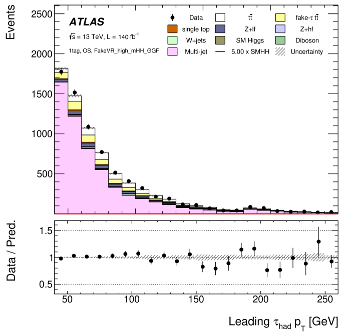

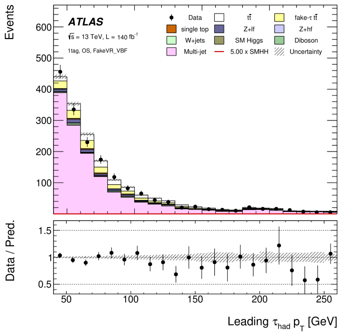

(A) (B) (C)

FIGURE 4.21: Validation of the multi-jet estimate in the 1-tag OS multi-jet validation region showing the leading τ_{had} p_T distributions for the **(a)** low-m_{HH} ggF, **(b)** high-m_{HH} ggF and **(c)** VBF categories in the $\tau_{had}\tau_{had}$ channel.

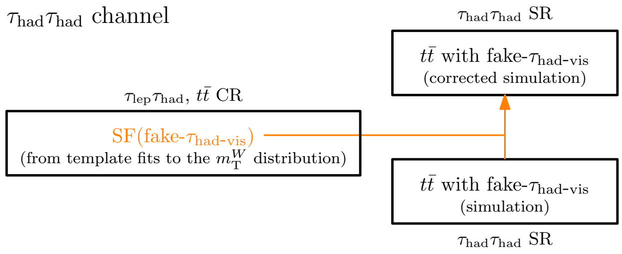

FIGURE 4.22: Schematic depiction of the fake-$\tau_{\text{had-vis}}$ scale-factor method to estimate the $t\bar{t}$ background with fake-$\tau_{\text{had-vis}}$ in the $\tau_{\text{had}}\tau_{\text{had}}$ channel.

Fake- $\tau_{\text{had-vis}}$ background from $t\bar{t}$ production

Background events with fake-$\tau_{\text{had-vis}}$ from $t\bar{t}$ production in the $\tau_{\text{had}}\tau_{\text{had}}$ channel are estimated using simulation. However, the fake-$\tau_{\text{had-vis}}$ misidentification efficiencies are corrected by scale factors (SFs) derived from data. A schematic depiction of this method is shown in 4.22.

The SFs are derived in the $t\bar{t}$ CR within the $\tau_{\text{lep}}\tau_{\text{had}}$ SLT category, as outlined in Section 4.8.1. For consistency with the $\tau_{\text{had}}\tau_{\text{had}}$ SR criteria, the $t\bar{t}$ CR is redefined to include events with $\tau_{\text{had-vis}}$ $|\eta| < 2.5$.

The SFs are determined as a function of the p_{T} of the fake-$\tau_{\text{had-vis}}$, separately for 1- and 3-prong fake-$\tau_{\text{had-vis}}$ objects. This is achieved by fitting the transverse mass of the W-boson (m_{T}^{W}) distribution of simulated events to data using a profile-likelihood fit.

The m_{T}^{W} distribution fit enables the disentanglement of contributions from $t\bar{t}$ events with true- and fake-$\tau_{\text{had-vis}}$, while accounting for commonalities in the modelling of $t\bar{t}$ simulation.

Separate fits are conducted for different trigger categories.

For 1-prong fake-$\tau_{\text{had-vis}}$, the SFs are approximately unity for fake-$\tau_{\text{had-vis}}$ p_{T} values below 40 GeV, decreasing to SF ~ 0.6 for fake-$\tau_{\text{had-vis}}$ p_{T} values above 70 GeV. The SFs for 3-prong fake-$\tau_{\text{had-vis}}$ are generally about 20% larger than those for the 1-prong counterparts.

The $t\bar{t}$ background contribution with fake-$\tau_{\text{had-vis}}$ in the $\tau_{\text{had}}\tau_{\text{had}}$ SR is estimated from simulated events that pass the SR selection, with weights determined by the corresponding SFs for each fake-$\tau_{\text{had-vis}}$ in the event.

Uncertainties in the detector response and the modelling of $t\bar{t}$ events, along with other minor contributing processes, are considered in the likelihood fit when extracting the SFs.

The covariance matrix of the measured SFs, which encompasses all statistical and systematic uncertainties in the measurement, is diagonalised. The resulting eigenvectors are employed to define independent nuisance parameters (NPs), which are then incorporated into the final signal extraction fit. Theoretical modelling uncertainties in simulated $t\bar{t}$ events, to which the SFs are applied, are estimated as detailed in Section 4.12 and are also integrated into the final signal extraction fit.

When estimating the fake-$\tau_{\text{had-vis}}$ background from multi-jet production using the fake-factor method (Section 4.8.3), a significant portion of $t\bar{t}$ events featuring at least one fake-$\tau_{\text{had-vis}}$ must be subtracted from data in the OS region with 2 b-tagged jets and anti-ID conditions (SR Template). This is done to estimate the multi-jet contribution in the $\tau_{\text{had}}\tau_{\text{had}}$ SR. The modelling of the simulated $t\bar{t}$ events with fake-$\tau_{\text{had-vis}}$ in the anti-ID region is adjusted using SFs obtained through the same method as described above. These SFs are measured in a control region akin to the $t\bar{t}$ CR, with the exception that the $\tau_{\text{had-vis}}$ candidate must meet the anti-$\tau_{\text{had-vis}}$ requirements.

The measured SFs for 1-prong fake-$\tau_{\text{had-vis}}$ in the anti-ID region closely approach unity for fake-$\tau_{\text{had-vis}}$ p_{T} values below 40 GeV, mirroring the trend observed in the ID region. The SFs then follow the same trend of decreasing in value with increasing fake-$\tau_{\text{had-vis}}$ p_{T}.

For 3-prong fake-$\tau_{\text{had-vis}}$, the SFs are generally about 10%–20% larger than those for the 1-prong fake-$\tau_{\text{had-vis}}$ objects.

4.9 Multivariate analysis

The event preselection presented in Table 4.3 is not optimised in terms of sensitivity to pair production of Higgs bosons. A set of Boosted Decision Trees (BDTs) [118] is used to maximise the sensitivity of the analysis to the signal processes. The output of a multivariate algorithm is used as a final discriminant for the signal extraction, as described in Section 4.14. Section 4.10.1 explains the general MVA approach, while Section 4.11 give the details of the MVA trainings in the $\tau_{had}\tau_{had}$, $\tau_{lep}\tau_{had}$ channels.

4.10 Introduction to Boosted Decision Trees (BDT)

Boosted Decision Trees (BDTs) are prominent classification methods in high-energy physics utilized to categorize events into distinct groups, often labeled as "signal" (S) and "background" (B). A decision tree represents a binary-tree structure, illustrated in Figure 4.23. It sequentially evaluates various variables x_i from a training dataset with known event classifications (signal or background). Each split in the tree makes decisions based on individual variables, progressing until reaching a stop criterion like MaxDepth or MinNodeSize.

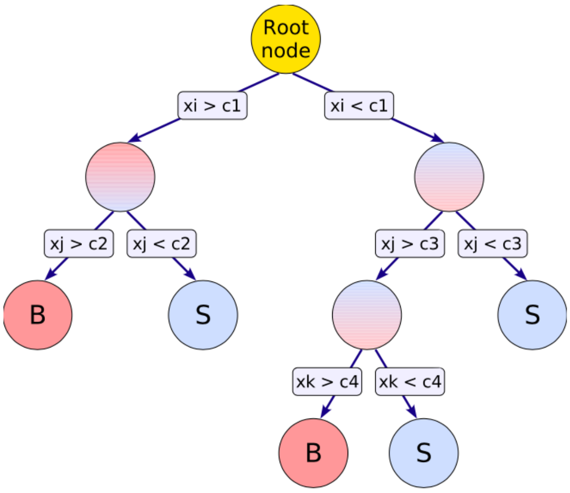

FIGURE 4.23: A schematic depiction of a decision tree structure [118].

At each split, the tree selects the variable that maximizes the separation between signal and background events. Leaf nodes at the bottom of the tree are labeled "S" for signal and "B" for background based on the majority classification of events in those nodes, effectively delineating the phase space into signal and background regions.

During training, decisions are based on various separation criteria. The standard criterion, the Gini-Index, measures purity (p) after a cut and is defined as $p \cdot (1-p)$, where p is given by:

$$p = \frac{S}{S+B}.$$

Boosting amplifies this process by employing multiple trees to form a forest. Each tree is constructed from the same dataset, but events are weighted differently in each tree. These trees are then combined into a unified classifier through weighted averaging. Boosting enhances stability and improves separation compared to a single decision tree. In "Adaptive" boosting, misclassified events are assigned higher weights in subsequent trees based on the misclassification rate (err) of the previous tree, given by:

$$\alpha = \frac{1-\text{err}}{\text{err}}.$$

The event weights are then normalized. The boosted event classification $y_{\text{Boost}}(x)$ is computed by aggregating individual classifier results ($h(x)$) as follows:

$$y_{\text{Boost}}(x) = \frac{1}{N_{\text{collection}}} \sum_{i}^{N_{\text{collection}}} \ln(\alpha_i) \cdot h_i(x),$$

where $N_{\text{collection}}$ is the total number of classifiers used in the boosted event classification. Smaller (larger) $y_{\text{Boost}}(x)$ values indicate a background-like (signal-like) event. After BDT training, the BDT's classification output assigns a "score" to events based on their input variable values, reflecting their "background-like" or "signal-like" nature. Figure 4.24 illustrates separate score distributions for background and signal events using the training and testing samples. Comparing these distributions helps ensure the BDT is not "overtrained," meaning it doesn't excessively use sample-specific features during training that are not generally useful for signal-background separation, resulting in less powerful separation on independent testing samples compared to training samples.

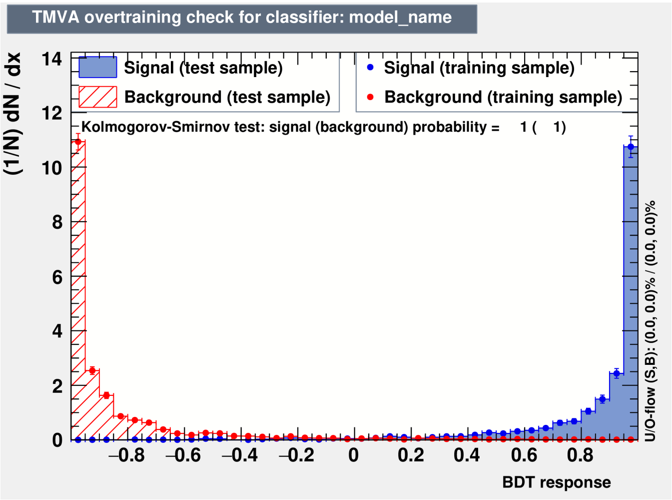

FIGURE 4.24: Separate score distributions for background and signal events using the training and testing samples.

4.10.1 General MVA and optimisation strategy

Folding strategy

The MVA strategy is designed to guarantee a reliable and unbiased estimation of the analysis sensitivity. This necessitates that simulated events are not used simultaneously in defining the BDT (including its hyperparameters and input variables) and generating the histogram templates for the BDT output score distributions.

The simplest strategy, which adheres to this requirement, involves dividing the available set of simulated events into three equal partitions. In our specific implementation, this partitioning is based on the event number.

Model	Fold 0 `event_number` $\%3 = 0$	Fold 1 (`event_number` $\%3 = 1$)	Fold 2 (`event_number` $\%3 = 2$)
BDT 0	Training	Validation	Testing
BDT 1	Testing	Training	Validation
BDT 2	Validation	Testing	Training

TABLE 4.5: Partitioning of simulated events for training, optimization, and evaluation of BDT models.

Subsequently, three distinct BDT models are trained, each utilizing a different partition of the available simulated events (referred to as "training folds," see Table 4.5). The same set of hyperparameters and input variables is used for each training. These selections are made by optimizing the BDT's performance on the "validation folds," which are not seen during training.

The simulated events within the "testing folds" are employed in creating the histogram fit templates. By design, these events are not involved in the BDT optimization process, ensuring an unbiased estimation of the expected analysis significance.

Optimization of Hyperparameters

Certain MVA training hyperparameters play a crucial role in determining the classification accuracy of the BDT. Key factors include the number of trees (`NTrees`) in the ensemble and the depth of each decision tree (`MaxDepth`).

An integrated optimization process is conducted for these hyperparameters. For a specific combination of hyperparameter values, a set of BDTs is trained following the folding protocol detailed in Section 4.10.1. Subsequently, the binned distribution of the BDT output score is computed separately for both signal and the combined background, using the simulated events found in the validation folds. The same algorithm that defines the binning for the likelihood fit (see Section 4.15.1) is employed for this purpose. The binned signal significance serves as the performance metric,

$$Z = \sqrt{\sum_{i \in \text{bins}} 2 \left((s_i + b_i) \log \left(1 + \frac{s_i}{b_i} \right) - s_i \right)}, \tag{4.5}$$

where s_i and b_i represent the anticipated numbers of signal and background events in bin i, respectively.

Hyperparameter values are explored within predefined ranges, contingent on the analysis region and BDT type. Bayesian optimization is employed to favorably select hyperparameter configurations that yield higher values for the binned significance. The ultimate hyperparameter set is chosen from the pool of parameter points encountered during the optimization process.

Selection of Input Variables

A large number of kinematic variables with discriminative potential can be defined for the $bb\tau\tau$ system. However, it is advantageous to streamline this set by removing highly correlated or redundant observables. The goal is to retain a "minimal" yet "comprehensive" set of inputs that maintains near-maximal discrimination power. (It's worth noting that while this variable selection is not strictly mandatory—provided that all variables utilized as inputs to the BDT are well-modeled—it is viewed as a simplification.)

The process begins with a list of all available variables, from which a reasonably minimal set is constructed iteratively:

- A small set of core "baseline" input variables is always incorporated. (The specific variables in the baseline set are contingent on the BDT, and will be elaborated on below.)
- Additional variables are chosen from the remaining list in a step-by-step manner: at each juncture, the observable that leads to the most substantial enhancement of the binned signal significance (calculated in accordance with Eq. 4.5 on the validation folds) is selected.

- In the event that no extra variable results in an augmentation of the validation significance, the variable with the smallest impact is included instead.
- If no progress is observed over N_p consecutive steps, the optimization process is terminated.

It's important to acknowledge that such thoughtful optimization strategies can be susceptible to statistical noise in the performance measure employed to guide the algorithm. To mitigate the impact of statistical fluctuations on the significance measure Z, efforts are made to compute the binned significance on a coarser binning compared to that used in the fit, as elucidated below.

4.11 $bb\tau\tau$-Analysis MVA strategies

In this section the MVA studies performed for both the channels $\tau_{had}\tau_{had}$ and $\tau_{lep}\tau_{had}$ (SLT and LTT) channels will be presented.

4.11.1 ggF/VBF BDT

The analysis presented in this thesis is utilising the idea to categorize an event into ggF signal or VBF HH signal after an event is checked for the number of jets as described in Section 4.6). The BDT is trained using ggF HH as signal and VBF HH as background. The final BDT scores are achieved by optimising both the kinematic variables and hyperparameters for the two channels (τ_{had} τ_{had} and τ_{lep} τ_{had}) of the analysis as mentioned in the section 4.10.1. The aim of this classification is to improve the κ_{2V} constraint by creating a dedicated category for VBF events.

The BDT is only applied to VBF candidate events, and only such events are used in the training. VBF candidate events are defined as events that have at least two jets in addition to the $H \to bb$ ones. Nearly half of the ggF *HH* events pass the VBF candidate requirement and the other half fail, while around 80%

of the VBF *HH* events pass. The BDT is trained so that ggF-like [9] events are assigned with the scores near 1.0 while VBF-like [10] events are assigned with the scores near -1.0. Accordingly, events with the scores below a chosen cut value (working point) fall into the VBF category.

Kinematic variable optimisation

The procedure of optimising the variable used to train the BDT for the categorization of ggF and VBF HH signal is explained in the Section 4.10.1. As the last step of the BDT optimisation, the minimal set of training variables offering near-maximal separation power is determined. This is done by starting from a small set and iteratively adding variables one at a time from a pre-defined list of candidate variables. The variable leading to the largest increase (or minimal decrease) in Z is included, until no changes are observed. The starting set of variables includes the invariant mass of the VBF jets, defined as the two jets with the highest p_{T} not associated with the $H \rightarrow b\bar{b}$ decay, and their pseudorapidity gap $(\Delta\eta_{jj}^{\mathrm{VBF}})$. The final set of variables for the categorisation BDTs for each channel is summarised in Table 4.6. It includes the VBF jets pseudorapidity product, their angular separations $(\Delta\phi_{jj}^{\mathrm{VBF}}$ and $\Delta R_{jj}^{\mathrm{VBF}})$ and the invariant mass m_{HH}. In addition, the Fox-Wolfram moments f_i of i-th order [119] as well as their modified definitions for usage in hadron collider experiments h_i have shown to further increase the separation power, together with the centrality C of the τ leptons and selected jets, defined as $C = \frac{\sum_i p_{\mathrm{T}}(i)}{\sum_i E(i)}$, and their effective mass. The distributions of the resulting BDT scores are shown in Fig. 4.25 for all three channels of the analysis. VBF candidate events are assigned to the VBF category if their BDT score is evaluated below a set threshold. The value of this cut is optimised to achieve the best sensitivity to the signal strength modifiers κ_λ and

---

[9] A MVA score near 1 suggests a resemblance to the signal. Since ggF is designated as the signal, an event resembling ggF is expected to exhibit a score close to 1.

[10] A MVA score near -1 suggests a resemblance to the background. Since VBF is designated as the background, an event resembling ggF is expected to exhibit a score close to 1.

κ_{2V}, along with the upper limits on HH production for ggF and VBF production modes separately and combined. The BDT cut values are set to 0.1, -0.13 and -0.1 for the $\tau_{\text{had}}\tau_{\text{had}}$, $\tau_{\text{lep}}\tau_{\text{had}}$ SLT and $\tau_{\text{lep}}\tau_{\text{had}}$ LTT SRs respectively.

Variable	$\tau_{\text{had}}\tau_{\text{had}}$	$\tau_{\text{lep}}\tau_{\text{had}}$ SLT	$\tau_{\text{lep}}\tau_{\text{had}}$ LTT
m_{jj}^{VBF}	✓	✓	✓
$\Delta\eta_{jj}^{\text{VBF}}$	✓	✓	✓
$\text{VBF}\eta_0 \times \eta_1$	✓	✓	
$\Delta\phi_{jj}^{\text{VBF}}$	✓		
$\Delta R_{jj}^{\text{VBF}}$		✓	
$\Delta R_{\tau\tau}$	✓		
m_{HH}	✓		
f_2^a	✓		✓
C^a		✓	✓
m_{Eff}^a		✓	
f_0^c		✓	✓
f_0^a			✓
h_3^a			

TABLE 4.6: Input variables for the VBF-ggF categorisation BDTs in each of the three analysis channels. The superscripts a and c specify the selection of jets that are taken into account for the calculation in addition to the two τ-lepton candidates. For variables with **a c**, only the four-momenta of central jets, i.e. jets with $|\eta| < 2.5$, are included, while an a indicates that all available jets are included.

The distribution of the optimised variables as a comparison between ggF and VBF signal are shown in Appendix A.3.

Hyperparameter optimisation

A 2-D scan was performed by using the various range of maximum depth of the decision tree (`MaxDepth`) and the number of trees (`NTrees`) in order to find the optimal combination of hyperparameters. `NTrees` and `MaxDepth` were allowed to vary from 100 to 1000 and from 2 to 10, respectively, as shown in Figure 4.26. The number of trees and their depth are chosen to maximise the value of the number-counting significance (Z) as shown in equation 4.5 computed from the binned distribution of the BDT discriminant.

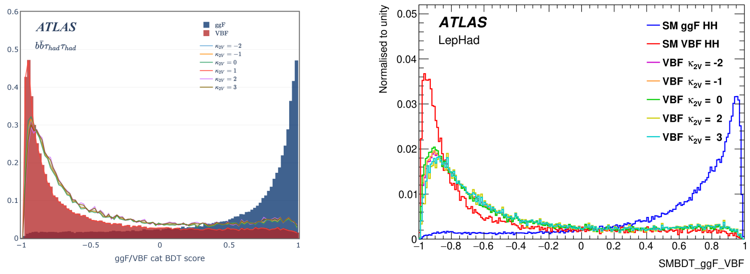

(A) ggF/VBF BDT distribution for the τ_{had} τ_{had} channel

(B) ggF/VBF BDT distribution for the τ_{lep} τ_{had} -SLT channel

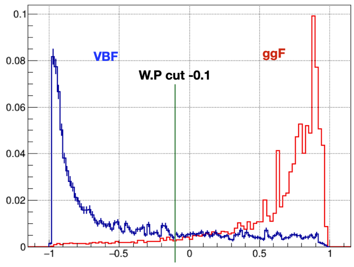

(C) ggF/VBF BDT distribution for the τ_{lep} τ_{had} -LTT channel

FIGURE 4.25: Figures (a), (b), and (c) display different aspects of the BDT analysis. (**a**) shows the ggF/VBF BDT score distributions for $bb\tau_{had}\tau_{had}$, (**b**) shows the ggF/VBF BDT score distributions for $bb\tau_{lep}\tau_{had}$-SLT, (**c**) shows the ggF/VBF BDT score distributions for $bb\tau_{lep}\tau_{had}$-LTT channels.The signal refers to the ggF process, while the background denotes the VBF process. The BDT cut values are set to 0.1, -0.13 and -0.1 for the τ_{had} τ_{had} , τ_{lep} τ_{had} SLT and τ_{lep} τ_{had} LTT SRs respectively

The Final list of the hyperparameters optimised for the (**a**) τ_{had} τ_{had} and (**b**) $\tau_{\text{lep}}\tau_{\text{had}}$ SLT and (**c**) $\tau_{\text{lep}}\tau_{\text{had}}$ LTT are shown in the Table 4.7

Hyperparameter	$\tau_{had}\tau_{had}$	$\tau_{lep}\tau_{had}$ SLT	$\tau_{lep}\tau_{had}$ LTT
NTrees	109	126	292
MaxDepth	6	4	2
MinNodeSize	1%	1%	1%
BoostType	Grad	Grad	1%
Shrinkage	0.2	0.2	0.2
IgnoreNegWeightsInTraining	True	True	True

TABLE 4.7: Optimised hyperparameters for the BDT in the (**b**) τ_{had} τ_{had} (**b**) $\tau_{\text{lep}}\tau_{\text{had}}$ SLT (**c**) $\tau_{\text{lep}}\tau_{\text{had}}$ LTT.

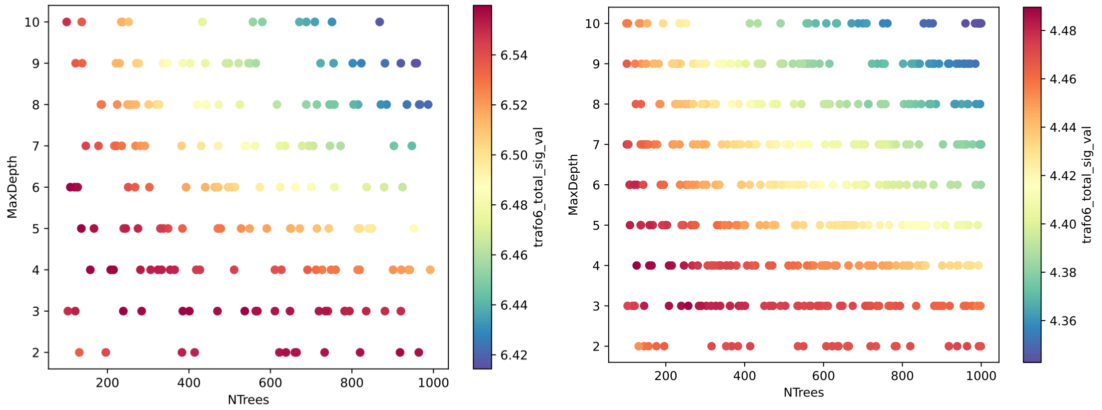

(A) $\tau_{\text{had}}\tau_{\text{had}}$ channel.

(B) $\tau_{\text{lep}}\tau_{\text{had}}$ SLT channel.

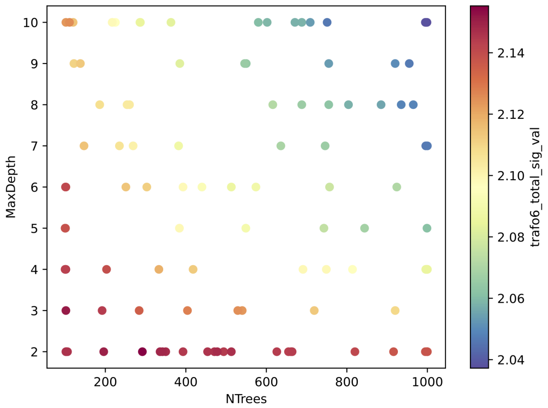

(C) $\tau_{\text{lep}}\tau_{\text{had}}$ LTT channel.

FIGURE 4.26: Hyperparameters optimization for the ggF/VBF BDT for the three channels. (**a**) $\tau_{\text{had}}\tau_{\text{had}}$, (**b**) $\tau_{\text{lep}}\tau_{\text{had}}$ SLT, (**c**) $\tau_{\text{lep}}\tau_{\text{had}}$ LTT

4.11.2 Signal region MVA Discriminants

In order to enhance the discrimination between the HH signal and the background, BDTs are employed in each of the analysis channels. These SR-specific BDTs, totalling nine, are tailored to each analysis category. The signal in the ggF high-m_{HH} and VBF categories corresponds to the ggF and VBF Standard Model production of HH pairs, respectively. In the ggF low-m_{HH} category, the signal is defined as $ggFHH$ production with a coupling strength modifier of $\kappa_{\lambda} = 10$. The training process employs the sum of all backgrounds normalized to their respective cross-sections. The BDTs are trained on events selected within each respective category. For VBF category BDTs, events from both VBF and ggF categories are utilized to maximize sample size.

To optimize and evaluate the BDTs, the simulated events are divided into three samples using the procedure described in Section 4.6. The number of trees and their depth are determined to maximize the signal significance Z calculated from the binned distribution of the BDT output as shown in Tables 4.8, 4.9 and 4.10 respectively.

TABLE 4.8: Training hyperparameters chosen for the BDTs in the $\tau_{\text{had}}\tau_{\text{had}}$ analysis categories.

Hyperparameter	low-m_{HH} ggF SR	high-m_{HH} ggF SR	VBF SR
NTrees	204	241	465
MaxDepth	2	3	3
MinNodeSize	1%	1%	1%
BoostType	Grad	Grad	Grad
Shrinkage	0.2	0.2	0.2
IgnoreNegWeightsInTraining	True	True	True

TABLE 4.9: Training hyperparameters chosen for the BDTs in the $\tau_{\text{lep}}\tau_{\text{had}}$-SLT analysis categories.

Hyperparameter	low-m_{HH} ggF SR	high-m_{HH} ggF SR	VBF SR
NTrees	421	152	406
MaxDepth	5	5	4
MinNodeSize	1%	1%	1%
BoostType	Grad	Grad	Grad
Shrinkage	0.2	0.2	0.2
IgnoreNegWeightsInTraining	True	True	True

TABLE 4.10: Training hyperparameters chosen for the BDTs in the $\tau_{\text{lep}}\tau_{\text{had}}$-LTT analysis categories.

Hyperparameter	low-m_{HH} ggF SR	high-m_{HH} ggF SR	VBF SR
NTrees	122	235	239
MaxDepth	6	5	3
MinNodeSize	1%	1%	1%
BoostType	Grad	Grad	Grad
Shrinkage	0.2	0.2	0.2
IgnoreNegWeightsInTraining	True	True	True

The input variables for the BDTs are selected to maximize signal-to-background separation for each trained BDT for the ggF signal region is summarised in table 4.11 while for the VBF signal region is summarised in table 4.12 while the detail explanation of these variables is also provided in the appendices A.4 and A.5.

TABLE 4.11: Optimized list of variables for the $b\bar{b}\tau^-\tau^+$ analysis for the ggF signal regions.

Variable	$\tau_{\text{had}}\tau_{\text{had}}$		$\tau_{\text{lep}}\tau_{\text{had}}$ SLT		$\tau_{\text{lep}}\tau_{\text{had}}$ LTT	
	low-m_{HH}	high-m_{HH}	low-m_{HH}	high-m_{HH}	low-m_{HH}	high-m_{HH}
m_{bb}	✓	✓	✓	✓	✓	✓
$m_{\tau\tau}^{\text{MMC}}$	✓	✓	✓	✓	✓	✓
m_{HH}	✓	✓	✓	✓	✓	✓
ΔR_{bb}	✓	✓	✓	✓	✓	
$\Delta R\left(\tau_0, \tau_1\right)$	✓	✓	✓	✓	✓	✓
N(jets)	✓	✓	✓			
$p_{\text{T}}(HH)$		✓	✓			
H_{T}	✓			✓	✓	✓
T_1		✓	✓	✓	✓	✓
T_2	✓				✓	✓
$E_{\text{T}}^{\text{miss}}$	✓	✓	✓			
$E_{\text{T}}^{\text{miss}}$ Centrality					✓	
M_{T2}	✓				✓	
m_T^W			✓	✓	✓	
$m_{\text{T}}\left(\tau_1\right)$		✓		✓	✓	
$p_{\text{T}}\left(\tau_0\right)$	✓		✓	✓		
$p_{\text{T}}\left(\tau_1\right)$	✓		✓	✓		
$p_{\text{T}}\left(b_0\right)$	✓		✓			✓
$p_{\text{T}}\left(b_1\right)$				✓		
$p_{\text{T}}(bb)$						✓
$p_{\text{T}}(\tau\tau)$						✓
$\Delta p_{\text{T}}\left(\tau_0, \tau_1\right)$					✓	✓
$\eta\left(\tau_0\right)$	✓	✓				
$\eta\left(\tau_1\right)$	✓	✓				
$\Delta\eta\left(\tau_0, \tau_1\right)$					✓	
$\Delta\phi\left(bb, E_{\text{T}}^{\text{miss}}\right)$	✓	✓				
$\Delta\phi(bb, \tau\tau)$	✓	✓				✓
$\Delta\phi\left(\tau\tau, E_{\text{T}}^{\text{miss}}\right)$			✓	✓	✓	✓
$\Delta\phi\left(\tau_1, E_{\text{T}}^{\text{miss}}\right)$					✓	✓
DL1r quantile (b_0)	✓	✓		✓		
DL1r quantile (b_1)	✓	✓		✓		
$\Delta R\left(b_0, \tau_0\right)$	✓	✓	✓			
$\Delta R\left(b_1, \tau_1\right)$		✓	✓			
$\Delta R\left(b_1, \tau_0\right)$			✓	✓		
$m_{\text{eff}}(\tau\tau j)$	✓					
$m_{\text{eff}}(\tau\tau bb)$						✓
$m\left(b_0\tau_0\right)$						✓
$m\left(b_1\tau_0\right)$						✓
m_{HH}^*	✓					✓
$m_H H$ scaled						✓
cent$(bb\tau\tau)$	✓	✓				
spher$(bb\tau\tau)$	✓	✓				
pflow $(bb\tau\tau)$		✓				
coshelicity (bb)			✓	✓		

TABLE 4.12: Optimized list of variables for the $b\bar{b}\tau^{-}\tau^{+}$ analysis for the VBF signal regions.

Variable	$\tau_{\text{had}}\tau_{\text{had}}$	$\tau_{\text{lep}}\tau_{\text{had}}$ SLT	$\tau_{\text{lep}}\tau_{\text{had}}$ LTT
m_{HH}	✓	✓	✓
m_{bb}	✓	✓	✓
$m_{\tau\tau}^{\text{MMC}}$	✓	✓	✓
ΔR_{bb}	✓	✓	
$\Delta R\,(\tau_0, \tau_1)$	✓	✓	
VBF $\eta_0 \times \eta_1$	✓		✓
$\Delta\eta_{ji}^{\text{VBF}}$	✓	✓	
$\Delta\phi_{ji}^{\text{VBF}}$	✓		
$\Delta R_{jj}^{\text{VBF}}$	✓	✓	
m_{jj}^{VBF}	✓	✓	✓
N(jets)			✓
$\mathbf{H}_{\text{T}}$		✓	
s_{T}			✓
T_2			✓
m_T^W			✓
$\Delta\eta^{HH}$		✓	
$p_{\text{T}}(HH)$			✓
m_{HH}^{*}			✓
m_{HH} scaled			✓
$p_{\text{T}}\,(\tau_0)$			✓
$p_{\text{T}}(\tau\tau)$			✓
$p_{\text{T}}\,(b_0)$			✓
$\eta\,(\tau_0)$	✓		
$\eta\,(\tau_1)$	✓		
$\Delta R\,(b_0, \tau_0)$			
Thrust $\text{T}(\tau\tau jf)$	✓		
Circularity $\text{C}(\tau\tau jf)$	✓		
Planar Flow $\text{P}(\tau\tau jf)$		✓	
$f_0(\tau\tau jf)$		✓	
$f_2(\tau\tau jf)$		✓	
$f_4(\tau\tau jf)$		✓	
$m_{\text{eff}}(\tau\tau jf)$		✓	
$\cos\theta^{+}$			✓
$\cos(\theta)_{\tau\tau}^{\text{helicity}}$			✓

The variables are arranged in a list ordered by their impact on the signal significance Z, following the same procedure as outlined in Section 4.15.1. The initial set for each analysis SR and category includes the invariant masses of the selected b-jets (m_{bb}), τ-lepton pair $\left(m_{\tau\tau}^{\mathrm{MMC}}\right)$, and HH system (m_{HH}). It also encompasses the angular separations between b-jets (ΔR_{bb}) and between τ-leptons $(\Delta R_{\tau\tau})$. In the $\tau_{\text{lep}}\,\tau_{\text{had}}$ LTT high-m_{HH} category, ΔR_{bb} is omitted, and in the $\tau_{\text{lep}}\,\tau_{\text{had}}$ LTT VBF category, both ΔR_{bb} and $\Delta R_{\tau\tau}$ are excluded. Additional variables, determined via Z-based optimization, fall into several categories. Variables requiring the presence of a charged lepton are excluded in the $\tau_{\text{had}}\,\tau_{\text{had}}$ SR. Higgs candidates H are reconstructed from either b-jet or τ-lepton pairs. In the low- and high-m_{HH} categories, variables describing the kinematic properties of the selected b-jets and τ-leptons are included. This incorporates the p_T of the leading and subleading b-jets and τ leptons, along with their pseudorapidities and the transverse mass of the τ leptons. Angular separations between (sub)leading b-jet and (sub)leading τ lepton, along with the pseudorapidity separation and p_T difference between the selected τ-lepton candidate and the charged lepton are considered. Variables related to the reconstructed H candidate topologies include azimuthal angular separation between b-jet pair and τ-lepton pair, as well as between either b-jet or τ-lepton pair and the magnitude E_T^{miss} of the missing p_T vector $\vec{p}_T^{\text{miss}}$. Further variables encompass event properties like the transverse mass of the W boson candidate in the $\tau_{\text{lep}}\tau_{\text{had}}$ channel, topness variable [120], reduced and scaled invariant mass of the HH system, p_T of the reconstructed HH system, and effective mass of the HH decay products. Distinctive event configurations are represented through Fox-Wolfram moments, circularity, sphericity, and planar flow variables reconstructed from the HH decay products. Finally, b-tagging information is provided by the quantile distribution of the DL1r tagger output for the selected b-jets, which serves as a training variable. For VBF categories, additional variables are included to target specific features of VBF HH events.

$\tau_{had}\tau_{had}$ pre-fit MVA variables modelling

The following shows a representative set of the pre-fit MVA input variable distributions in each of the $\tau_{had}\tau_{had}$ signal regions. In all the plots, the background is adjusted using scale factors obtained from a full fit to data. Figure 4.27 shows how key variables are modelled in the three signal regions.

$\tau_{lep}\tau_{had}$-SLT pre-fit MVA variables modelling

The following figures show a representative set of the pre-fit MVA input variable distributions in each of the $\tau_{lep}\tau_{had}$-SLT signal regions. In all the plots, the background is adjusted using scale factors obtained from a full fit to data. Figure 4.29 shows how key variables are modelled in the three signal regions, whereas figure 4.30 shows new variables introduced for the signal-background BDT in each region.

$\tau_{lep}\tau_{had}$-LTT pre-fit MVA variables modelling

The following figures show a representative set of the pre-fit MVA input variable distributions in each of the $\tau_{lep}\tau_{had}$-LLT signal regions. In all the plots, the background is adjusted using scale factors obtained from a full fit to data. Figure 4.31 shows how key variables are modelled in the three signal regions, whereas figure 4.32 shows new variables introduced for the signal-background BDT in each region.

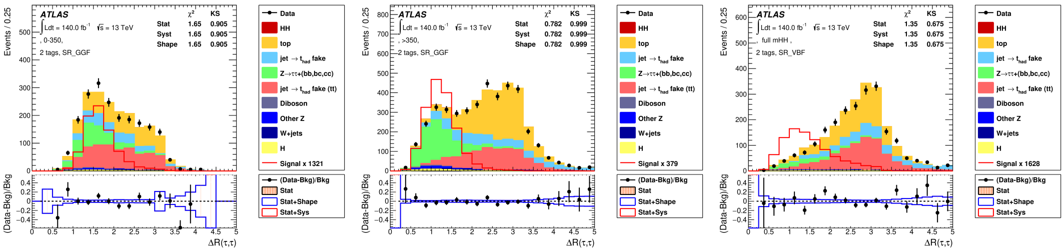

(A) low-m_{HH} ggF SR (B) high-m_{HH} ggF SR (C) VBF SR

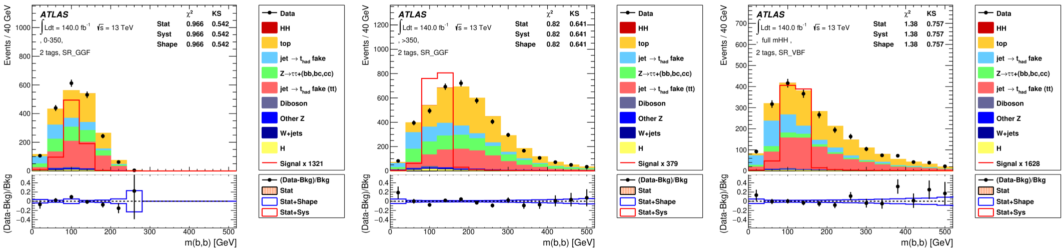

(D) low-m_{HH} ggF SR (E) high-m_{HH} ggF SR (F) VBF SR

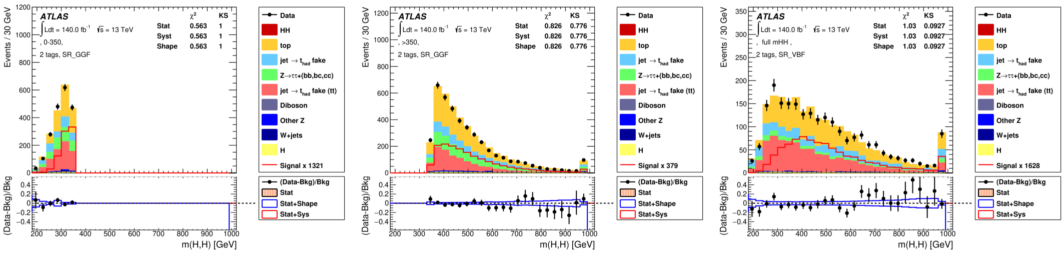

(G) low-m_{HH} ggF SR (H) high-m_{HH} ggF SR (I) VBF SR

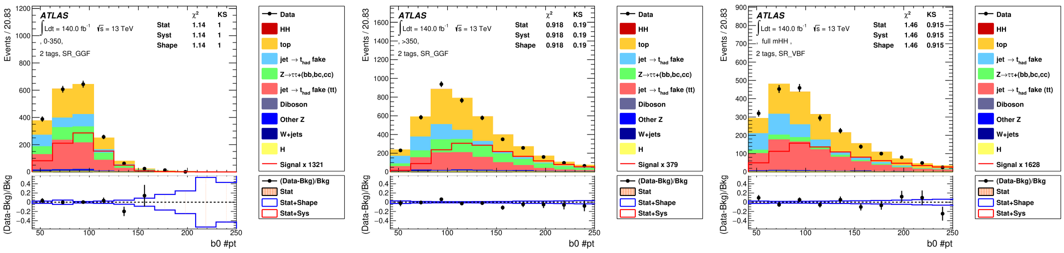

(J) low-m_{HH} ggF SR (K) high-m_{HH} ggF SR (L) VBF SR

FIGURE 4.27: Representative set of pre-fit MVA input variable distributions in the $\tau_{had}\tau_{had}$ SRs.

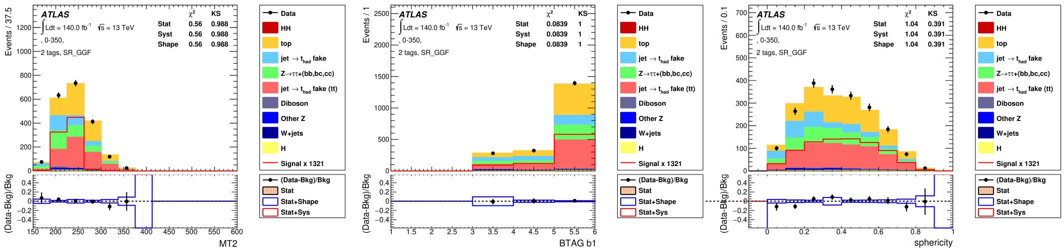

(A) low-m_{HH} ggF SR

(B) low-m_{HH} ggF SR

(C) low-m_{HH} ggF SR

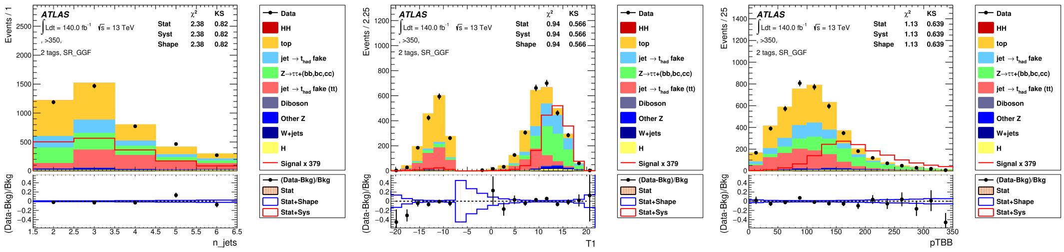

(D) high-m_{HH} ggF SR

(E) high-m_{HH} ggF SR

(F) high-m_{HH} ggF SR

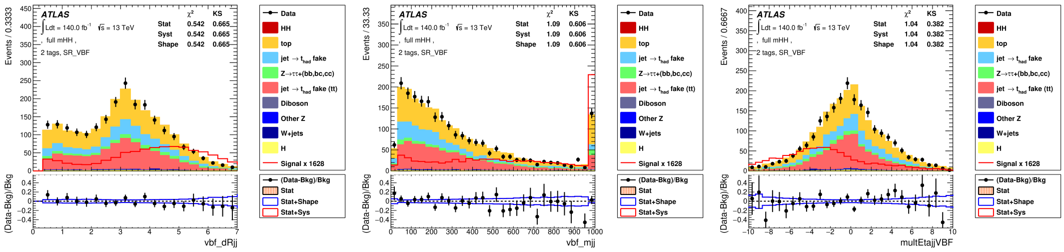

(G) VBF SR

(H) VBF SR

(I) VBF SR

FIGURE 4.28: Representative set of pre-fit MVA input variable distributions in the $\tau_{had}\tau_{had}$ SRs.

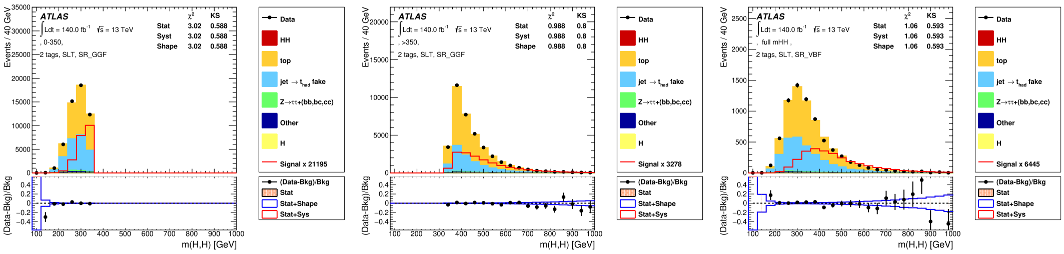

(A) low-m_{HH} ggF SR (B) high-m_{HH} ggF SR (C) VBF SR

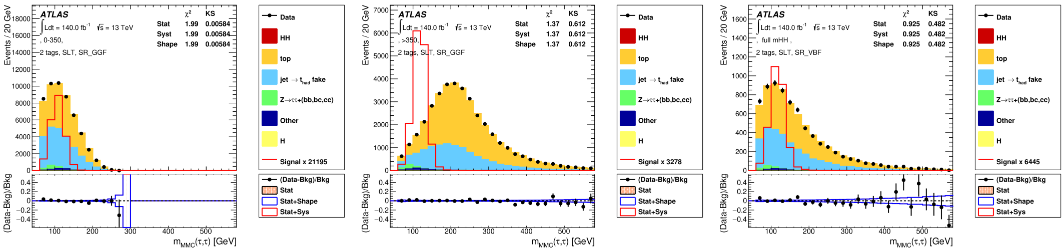

(D) low-m_{HH} ggF SR (E) high-m_{HH} ggF SR (F) VBF SR

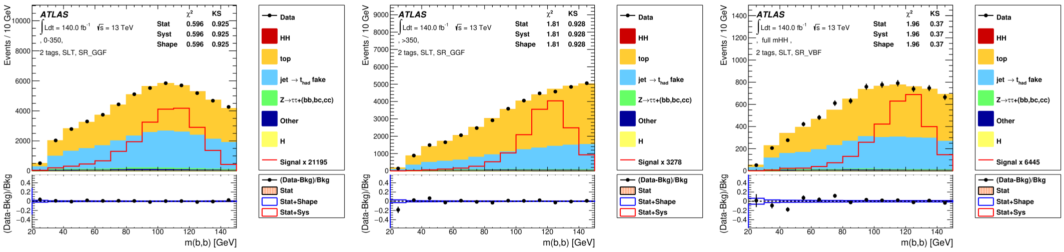

(G) low-m_{HH} ggF SR (H) high-m_{HH} ggF SR (I) VBF SR

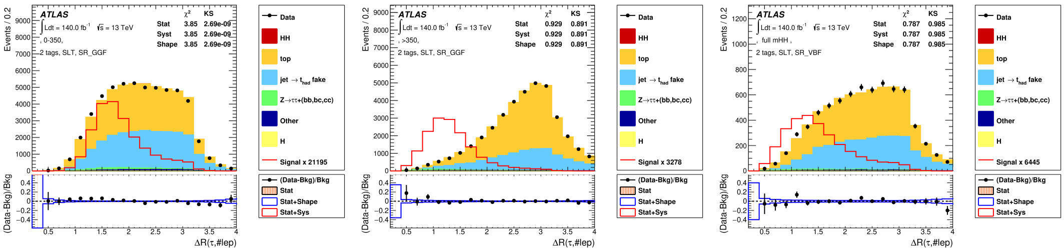

(J) low-m_{HH} ggF SR (K) high-m_{HH} ggF SR (L) VBF SR

FIGURE 4.29: Representative set of pre-fit MVA input variable distributions in the $\tau_{lep}\tau_{had}$ SLT SRs.

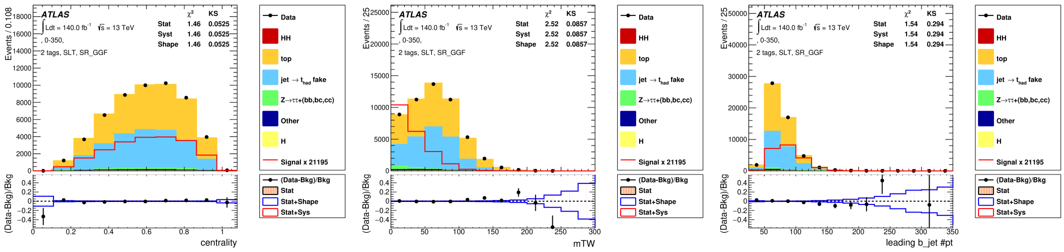

(A) low-m_{HH} ggF SR (B) low-m_{HH} ggF SR (C) low-m_{HH} ggF SR

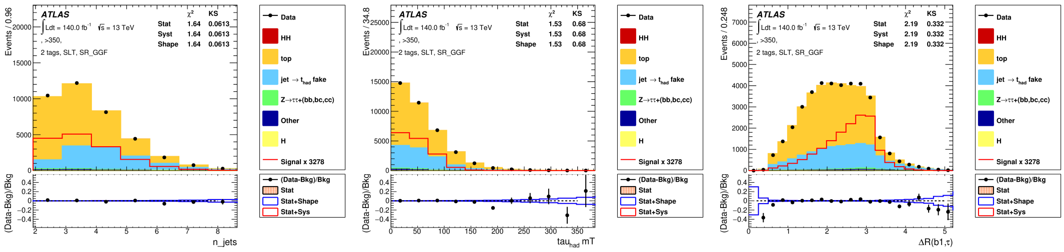

(D) high-m_{HH} ggF SR (E) high-m_{HH} ggF SR (F) high-m_{HH} ggF SR

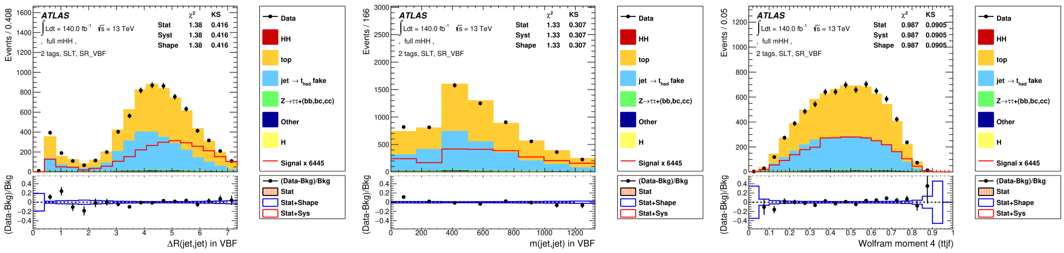

(G) VBF SR (H) VBF SR (I) VBF SR

FIGURE 4.30: Representative set of pre-fit MVA input variable distributions in the $\tau_{lep}\tau_{had}$ SLT SRs.

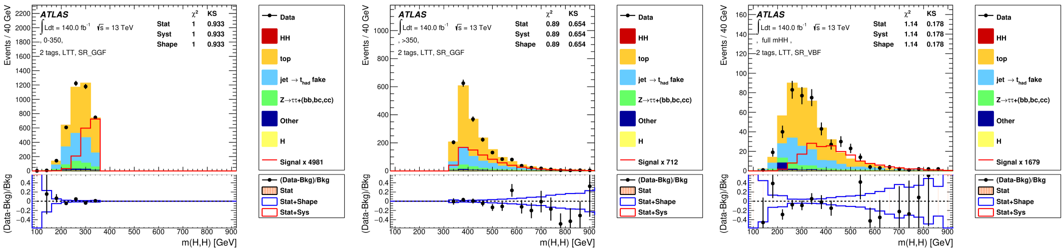

(A) low-m_{HH} ggF SR (B) high-m_{HH} ggF SR (C) VBF SR

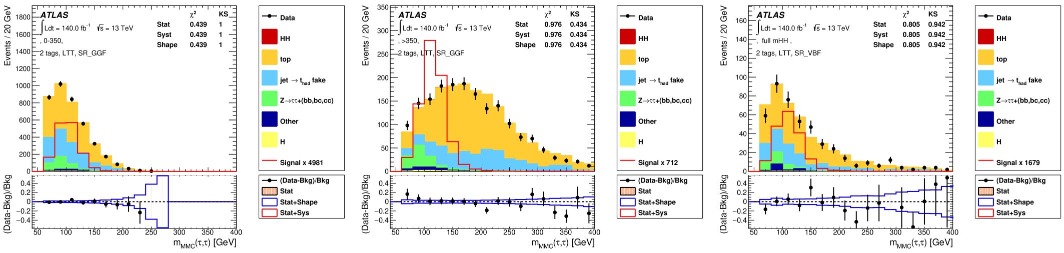

(D) low-m_{HH} ggF SR (E) high-m_{HH} ggF SR (F) VBF SR

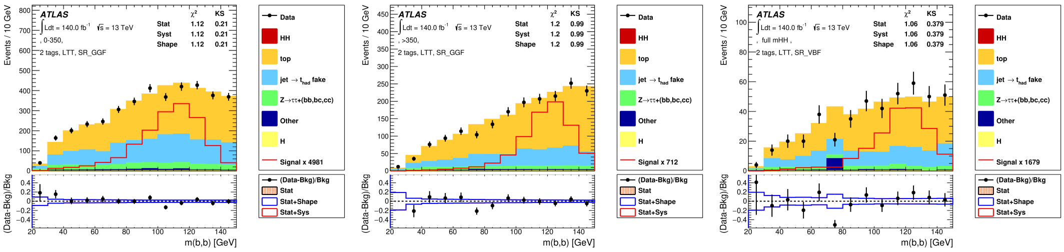

(G) low-m_{HH} ggF SR (H) high-m_{HH} ggF SR (I) VBF SR

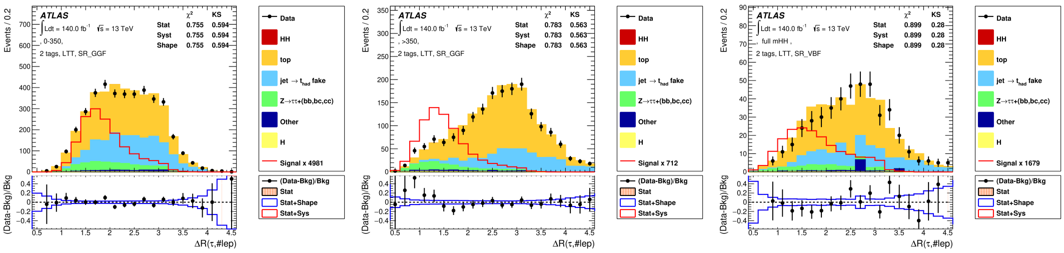

(J) low-m_{HH} ggF SR (K) high-m_{HH} ggF SR (L) VBF SR

FIGURE 4.31: Representative set of pre-fit MVA input variable distributions in the $\tau_{lep}\tau_{had}$ LTT SRs.

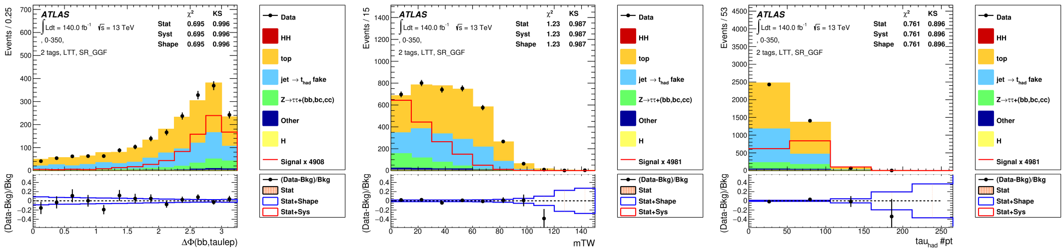

(A) low-m_{HH} ggF SR (B) low-m_{HH} ggF SR (C) low-m_{HH} ggF SR

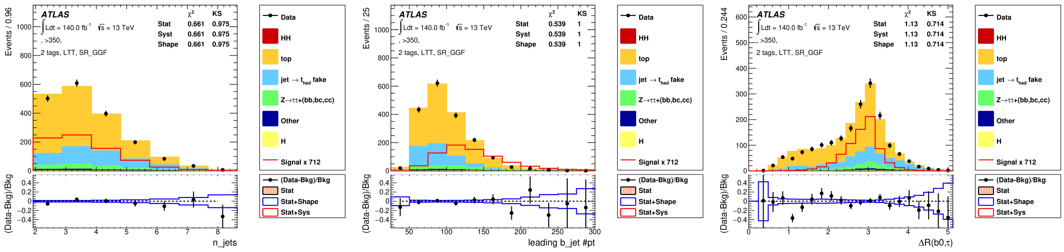

(D) high-m_{HH} ggF SR (E) high-m_{HH} ggF SR (F) high-m_{HH} ggF SR

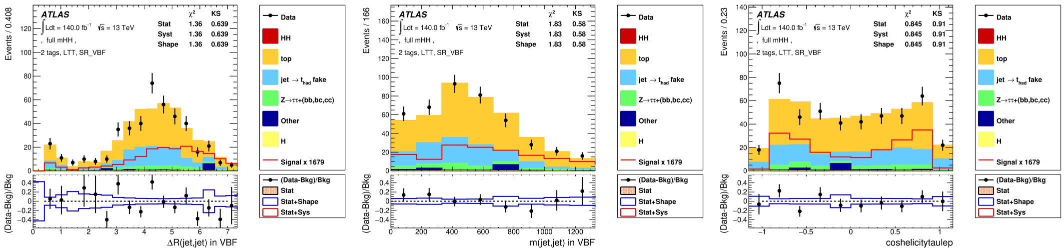

(G) VBF SR (H) VBF SR (I) VBF SR

FIGURE 4.32: Representative set of pre-fit MVA input variable distributions in the $\tau_{lep}\tau_{had}$ LTT SRs.

4.12 Systematic uncertainities

The systematic uncertainties related to both the estimation of backgrounds and signal in the $\tau_{\text{lep}}\,\tau_{\text{had}}$ and $\tau_{\text{had}}\,\tau_{\text{had}}$ SRs are evaluated and eventually propagated to the final fit. These systematic included both sets of experimental and theoretical modelling uncertainties and will be summarised in the following sections.

4.12.1 Experimental uncertiainities

The uncertainties arising from the experiment depends upon the factors such as data collection conditions, detector specifications, and techniques employed for object reconstruction and identification. These uncertainties are consistent across different analyses and have been incorporated in accordance with the ATLAS Collaboration's guidelines for this study documented in the thesis. They are detailed below, along with a comprehensive list of all the experimental uncertainties considered in the analysis.

Luminosity and pile-up

The measured integrated luminosity of the dataset used for the results presented in this chapter has an associated uncertainty of 0.83% [121]. This uncertainty in normalization is taken into account for all simulated signal and background samples, where the normalization is not treated as a variable in the fitting process. The luminosity uncertainty is consistent across all processes it applies to. Additionally, the pileup profile of the simulated events is adjusted to align with the data.

Trigger requirements

Scale factors for trigger efficiency are computed based on the p_T of the triggering object. This correction accounts for the disparity in trigger efficiency between simulation and actual data. The uncertainties associated with these trigger scale factors are extended as systematic uncertainties linked to the trigger selection process.

Jets

Jet energies necessitate calibration post-reconstruction to accommodate detector characteristics and the intricacies of the jet reconstruction algorithm, while also addressing discrepancies in the jet response observed between collected data and MC simulations. The uncertainties associated with jet energy scale corrections (JES) are contingent upon the p_{T} and η of the jet. These uncertainties stem from various sources and are categorized into three sets of uncorrelated uncertainties [67]. Additionally, an uncertainty in the jet energy resolution (JER) is incorporated, considering disparities in energy resolution between simulations and data, along with experimental uncertainties related to measuring the jet energy resolution [122].

b-tagging

b-tagging corrections in MC simulations encompass scale factors applied to counter variations in flavour-tagging efficiency observed between simulated data and actual data. These factors are assessed independently for b, c, and light-flavour jets with respect to the jet's p_{T} and η [123]. The correction factors encompass distinct sources of uncertainties, which are disaggregated into uncorrelated components, resulting in three uncertainties for c-jets, four uncertainties for b-jets, and five uncertainties for light-flavour jets.

τ_{had}

The efficiency of τ_{had} reconstruction and identification in MC is adjusted using scale factors determined as a function of $\tau_{\text{had-vis}}\, p_T$ to accommodate disparities between simulation and actual data [75]. Systematic uncertainties arising from the efficiency scale factors are taken into account.

The energy scale of $\tau_{\text{had-vis}}$ is calibrated post-reconstruction. Any remaining discrepancies between simulation and data, along with uncertainties in the energy scale corrections, are considered as systematic uncertainties [75]. Furthermore, specific uncertainties related to the removal of overlap between τ and electrons are incorporated.

Background Modeling Uncertainties for MC-Based Processes

Modeling uncertainties pertain to our understanding of background and signal processes as simulated in MC. These uncertainties hinge on the settings used in theoretical cross-section calculations and MC simulations, including factors like PDF sets, factorization and renormalization scales, α_s, matrix element generators, parton shower models, and tuning parameters. Theoretical uncertainties in cross-section calculations impact only the normalization and are consistent across all analyses. However, uncertainties in acceptance, which influence both normalization and shape, are contingent on the analysis-specific selections applied.

Background modeling uncertainties for MC-based processes encompass both theoretical cross-section uncertainties and acceptance uncertainties. Cross-section uncertainties solely affect normalizations and are applied universally to all backgrounds (with the exception of $t\bar{t}$ and Z+HF processes, which have freely floating normalization factors in the fit). Acceptance uncertainties have the potential to impact both normalizations and the shapes of final discriminant distributions. Typically, their contribution is divided into a normalization acceptance uncertainty, affecting event yields in the signal region, and a shape uncertainty, influencing the form of the final discriminant distributions.

Acceptance uncertainties for minor backgrounds ($Z+$ light-flavor jets, $W+$ jets, and Diboson) are adopted from the ATLAS SM $VHbb$ analysis [124]. Meanwhile, acceptance uncertainties for $t\bar{t}$ $Z+$ HF jets, single-top (Wt channel), $t\bar{t}H$, and ZH processes are estimated within the signal regions (and control regions for $t\bar{t}$ and $Z+$ HF jets) of this analysis through comparisons between nominal and alternative MC simulated samples or samples with varied event weights, as elaborated in subsequent sections.

The normalisation acceptance uncertainties are derived by comparing the acceptance, denoted as A_i for each alternative sample i, to the acceptance of the nominal sample. Equivalently, we compare the expected number of events, denoted as N_i for each variation i, to the nominal expected events in the signal regions for all samples normalized to the same cross-section:

$$\sigma_A^i = \frac{A^i_{\text{variation}} - A_{\text{nominal}}}{A_{\text{nominal}}} = \frac{N^i_{\text{variation}} - N_{\text{nominal}}}{N_{\text{nominal}}}.$$

If one region in the final fit is more effective than others at constraining a certain normalization factor, a relative normalisation acceptance uncertainty is assigned. This is estimated by comparing the relative number of events predicted by the alternative model in one region R to another region R', in relation to the same fraction in the nominal model:

$$\sigma_{A_R/A_{R'}} = \frac{\frac{A_{\text{variation},R}}{A_{\text{variation},R'}} - \frac{A_{\text{nominal},R}}{A_{\text{nominal},R'}}}{\frac{A_{\text{nominal},R}}{A_{\text{nominal},R'}}} = \frac{\frac{N_{\text{variation},R}}{N_{\text{variation},R'}} - \frac{N_{\text{nominal},R}}{N_{\text{nominal},R'}}}{\frac{N_{\text{nominal},R}}{N_{\text{nominal},R'}}}.$$

Acceptance uncertainties for the normalization of backgrounds are applied across all regions and treated as correlated between regions, except for $t\bar{t}$ and $Z+$ HF backgrounds, whose normalizations are unconstrained (floated) in the global likelihood fit. For these two processes, relative acceptance uncertainties between regions with a shared underlying normalization are applied. Shape acceptance uncertainties are applied when discrepancies are identified in the final discriminant distributions of the nominal and alternative samples. This comparison is conducted by examining the normalized distributions of the BDT scores and calculating the ratio of alternative to nominal events per bin.

Uncertainties on $t\bar{t}$

The normalisation of the $t\bar{t}$ background is estimated from data in likelihood fits, so the analysis is not sensitive to uncertainties in its expected cross-section. The normalisation is freely floated in the final fit and correlated between the SRs and the Z+HF CR.

Relative acceptance normalisation uncertainties are applied on $t\bar{t}$ in all channels of the analysis to account for potential differences in the normalisation between the SRs and the Z+HF CR. Shape variations are also checked and applied, correlated with the relative acceptance uncertainties on the normalisation, where found to be relevant.

Uncertainties for $Z + \mathrm{HF}$ Processes

For $Z + \mathrm{HF}$ processes, uncertainties arise from various sources related to the modeling of hard-scatter events and parton showers. These uncertainties are assessed by comparing the nominal sample with an alternative $MADGRAPH5\_AMC@NLO + PYTHIA8$ sample. The alternative sample incorporates up to three additional partons in the final state, achieving NLO accuracy in the QCD coupling. This is accomplished by merging additional jet multiplicities using the FxFx NLO matrix-element and parton-shower merging prescription [125]. The alternative samples employ the A14 parton-shower tune and the NNPDF2.3Lo PDF set. Uncertainties stemming from missing higher-order QCD corrections are evaluated through variations in renormalization and factorization scales, along with PDF and α_S variations.

The impact of higher-order electroweak corrections for $Z + \mathrm{HF}$ processes is found to be negligible and thus not considered. The matching between matrix-element calculation and parton-shower is scrutinized by varying the SHERPA matching parameter (CKKW) and the resummation scale (QSF). All these sources of uncertainty influence the fractional contribution of $Z + \mathrm{HF}$ in each analysis category, with the most significant effect arising from renormalization and factorization scale variations, ranging up to 13% of the nominal values depending on the analysis category and signal region (SR).

Among these uncertainties, the modeling of the hard-scatter and the parton-shower, as compared with the alternative $MADGRAPH5\_AMC@NLO + PYTHIA8$ sample, is the most influential on the shape of the BDT score in the analysis SRs. This same source of uncertainty also has a notable impact on the shape of the m_{ll} variable in the CR. It is treated as a dedicated uncertainty independent from the BDT score shape uncertainty in the likelihood fit.

Additionally, an extra systematic uncertainty is incorporated to account for any remaining discrepancy between data and MC simulation in the dedicated CR, based on the p_T of the selected lepton pair. This uncertainty is applied in all analysis SRs as a function of the p_T of the τ lepton pair selected from the MC truth record.

4.12.2 Uncertainties in Signal Modeling

For the SM ggF and VBF processes in the production of HH signals, uncertainties arising from uncalculated higher-order QCD corrections are assessed. These uncertainties are determined by independently varying the renormalization and factorization scales within the hard-scatter calculation, alongside variations in PDFs and the strong coupling constant (α_S).

Additionally, uncertainties related to parton showers are evaluated by comparing the nominal samples against alternative PowHEG+Herwig7 samples specifically for the ggF HH process. All identified sources of uncertainty impact the fractional contribution of the signal in each analysis category. However, it's important to note that variations in the BDT score are only considered for the parton shower uncertainties associated with the ggF HH process.

Estimates for Other MC-Based Backgrounds

For minor backgrounds, such as single-top s- and t-channels, $Z+$ light-flavour jets, $W+$ jets, and di-boson processes, acceptance uncertainties only affect the normalization. Specifically, a 20% acceptance uncertainty is applied for the single-top production in s- and t-channels, while the $Z+$ light-flavour jets backgrounds receive an uncertainty of 23%.

Regarding $W+$ jets, a 37% acceptance uncertainty is applied in the $\tau_{\text{lep}}\tau_{\text{had}}$ channel, while 50% is assigned to the $\tau_{\text{had}}\tau_{\text{had}}$ channel, accounting for contributions from fake τ leptons. Additionally, acceptance uncertainties of 25%, 26%, and 20% are applied to WW, WZ, and ZZ processes, respectively.

4.13 Data-driven background modelling uncertianities

The final group of systematic uncertainties addresses the modeling of background processes that involve pseudo-τ_{had} candidates, estimated through data-driven or semi-data-driven methodologies as previously elaborated in Section 4.8.2.

4.13.1 Processes with fake- τ_{had} candidates in the τ_{lep} τ_{had} channel

Several sources of uncertainty are considered for the estimation of the fake background:

- The statistical uncertainty associated with the values of $\text{FF}_{t\bar{t}}$, FF_{QCD}, and r_{QCD} is taken into account and propagated to the final estimates of the fake background.

- To account for uncertainties in non-$t\bar{t}$ backgrounds being subtracted from the data, a conservative 30% uncertainty is assigned. This is achieved by varying the Fake Factor (FF) up and down by 30% when applying it to non-$t\bar{t}$ backgrounds that pass the anti-ID selection.

- The uncertainty stemming from the $t\bar{t}$ modeling is evaluated by comparing the fake background derived with and without the $t\bar{t}$ reweighting (for more details, refer to Section 4.8.2). The latter method is ultimately adopted, as it exhibits a higher variation, covering all fake backgrounds derived using variation samples.

- The value of $\mathrm{r}_{\mathrm{QCD}}$ is highly sensitive to the normalization and shape of the $t\bar{t}$ background. However, given the similarity between $\mathrm{FF}_{\mathrm{QCD}}$ and $\mathrm{FF}_{t\bar{t}}$, $\mathrm{r}_{\mathrm{QCD}}$ has a relatively small impact on the combined fake factor in practice. Therefore, the uncertainty on $\mathrm{r}_{\mathrm{QCD}}$ is estimated by varying the value from 0 to 0.5.

4.13.2 Processes with fake- τ_{had} candidates in the τ_{had} τ_{had} channel

As mentioned in section 4.8.3 that in the τ_{had} τ_{had} channel the background with fake- τ_{had} are measured for multi-jet and $t\bar{t}$ productions. So the sources of uncertainties will be taking into account for the both the method adopted in estimating fake- τ_{had} backgrounds.

Modelling of the multijet background

Uncertainties in the estimate of the simulated $\tau_{\text{had-vis}}$ background from multi-jet production include statistical variations in FFs and TFs (mentioned in the 4.8.3), along with uncertainties in the normalization and shape of non-multi-jet backgrounds. These non-multi-jet backgrounds are subtracted from the data when constructing the S) Template. Additionally, an uncertainty factor is introduced to address the extrapolation from SS to Opposite OS events. This systematic variation is determined by comparing FFs computed from SS and OS events with at least one b-tagged jet. For OS events, an additional criterion is applied: $m_{\tau\tau}^{\mathrm{MMC}} > 110$ GeV and $E_{\mathrm{T}}^{\mathrm{miss}}/\sigma\left(E_{\mathrm{T}}^{\mathrm{miss}}\right) < 3$, where $\sigma\left(E_{\mathrm{T}}^{\mathrm{miss}}\right)$ represents the event-based approximation to the resolution of $E_{\mathrm{T}}^{\mathrm{miss}}$ [126]. This ensures that the sample is predominantly composed of multi-jet events. The fidelity of modeling the multi-jet background is thoroughly assessed for closure in the SS Control Regions with 1 and 2 b-tagged jets, demonstrating commendable agreement between observed data and predictions.

Modeling of the $t\bar{t}$ Background with Simulated τ_{had} Candidates

The likelihood fit, used to extract SFs, accounts for uncertainties related to detector response and the modeling of backgrounds such as single top-quark, $W/Z+$ jets, and $t\bar{t}$ events with simulated τ_{had} candidates. Additionally, uncertainties in replicating the trigger requirements for $\tau_{\text{had-vis}}$ are taken into consideration. The covariance matrix of the measured SFs encompasses all statistical and systematic uncertainties. It is diagonalized, resulting in eigenvectors that define independent nuisance parameters. These parameters are then integrated into the final signal extraction fit.

4.14 Statistical Analysis

In the context of particle physics, this analysis is essentially a search for a theoretical process that has yet to be experimentally observed. It involves a statistical hypothesis test where we first establish the null hypothesis, H_0, which describes the known background processes. The observed data are then assessed for their level of agreement with this null hypothesis. If the data deviate significantly from what is expected under the null hypothesis, we have grounds to claim a discovery.

In contrast, when it comes to setting exclusion limits on a potential new signal, we test the compatibility of the alternative hypothesis, H_1, which includes both the background and the proposed signal, with the data. If the observed data are inconsistent with this hypothesis, we can rule out the presence of the new signal.

The outcome of our search is quantified using a p-value, which represents the likelihood, given H, of encountering data with the same level of inconsistency with the predictions of H or greater. A p-value below a certain threshold implies that the given hypothesis is incompatible with the observed data. This p-value is typically converted into a significance level, denoted as Z, defined so that a normally distributed variable with Z standard deviations above its mean has an upper-tail probability equal to p:

$$Z = \Phi^{-1}(1 - p) \tag{4.6}$$

Here, Φ^{-1} represents the quantile function (inverse of the cumulative distribution) of the standard Gaussian.

In the realm of particle physics, specific thresholds have been established for claiming discoveries or setting exclusion limits. For instance, the community employs a threshold of $Z = 5$ (corresponding to $p = 2.87 \times 10^{-7}$) to reject the background-only hypothesis and assert a discovery. On the other hand, when aiming to exclude an alternative signal hypothesis, a threshold of $p = 0.05$ (equivalent to a 95% CL, or $Z = 1.64$) is utilized.

Exclusion limits are determined in cases where no new signal is discovered. They typically represent upper bounds on the cross section of the hypothetical new signal. This implies that if such a process exists, it must occur with a cross section below this specified value, with a certain level of confidence (typically

95% CL).

During the development of the analysis, it is beneficial to assess the sensitivity by calculating the expected significance or exclusion limit prior to examining the actual observed data. This can be achieved by computing the median significance or median exclusion limit using "Asimov" datasets, which are constructed based on a predefined assumption, either H_1 to mimic the presence of the signal or H_0 to emulate the background-only scenario, rather than the actual observed data.

4.14.1 Profile Likelihood Ratio

In particle physics, the profile likelihood ratio, often used as a test statistic [127], is employed in the frequentist approach to calculate p-values. This method encompasses both the signal and background models, involving the parameter of interest, such as the signal process's cross-section, as well as nuisance parameters that represent systematic uncertainties. These nuisance parameters are not assumed to be known a priori and must be inferred (profiled) from the data.

For a hypothesis test based on a binned distribution of a discriminating variable x, the likelihood function can be represented as the product of Poisson probabilities across all bins:

$$L(n \mid \mu, \theta) = \prod_{i=1}^{N} \frac{(\mu s_i + b_i)^{n_i}}{n_i!} e^{-(\mu s_i + b_i)},$$

Here, n denotes the number of observed data events, μ signifies the signal strength (defined as $\mu = \sigma/\sigma_{\text{theory}}$, where $\mu = 1$ represents the theoretical expectation and $\mu = 0$ indicates no signal), s refers to the expected number of signal events, b represents the expected number of background events, and θ encompasses a set of nuisance parameters affecting the signal and background predictions. These parameters could be known, estimated from Monte Carlo (MC), or derived from the data.

The profile likelihood ratio is defined as:

$$\lambda(\mu) = \frac{L(\mu, \hat{\hat{\theta}})}{L(\hat{\mu}, \hat{\theta})}.$$

In this ratio, the numerator denotes the profile likelihood function. $\hat{\hat{\theta}}$ represents the value of θ that maximizes the likelihood L for the given μ (it is the conditional maximum-likelihood estimator of θ) and varies with μ. The denominator is the maximized (unconditional) likelihood function. $\hat{\mu}$ and $\hat{\theta}$ denote the values obtained by maximizing the likelihood, serving as the maximum-likelihood (ML) estimators of μ and θ. As $\lambda(\mu)$ is defined, it follows that $0 \leq \lambda \leq 1$. A value of λ close to 1 suggests good agreement between the data and the tested μ value.

The test statistic, quantifying the degree of inconsistency between the data and the hypothesized μ, is derived from the profile likelihood ratio:

$$q_\mu = -2 \ln \frac{L(\mu, \hat{\hat{\theta}})}{L(\hat{\mu}, \hat{\theta})}.$$

Higher values of q_μ imply greater incompatibility between the observed data and the tested μ. The hypothesis test involves assessing the level of incompatibility between the observed data and the hypothesized μ value directly, utilizing the test statistic q_μ to measure the discrepancy and then computing the p-value:

$$p_\mu = \int_{q_{\mu,\text{obs}}}^{\infty} f(q_\mu \mid \mu)\, dq_\mu,$$

Here, $q_{\mu,\text{obs}}$ denotes the observed data's test statistic value, and $f(q_\mu \mid \mu)$ represents the probability density function of q_μ, given the signal strength μ.

Discovery

To claim a discovery of a new signal, it is crucial to reject the null hypothesis H_0, which represents the background-only scenario. This is accomplished by demonstrating the incompatibility of the observed data with H_0, using the test statistic q_0:

$$q_0 = -2 \ln \frac{L(0, \hat{\hat{\theta}})}{L(\hat{\mu}, \hat{\theta})}, \tag{4.7}$$

where $\mu = 0$ in Equation 4.14.1, followed by the computation of its observed p-value:

$$p_0 = \int_{q_{0,\text{obs}}}^{\infty} f(q_0 \mid 0) \, dq_0 \tag{4.8}$$

If p_0 falls below the threshold of 2.87×10^{-7}, corresponding to a 5σ significance, it implies that the observed data are incompatible with the background-only hypothesis. Hence, a discovery can be claimed. The experiment's sensitivity to detecting a particular signal's discovery can be evaluated by computing the expected median significance using an Asimov dataset constructed with background plus signal, setting $\mu = 1$, instead of utilizing the actual observed data.

Exclusion Limit

The test statistics described in Equation 4.14.1 are also applicable for excluding a specific theory by computing it for $\mu = 1$:

$$q_1 = -2 \ln \frac{L(1, \hat{\theta})}{L(\hat{\mu}, \hat{\theta})} \tag{4.9}$$

A smaller value of q_1 indicates a greater compatibility of the data with the theory and lesser compatibility with the pure background expectations. The probability density functions $f(q_1 \mid 1)$ and $f(q_1 \mid 0)$, given $\mu = 1$ or $\mu = 0$, respectively, are derived from MC samples. The ability of the analysis to discern the sought-after model from the background relies on distinguishing between these two probability density functions.

Initially, determining the expected exclusion limit on the new signal is essential in the analysis design. By defining $\tilde{q}_1$ as the median of the $f(q_1 \mid 0)$

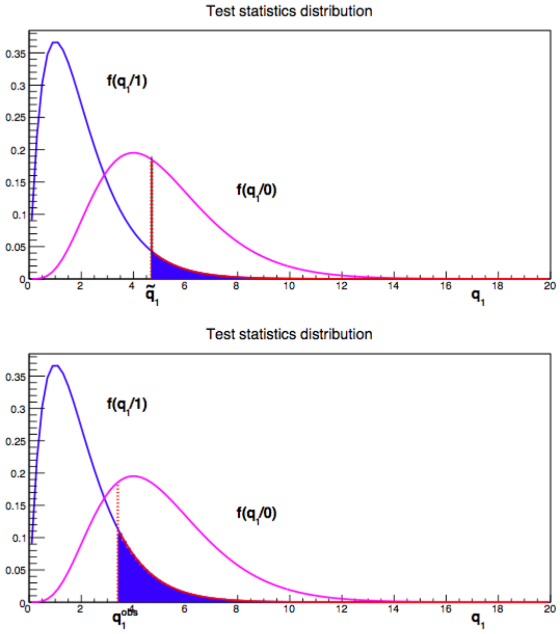

FIGURE 4.33: Construction of the CL^{exp}_{s+b} (upper plot) and CL^{obs}_{s+b} (lower plot). In both cases the CL_{s+b} is given by the blue area.

function (essentially the average outcome for a background-only experiment), the so-called CL^{exp}_{s+b} can be calculated as:

$$CL^{\text{exp}}_{s+b} = \int_{\tilde{q}_1}^{\infty} f(q_1 \mid 1)\, dq_1 \tag{4.10}$$

This represents the median CL at which the experiment can exclude the signal with $\mu = 1$ in a background-only scenario. A smaller expected CL obtained this way implies a better capability of the experiment to exclude the signal.

By calculating q_1^{obs} with the observed data, the observed exclusion CL is determined by:

$$CL^{\text{obs}}_{s+b} = \int_{q_1^{\text{obs}}}^{\infty} f(q_1 \mid 1)\, dq_1 \tag{4.11}$$

Figure 4.33 illustrates the construction of CL^{exp}_{s+b} and CL^{obs}_{s+b}.

The method commonly used for setting exclusion limits for new physics signals is the "modified frequentist approach," CL_s [128]. This approach is more conservative compared to CL_{s+b} and is adopted to prevent the exclusion of signals due to underfluctuations of the background. The CL_b can be defined as:

$$CL_b^{\text{obs}} = \int_{q_1^{\text{obs}}}^{\infty} f(q_1 \mid 0)\, dq_1 \tag{4.12}$$

If the background experiences an underfluctuation, both CL_{s+b} and CL_b can be small. This implies that q_1^{obs} is inconsistent not only with the signal plus background hypothesis but also with the background-only hypothesis. In such cases, the CL_s method is utilized to avoid unwarranted exclusion. It employs CL_s as the CL:

$$CL_s = \frac{CL_{s+b}}{CL_b} \tag{4.13}$$

CL_s is always greater than CL_{s+b}, making it a conservative choice. This approach makes it more difficult to exclude potential signals. If CL_s is less than 5%, the observed data can exclude the signal with $\mu = 1$ at 95% CL. In searches for new physics, exclusion limits are typically set on the signal strength μ (or on the cross section), rather than simply determining whether a signal with a given cross section and $\mu = 1$ is excluded or not. The test statistics q_μ is a function of μ. For each value of μ, the analysis for the case $\mu = 1$ demonstrated above can be repeated to ascertain the value of $\mu = \mu^*$ for which CL_s equals 5%. By increasing μ, $CL_s(\mu)$ decreases. Thus, μ^* signifies the upper limit on μ, indicating that a signal with $\mu \geq \mu^*$ can be excluded at the 95% CL.

4.15 Fit Model for $HH \to b\bar{b}\tau^+\tau^-$

The analysis $HH \to b\bar{b}\tau^+\tau^-$ events involves a simultaneous binned maximum-likelihood fit to the output distributions of the MVA over all event categories: $\tau_{\text{had}}\tau_{\text{had}}$ and $\tau_{\text{lep}}\tau_{\text{had}}$ as summarised in table 4.13. Additionally, it includes fitting to the m_{ll} distribution in the Z+Heavy Flavor Control Region (Z+HF CR) as outlined in Section 4.6 and Section 4.7.

	low-m_{HH} SR	high-m_{HH} SR	VBF SR	Inclusive
$\tau_{\text{had}}\tau_{\text{had}}$	BDT	BDT	BDT	-
$\tau_{\text{lep}}\tau_{\text{had}}$ SLT	BDT	BDT	BDT	-
$\tau_{\text{lep}}\tau_{\text{had}}$ LTT	BDT	BDT	BDT	-
$Z+$HF CR	-	-	-	m_{ll}

TABLE 4.13: Regions entering the fit and fitted observable in each analysis region and channel.

The likelihood function for the analysis can be expressed as:

$$\mathcal{L}(\boldsymbol{\mu}, \boldsymbol{\theta}; \text{data}) = \prod_{c=1}^{N_{\text{cats}}} \mathcal{L}_c(\boldsymbol{\mu}, \boldsymbol{\theta}; \text{data}) \prod_{k \in \text{constraint NPs}} f_k(\theta_k) \tag{4.14}$$

Here, $\boldsymbol{\mu}$ and $\boldsymbol{\theta}$ are vectors representing the parameters of interest (POIs) and nuisance parameters (NPs) respectively. N_{cats} signifies the number of analysis categories. The term $\mathcal{L}_c$ refers to the likelihood function for category c. Certain categories of NPs are subject to external constraints denoted by f_k.

The POIs are the parameters targeted for measurement, such as the signal strength denoted as μ, or coupling modifiers like κ_λ and κ_{2V}. The fit model encompasses NPs, some of which are solely determined from data and are referred to as unconstrained. Other parameters are constrained using information from auxiliary measurements in addition to the data. These parameters, known as constrained, quantify the impact of systematic uncertainties on the measurement.

In each category, the likelihood is represented in binned form as the product of Poisson distributions, one for each analysis bin:

$$\mathcal{L}_c(\boldsymbol{\mu}, \boldsymbol{\theta}; \text{data}) = \prod_{i=1}^{n_{\text{bins}}} P\left(\sum_s N^c_{\boldsymbol{H}_s}(\boldsymbol{\mu}) + \sum_b N^c_{\boldsymbol{B}_b}, n_i\right) \tag{4.15}$$

Here, n_i denotes the observed number of data events in each bin, and $\sum_s N^c_{H_s}(\boldsymbol{\mu}) + \sum_b N^c_{B_b}$ represents the combined signal and background yields.

The evaluation of the POIs is conducted using a statistical test relying on the profile likelihood ratio:

$$\Lambda(\mu) = \frac{L(\mu, \hat{\hat{\theta}}(\mu))}{L(\hat{\mu}, \hat{\theta})} \tag{4.16}$$

In the numerator, the NPs are set to their profiled values $\hat{\hat{\theta}}$, which conditionally maximize the likelihood function for fixed values of POIs μ. In the denominator, both the POIs and NPs are set to their best-fit values $\hat{\mu}$ and $\hat{\theta}$ respectively, which maximize the likelihood without any conditions. In the asymptotic regime, where the likelihood approximately follows a Gaussian distribution, the value of $-2\ln\Lambda(\mu)$ conforms to a χ^2 distribution with degrees of freedom equal to the dimensionality of the vector μ.

4.15.1 Binning

The MVA output score distributions are initially constructed with a fine binning scheme and are subsequently rebinned to create the fit templates. The aim is to strike a balance between reducing the number of bins, maximizing the retained expected sensitivity, and ensuring the stability and validity of the fit, especially in the context of the asymptotic approximation. The same rebinning algorithm, known as Trafo60, is utilized for both $\tau_{\text{lep}}\,\tau_{\text{had}}$ and $\tau_{\text{had}}\,\tau_{\text{had}}$ channels.

All BDT score histograms are constructed with 2090 bins using a non-uniform binning strategy. The scores are distributed from -1 to 0.990 with a bin width of 10^{-3} (1990 bins). For the range from 0.990 to 1, an even finer bin width of 10^{-4} is employed (100 bins), capturing the most signal-like scores.

The rebinning process commences with these finely binned histograms. Bins are iteratively merged, starting from the most signal-like MVA bins, until specific criteria are met.

In this analysis, the following general function is used to transform the BDT output histograms:

$$Z(I[k,l]) = Z\left(z_s, n_s(I[k,l]), N_s, z_b, n_b(I[k,l]), N_b\right)$$

where:

- $I[k,l]$ represents an interval of histograms, encompassing bins from k to l.
- N_s and N_b denote the total number of signal and background events in the histogram, respectively.
- $n_s(I[k,l])$ and $n_b(I[k,l])$ stand for the total number of signal and background events in the interval $I[k,l]$.
- z_s and z_b are parameters utilized to fine-tune the algorithm.

For this analysis, the function takes the form:

$$Z = z_s \frac{n_s}{N_s} + z_b \frac{n_b}{N_b}$$

Here, the values $(z_s, z_b) = (10, 5)$ have been chosen for the BDT in all analysis regions. The higher value for z_s compared to z_b facilitates finer binning in the high BDT output score regime, which exhibits a very high signal-to-background ratio.

The rebinning process begins with the rightmost bin (high-BDT score) of the original histogram. Bins are progressively added from right to left, expanding the range of the interval $I[k,$ last], and Z is recalculated at each step. Once $Z\left(I\left[k_0\,, \text{last}\,\right]\right) > 1$, all bins in the interval $I\left[k_0\,, \text{last}\,\right]$ are merged into a single bin. In this context, "last" refers to the rightmost bin of the original histogram in the first iteration. After each iteration, the "last" bin is the rightmost one, excluding any newly formed bins from previous iterations.

Additionally, two further criteria are enforced after each iteration, and the above steps are repeated until these conditions are met:

- The MC statistical uncertainty on the sum of backgrounds in each bin is required to be less than 20%.

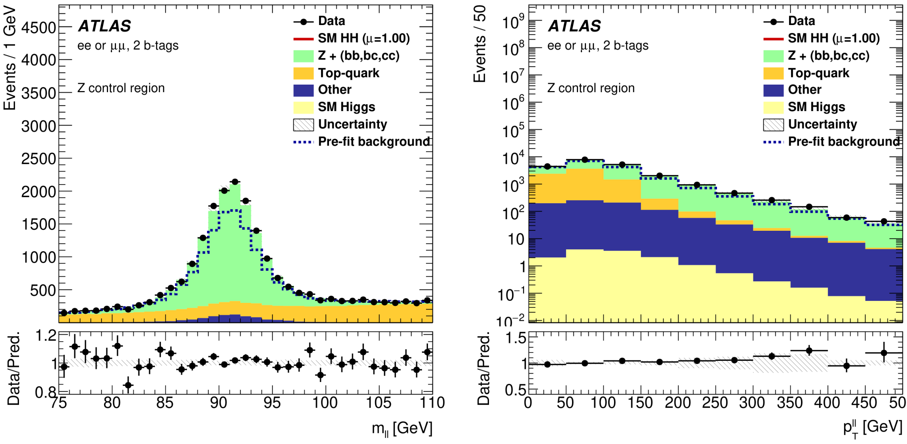

(A) (B)

FIGURE 4.34: Post-fit modelling of the di-lepton invariant mass (a) and p_T (b) distribution in the CR. In both cases the NP extracted from the fit to m_{ll} are used.

- Each bin must contain an expected number of background events greater than 3.

4.15.2 Z+HF CR fit

The modelling of the $Z + HF$ background in the CR defined in section 4.7 is validated through a fit to data in the CR, with the SRs still blinded. This also results in a more accurate estimate of the $Z +$ HF normalisation factor.

The default fit configuration as defined in previous sections, has floating normalisation factors for $Z+$HF and $t\bar{t}$ processes and no normalisation uncertainties originating from modelling for the two samples, since they are implemented as extrapolation uncertainties in the various signal regions.

Figure 4.34 shows the post-fit distributions of the m_{ll} and p_{T}^{ll} after a fit to the m_{ll} distribution; a good description of the data is achieved for the Zp_{T} variable.

Chapter 5

Results and Future Prospects

In Chapter 4, the main analysis strategy is explained in detail. While in this chapter, the main analysis results will be presented. As already explained in Section 4.6, the analysis events are categorized into three main channels, i.e., $bb\tau_{\text{had}}\tau_{\text{had}}$ and $bb\tau_{\text{lep}}\tau_{\text{had}}$-SLT and $bb\tau_{\text{lep}}\tau_{\text{had}}$-LTT, followed by further categorization into ggF and VBF. Thus, in this chapter, the results will be presented first for the individual channels and then combined results for all the channels.

The findings will encompass setting limits on both observed and expected signal strengths (μ_{ggF} and μ_{VBF}), as well as constraining the Higgs self-coupling ($\kappa_\lambda = \lambda_{HHH}/\lambda_{HHH}^{SM}$) and the coupling constants between two vector bosons and two Higgs bosons ($\kappa_{2V} = g_{HHVV}/g_{HHVV}^{SM}$). Additionally, this chapter will provide insights into potential future research directions.

5.1 $bb\tau_{\text{lep}}\tau_{\text{had}}$ channel results

In this section SM production HH productions, κ_λ and κ_{2V} postfit results will be described. The postfit results will be compared with the expected numbers. The expected results are estimated by performing fit for the “Asimov” dataset. Asimov is a dataset in which all observed quantities are set equal to their expected values. The τ_{lep} τ_{had} fit includes the τ_{lep} τ_{had} SLT and LTT signal regions and the $\text{Z} + \text{HF}$ control region.

The $bb\tau_{\text{lep}}\tau_{\text{had}}$ post-fit expected[1] and observed limits for the SM pair production of Higgs bosons are documented in table 5.1. These numbers shows the 95% CL expected and observed upper limits on the HH signal strength (ggF+VBF), as well as separately for each production mode for the $\tau_{\text{lep}}\tau_{\text{had}}$ channels and their combination.

		μ_{HH}	μ_{ggF}	μ_{VBF}
$\tau_{\text{lep}}\tau_{\text{had}}$ SLT	Observed	16.4	16.9	133
	Expected	6.4	6.6	128
$\tau_{\text{lep}}\tau_{\text{had}}$ LTT	Observed	22	18	767
	Expected	20	21	323
$\tau_{\text{lep}}\tau_{\text{had}}$	Observed	16.0	15.9	213
	Expected	$5.98^{+2.3}_{-1.7}$	$6.04^{+2.3}_{-1.6}$	$112^{+43.9}_{-31.3}$

TABLE 5.1: Observed and expected 95% CL limits on the HH signal strength (ggF+VBF), as well as separately for each production mode in the $\tau_{\text{lep}}\tau_{\text{had}}$ channel.

The results summarised in table 5.1 indicates that for the SLT channel of the $\tau_{\text{lep}}\tau_{\text{had}}$ analysis, the difference between observed and expect limit on μ_{HH} is larger compare to LTT results. This is expected due to the fact that an excess is noted with respect to the SM hypothesis (μ_{HH} = 1) at 2.3 σ from the individual fit of the $\tau_{\text{lep}}\tau_{\text{had}}$ SLT SR. This effect can also be visualised in the figure 5.1b. Similar behaviour (large difference in the expected and observed limit for the LTT μ_{VBF}) can be noted. This is arising due to an access (significance of 2-sigma) in the VBFSR as shown in figure 5.1f.

Table 5.2 displays the predicted 95%CL intervals for κ_λ (κ_{2V}) values based on the negative log-likelihoods (NLL) calculated as a function of κ_λ (κ_{2V}). The NLL calculations were performed assuming the standard model (SM) hypothesis for HH production. Figure 5.2 illustrates the expected and observed profiles of the

---

[1] The expected upper limits for the separate production mode signal strengths are derived by assuming background only hypothesis

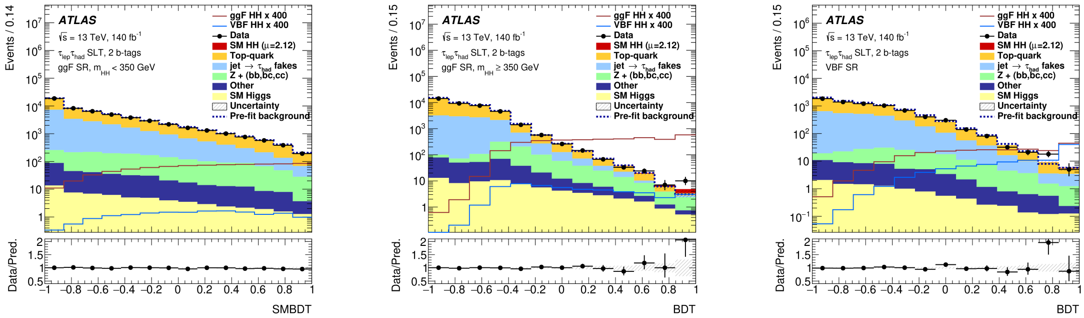

(A) SLT BDT score in the low-m_{HH}

(B) SLT BDT score in the high-m_{HH}

(C) SLT BDT score in theVBFSR

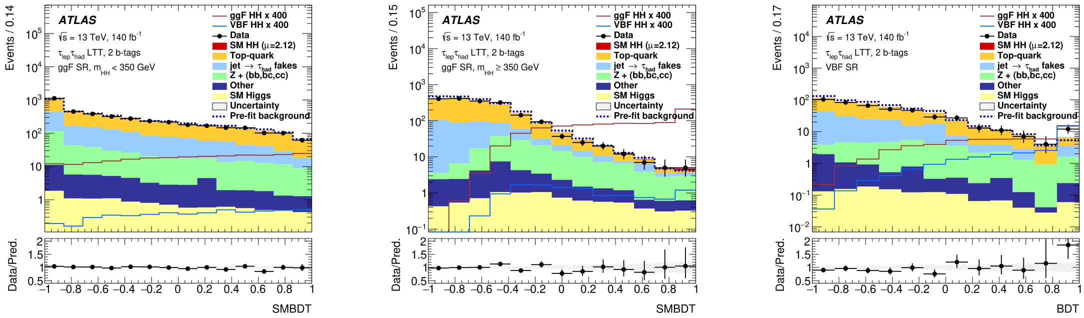

(D) LTT BDT score in the low-m_{HH}

(E) LTT BDT score in the low-m_{HH}

(F) LTT BDT score in the VBFSR

FIGURE 5.1: The plots display distributions obtained from a combined fit to the data, assuming the Standard Model hypothesis. The ggF and VBF signal distributions are superimposed and scaled up by a factor of 400 compared to the SM expectation. The dashed histograms represent the total background before the fit. The lower panels illustrate the ratio of data to the total sum of signal and background after the fit, with hatched bands indicating the associated statistical and systematic uncertainties. To enhance clarity in the viewing, these histograms employ uniform bin widths, although their contents correspond to those utilized in the fit as mentioned in the section 4.15.1.

	95% CI for κ_λ	95% CI for κ_{2V}
Observed LTT	[-9.04,16.32]	[-4.88,0.04],[2.27,7.16]
Observed SLT	[-8.29,0.90],[7.53,14.37]	[-1.28,3.47]
Observed $\tau_{\text{lep}}\tau_{\text{had}}$	[-7.87,0.29],[8.01,13.92]	[-1.54,3.71]
Expected LTT	[-8.74,15.82]	[-2.86,5.14]
Expected SLT	[-5.01,12.37]	[-0.67,2.85]
Expected $\tau_{\text{lep}}\tau_{\text{had}}$	[-4.67,11.87]	[-0.64,2.83]

TABLE 5.2: Observed and expected 95% CL intervals for κ_λ and κ_{2V} in the $\tau_{\text{lep}}\tau_{\text{had}}$ channel.

NLL as functions of κ_λ and κ_{2V}, respectively. These profiles are shown separately for each of the two $\tau_{\text{lep}}\tau_{\text{had}}$ channels, as well as for their combined results. In terms of expected sensitivity, the SLT channels exhibit the highest impact.

For the SLT channel, the observed profile for κ_λ reaches a minimum around -5. This is primarily influenced by an excess observed in the high $\mathrm{m_{HH}}$ region, indicating a preference for parameters that increase the signal contribution. Conversely, positive values of κ_λ with equivalent cross section are less favored due to the absence of an excess in the low $\mathrm{m_{HH}}$ region. Regarding κ_λ, the combined $\tau_{\text{lep}}\tau_{\text{had}}$ result is also predominantly influenced by the SLT channel.

As for κ_{2V}, the profile from the LTT channel indicates a deviation from the Standard Model hypothesis at a significance of 2-sigma, driven by an excess observed in the VBF SR. In contrast, the SLT channel does not exhibit a similar excess, resulting in a best-fit value that is compatible with the Standard Model within approximately 1-sigma.

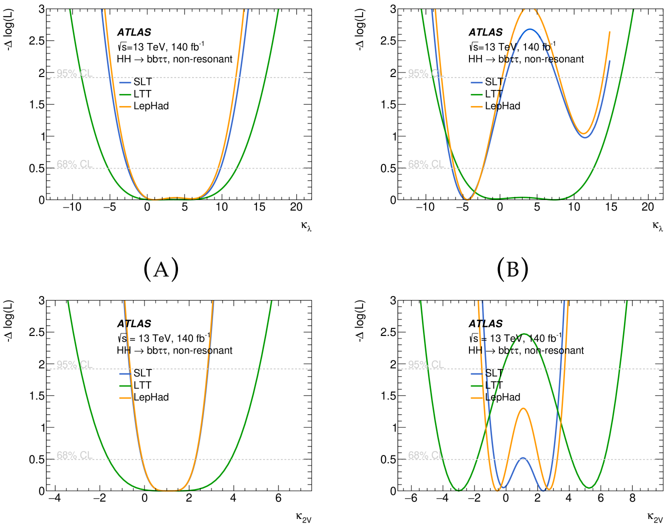

(A)

(B)

(C)

(D)

FIGURE 5.2: The negative logarithm of the likelihood ratio, comparing various hypotheses for κ_λ (top) and κ_{2V} (bottom) to an Asimov dataset (left) and actual data (right). The curves are presented for both individual $\tau_{\mathrm{lep}}\,\tau_{\mathrm{had}}$ channels and their combined results.

5.2 $bb\tau_{\mathrm{had}}\tau_{\mathrm{had}}$ channel results

Table 5.3 shows the 95% CL observed and expected upper limits on the HH signal strength (ggF+VBF), as well as separately for each production mode, obtained from either a one-dimensional fit of μ_{ggF} (μ_{VBF}) while fixing the other signal strength to 1, or a simultaneous 2D fit of μ_{ggF} and μ_{VBF}[44], in the $\tau_{\mathrm{had}}\,\tau_{\mathrm{had}}$ channel. Table 5.4 reports the observed and expected 95% CL intervals of κ_λ (κ_{2V}) values, determined by the negative log-likelihoods (NLL) as a function of κ_λ (κ_{2V}). The NLL results are evaluated under the SM HH production hypothesis.

Figure 5.3 shows the postfit distributions for the $bb\tau_{\mathrm{had}}\tau_{\mathrm{had}}$ channel. From the figure we can see that how the fit make the data to MC comparison better.

	μ_{HH}	μ_{ggF}	μ_{VBF}
$\tau_{\mathrm{had}}\tau_{\mathrm{had}}$	observed	3.4	3.6
	expected	3.9	4.0

TABLE 5.3: Observed and expected 95% CL limits on the HH signal strength (ggF+VBF), as well as separately for each production mode in the $\tau_{\mathrm{had}}\tau_{\mathrm{had}}$ channel.

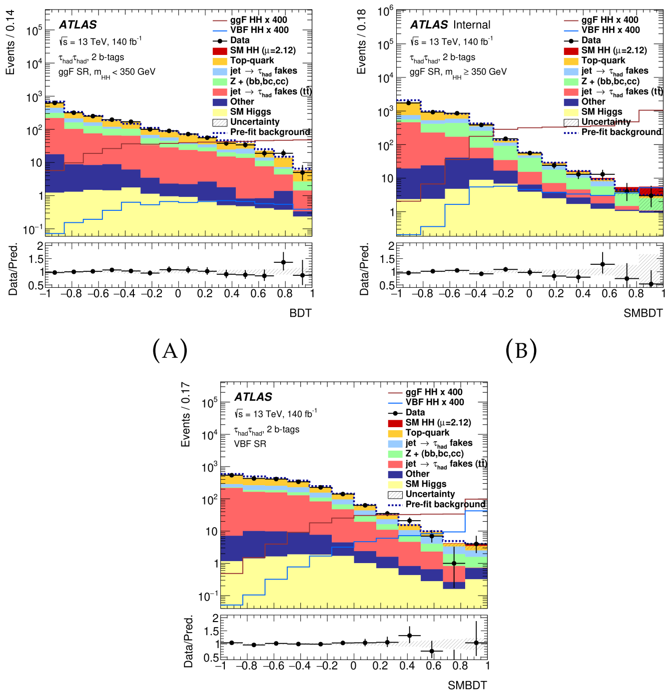

(A)

(B)

(C)

FIGURE 5.3: The figure displays post-fit BDT distributions for the $\tau_{\text{had}}\tau_{\text{had}}$ channel following a combined fit to data under the Standard Model assumption. The ggF and VBF signal distributions are superimposed and scaled to 400 times the SM expectation. Dashed histograms represent the total pre-fit background. The lower panels depict the data-to-total post-fit signal and background ratio, with hatched bands indicating the associated statistical and systematic uncertainties. To enhance visualization, the histograms utilize uniform bin widths rather than the bin edges employed in the fit, while maintaining the same bin contents.

	95% CI for κ_λ	95% CI for κ_{2V}
Observed	[-1.46,7.97]	[-0.22,2.40]
Expected	[-2.76,9.44]	[-0.41,2.59]

TABLE 5.4: Observed and expected 95% CL intervals for κ_λ and κ_{2V} in the $\tau_{\text{had}}\tau_{\text{had}}$ channel.

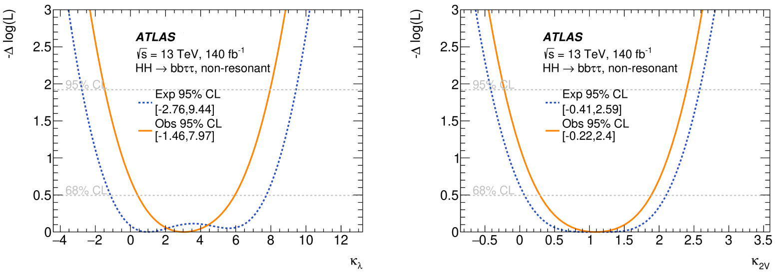

(A)

(B)

FIGURE 5.4: Negative logarithm of the likelihood ratio comparing different κ_λ (a) and κ_{2V} (b) hypotheses for the fit to data and Asimov dataset constructed under the SM hypothesis in the $\tau_{\text{had}}\,\tau_{\text{had}}$ channel.

Figure 5.4 illustrates the anticipated and observed likelihood scans for the κ_λ and κ_{2V} parameters. In the fit involving κ_λ (κ_{2V}), all other couplings impacting both single-Higgs and di-Higgs production, including κ_{2V} (κ_λ), are fixed at their Standard Model predictions. Notably, when fitting the data, stronger constraints are obtained for both parameters compared to what was initially expected. This is attributed to the presence of fitted negative signal strengths. Specifically, for κ_λ, the scan converges towards the point with the minimum cross section, as the predictions for HH cannot be zero for any value of the parameter.

5.3 Combined Results for $b\bar{b}\tau^+\tau^-$ analysis

In this section, we present the results for the $b\bar{b}\tau^+\tau^-$ channel based on the analysis of the BDT score distributions in the 9 orthogonal categories. These distributions are depicted in Figures 5.1 and 5.3, following a maximum likelihood fit to the $L(\mu_{HH}, \theta)$ function.

The observed data aligns well with the predicted values within the assessed uncertainties. The maximum likelihood estimator for the total HH production signal strength, denoted as $\hat{\mu}_{HH}$, is determined to be 2.2 ± 1.7 through the combined fit to the data. This estimate encompasses both statistical and systematic uncertainties, obtained by varying the log-likelihood based test statistics Λ by one unit.

Furthermore, the maximum likelihood estimators for the unconstrained normalization factors of the $t\bar{t}$ and $Z+$ heavy-flavor backgrounds are found to be 0.96 ± 0.03 and 1.34 ± 0.08, respectively, following the combined fit to the data.

An observed 95% confidence level (CL) upper limit of 5.9 is set on μ_{HH}, compared to an expected limit of 3.1 in the background-only hypothesis ($\mu_{HH} = 0$).

Additionally, by simultaneously fitting μ_{ggF} and μ_{VBF}, observed (expected) upper limits of 5.8 (3.2) and 91 (72) are established for each production mode, assuming that the signal strength parameters can vary independently.

In scenarios where either μ_{VBF} or μ_{ggF} is fixed to the Standard Model prediction, the observed (expected) upper limits are set at 5.8 (3.2) and 94 (71), respectively.

Table 5.5 provides a summary of the signal strength upper limits, both individually for each signal region (SR) and from the combined fit. The results for the individual channels are derived from the combined likelihood fit of the BDT score distribution in a single SR, along with the $m_{\ell\ell}$ distribution from the dedicated control region (CR).

Notably, the observed limit on μ_{HH} from the combined fit is slightly more conservative than the expected limit due to an excess observed in the $\tau_{\text{lep}}\tau_{\text{had}}$ SLT SR, particularly in the high-m_{HH} category. The local significance of this excess is calculated to be 2.3σ with respect to the SM hypothesis ($\mu_{HH} = 1$), based on the individual fit of the $\tau_{\text{lep}}\tau_{\text{had}}$ SLT SR.

In Figure 5 the observed and expected values of $-\Delta \log(L)$ are plotted against the coupling strength modifiers κ_λ and κ_{2V}. These plots assume that all other coupling modifiers are at their SM predictions. The combined fit allows us to establish observed (expected) 95% confidence intervals for κ_λ in the range of $[-3.2, 9.1]$ ($[-2.4, 9.2]$) when assuming $\kappa_{2V} = 1$), and for κ_{2V} in the range of $[-0.5, 2.7]$ ($[-0.2, 2.4]$) when assuming $\kappa_\lambda = 1$). Further constraints are imposed on κ_λ and κ_{2V} when considering the possibility of both coupling strength modifiers varying simultaneously.

		μ_{HH}	μ_{ggF}	μ_{VBF}
$\tau_{\mathrm{had}}\,\tau_{\mathrm{had}}$	observed	3.4	3.6	87
	expected	3.9	4.0	103
$\tau_{\mathrm{lep}}\,\tau_{\mathrm{had}}$ SLT	observed	16.4	16.9	133
	expected	6.4	6.6	128
$\tau_{\mathrm{lep}}\,\tau_{\mathrm{had}}$ LTT	observed	22	18	767
	expected	20	21	323
Combined	observed	5.9	5.8	91
	expected	$3.1^{+2.8}_{-1.4}$	$3.2^{+2.8}_{-1.5}$	72^{+63}_{-33}

TABLE 5.5: This table presents the observed and expected 95% confidence level upper limits for μ_{HH}, μ_{ggF}, and μ_{VBF} obtained from individual likelihood fits in different channels, along with the combined results. The limits for μ_{ggF} and μ_{VBF} are provided both from a simultaneous fit of both signal strengths and from independent fits for single production modes. The uncertainties associated with the combined expected upper limits are represented by a 2σ uncertainty band.

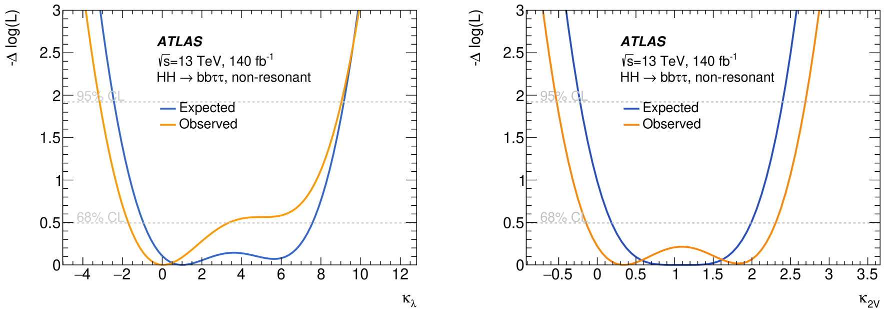

(A)

(B)

FIGURE 5.5: The plots display the values of $-\Delta\log(L)$ for various κ_λ (a) and κ_{2V} (b) hypotheses. The results are derived from fits to both the observed data (shown in orange) and an Asimov dataset (depicted as dashed blue lines) generated under the assumption of the Standard Model hypothesis. For each scenario, all coupling modifiers except the parameter being scanned are held at their SM values.

5.4 Future prospects of the Analysis

The analysis of $HH \rightarrow b\bar{b}\tau^+\tau^-$ stands out as a particularly promising channel within the broader field of HH studies, as highlighted in the previously published paper [129] in combination with other HH searches ($b\bar{b}b\bar{b}$, $b\bar{b}\gamma\gamma$) in ATLAS. Looking ahead to Run 3 of the LHC, there is substantial interest in delving deeper into the $b\bar{b}\tau^+\tau^-$ final state in the context of both resonant and non-resonant searches. In a prior publication addressing both resonant and non-resonant searches [11], in which the authors has also made a significant contributions observed an excess in the resonant search at a resonance mass of 1TeV, yielding a local (global) significance of 3.1 σ (2.0 σ), as depicted in Figure 5.6.

Building upon this groundwork, future analyses could exploit the combined dataset from both LHC Run 2 and Run 3 and capitalizing on enhanced reconstruction techniques for example better τ-had identification, novel strategies to mitigate fake backgrounds, and more accurate estimation methods. Analytical techniques could also be improved by re-optimizing MVA techniques, such as investigating the GNN approach [130] etc. This integrated strategy holds significant promise for unearthing further insights into the behavior of Higgs boson pairs, thereby advancing our understanding of the underlying physics.

Furthermore, looking forward, the exploration of Higgs pair production remains a compelling area of investigation, especially with the forthcoming High-Luminosity LHC (HL-LHC) era. Preliminary results indicate the projected sensitivity to non-resonant Higgs boson pair production in the $b\bar{b}\tau^+\tau^-$ final state, using the ATLAS detector at the HL-LHC [131]. This study assumes 3000 fb^{-1} of proton-proton collisions at a center-of-mass energy of 14 TeV. The estimated 95% confidence level upper limit on the SMl Higgs boson pair production rate, with and without systematic uncertainties, is 0.71 and 0.49 times the SMl expectation, respectively, concerning the background-only hypothesis. This yields a signal significance of 2.8σ and 4.0σ, respectively. Assuming Standard Model

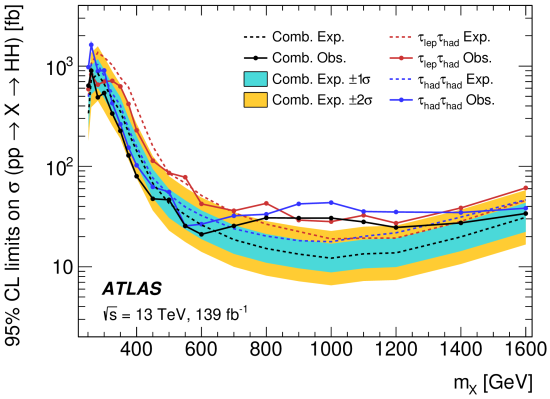

FIGURE 5.6: Limits at the 95% confidence level (CL) on the cross-section for resonant HH production are presented as a function of the scalar resonance mass m_X. The dashed lines represent the limits from each individual channel. The combined limits from both channels are represented by the black lines. The turquoise and yellow bands correspond to the $\pm 1\sigma$ and $\pm 2\sigma$ variations around the expected combined limit, respectively. These limits are determined using the profile-likelihood test statistic along with the modified frequentist CLs technique [11].

couplings, the modifier κ_λ self-coupling is estimated to be constrained to the 1σ confidence interval [0.3, 1.9] ∪ [5.2, 6.7]. In the absence of a Higgs boson pair production signal, values of κ_λ [1.7, 5.4] ([2.4, 4.5]) are projected to be excluded at the 95% confidence level.

Chapter 6

ATLAS upgrade for HL-LHC: Performance evaluation of Low Gain Avalanche Diodes for the High Granularity Timing Detector

6.1 The High Luminosity upgrade program for LHC

The upcoming high luminosity LHC (HL-LHC) physics program holds great promise for researchers in the field. The upgraded accelerator is poised to deliver an unprecedented integrated luminosity of approximately 3000fb^{-1} over a span of 10 years to the ATLAS and CMS detectors. This extended operational period will empower scientists to delve even deeper into the quest for new physics and gain a more comprehensive grasp of the particle physics searches for example Higgs boson's properties [9]. The new phase of the LHC will incorporate various cutting-edge technologies, which are depicted and summarized in Fig. 6.1.

Yet, alongside this groundbreaking proton-proton luminosity comes fresh experimental hurdles. The experiments will need to contend with the aging of the existing detectors in a radiation-intensive environment. Additionally, they must

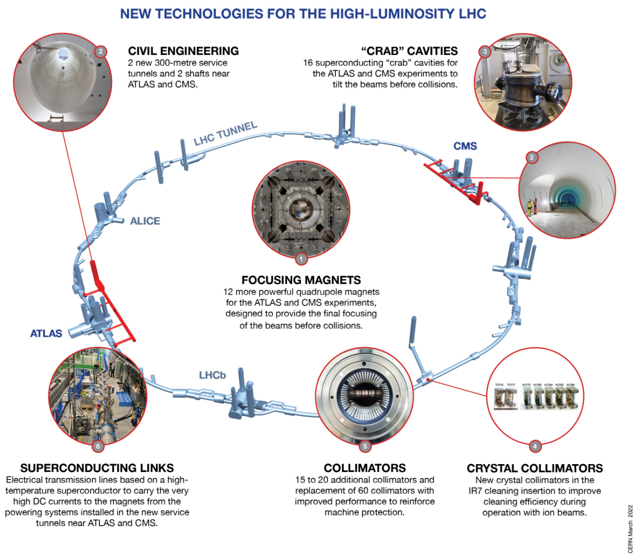

FIGURE 6.1: The LHC/HL-LHC project schedule (updated in February 2022).

develop innovative techniques to accurately isolate and measure the outcomes of the most intriguing collisions. Tackling these challenges demands a wealth of expertise and proficiency from the dedicated researchers and engineers driving the project forward. However, the potential payoffs are monumental in terms of advancing our comprehension of the universe and the fundamental principles governing it. The most recent HL-LHC schedule is shown in figure 6.2.

FIGURE 6.2: The LHC/HL-LHC project schedule (updated in February 2022).

6.2 The Next Phase: ATLAS Upgrade with High-Granularity Timing Detector

6.2.1 Preparing ATLAS for the future – The ATLAS phase 2 upgrade

For the ATLAS detector to operate effectively under the increased luminosity of 5-8 times and to fully exploit on the benefits of the HL-LHC upgrade, several critical issues must be addressed. This significant overhaul, scheduled for 2026-2028 during the LHC Long Shutdown 3 (LS3), is referred to as "the phase 2 upgrade."

The challenges and considerations for the ATLAS upgrade encompass:

- The trigger and data acquisition system, necessitating accommodation for higher trigger rates.
- The tracking system, involving the transition from the gas-based TRT outer tracker to a full silicon version. This upgrade aims to enhance event recording rates and improve background rejection.
- The luminosity measurement system, aimed at achieving precise measurements as detailed in Chapter 1, Section 2.
- The muon spectrometer, targeting improvements in efficiency, resolution, isolation and coverage.
- The development of strategies to effectively reject significantly higher pile-up contributions during high luminosity operation, as illustrated in Fig. 2.9.

Corresponding projects have been proposed and scheduled, including the Inner Tracker (ITk) Pixel [133] and Strip [8], the Liquid Argon Calorimeter

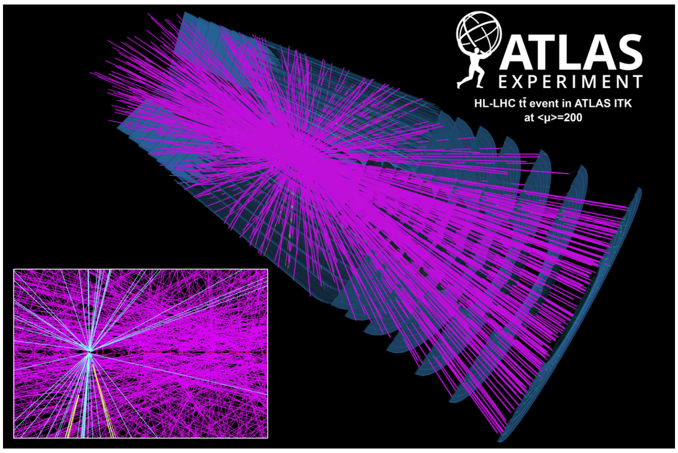

FIGURE 6.3: In the HL-LHC phase, a simulated $t\bar{t}$ event was generated under conditions of an average pile-up of 200 collisions per bunch crossing at the ATLAS detector [132].

(LAr) [134], the Tile Calorimeter [135], the High-Granularity Timing Detector (HGTD) [136], the Muon Spectrometer [137], and the Trigger and Data Acquisition (TDAQ) [138]. This thesis primarily focuses on the HGTD upgrade, which introduces innovative silicon detector technology and introduces the concept of 4-D tracking (depicted in Fig. 6.4) with a precision of 30 ps, marking a significant milestone in particle experimentation.

6.2.2 The High-Granularity Timing Detector (HGTD) in ATLAS Phase 2

The HGTD is a proposed component [136], [139] for the ATLAS experiment, slated for integration in the phase 2 upgrade in preparation for the HL-LHC, set to commence operations in 2029. Operating at significantly higher luminosity, the HL-LHC will yield a substantial increase in collision rates. The HGTD has been engineered to manage this heightened collision rate by providing precise timing measurements.

One of the primary functions of the HGTD is to address the challenge of pile-up, which refers to the occurrence of multiple proton-proton collisions within the same bunch crossing. This phenomenon complicates the differentiation of

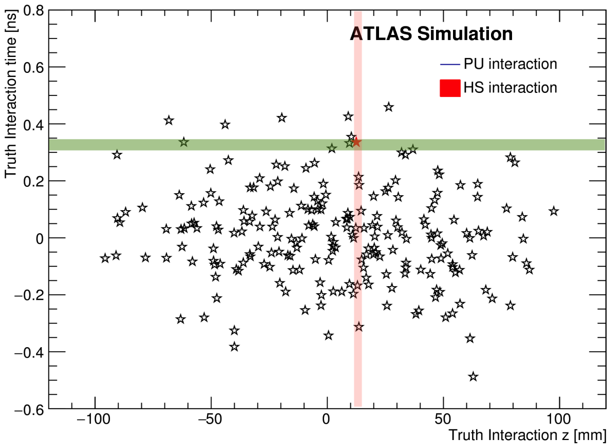

FIGURE 6.4: This figure depicts simulated interaction distributions along both the Spatial axis (aligned with the LHC beam line) and Timing axis (measured from the central time of the bunch crossing) for a single HL-LHC bunch crossing. Approximately 200 pile-up interaction vertices are indicated by stars. These pile-up vertices are denoted in black. A single hard scattering vertex is marked by a red star. The red band represents the nominal Inner Tracker (ITk) resolution in the forward region (2mm) for soft particles in the spatial direction, while the green band corresponds to the expected time resolution of the High-Granularity Timing Detector (HGTD) (50 ps) in the timing direction. (Figure adapted from [136]).

particles produced in each collision. The HGTD's remarkable timing resolution enables the separation of signals from distinct collisions, thereby mitigating the impact of pile-up on ATLAS measurements through the implementation of 4-D tracking. As illustrated in Fig. 6.4, the precise timing data furnished by the HGTD greatly facilitates the isolation of the hard-scattering vertex, which serves as our signal candidate.

In addition to its timing capabilities, the HGTD will supply supplementary tracking information, enhancing the identification of particle types and the reconstruction of particle trajectories when paired with the inner tracker. The HGTD system comprises two sealed vessels, each housing two instrumented double-sided layers affixed to cooling and support disks. These layers employ Low Gain Avalanche Detectors (LGAD) sensor technology, utilizing silicon sensors with moderate gain to enhance timing performance. Positioned in the gap region between the barrel and end-cap calorimeters (as depicted in Fig. 6.5), approximately ±3.5m from the nominal interaction point, the HGTD spans a pseudo-rapidity range from 2.4 to 4.0.

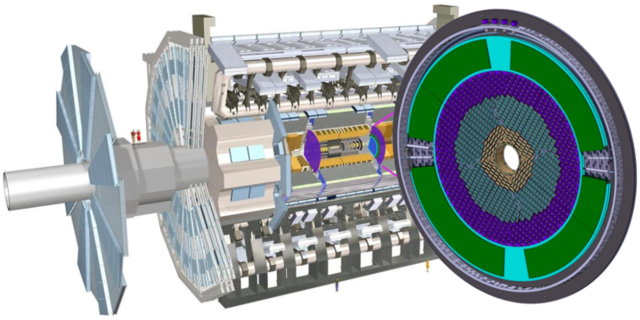

FIGURE 6.5: HGTD position in the ATLAS at the HL-LHC[136].

Figure 6.6 offers an encompassing portrayal of the key components constituting the HGTD for integration onto each of the end-cap calorimeters. These elements encompass the hermetic vessel, inclusive of its front and rear covers, as well as inner and outer rings. Complementing this, the assembly includes two instrumented double-sided layers securely positioned within cooling disks, featuring sensors on both the front and back faces. Moreover, the setup incorporates two moderator components strategically placed internally and externally to the hermetic vessel. This comprehensive arrangement is pivotal in ensuring the precise and effective operation of the HGTD for accurate timing measurements.

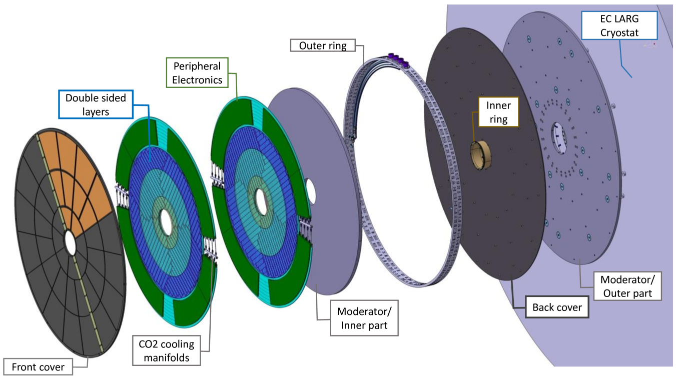

FIGURE 6.6: HGTD system composition [136].

The HGTD will measure the arrival times of minimum-ionizing particles with an average time resolution of approximately 30 ps per track at the onset of HL-LHC operations. Towards the conclusion of the HL-LHC operation, the time resolution is anticipated to be slightly degraded to 50 ps.

Regarding the HGTD's layout of LGAD sensors (outlined in Table 6.1), each sensor features an active area measuring 19.5mm × 19.5 mm, resulting in a total of 16,064 sensors covering the entire HGTD area, with a 15 × 15 pixel array on each sensor.

Pseudo-rapidity coverage	$2.4 < \lvert\eta\rvert < 4.0$
Thickness in z	$75\ \mathrm{mm}(+50\ \mathrm{mm}$ moderator)
Position of active layers in z	$\pm 3.5\ \mathrm{m}$
Weight per end-cap	$350\ \mathrm{kg}$
Radial extension:	
Total	$110\ \mathrm{mm} < r < 1000\ \mathrm{mm}$
Active area	$120\ \mathrm{mm} < r < 640\ \mathrm{mm}$
Pad size	$1.3\ \mathrm{mm} \times 1.3\ \mathrm{mm}$
Active sensor thickness	$50\mu\mathrm{m}$
Number of channels	$3.6\mathrm{M}$
Active area	$6.4\ \mathrm{m}^2$
Module size	$30 \times 15\mathrm{pads}(4\ \mathrm{cm} \times 2\ \mathrm{cm})$
Modules	8032
Collected charge per hit	$> 4.0\mathrm{fC}$
Average number of hits per track	
$2.4 < \lvert\eta\rvert < 2.7 \quad (640\ \mathrm{mm} > r > 470\ \mathrm{mm})$	≈ 2.0
$2.7 < \lvert\eta\rvert < 3.5 \quad (470\ \mathrm{mm} > r > 230\ \mathrm{mm})$	≈ 2.4
$3.5 < \lvert\eta\rvert < 4.0 \quad (230\ \mathrm{mm} > r > 120\ \mathrm{mm})$	≈ 2.6
Average time resolution per hit (start and end of operational lifetime)	
$2.4 < \lvert\eta\rvert < 4.0$	$\approx 35\mathrm{ps}$ (start), $\approx 70\mathrm{ps(end)}$
Average time resolution per track (start and end of operational lifetime)	$\approx 30\mathrm{ps}$ (start) $\approx 50\mathrm{ps(end)}$

TABLE 6.1: Main parameters of the HGTD design. The table is taken from [136] with the recent updates implemented.

The detector is designed to encompass a pseudo-rapidity range of $2.4 < |\eta| < 4.0$, achieved through multiple layers of LGAD sensors, possessing an active thickness of 50 μm. It comprises a total of 3.6 million channels and an active area of 6.4 m^2. The modules are sized at 2 cm × 2 cm with a pixel dimension of 1.3 mm × 1.3 mm. The collected charge per hit must exceed 4.0 fC. The average number of hits per track typically ranges from 2.0 to 2.6, contingent on the pseudo-rapidity range. The average time resolution per hit at the start and end of the operational lifetime is $\approx 35\mathrm{ps}$ and $\approx 70\mathrm{ps}$, respectively, while the average time resolution per track is $\approx 30\mathrm{ps}$ at the start and $50\mathrm{ps}$ at the end. The main parameters of the HGTD design are summarized in the Tab. 6.1.

6.3 Performance Evaluation of the Low Gain Avalanche Detectors in Test Beam at CERN and DESY

As detailed in Section 6.2.2, the HGTD [136], [139] will be installed in the end-cap/forward region of the ATLAS detector. Covering a pseudorapidity, η, range from 2.4 to 4.0, it will enhance the capabilities of the envisaged new inner tracker [133], [8] to mitigate pile-up effects on final physics states involving forward jets/particles. Given the anticipated high radiation levels in this region, corresponding to an integrated luminosity of $4000\mathrm{fb}^{-1}$, the detector's sensors and front-end electronics must withstand a neutron equivalent fluence of up to $2.5 \times 10^{15}\mathrm{n_{eq}/cm^2}$ and a total ionizing dose of $2\mathrm{MGy}$. This estimation is made at a distance of $120\ \mathrm{mm}$ from the beam pipe. With a safety factor of 1.5 in mind, the inner (middle) ring of the detector should be replaced every $1000\mathrm{fb}^{-1}$ ($2000\mathrm{fb}^{-1}$) to maintain optimal performance levels.

The HGTD is poised to measure the time of a minimum ionizing particle (MIP) with a resolution ranging from roughly $30\mathrm{ps}$ at the onset of HL-LHC operations to about $50\mathrm{ps}$ towards the end. This yields an average time resolution per hit of $35\mathrm{ps}$ and $70\mathrm{ps}$, respectively. Considering the necessity for precise time measurements alongside high radiation tolerance, the sensors chosen for the HGTD employ LGAD technology [140]. These sensors boast an active layer thickness of $50\mu\mathrm{m}$ and a pad area of $1.3 \times 1.3\ \mathrm{mm}^2$ as summarised in table 6.1. The time resolution is closely tied to the analog performance of the front-end, rendering the design of the read-out Application-Specific Integrated Circuit (ASIC) a formidable task. It is crucial for the time jitter to remain sufficiently low so as not to compromise the sensor's performance.

The HGTD ASIC, also known as the ATLAS LGAD Time Read Out Chip (ALTIROC) [141], features a discriminator set at $\sim 2\text{fC}$. It is engineered to provide precise time measurements even for low charges, reaching values as low as 4fC. This capability is essential to account for the reduction in sensor gain resulting from radiation exposure. Ensuring a minimum hit efficiency of 95%, while factoring in the jitter of the ALTIROC, this 4fC threshold aptly fulfills the requirements of the HGTD.

The results presented in the following sections are already published in the paper [10]. The author has the significant contribution to the paper both in obtaining the results and collecting the data during 2018 and 2019. In 2018 the tests were carried out at the CERN SPS [142] with a high-energy pion beam, while in 2019 they were carried out at the DESY II Test Beam Facility [143] with an electron beam.

6.4 Sensor Characteristics

In this section, we outline the key attributes and characteristics of the sensors subjected to various irradiation campaigns. The section provides details on the levels of irradiation applied and includes an initial overview of the electrical properties.

6.5 Low Gain Avalanche Detectors

The LGAD sensors are thin n-on-p silicon devices originally developed by the Centro National de Microelectrónica (CNM) in Barcelona, in collaboration with the CERN-RD50 initiative [140, 144, 145]. Their design was subsequently refined to optimize high-precision time measurements. LGADs operate by implanting a highly doped p-type layer, a few micrometers thick, between the high-resistivity p-type bulk and the n+ implant. This configuration acts as a high-field charge multiplication layer, providing a moderate gain typically ranging from 5 to 70.

The tested prototypes were manufactured by both CNM and Hamamatsu Photonics (HPK). Wafers (W) from both vendors encompass various pad structures, including single-pad diodes and segmented arrays of pad diodes with differing granularities. CNM sensors were produced on 4-inch silicon-on-silicon wafers, featuring an active thickness of $50\mu\mathrm{m}$ and a resistivity of 12 $\mathrm{k\Omega cm}$. These sensors were mounted on a 300 $\mu\mathrm{m}$-thick support wafer, with an additional 1 $\mu\mathrm{m}$ of buried oxide layer (refer to figure 6.7).

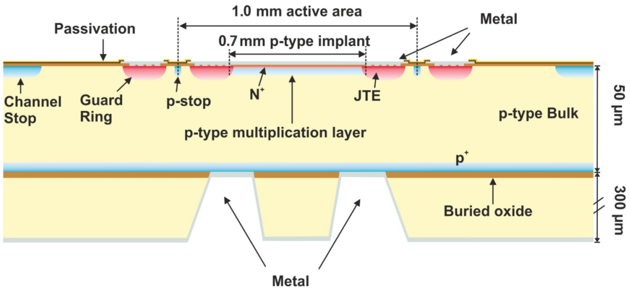

FIGURE 6.7: Cross section of a single-pad CNM LGAD sensor [10].

To enhance radiation hardness, CNM explored different doping materials: Boron for wafer 4[1], a combination of Boron and Carbon for wafer 5[2], and Gallium for wafer 6[3] [146]. Carbon-enriched LGADs aimed to achieve similar performance to Boron-based ones, but at lower bias voltages. Conversely, HPK sensors were produced on 6-inch silicon-on-insulator wafers, featuring an active thickness ranging from 45 $\mu\mathrm{m}$ to 46 $\mu\mathrm{m}$, and a resistivity between 3.4 $\mathrm{k\Omega cm}$ and 4.6 $\mathrm{k\Omega cm}$. HPK exclusively used Boron to manufacture two types of LGADs with distinct doping profiles, offering varying gain layer depths (1.6 $\mu\mathrm{m}$ for type-3.1 and 2.2 $\mu\mathrm{m}$ for type-3.2), edge sizes of 300 $\mu\mathrm{m}$ and 500 $\mu\mathrm{m}$, as well as different nominal inter-pad distances (ranging from 30 $\mu\mathrm{m}$ to 95 $\mu\mathrm{m}$) in the case of

---

[1] CNM production run 10478.

[2] CNM production run 10478.

[3] CNM production run 10924.

2×2 arrays. The tests reported in this paper were conducted on CNM single-pad sensors, featuring an overall active area of $1 \times 1\ \mathrm{mm}^2$, a gain layer of about $0.7 \times 0.7\ \mathrm{mm}^2$, and a single guard ring (GR) structure of $0.135\ \mathrm{mm}$. Additionally, tests were carried out on HPK single-pad and 2×2 array sensors, boasting an overall active area of $1.3 \times 1.3\ \mathrm{mm}^2$. Schematic views of the CNM and HPK single-pad LGAD sensors are illustrated in figures 6.8 and 6.9.

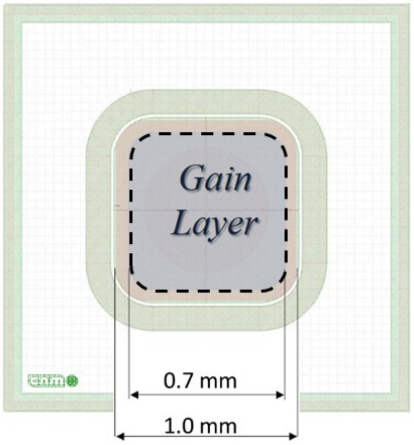

Figure 6.8: Geometry of CNM.

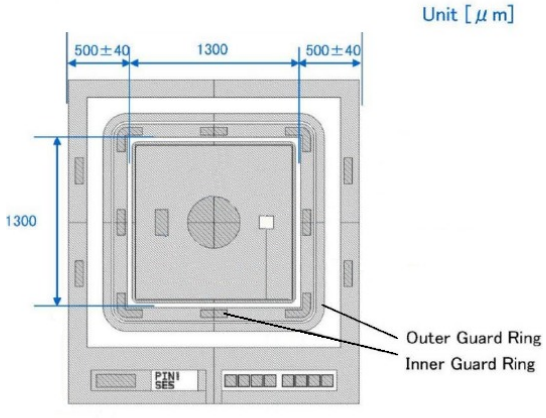

Figure 6.9: HPK 3.1 single-pad LGAD sensors

6.5.1 Radiation Effects

In silicon, radiation-induced damage primarily leads to a decrease in the effective doping concentration and the removal of acceptors. This introduces trapping centers, reducing the mean free path of charge carriers and increasing leakage current [147]. Additionally, a surface effect occurs with the accumulation of positive charge in the oxide ($\mathrm{SiO_2}$) and the $\mathrm{Si} - \mathrm{SiO_2}$ interface, affecting interpixel capacitance. These factors significantly influence detector performance and charge collection efficiency. For LGADs, radiation damage leads to a degradation of gain with fluence at a fixed voltage [148]. As a result, it becomes necessary to increase the applied bias voltage after irradiation to partially compensate for this loss.

To assess LGAD performance following irradiation, sensors were exposed to fluences up to $3 \times 10^{15} \mathrm{n_{eq}/cm^2}$ at various facilities using different particle types and energies. The primary facilities included the TRIGA reactor in Ljubljana for 1 MeV neutrons, the CERN Proton Synchrotron (PS) IRRAD facility for 24 GeV protons, and the CYRIC facility in Japan for 80 MeV protons. Table 6.2 provides details of the LGAD sensors tested in beam experiments, including information on the manufacturer, sensor IDs, multiplication layer implant type, irradiation type, and fluence. Additionally, it includes a designated device name for ease of reference. The table also contains relevant information, such as sensor type (Boron, Carbon, Gallium, 3.1, or 3.2), geometry (single-pad or array), irradiation level in units of $10^{14} \mathrm{n_{eq}/cm^2}$, and the type of particle to which the devices were exposed.

6.5.2 I-V and C-V Measurements

Prior to the beam test, electrical measurements were conducted on the sensors using a cooled probe station equipped with needle contacts. The objective was to analyze the gain layer voltage (V_{gl}), full depletion voltage (V_{fd}), and breakdown voltage (V_{bd}) of each sensor by performing current-voltage (I-V) and capacitance-voltage (C-V) scans with the guard ring grounded.

Figure 6.10 illustrates the I-V characteristics of several tested sensors. For both CNM and HPK sensors, it was observed that prior to irradiation, there existed a bulk leakage current of approximately $1 \mathrm{nA}$. Following irradiation, this value increased to around $0.1 \mu\mathrm{A}$, showing an increase of approximately two orders of magnitude. Interestingly, Gallium-type LGADs exhibited leakage currents about two orders of magnitude higher than their counterparts at lower fluences.

For unirradiated devices, the breakdown voltage (V_{bd}) was observed to be below 100 V at $-30°\mathrm{C}$ for CNM sensors, 140 V for HPK-3.2, and 270 V for HPK-3.1

Device name	Vendor	Sensor ID	Implant	Irradiation type	Fluence $\left[\mathrm{n_{eq}/cm^2}\right]$
LGA35	CNM	W9LGA35	Boron	unirradiated	
Boron S	CNM	W4S1030	Boron	unirradiated	
Boron S1n	CNM	W4S1095	Boron	n	1×10^{14}
Boron S6n	CNM	W4S1016	Boron	n	6×10^{14}
Boron S1p	CNM	W4S1067	Boron	p	1×10^{14}
Carbon S	CNM	W5S1013	Boron+Carbon	unirradiated	
Carbon S1n	CNM	W5S1005	Boron+Carbon	n	1×10^{14}
Carbon S1p	CNM	W5S1038	Boron+Carbon	p	1×10^{14}
Gallium S	CNM	W6S1021	Gallium	unirradiated	
Gallium S1n	CNM	W6S1007	Gallium	n	1×10^{14}
Gallium S30n	CNM	W6S1006	Gallium	n	30×10^{14}
Gallium S1p	CNM	W6S1028	Gallium	p	1×10^{14}
3.1 A	HPK	3.1 W8 2x2 SE5IP3	Boron	unirradiated	
3.1 S8n	HPK	3.1 W8 P2LGE5	Boron	n	8×10^{14}
3.1 S10p	HPK	3.1 W8 LGE5	Boron	p	10×10^{14}
3.2 A	HPK	3.2 W18 2x2 SE5IP3	Boron	unirradiated	
3.2 S8n	HPK	3.2 W18 P4LGE5	Boron	n	8×10^{14}
3.2 A15n	HPK	3.2 W18 2x2 SE5IP3	Boron	n	15×10^{14}
3.2 S15n	HPK	3.2 SE3 (high gain)	Boron	n	15×10^{14}

TABLE 6.2: List of CNM and HPK LGAD sensors investigated during the 2018–2019 beam test campaigns, categorized as single-pads ("S") or arrays ("A") with the details on the multiplication layer implant, irradiation level, and type.

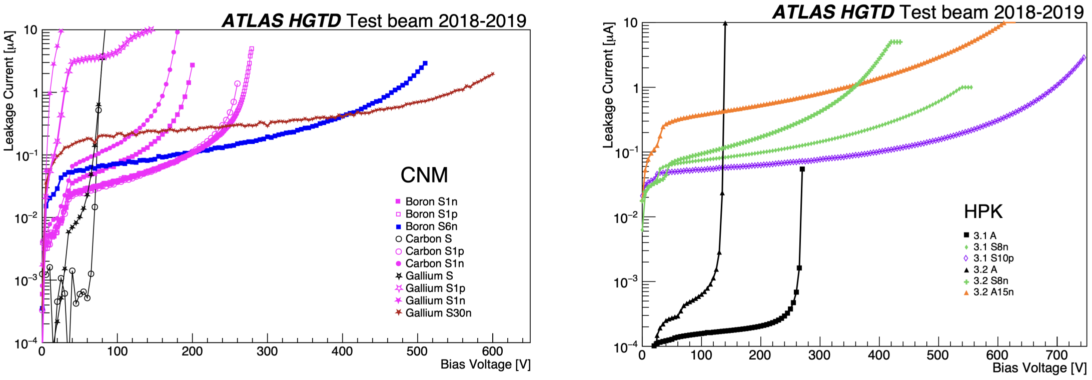

FIGURE 6.10: Leakage current-voltage characteristics of CNM (left) and HPK (right) sensors. It is important to note that all measurements were conducted at a temperature of −30°C, except for the two unirradiated HPK devices, which were tested at 20°C [10].

at $20°\mathrm{C}$. Subsequently, the I-V curve for HPK sensors was measured at $-30°\mathrm{C}$, revealing V_{bd} values of 70 V for HPK-3.2 and 200 V for HPK-3.1 [138]. This behavior aligns with expectations, as breakdown voltage tends to decrease with lower temperatures and increase with higher fluences.

The C-V measurements shown in Figure 6.11 highlight the gain layer voltage (V_{gl}) and full depletion voltage (V_{fd}) for unirradiated HPK sensors. Specifically, V_{gl} was measured at 40 V for HPK-3.1 and 55 V for HPK-3.2, while V_{fd} was determined to be 50 V for HPK-3.1 and 65 V for HPK-3.2. This discrepancy arises from the variance in gain layer depth, where a deeper gain layer necessitates higher bias for full depletion, as evidenced in the case of HPK-3.2. Comparable measurements for CNM sensors demonstrated analogous V_{gl} and V_{fd} values below 50 V [146]. Moreover, the detector capacitance was measured to be $C = 2.9\mathrm{pF}$ for both CNM and HPK sensors.

In summary, the I-V and C-V measurements provided crucial insights into the electrical characteristics of the tested sensors, shedding light on their behavior under various conditions.

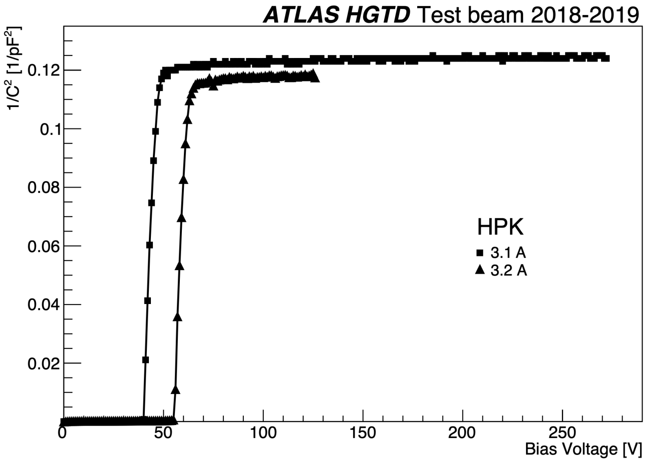

FIGURE 6.11: Unirradiated HPK sensors capacitance-voltage dependence showing a full depletion voltage of 50V for HPK-3.1 and 65V for HPK-3.2 [10].

6.6 Experimental Setups for Test Beams

The HGTD beam test campaigns were carried out at two different facilities: the CERN SPS H6A line [142] , utilizing a high-momentum $120\mathrm{GeV}$ pion beam, and the DESY TB 22 line [143], employing a $5\mathrm{GeV}$ electron beam. While the setups share similarities, there were specific adaptations made at DESY to mitigate multiple scattering effects. This included a reduction in the number of simultaneously evaluated Devices Under Test (DUTs). The DUTs were positioned between the two telescope arms, as shown in Figure 6.12.

At CERN, up to six DUTs were accommodated in a thermally insulated enclosure capable of reaching temperatures as low as $-40°\mathrm{C}$ [149]. Measurements were conducted at both $-30°\mathrm{C}$ and $-20°\mathrm{C}$.

At DESY, a maximum of three DUTs were tested concurrently, and a cooling system comprising a styrofoam box with a designated compartment for dry ice packs was employed [150]. Temperature levels were monitored using a Pt100 sensor, maintained within the range of $-40°\mathrm{C}$ to $-25°\mathrm{C}$.

In both test beam configurations, a beam telescope [151] was utilized for position-dependent measurements. This facilitated the evaluation of sensor efficiency and charge uniformity as a function of the incident particle's position. Additionally, an independent time reference was supplied to the Data Acquisition (DAQ) system through a Silicon Photomultiplier (SiPM) assembly [152].

6.6.1 Waveform Analysis

The following steps were carried out for waveform analysis:

1. Conversion of oscilloscope binary data into a ROOT ntuple containing raw waveform information of each DUT, sampled with a time bin of 25 ps. A typical LGAD signal is illustrated in Figure 6.13.

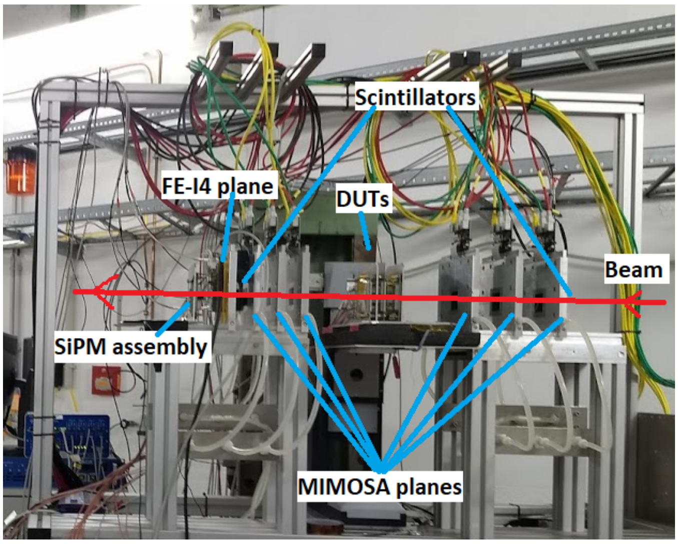

FIGURE 6.12: Schematic representation of the beam tracking system with DUT placement [10].

2. Determination of pulse polarity, maximum, minimum, start, and stop points of the signal. A check for the complete pulse within the oscilloscope acquisition window was performed.

3. Computation of pedestal and noise in the range from the 10% to 90% points before the start of the pulse. Pedestal was defined as the mean, and noise as the standard deviation of a Gaussian fit. The obtained pedestal value was subtracted from all data points of the waveform on an event-by-event basis. Re-calculation of the minimum, maximum, start, and stop points followed.

4. Computation of waveform properties including charge (q), rise time, jitter, signal-to-noise ratio, and Time Of Arrival (TOA) at different thresholds.

For each event, the charge (q) was determined by dividing the integral of the pulse by the transimpedance of the read-out board (R_b) and the gain of the voltage amplifier (G_{ampl}):

$$q = \frac{\int_{\text{start}}^{\text{stop}} A dt}{R_b \times G_{\text{ampl}}} \tag{6.1}$$

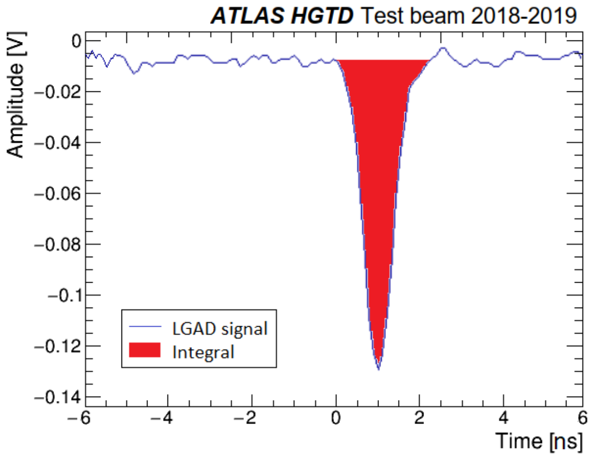

FIGURE 6.13: LGAD recorded waveform. The signal integral is shown by the red area.

The Time Of Arrival (TOA) was obtained using the Constant Fraction Discriminator (CFD) method. The TOA is defined as the point at which the signal crosses a predefined fraction (f_{CFD}) of its total amplitude. For the time resolution estimate, the TOA value at $f_{CFD} = 20\%$ was used for the time references and the unirradiated DUTs, whereas for the irradiated DUTs, the TOA value was taken at $f_{CFD} = 50\%$. The impact of this choice on the time resolution estimate is discussed in section 6.7.3.

The final step was to create a merged file containing the oscilloscope data along with the telescope-reconstructed data for user analysis.

6.6.2 Track Reconstruction

The telescope, in conjunction with the FE-I4, played a crucial role in providing tracking information to reconstruct particle trajectories and pinpoint the precise impact point on the DUT. This process relied on six MIMOSA planes, as shown in figure 6.12. The positions of the MIMOSA, FE-I4, and DUT planes were known with a precision of $1\ \mathrm{mm}$ along the beamline (z direction). This information, combined with recorded hits from each MIMOSA plane, enabled the reconstruction of particle trajectories and determination of the (x, y) coordinates of hits on the DUT planes.

After eliminating "hot" pixels from the MIMOSA planes (those with an occupancy greater than ten times the average), the remaining hits were organized into clusters. For tracking purposes, only clusters with a maximum of 6 hits were considered. In the FE-I4 plane, a cluster was required to have a maximum of 2 neighboring hits. The cluster coordinates were calculated as the centroids of the hit coordinates in x and y. Subsequently, only events with exactly one cluster in the FE-I4 plane were retained.

The alignment of the MIMOSA planes was achieved through iterative adjustments of their coordinates in x and y relative to a reference plane. This process aimed to minimize the discrepancy between the reconstructed track position at the MIMOSA plane and the measured hit position in the same plane. The position resolution was determined from the fitting performed during the alignment procedure.

For data collected at CERN SPS, a track fitting procedure was applied. Using the z position of the MIMOSA planes along the beam axis, along with the x and y positions of the hits in these planes, 3D-tracks were constructed, starting with the planes closest to the FE-I4. The reconstructed tracks were required to coincide with a hit in the FE-I4 plane, and only events with a single reconstructed track through the six MIMOSA planes were considered. The track fitting procedure was slightly modified for data collected at DESY, taking into account differences in the experimental setup and beam type. Tracking was initiated in the upstream MIMOSA planes, and no matching requirement was imposed between the extrapolated track and the FE-I4 cluster [153]. Events with more than one candidate track were retained if the candidate tracks were compatible with kinks resulting from multiple scattering along a single track.

Once the tracks were reconstructed, their trajectories were evaluated at the z coordinates of the DUTs to determine the (x, y) coordinates of the hits. This information was then stored in a file. The precision on the position of the extrapolated reconstructed track in the DUT planes was approximately 3 μm in both the x and y directions.

6.7 Results

In this section, we present a comprehensive evaluation of LGAD sensor performance, both pre- and post-irradiation, using particle beams and utilizing reconstructed track information. We delve into key LGAD properties: collected charge, time resolution.

To mitigate background contributions, two types of cuts were employed (see Figure 6.14). First, a geometrical cut based on the relative positions of the DUT and time references (LGA35, SiPM) within the FE-I4 ROI was applied. Additionally, a timing cut was imposed, utilizing a 2 ns window centered around the maximum of the time difference distribution between the Time of Arrival (TOA) of the DUT and SiPM, as read out by the same oscilloscope. The TOA was determined for all devices using the Constant Fraction Discriminator (CFD) method, with $f_{\mathrm{CFD}} = 20\%$ for unirradiated DUTs and references, and $f_{\mathrm{CFD}} = 50\%$ for irradiated DUTs.

Figure 6.14 showcases reconstructed tracks inside the FE-I4 ROI at the DUT plane, both before and after the timing cut application. Following the geometry-based cleaning selections, the remaining events represent reconstructed tracks that traverse the DUT within the FE-I4 ROI.

In order to aid in the interpretation regarding irradiation fluence, data points corresponding to the same fluence level are depicted in matching colors. Solid markers signify neutron irradiation, while empty markers denote proton irradiation. Black points, whether solid or empty, correspond to unirradiated DUTs.

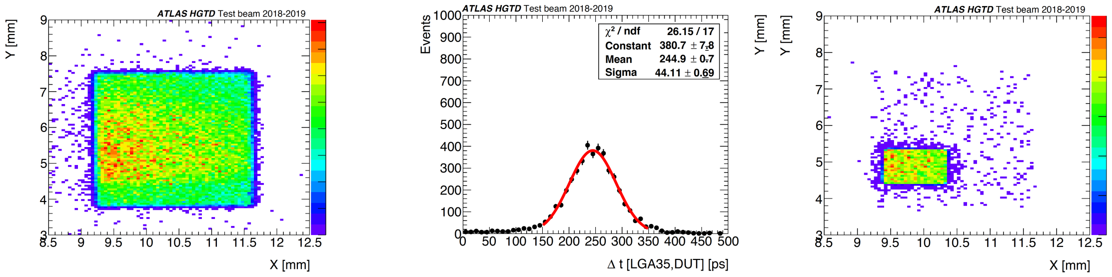

(A) (B) (C)

FIGURE 6.14: Reconstructed tracks inside the FE-I4 ROI at the DUT plane (a) before and (c) after the timing cut. (b) Time difference distributions between the DUT and LGA35.

6.7.1 Collected Charge

Collected charge is a critical parameter for assessing the performance of LGAD sensors. As specified in Table 6.2, a minimum threshold of 4 fC is set for a sensor to be considered valid. From the selected events, following the application of the cleaning criteria, a charge distribution was obtained for each DUT using Equation 6.1. These distributions were then fitted with a Landau-Gaussian convoluted function. The reported collected charge for each sensor is identified as the Most Probable Value (MPV) from this fit, denoted as Charge $\mathrm{MPV_M}$ for subsequent calculations.

To illustrate, Figure 6.15 presents a charge distribution for Carbon S1p operated at a bias voltage of 220 V, both before (left) and after (right) the application of cleaning selections. The right-hand side of Figure 6.15 also includes the resulting fit function with an MPV of 9.8 fC. It's worth noting that the negative charge remaining after the cleaning cuts may arise from noise events or fluctuating signals resulting from particles hitting the sensor's edge.

Figures 6.16a and 6.16b display the results for CNM and HPK sensors, respectively. Unirradiated sensors consistently exhibit high collected charge, even at low bias voltages. Conversely, irradiated sensors yield a lower collected charge compared to their unirradiated counterparts at the same bias voltage. They require a higher bias voltage to achieve a similar performance. The gain

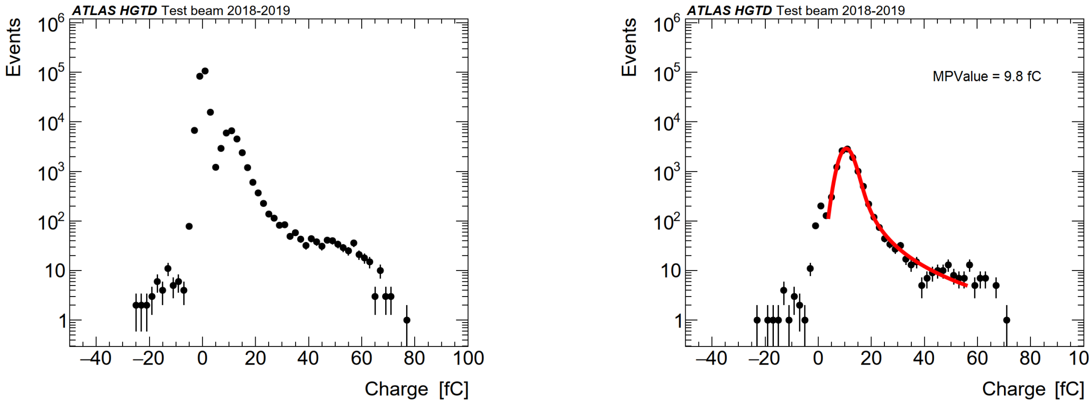

(A)

(B)

FIGURE 6.15: Charge distribution of Carbon S1p operated at 220 V, before (a) and (b) after applying the signal selections. The fit function with an MPV of 9.8 fC is shown in (b).

of the sensors decreases with irradiation; the higher the fluence, the greater the bias voltage required to attain the minimum required charge of 4 fC for accurate timing.

For the CNM sensors, three types underwent irradiation at a fluence of 10^{14} $\mathrm{n_{eq}/cm^2}$ with neutrons (S1n DUTs) and protons (S1p DUTs). A comparison reveals that neutron-irradiated DUTs demonstrate superior performance at the same bias voltage. Specifically, Carbon S1n collects more charge than Boron S1n, while Gallium S1n requires more voltage to yield the same charge. This corroborates findings from laboratory data [154]. Unirradiated DUTs, such as Boron S6n and Gallium S30n, were not operated at higher voltages to prevent premature sensor failure.

Regarding HPK sensors, 3.2 A did not function adequately at low temperatures and could not be operated at voltages exceeding $-70\,\mathrm{V}$ due to self-triggering issues [139], [154]. Nevertheless, after irradiation, type-3.2 demonstrated improved performance compared to type-3.1, as evident in the case of 3.2 S 8 n which required less voltage to achieve comparable performance than 3.1 S8 n. Type-3.2 possesses a deeper and higher-dose multiplication layer, resulting in a reduced acceptor removal rate. Consequently, the gain is higher at the same voltage for the same irradiation level. This aligns with the observations in Figure 5.8 (a) in [139].

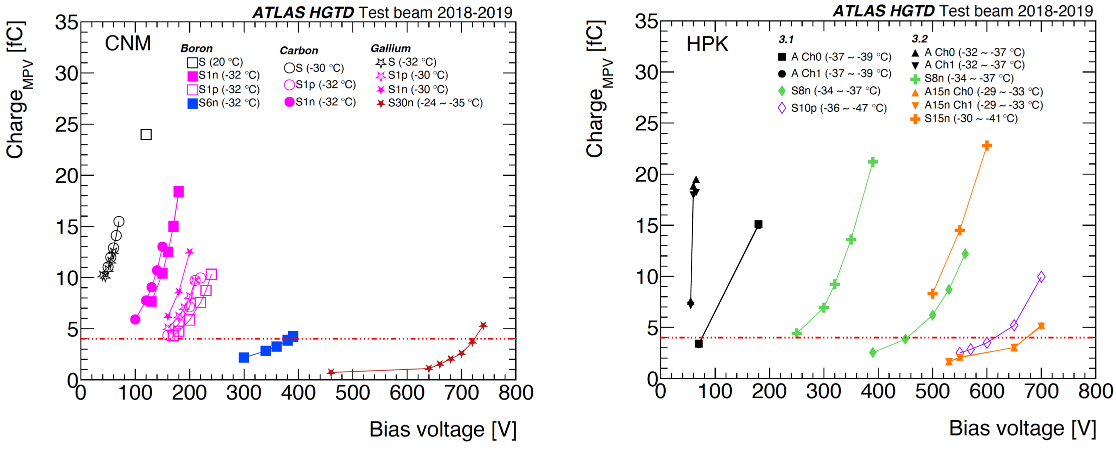

(A) (B)

FIGURE 6.16: (a) Collected charge results for CNM (b) and HPK sensors. The horizontal line drawn represents the HGTD requirement specific to minimum collected charge value of 4 fC.

6.7.2 Charge Uniformity

To investigate the uniformity of charge distribution within the sensors pads, a two-dimensional (2D) occupancy map was constructed. This map depicts the occupancy as a function of the reconstructed particle position in the DUT plane. To simplify interpretation and increase the event count, the charge uniformity was assessed along the x-axis, integrating over the y-axis. The active area of the sensor was divided into ten bins of $0.1 \times 1\ \mathrm{mm}^2$, as illustrated in Figure 6.17 (left). In each bin k, the collected charge, denoted as Charge $_{MPV_k}$, was calculated. An example of the charge distribution in one bin, along with a fitted Landau-Gaussian function for DUT Carbon S1p, is shown in Figure 6.17 (right).

The uniformity of the charge was assessed for each DUT at the maximum applied voltage. Figure 6.16 demonstrates how the collected charge varies with bias voltage and irradiation level. To facilitate comparison between sensors with different collected charges, the value computed in each bin is normalized to the overall collected charge of the sensor. Thus, the uniformity of the charge along the x-axis is expressed as a relative charge, defined as:

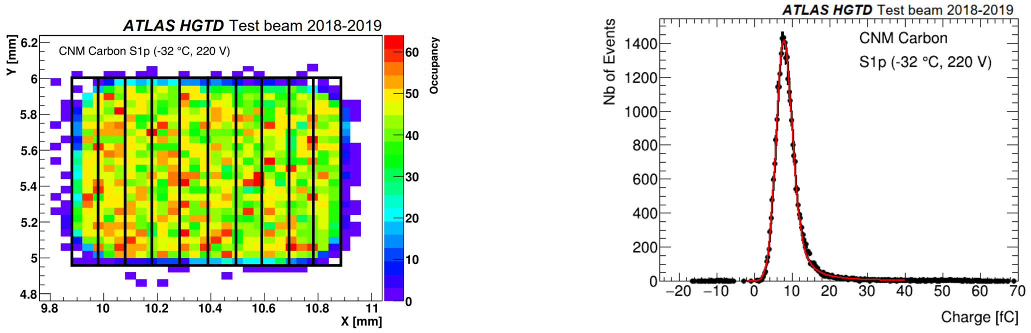

(A)

(B)

FIGURE 6.17: On the left, we observe a 2D map illustrating the hit distribution in relation to the reconstructed particle position within the DUT plane for Carbon S1p, which was operated at a bias voltage of 220 V. The black boxes represent the bins along the x-axis. On the right, we have the charge distribution computed within a bin size of $0.1 \times 1\ \mathrm{mm}^2$.

$$\text{Relative Charge} = \frac{\text{Charge}_{MPV_k}}{\text{Charge}_{MPV}} \tag{6.2}$$

Figure 6.18 illustrates the uniformity for CNM sensors, while Figure 6.19 displays the results for HPK sensors. The uniformity along the y-axis was also examined and found to be similar. Small deviations were observed for the unirradiated and low-fluence CNM sensors. The uniformity of Carbon S1p exhibited slightly larger deviations, but these remained within 10% of the average and were not deemed significant. Similarly, the uniformity of Gallium S30n showed a spread within 5% over most of its surface. The tested HPK sensors demonstrated excellent uniformity across all fluences. At the highest fluence, A15n-ch0 exhibited a more pronounced decrease in relative charge at the edges compared to other DUTs. Generally, for both vendors, larger deviations were noticeable at the periphery of the sensors, attributable to edge effects.

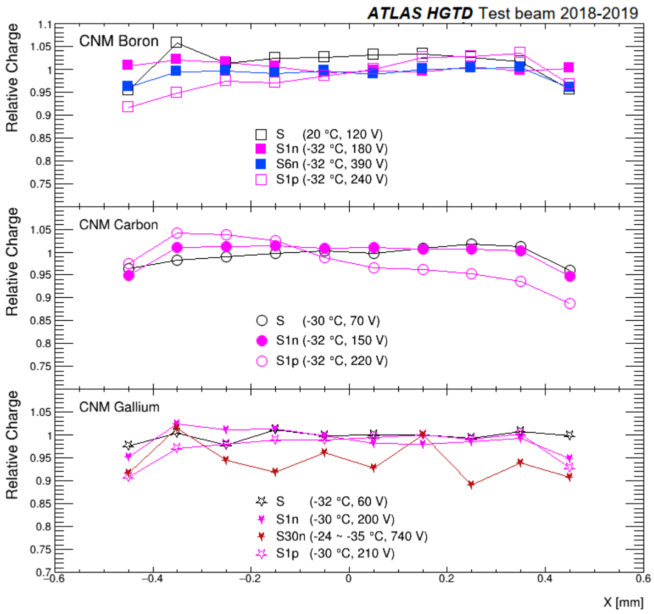

FIGURE 6.18: Relative charge along the x-axis for CNM Boron, Carbon and Gallium sensors, indicating the temperature and the bias voltage of operation.

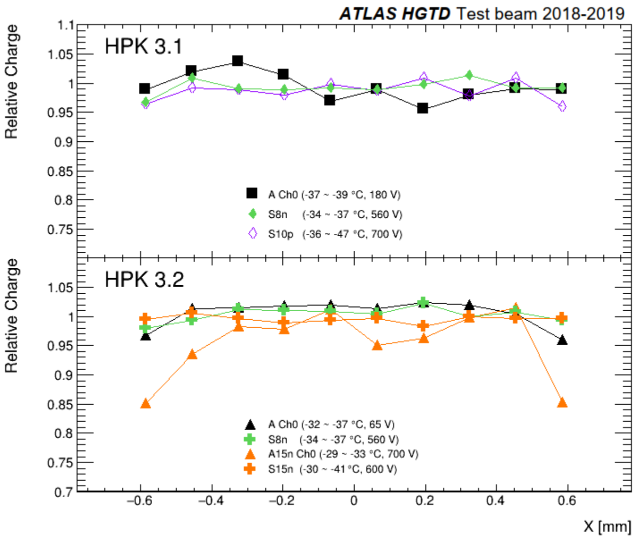

FIGURE 6.19: Relative charge along the x-axis for HPK 3.1 and 3.2 sensors, indicating the temperature and the bias voltage of operation.

6.7.3 Time Resolution

Time resolution is a crucial parameter in evaluating sensor performance. It can be determined as follows:

$$\sigma^2_{\text{LGAD}} = \sigma^2_{\text{Landau}} + \sigma^2_{\text{Time walk}} + \sigma^2_{\text{Jitter}} \tag{6.3}$$

The Landau fluctuations, σ_{Landau}, result from non-uniform energy deposition along the particle path within the sensor. Thinner sensors reduce this effect but may suffer from increased capacitance and lower deposited charge. Thus, a compromise must be struck. The time walk effect, $\sigma_{\text{Time walk}}$, arises from signals of different amplitudes reaching a fixed discriminator at different times. This can be mitigated with specific reconstruction techniques. The jitter term, σ_{Jitter}, is proportional to electronic noise and rise time, inversely proportional to signal slope.

For all combinations of DUTs and references tested together, a distribution of TOA differences was built to extract the DUT time resolution. The width of the time difference distribution between devices i and j is given by:

$$\sigma_{i,j} = \sigma_i \oplus \sigma_j \tag{6.4}$$

where σ_i and σ_j are the individual time resolutions of the two devices, and $\sigma_{i,j}$ is estimated as the width of a Gaussian function fit.

When exactly three devices are considered, it is possible to derive the individual time resolutions by measuring the resolution of several time differences. For example, considering two references and a DUT, the time resolution of the DUT can be extracted as:

$$\sigma_{\text{DUT}} = \sqrt{\frac{\sigma^2_{\text{DUT-Ref1}} + \sigma^2_{\text{DUT-Ref2}} - \sigma^2_{\text{Ref2-Ref1}}}{2}} \tag{6.5}$$

When more than three devices are considered simultaneously, the system is over-constrained, and one way to determine the individual time resolutions is through a χ^2 minimization:

$$\chi^2 = \sum_{i=1}^{N} \sum_{j=1}^{j<i} \frac{\left(\sigma_{ij}^2 - \sigma_i^2 - \sigma_j^2\right)^2}{\sigma_{\sigma_{ij}^2}^2} \tag{6.6}$$

For each DUT, the two references (LGA35 and SIPM) were used to compute its time resolution using Eq. (6.5). An example of a time difference distribution together with the Gaussian fit function used to extract the resolution is shown in Figure 6.14 (figure b).

Figures 6.20 and 6.21 illustrate the time resolution as a function of the bias voltage for CNM and HPK sensors, respectively. Both figures show an improvement in time resolution with higher bias voltages.

For Gallium sensors in Figure 6.20, neutron- and proton-irradiated sensors at a fluence of $10^{14}\mathrm{n_{eq}/cm^2}$ were tested. DUT Gallium S1n achieves a time resolution of $27.4\mathrm{ps}$, suggesting that neutron irradiation causes less damage compared to proton irradiation. The latter results in a time resolution of $38.3\mathrm{ps}$ at the same bias voltage for DUT Gallium S1p.

The same trend is observed for Carbon sensors in the bias voltage range of $150\ \mathrm{V}$ to $160\ \mathrm{V}$, where both neutron- and proton-irradiated sensors were tested. The neutron-irradiated one shows better performance.

Gallium S30n reaches the target time resolution at the expense of being operated at a rather high voltage. Detailed studies on the uniformity of the time resolution within the pad for this sensor are included in [150].

Figure 6.21 for HPK 3.2 sensors is in agreement with figure 5.11 (a) in [136]. At $8 \times 10^{14}\mathrm{n_{eq}/cm^2}$, HPK 3.2 performs better than HPK 3.1. For HPK sensors, a conclusion on the impact of the irradiation type on the sensor performance cannot be made. DUT $3.2\ \mathrm{S8n}$ achieves the best resolution of about $30\mathrm{ps}$ at $400\ \mathrm{V}$.

The time resolution, along with the collected charge obtained in Section 6.7.1,

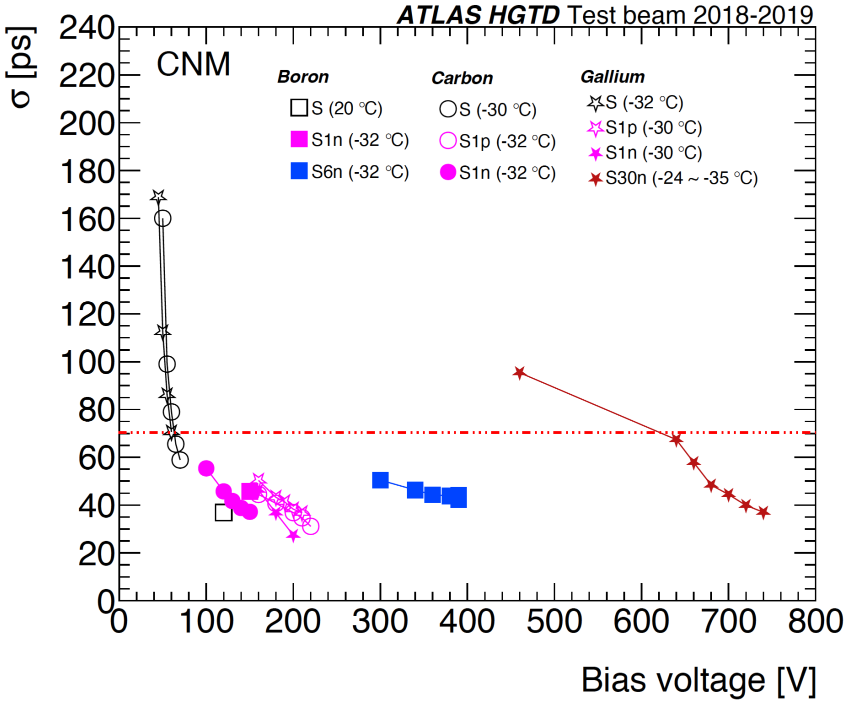

FIGURE 6.20: Time resolution as a function of the bias voltage for CNM Boron, Carbon and Gallium sensors.

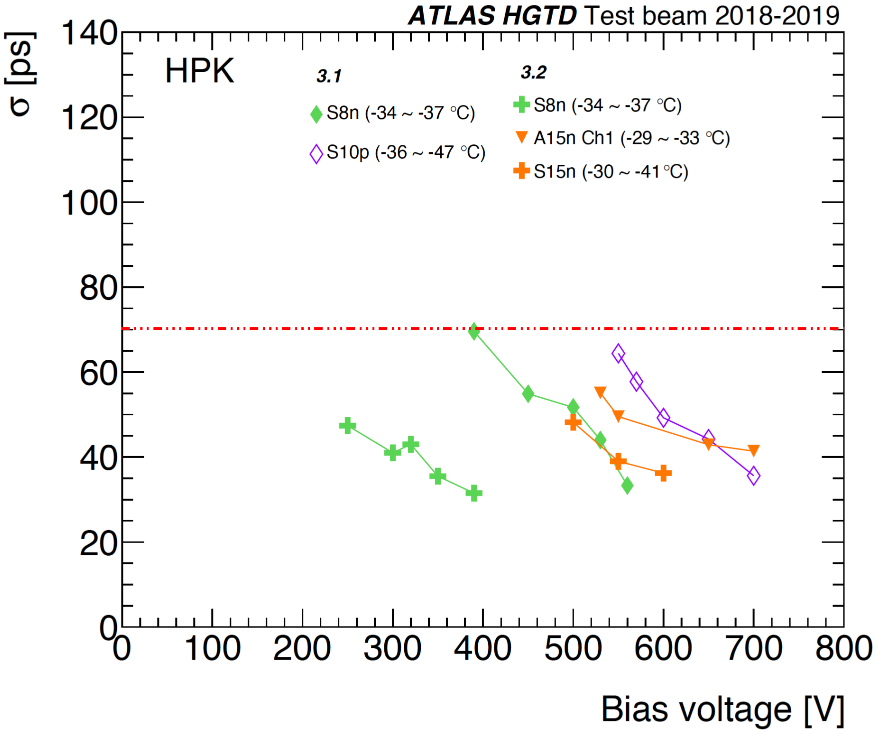

FIGURE 6.21: Time resolution as a function of the bias voltage for HPK 3.1 and 3.2 sensors.

allows us to define the best operating voltage point for each sensor and irradiation level. Looking at these two key parameters in Figure 6.22, we observe that for irradiated DUTs from both vendors, all sensors follow the same trend. This figure is in agreement with figure 5.8 (a) in [136] for HPK 3.2 sensors. The plot is divided into four regions where LGADs meeting the HGTD requirements in terms of collected charge $> 4\text{fC}$ and time resolution $< 70\text{ps}$ appear in the bottom right area.

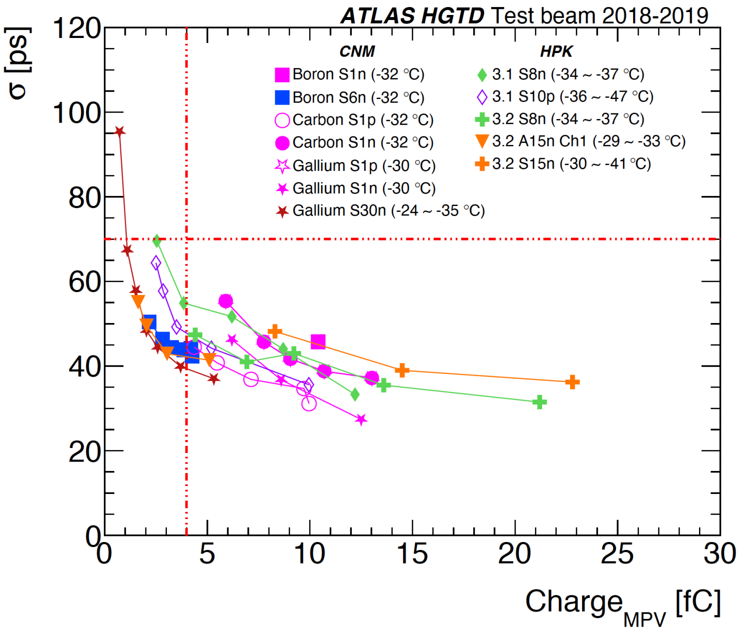

FIGURE 6.22: Time resolution as a function of the bias voltage for HPK 3.1 and 3.2 sensors.

6.8 Conclusion

The ATLAS High Granularity Timing Detector is poised to revolutionize time measurements of Minimum Ionizing Particles (MIPs) through the integration of LGADs bump-bonded to ALTIROC chips. In this study, the LGAD components have been individually scrutinized before the holistic module performance evaluation. The outcomes of LGAD assessments, conducted at CERN SPS and DESY test beam facilities, encompass unirradiated as well as irradiated sensors exposed to neutrons or protons at varying fluences. Two distinct sensor structures, encompassing single-pads and 2×2 pad arrays, sourced from CNM and HPK, have been the subject of our inquiry. The paper underscores key LGAD properties: collected charge, time resolution, and hit reconstruction efficiency.

In the case of CNM LGADs, an investigation into diverse doping materials was pursued to enhance radiation resilience. Boron plus Carbon sensors outperform their Boron counterparts in charge collection at identical fluences and bias voltages. Conversely, Gallium-based sensors exhibit a reduction in charge collection. The inclusion of Carbon proves instrumental in diminishing the operational voltage required to achieve comparable charge accumulation, a crucial factor at higher fluences where conventional LGADs necessitate elevated voltages for optimal performance. The transition from Boron to Gallium doping does not yield discernible advantages, substantiating the decision to abstain from further exploration along this trajectory—a finding corroborated by laboratory measurements.

In the realm of HPK LGADs, two distinct doping profiles were subjected to scrutiny. Notably, Type-3.2 demonstrates superior performance post-irradiation, outclassing Type-3.1 and consequently earning its designation as the baseline choice in the HGTD TDR. The initially inferior performance of Type-3.2 prior to irradiation is attributed to the heightened Boron dose.

All evaluated LGADs satisfy the HGTD mandate of a charge collection exceeding $4\mathrm{fC}$ for optimal ALTIROC operation conducive to precise timing measurements. These sensors achieve time resolutions beneath 70 ps, while also attaining a hit reconstruction efficiency surpassing 95% at a $2\mathrm{fC}$ threshold when operated at peak voltage levels. The test beam results align seamlessly with laboratory measurements. Notably, Gallium S30n emerges as a frontrunner, demonstrating compliance with HGTD prerequisites in terms of charge collection, time resolution, and hit efficiency following a fluence of $3 \times 10^{15}\mathrm{n_{eq}/cm^2}$.

Additionally, ongoing R&D efforts are underscored in our recent publication [155]. Our exploration encompasses Carbon-enriched LGAD samples procured from Fondazione Bruno Kessler (FBK) in Italy, Institute of Microelectronics (IME) Chinese Academy of Sciences in China, and University of Science and Technology of China (USTC)-IME. Throughout 2021 and 2022, these LGADs underwent irradiation simulations to replicate end-of-life conditions, subsequently subjecting them to rigorous testing at DESY and CERN particle beam facilities. Even after irradiation at fluences ranging from 1.5 to 2.5×10^{15} $\mathrm{neq/cm^2}$, the LGADs—operating at voltages below 550 V—successfully meet the specified objectives. These sensors consistently achieve a collected charge exceeding 4 fC, ensuring an optimal time resolution below 70 ps. Moreover, they maintain an efficiency greater than 95% across their surfaces at a charge threshold of 2 fC. These encouraging results validate the feasibility of employing LGAD-based timing detectors for the HL-LHC.

Appendix A

Appendix

A.1 Parametrisation procedure

The HH production via ggF and VBF modes depends fundamentally on $\kappa_\lambda, \kappa_t, \kappa_V$ and κ_{2V} coupling modifiers. Given the higher cross-section, the ggF production mode gives the strongest handle on κ_λ, while the VBF topology has a unique sensitivity to κ_{2V} because the ggF process does not involve the $VVHH$ interaction. In the SM, the first and the third tree-level Feynman diagrams in figure 1.7 interfere destructively. However, if κ_{2V} deviates from its SM value, the cross-section is significantly enhanced and the kinematics get harder.

The complete simulation of HH samples with a fine grid in the $(\kappa_\lambda, \kappa_{2V})$ plane is computationally expensive and time-consuming. To overcome this limitation, a representative number of MC simulation samples for selected coupling values are produced as described in 4.2.1, and a sample combination technique is employed to model the signal hypothesis across the coupling parameter space.

The process of combining a few samples in such a way as to cover the entire parameter space of coupling constants is based on exploiting the underlying mathematics of the differential cross-section formula.

ggF *HH* Parametrization

The ggF *HH* production process described by the triangle and box diagrams, as depicted in Figure 1.7. These diagrams involve the coupling modifiers κ_λ and

κ_t.

The differential cross section for ggF *HH* production can be expressed as:

$$\begin{aligned}\frac{d\sigma\left(\kappa_\lambda,\kappa_t\right)}{dm_{HH}} &= \left|A\left(\kappa_t,\kappa_\lambda\right)\right|^2\\ &= \left|\kappa_\lambda\kappa_t M_\Delta\left(m_{HH}\right)+\kappa_t^2 M_\Box\left(m_{HH}\right)\right|^2\\ &=\kappa_\lambda^2\kappa_t^2\left|M_\Delta\left(m_{HH}\right)\right|^2\\ &\quad+\kappa_\lambda\kappa_t^3\left[M_\Delta^*\left(m_{HH}\right)M_\Box\left(m_{HH}\right)\right.\\ &\quad+\left.M_\Box^*\left(m_{HH}\right)M_\Delta\left(m_{HH}\right)\right]\\ &\quad+\kappa_t^4\left|M_\Box\right|^2\\ &=\kappa_\lambda^2\kappa_t^2 a_1\left(m_{HH}\right)\\ &\quad+\kappa_\lambda\kappa_t^3 a_2\left(m_{HH}\right)\\ &\quad+\kappa_t^4 a_3\left(m_{HH}\right).\end{aligned} \tag{A.1}$$

Setting κ_t to its SM prediction ($\kappa_t = 1$), Equation A.1 simplifies to an equation quadratically dependent on the κ_λ coupling value:

$$\frac{d\sigma\left(\kappa_\lambda\right)}{dm_{HH}} = \kappa_\lambda^2 a_1\left(m_{HH}\right)+\kappa_\lambda a_2\left(m_{HH}\right)+a_3\left(m_{HH}\right) \tag{A.2}$$

In Equation (A.2), the a_i matrix element expansion values depend on m_{HH}, which cannot be trivially derived as an analytic function.

To address this, for a given κ_λ, the cross-section in each m_{HH} bin can be determined by solving a set of linear equations for a_1, a_2, and a_3, using three different cross-section values (in the same m_{HH} bin) for three different κ_λ values. This reweighting approach based on truth-m_{HH} weights does not allow for a continuous variation in κ_λ (or κ_t, or both). Instead, fixed values can be probed for one coupling at a time.

To overcome this limitation and enable the analysis to be described by a parametric likelihood in κ_λ, the expected number of events and the discriminant distributions are obtained by a linear combination of samples. These samples are generated from Eq. (A.1) with linear coefficients expressed as functions of (κ_λ, κ_t) at reconstruction level. The basis of the linear combination is composed of the SM MC sample and two other samples (κ_λ=0 and κ_λ=20) obtained using the reweighting procedure from the SM sample.

$$\begin{aligned}\text{sample}\,(\kappa_\lambda, \kappa_t) = &\kappa_t^2 \Bigg[\left(\kappa_t^2 + \frac{\kappa_\lambda^2}{20} - \frac{399}{380}\kappa_\lambda\kappa_t\right)\text{sample}(0,1) + \\ &\left(\frac{40}{38}\kappa_\lambda\kappa_t - \frac{2}{38}\kappa_\lambda^2\right)\text{sample}(1,1) + \left(\frac{\kappa_\lambda^2 - \kappa_\lambda\kappa_t}{380}\right)\text{sample}(20,1)\Bigg]\end{aligned} \tag{A.3}$$

Given a set of κ_λ, κ_t values, the signal distribution and yield are obtained by summing the signal distributions and yields of the three samples from the basis. In practice, the basis samples are processed through reconstruction and selection (or alternatively, the SM sample, after passing the analysis selections, is reweighted to the other κ_λ basis samples). Then, the signal component in the likelihood is described by three signal sub-components, evaluated by the distribution and yield of the three samples from the basis. Each component contributes to the signal likelihood with a weight that scales with the linear coefficient function of (κ_λ, κ_t) as in Eq. (A.3).

The validity of the κ_λ reweighting procedure is tested by checking the closure with a dedicated κ_λ=10 ggF *HH* sample for the BDT distributions in each of the analysis regions. This closure test is shown in Figure A.1.

VBF *HH* parametrisation

The VBF *HH* production dependence on κ_λ, κ_V and κ_{2V} coupling modifiers is modelled in a similar manner to the ggF mode, but with no truth reweighting. The kinematics of the VBF mode involves both the Higgs pair and the two VBF jets generated by the hadronisation of the two quarks that participate in the hard scattering. Given this topology, the reweighting approach is discarded, since it is not trivial to establish a limited number of variables that can fully describe

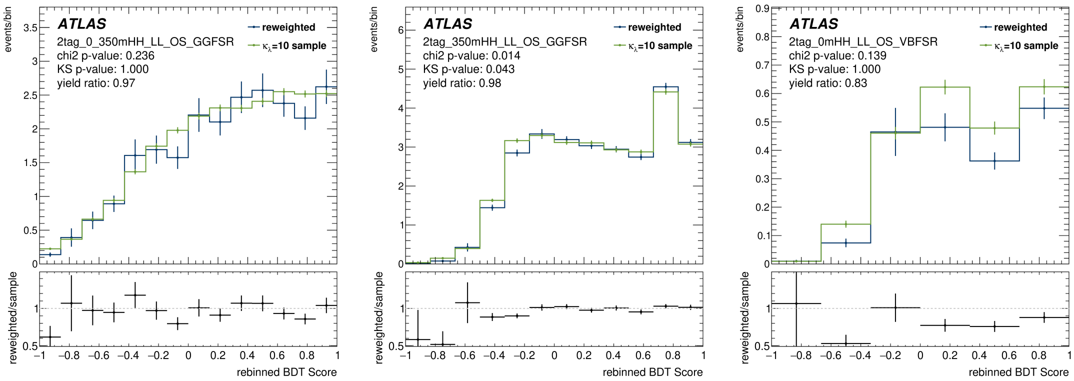

FIGURE A.1: Comparison of the SMBDT distributions between a dedicated κ_λ=10 ggF HH sample and a sample obtained using the reweighting procedure described in this section.

the VBF *HH* kinematics. Instead, a linear combination of the existing VBF *HH* MC samples allows to parametrise the VBF *HH* signals as a function of the three coupling modifiers κ_λ, κ_V and κ_{2V}, and is performed directly after reconstruction and selection, in order to generate the distribution of any variable for the desired κ_λ, κ_V and κ_{2V} values as described in the following.

As shown in Figure 1.8, the total amplitude for *HH* production via VBF at LO is given by the sum of three diagrams, scaling with κ_λ*κ_V , κ_{2V} and κ_V^2 respectively:

$$\mathcal{A}_{VBF}(\kappa_\lambda, \kappa_{2V}, \kappa_V) = A_1 \cdot \kappa_\lambda \kappa_V + A_2 \cdot \kappa_{2V} + A_3 \cdot \kappa_V^2, \tag{A.4}$$

where A_1, A_2 and A_3 represent the normalisation coefficients for each diagram. Hence, the differential cross section $\frac{d\sigma_{VBF}}{d\Phi}$ (where $d\Phi$ represents the infinitesimal phase space element) can be expressed as a function of the three coupling modifiers affecting the VBF *HH*production as follows:

$$
\begin{aligned}
\frac{d\sigma_{VBF}}{d\Phi}(\kappa_\lambda, \kappa_{2V}, \kappa_V) &\propto |\mathcal{A}_{VBF}(\kappa_\lambda, \kappa_{2V}, \kappa_V)|^2 \\
&= |A_1 \cdot \kappa_\lambda \kappa_V + A_2 \cdot \kappa_{2V} + A_3 \cdot \kappa_V^2|^2 \\
&= |A_1|^2 \cdot \kappa_\lambda^2 \kappa_V^2 + |A_2|^2 \cdot \kappa_{2V}^2 + |A_3|^2 \cdot \kappa_V^4 + (A_1 A_2^* + A_1^* A_2) \cdot \kappa_\lambda \kappa_V \kappa_{2V} \\
&\quad + (A_1 A_3^* + A_1^* A_3) \cdot \kappa_\lambda \kappa_V^3 + (A_2 A_3^* + A_2^* A_3) \cdot \kappa_{2V} \kappa_V^2 \\
&= x_1 \cdot \kappa_\lambda^2 \kappa_V^2 + x_2 \cdot \kappa_{2V}^2 + x_3 \cdot \kappa_V^4 + x_4 \cdot \kappa_\lambda \kappa_V \kappa_{2V} + x_5 \cdot \kappa_\lambda \kappa_V^3 + x_6 \cdot \kappa_{2V} \kappa_V^2
\end{aligned}
\tag{A.5}
$$

The differential VBF *HH* cross section can be written as a polynomial of the coupling modifiers κ_λ, κ_{2V} and κ_V, whose coefficients are identified by the x_i terms, with $i = 1, 2, ..., 6$. The following expression holds for the differential cross-section of the generic variable Φ for SM VBF *HH* events:

$$\frac{d\sigma_{VBF}}{d\Phi}(1, 1, 1) = x_1 + x_2 + x_3 + x_4 + x_5 + x_6. \tag{A.6}$$

This suggests the possibility of solving a system of linear equations, whose unknowns are represented by the x_i terms, while the constant term is identified with the distribution of any variable Φ (correctly normalized using the predicted cross section) extracted from an available VBF *HH* MC sample, simulated with a determined variation of the coupling values. Given the six unknowns x_i, six VBF *HH* reference samples, generated with different values of the couplings κ_λ, κ_{2V} and κ_V, are needed.

By inverting the 6×6 coefficient matrix of the system of linear equations, one can obtain an expression of the x_i variables in terms of the known $d\sigma_{VBF}/d\Phi(\kappa_{2V}, \kappa_\lambda, \kappa_V)$ distributions, extracted using the six basis samples. Finally, plugging the solutions for the x_i variables in Eq. (A.5), yields the distribution of any variable Φ for VBF *HH* events, simulated with any variation of the couplings κ_λ, κ_{2V} and κ_V in form of linear combinations of six reference samples, whose linear coefficients appear as functions of the probed κ_{2V}, κ_λ and κ_V

values.

This procedure results in a natural parametrisation of VBF *HH* events in the $(\kappa_\lambda, \kappa_{2V})$ plane (by fixing $\kappa_V = 1$), once a basis is chosen. The potential choices of basis are constrained by the available VBF *HH* MC samples, summarised in Table 4.2, and can be optimised depending on the desired effect for signal generation. The basis chosen for the VBF *HH* parametrisation was shown to be able to model the VBF *HH* kinematics across a large parameter space, reaching κ_{2V}, κ_λ and κ_V values well beyond the SM [156]:

$$\begin{aligned}
\frac{d\sigma_{VBF}}{d\Phi}(\kappa_{2V}, \kappa_\lambda, \kappa_V) = &\left(\frac{\kappa_{2V}^2}{5} - \frac{\kappa_{2V}\kappa_V^2}{5} - \frac{\kappa_{2V}\kappa_V\kappa_\lambda}{10} + \frac{\kappa_V^3\kappa_\lambda}{10}\right) \times \frac{d\sigma_{VBF}}{d\Phi}(3,1,1) \\
&+ \left(\frac{4\kappa_{2V}^2}{5} - \frac{4\kappa_{2V}\kappa_V^2}{5} - \frac{12\kappa_{2V}\kappa_V\kappa_\lambda}{5} + \frac{12\kappa_V^3\kappa_\lambda}{5}\right) \times \frac{d\sigma_{VBF}}{d\Phi}(\frac{1}{2},1,1) \\
&+ \left(-\frac{5\kappa_{2V}\kappa_V^2}{4} + \frac{5\kappa_{2V}\kappa_V\kappa_\lambda}{4} + \frac{\kappa_V^3\kappa_\lambda}{8} - \frac{\kappa_V^2\kappa_\lambda^2}{8}\right) \times \frac{d\sigma_{VBF}}{d\Phi}(1,2,1) \\
&+ \left(-\kappa_{2V}\kappa_V^2 + \kappa_{2V}\kappa_V\kappa_\lambda + \kappa_V^4 - \kappa_V^3\kappa_\lambda\right) \times \frac{d\sigma_{VBF}}{d\Phi}(0,0,1) \\
&+ \left(\frac{\kappa_{2V}\kappa_V^2}{36} - \frac{\kappa_{2V}\kappa_V\kappa_\lambda}{36} - \frac{\kappa_V^3\kappa_\lambda}{72} + \frac{\kappa_V^2\kappa_\lambda^2}{72}\right) \times \frac{d\sigma_{VBF}}{d\Phi}(1,10,1) \\
&+ \left(-\kappa_{2V}^2 + \frac{29\kappa_{2V}\kappa_V^2}{9} + \frac{5\kappa_{2V}\kappa_V\kappa_\lambda}{18} - \frac{29\kappa_V^3\kappa_\lambda}{18} + \frac{\kappa_V^2\kappa_\lambda^2}{9}\right) \times \frac{d\sigma_{VBF}}{d\Phi}(1,1,1).
\end{aligned} \tag{A.7}$$

The method is being validated likewise ggF parameterisation by comparing the reweighted distributions to dedicated simulated samples for different values of κ_λ and κ_{2V}.

A.2 $t\bar{t} - reweighting$

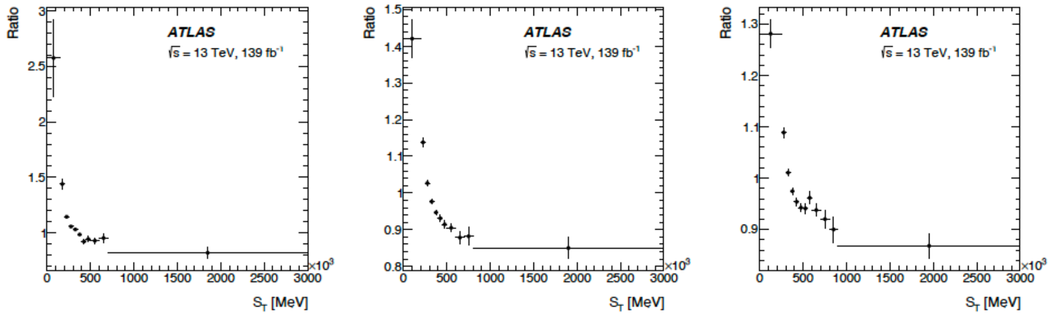

(a) $N_{\text{jets}} = 2$ (b) $N_{\text{jets}} = 3$ (c) $N_{\text{jets}} = 4$

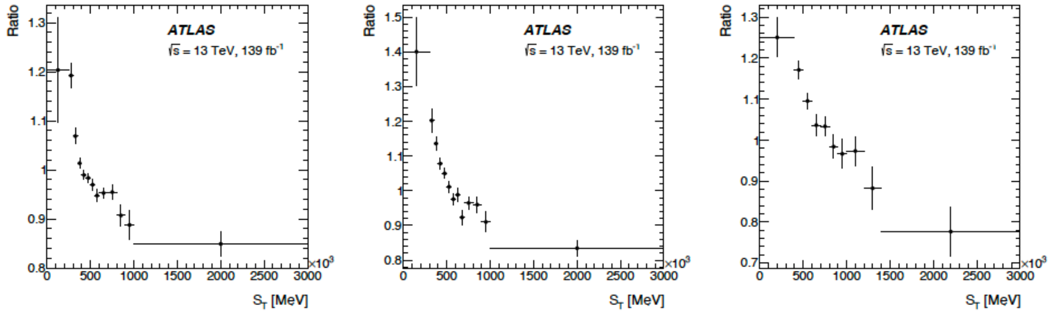

(d) $N_{\text{jets}} = 5$ (e) $N_{\text{jets}} = 6$ (f) $N_{\text{jets}} = 7$

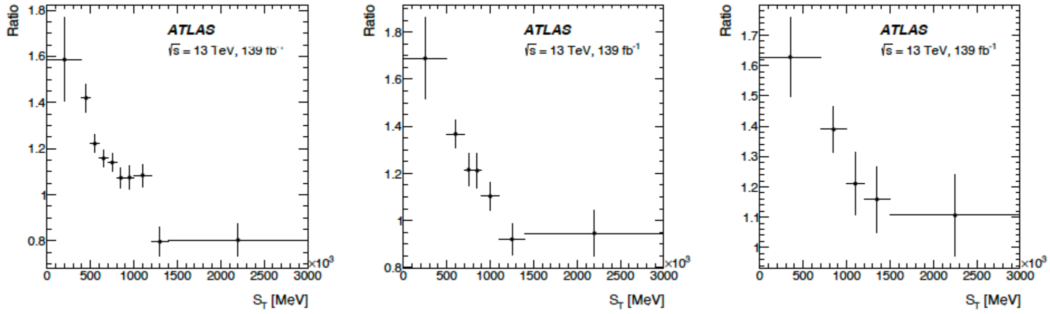

(g) $N_{\text{jets}} = 8$ (h) $N_{\text{jets}} = 9$ (i) $N_{\text{jets}} \leq 10$

FIGURE A.2: Shown are the scale factors for the $t\bar{t}$ shape correction as functions of H_T for various N_{jets}. The error bars represent the statistical uncertainties derived from both the data and simulated samples. Figures reproduced from internal analysis documents.

A.3 ggFVBF optimised variables

A.3.1 $\tau_{had}\tau_{had}$ ggFVBF BDT optimised variables

TABLE A.1: Input variables used for the ggF/VBF BDT training in the $\tau_{\text{had}}\tau_{\text{had}}$ channel.

Variable	Description
m_{HH}	Invariant mass of the HH system, reconstructed from the τ-lepton pair (using the MMC) and b-tagged jet pair
$\Delta R(\tau, \tau)$	The ΔR between the two visible τ decay products
VBF $\eta_0 \times \eta_1$	Product of the pseudorapidities of the leading and sub-leading VBF jets
$\Delta\eta_{jj}^{\text{VBF}}$	The $\Delta\eta$ between the two VBF jets
$\Delta\phi_{jj}^{\text{VBF}}$	The $\Delta\phi$ between the two VBF jets
m_{jj}^{VBF}	Invariant mass of the VBF jet system
fwm2$(\tau\tau jf)$	2$^{\text{nd}}$ order Fox-Wolfram moment, taking into account the τ-lepton pair and central and forward jets

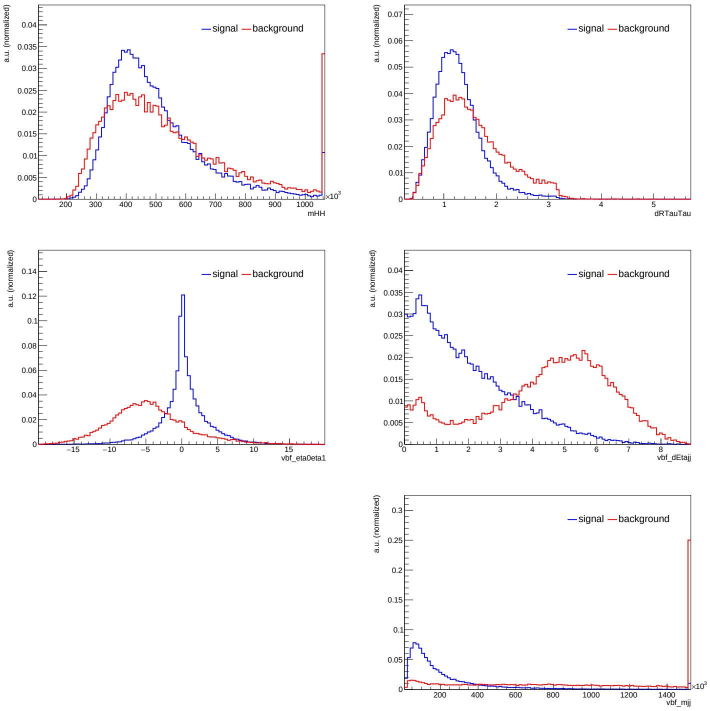

FIGURE A.3: Distributions of ggF/VBF BDT input variables in the $\tau_{had}\tau_{had}$channel showing the separation between the ggF *HH* events (labelled as signal in blue) and the VBF *HH* events (labelled as background in red).

A.3.2 $\tau_{lep}\tau_{had}$ SLT ggFVBF BDT optimised variables

TABLE A.2: Input variables used for the ggF-VBF BDT training in the $\tau_{\text{lep}}\tau_{\text{had}}$ SLT channel.

Variable	Description
$\text{cent}(\tau\tau jf)$	Centrality, taking into account the τ-lepton pair and central and forward jets
$\Delta\eta_{jj}^{\text{VBF}}$	The $\Delta\eta$ between the two VBF jets
$\Delta R_{jj}^{\text{VBF}}$	The ΔR of the VBF jet system
$\text{fwm0}(\tau\tau j)$	0^{th} order Fox-Wolfram moment, taking into account the τ-lepton pair and cer
$\text{mEff}(\tau\tau jf)$	Effective mass, taking into account the τ-lepton pair and central and forward
m_{jj}^{VBF}	Invariant mass of the VBF jet system
$\text{VBF}\eta_0 \times \eta_1$	Product of the pseudorapidities of the leading and sub-leading VBF jets

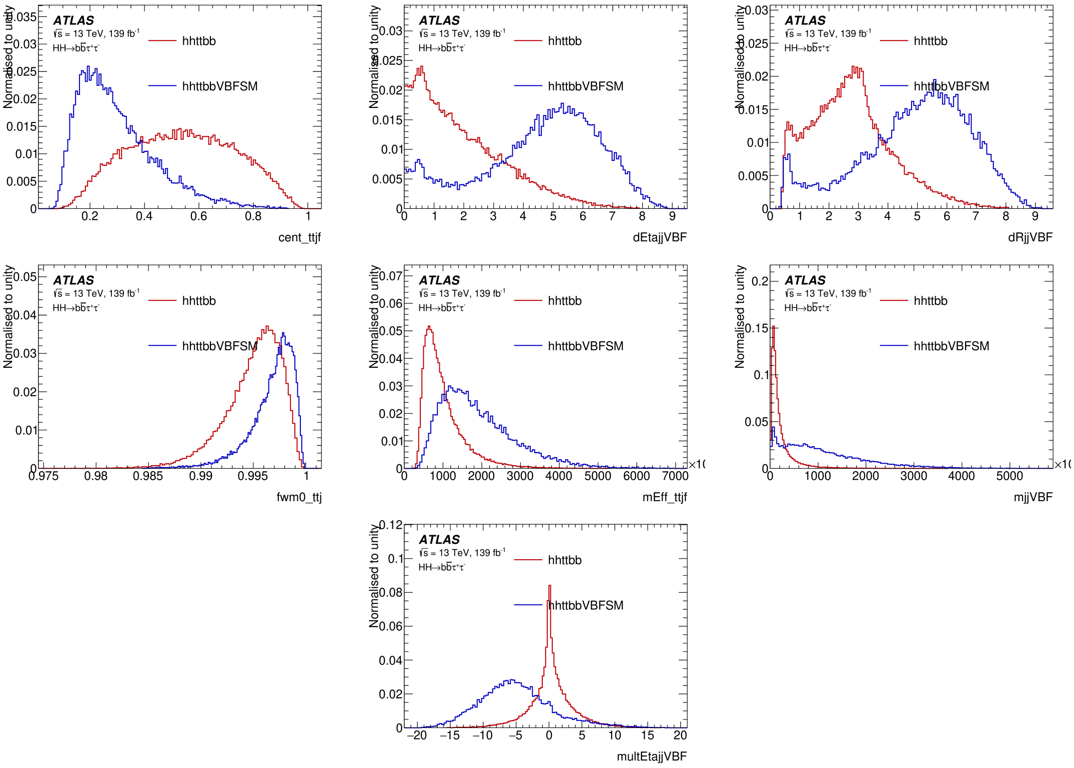

FIGURE A.4: Distributions of ggF/VBF BDT input variables in the $\tau_{lep}\tau_{had}$SLT channel showing the separation between the ggF *HH* events (in blue) and the SM VBF *HH* events (in red).

A.3.3 $\tau_{lep}\tau_{had}$ LTT ggFVBF BDT optimised variables

TABLE A.3: Input variables used for the ggF-VBF BDT training in the $\tau_{\text{lep}}\tau_{\text{had}}$ LTT channel.

Variable	Description
$\text{cent}(\tau\tau jf)$	Centrality, taking into account the τ-lepton pair and central and forward jets
$\Delta\eta_{jj}^{\text{VBF}}$	The $\Delta\eta$ between the two VBF jets
$\Delta R_{jj}^{\text{VBF}}$	The ΔR of the VBF jet system
$\text{fwm0}(\tau\tau jf)$	0^{th} order Fox-Wolfram moment, taking into account the τ-lepton pair and central and forward jets
$\text{mEff}(\tau\tau jf)$	Effective mass, taking into account the τ-lepton pair and central and forward jets
m_{jj}^{VBF}	Invariant mass of the VBF jet system
$\text{hcm}\,3(\tau\tau jf)$	3^{rd} order Had Fox-Wolfram moment, taking into account the τ-lepton pair and central and forward jets

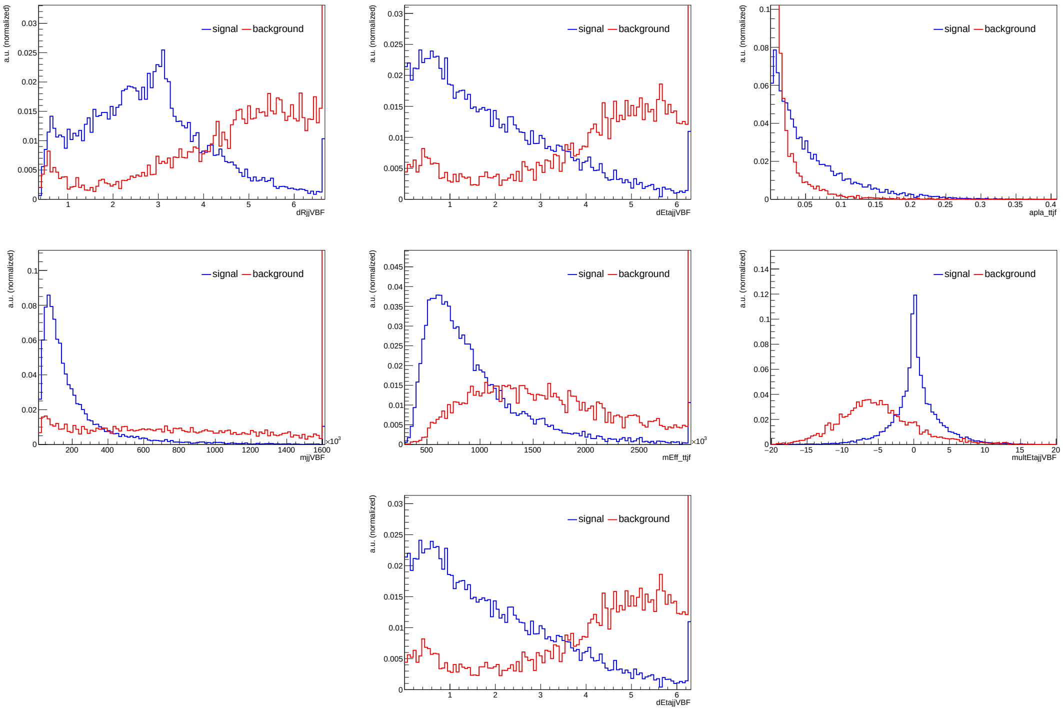

FIGURE A.5: Distributions of ggF/VBF BDT input variables in the $\tau_{lep}\tau_{had}$LTT channel showing the separation between the ggF *HH* events (in blue) and the SM VBF *HH* events (in red).

A.4 $\tau_{had}\tau_{had}$ ggF-SR optimised variables

A.4.1 $\tau_{had}\tau_{had}$ ggF low m_{HH} optimised variables

TABLE A.4: Input variables for the low-m_{HH}ggF BDT training in the $\tau_{\text{had}}\tau_{\text{had}}$ channel.

Variable	**Description**
m_{HH}	Invariant mass of the HH system, reconstructed from the τ-lepton pair (using the MMC) and b-tagged jet pair
m_{bb}	Invariant mass of the b-tagged jet pair system
$m_{\tau\tau}^{\text{MMC}}$	Invariant mass of the τ-lepton pair system, calculated using the MMC
$\Delta R(b, b)$	The ΔR between the two b-tagged jets
$\Delta R(\tau, \tau)$	The ΔR between the two $\tau_{\text{had-vis}}$
n_jets	Number of jets in the event
H_T	Total hadronic transverse energy in the event, perpendicular to the beamline
T_2	Topness, as defined in Ref. [120] assuming $\sigma_t = 15\text{GeV}$ and $\sigma_W = 5\text{GeV}$
E_T^{miss}	The missing transverse momentum of the event
M_{T2}	Stransverse mass, as defined in Ref. [157]
$p_T(\tau_0)$	Transverse momentum of the leading $\tau_{\text{had-vis}}$
$p_T(\tau_1)$	Transverse momentum of the sub-leading $\tau_{\text{had-vis}}$
$p_T(b_0)$	Transverse momentum of the leading b-tagged jet
$\Delta\phi(bb, E_T^{\text{miss}})$	The $\Delta\phi$ between the b-tagged jet pair system and missing transverse energy
$\Delta\phi(bb, \tau\tau)$	The $\Delta\phi$ between the b-tagged jet pair and τ-lepton pair systems
quant b_0	b-tagging quantile of leading b-tagged jet
quant b_1	b-tagging quantile of sub-leading b-tagged jet
m_{HH}^*	Reduced 4-object invariant mass, defined as $m_{HH}^* = m_{HH} - m_{bb} - m_{\tau\tau}^{\text{MMC}} + 250\text{GeV}$
$\Delta R(b_0, \tau_0)$	The ΔR between the leading b-tagged jet and $\tau_{\text{had-vis}}$
$\text{cent}(bb\tau\tau)$	Centrality, taking into account only the HH decay products
$m_{\text{eff}}(\tau\tau j)$	Effective mass, taking into account the τ-lepton pair and central jets
$\text{spher}(bb\tau\tau)$	Sphericity, taking into account only the HH decay products
$\eta(\tau_0)$	Pseudorapidity of the leading $\tau_{\text{had-vis}}$
$\eta(\tau_1)$	Pseudorapidity of the sub-leading $\tau_{\text{had-vis}}$

A.4.2 $\tau_{had}\tau_{had}$ ggF high m_{HH} optimised variables

TABLE A.5: Input variables for the low-m_{HH}ggF BDT training in the $\tau_{\text{had}}\tau_{\text{had}}$ channel.

Variable	**Description**
m_{HH}	Invariant mass of the HH system, reconstructed from the τ-lepton pair (using the MMC) and b-tagged jet pair
m_{bb}	Invariant mass of the b-tagged jet pair system
$m_{\tau\tau}^{\text{MMC}}$	Invariant mass of the τ-lepton pair system, calculated using the MMC
$\Delta R(b, b)$	The ΔR between the two b-tagged jets
$\Delta R(\tau, \tau)$	The ΔR between the two $\tau_{\text{had-vis}}$
n_jets	Number of jets in the event
H_T	Total hadronic transverse energy in the event, perpendicular to the beamline
T_2	Topness, as defined in Ref. [120] assuming $\sigma_t = 15\text{GeV}$ and $\sigma_W = 5\text{GeV}$
E_T^{miss}	The missing transverse momentum of the event
M_{T2}	Stransverse mass, as defined in Ref. [157]
$p_T(\tau_0)$	Transverse momentum of the leading $\tau_{\text{had-vis}}$
$p_T(\tau_1)$	Transverse momentum of the sub-leading $\tau_{\text{had-vis}}$
$p_T(b_0)$	Transverse momentum of the leading b-tagged jet
$\Delta\phi(bb, E_T^{\text{miss}})$	The $\Delta\phi$ between the b-tagged jet pair system and missing transverse energy
$\Delta\phi(bb, \tau\tau)$	The $\Delta\phi$ between the b-tagged jet pair and τ-lepton pair systems
quant b_0	b-tagging quantile of leading b-tagged jet
quant b_1	b-tagging quantile of sub-leading b-tagged jet
m_{HH}^*	Reduced 4-object invariant mass, defined as $m_{HH}^* = m_{HH} - m_{bb} - m_{\tau\tau}^{\text{MMC}} + 250\text{GeV}$
$\Delta R(b_0, \tau_0)$	The ΔR between the leading b-tagged jet and $\tau_{\text{had-vis}}$
$\text{cent}(bb\tau\tau)$	Centrality, taking into account only the HH decay products
$m_{\text{eff}}(\tau\tau j)$	Effective mass, taking into account the τ-lepton pair and central jets
$\text{spher}(bb\tau\tau)$	Sphericity, taking into account only the HH decay products
$\eta(\tau_0)$	Pseudorapidity of the leading $\tau_{\text{had-vis}}$
$\eta(\tau_1)$	Pseudorapidity of the sub-leading $\tau_{\text{had-vis}}$

A.4.3 $\tau_{had}\tau_{had}$ VBFSR optimised variables

TABLE A.6: Input variables for the high-m_{HH} ggF BDT training in the $\tau_{\text{had}}\tau_{\text{had}}$ channel.

Variable	**Description**
m_{HH}	Invariant mass of the HH system, reconstructed from the τ-lepton pair (using the MMC) and b-tagged jet pair
m_{bb}	Invariant mass of the b-tagged jet pair system
$m_{\tau\tau}^{\text{MMC}}$	Invariant mass of the τ-lepton pair system, calculated using the MMC
$\Delta R(b, b)$	The ΔR between the two b-tagged jets
$\Delta R(\tau, \tau)$	The ΔR between the two $\tau_{\text{had-vis}}$
n_jets	Number of jets in the event
T_1	Topness, as defined in Ref. [120] assuming σ_t = 5GeV and $\sigma_W = 5$GeV
E_T^{miss}	The missing transverse momentum of the event
$p_T(HH)$	Transverse momentum of the HH system
$m_T(\tau_1)$	Transverse mass of the sub-leading $\tau_{\text{had-vis}}$
$\Delta\phi(bb, E_T^{\text{miss}})$	The $\Delta\phi$ between the b-tagged jet pair system and missing transverse energy
$\Delta\phi(bb, \tau\tau)$	The $\Delta\phi$ between the b-tagged jet pair and τ-lepton pair systems
quant b_0	b-tagging quantile of leading b-tagged jet
quant b_1	b-tagging quantile of sub-leading b-tagged jet
$\Delta R(b_0, \tau_0)$	The ΔR between the leading b-tagged jet and $\tau_{\text{had-vis}}$
$\Delta R(b_1, \tau_1)$	The ΔR between the sub-leading b-tagged jet and $\tau_{\text{had-vis}}$
cent$(bb\tau\tau)$	Centrality, taking into account only the HH decay products
spher$(bb\tau\tau)$	Sphericity, taking into account only the HH decay products
pflow $(bb\tau\tau)$	Planar flow, taking into account only the HH decay products
$\eta(\tau_0)$	Pseudorapidity of the leading $\tau_{\text{had-vis}}$
$\eta(\tau_1)$	Pseudorapidity of the sub-leading $\tau_{\text{had-vis}}$

A.5 $\tau_{lep}\tau_{had}$-SLT ggF-SR optimised variables

A.5.1 SLT ggF low m_{HH} optimised variables

TABLE A.7: Input variables for the low-m_{HH} ggF BDT training in the $\tau_{\text{lep}}\tau_{\text{had}}$ SLT channel.

Variable	**Description**
m_{HH}	Invariant mass of the HH system, reconstructed from the τ-lepton pair (using the MMC) and b-tagged jet pair
m_{bb}	Invariant mass of the b-tagged jet pair system
$m_{\tau\tau}^{\text{MMC}}$	Invariant mass of the τ-lepton pair system, calculated using the MMC
$\Delta R(b, b)$	The ΔR between the two b-tagged jets
$\Delta R(\tau \text{ lep })$	The ΔR between the lepton and the hadronic τ system
mTW	The transverse mass of the reconstructed W boson
$\cos(\theta)_{b\bar{b}}^{\text{helicity}}$	The angle of two b-jets with respect to the Higgs rest frame
$p_T(\tau)$	Transverse momentum of the hadronic τ
$\Delta\phi\left(\tau\tau, E_T^{\text{miss}}\right)$	The $\Delta\phi$ between the τ-lepton pair system and missing transverse energy
E_T^{miss}	The missing transverse momentum of the event
n_jets	Number of jets in the event
$p_T\left(b_0\right)$	Transverse momentum of the leading b-tagged jet
T_1	Topness, as defined in Ref. [120] assuming $\sigma_t = 5\text{GeV}$ and $\sigma_W = 5\text{GeV}$.
$p_T(HH)$	Transverse momentum of the HH system
$\Delta R\left(b_1, \tau_1\right)$	The ΔR between the sub-leading b-tagged jet and lepton
$\Delta R\left(b_1, \tau_0\right)$	The ΔR between the sub-leading b-tagged jet and τ
$\Delta R\left(b_0, \tau_0\right)$	The ΔR between the leading b-tagged jet and τ
$p_T(\text{ lep })$	Transverse momentum of the lepton

A.5.2 SLT ggF high m_{HH} optimised variables

TABLE A.8: Input variables for the high-m_{HH} ggF BDT training in the $\tau_{\text{lep}}\tau_{\text{had}}$ SLT channel.

Variable	Description
m_{HH}	Invariant mass of the HH system, reconstructed from the τ-lepton pair (using the MMC) and b-tagged jet pair
m_{bb}	Invariant mass of the b-tagged jet pair system
$m_{\tau\tau}^{\text{MMC}}$	Invariant mass of the τ-lepton pair system, calculated using the MMC
$\Delta R(b, b)$	The ΔR between the two b-tagged jets
$\Delta R(\tau$ lep $)$	The ΔR between the lepton and the hadronic τ
mTW	The transverse mass of the reconstructed W boson
$\cos(\theta)_{b\bar{b}}^{\text{helicity}}$	The angle of two b-jets with respect to the Higgs rest frame
H_T	Total hadronic transverse energy in the event, perpendicular to the beamline
quant b_0	b-tagging quantile of leading b-tagged jet
T_1	Topness, as defined in Ref. [120]
quant b_1	b-tagging quantile of sub-leading b-tagged jet
$p_T(\tau)$	Transverse momentum of the τ
$\Delta R\left(b_1, \tau_0\right)$	The ΔR between the sub-leading b-tagged jet and τ
$\Delta\phi\left(\tau\tau, E_T^{\text{miss}}\right)$	The $\Delta\phi$ between the τ-lepton pair system and missing transverse energy
$p_T($ lep$)$	Transverse momentum of the lepton
$m_T(\tau)$	Transverse mass of the τ
$p_T\left(b_1\right)$	Transverse momentum of the sub-leading b-tagged jet

A.5.3 SLT VBF-SR optimised variables

TABLE A.9: Input variables for the VBF BDT training in the $\tau_{\text{lep}}\tau_{\text{had}}$ SLT channel.

Variable	**Description**
m_{HH}	Invariant mass of the HH system, reconstructed from the τ-lepton pair (using the MMC) and b-tagged jet pair
m_{bb}	Invariant mass of the b-tagged jet pair system
$m_{\tau\tau}^{\text{MMC}}$	Invariant mass of the τ-lepton pair system, calculated using the MMC
$\Delta R(b, b)$	The ΔR between the two b-tagged jets
$\Delta R(\tau$ lep $)$	The ΔR between the two τ-lepton pair system
m_{jj}^{VBF}	Invariant mass of the VBF jet system
fwm0 $(\tau\tau jf)$	0^{th} order Fox-Wolfram moment, taking into account the τ-lepton pair and central and forward jets
H_T	Total hadronic transverse energy in the event, perpendicular to the beamline
$\Delta R_{jj}^{\text{VBF}}$	The ΔR of the VBF jet system
$\text{mEff}(\tau\tau jf)$	Effective mass, taking into account the τ-lepton pair and central and forward jets
fwm4 (τjf)	4^{th} order Fox-Wolfram moment, taking into account the τ-lepton pair and central and forward jets
fwm2 $(\tau\tau jf)$	2^{nd} order Fox-Wolfram moment, taking into account the τ-lepton pair and central and forward jets
$\Delta\eta^{HH}$	The $\Delta\eta$ between the invariant mass of the HH system
$\Delta\eta_{jj}^{\text{VBF}}$	The $\Delta\eta$ between the two VBF jets
$\text{pflow}(\tau\tau jf)$	Planar flow, taking into account the τ-lepton pair and central and forward jets

A.6 $\tau_{lep}\tau_{had}$-LTT ggF-SR optimised variables

A.6.1 LTT ggF low m_{HH} optimised variables

TABLE A.10: Input variables for the low-m_{HH} ggF BDT training in the $\tau_{\text{lep}}\tau_{\text{had}}$ LTT channel.

Variable	**Description**
m_{HH}	Invariant mass of the HH system, reconstructed from the τ-lepton pair (using the MMC) and b-tagged jet pair
m_{bb}	Invariant mass of the b-tagged jet pair system
$m_{\tau\tau}^{\text{MMC}}$	Invariant mass of the τ-lepton pair system, calculated using the MMC
$\Delta R(b, b)$	The ΔR between the two b-tagged jets
$\Delta R(\tau$ lep $)$	The ΔR between the two τ-lepton pair system
mTW	The transverse mass of the reconstructed W boson
$\Delta p_T(\tau$ lep $)$	$p_T(\text{lep}) - p_T(\tau)$
$\Delta\phi\left(\text{lep}, E_T^{\text{miss}}\right)$	The $\Delta\phi$ between lepton and missing transverse energy
H_T	Total hadronic transverse energy in the event, perpendicular to the beamline
$\Delta\phi\left(\tau\tau, E_T^{\text{miss}}\right)$	The $\Delta\phi$ between the τ-lepton pair system and missing transverse energy
$m_T(\text{lep})$	Transverse mass of the MET and the lepton
MT2	STransverse momentum
$\Delta\eta(\tau$ lep $)$	The $\Delta\eta$ between the τ and lepton
T_1	Topness, as defined in Ref. [120] assuming $\sigma_t = 5\text{GeV}$ and $\sigma_W = 5\text{GeV}$.
T_2	Topness, as defined in Ref. [120] assuming $\sigma_t = 15\text{GeV}$ and $\sigma_W = 5\text{GeV}$.
E_T^{miss} Centrality	Position of the E_T^{miss} of the event in ϕ between τs.

A.6.2 LTT ggF high m_{HH} optimised variables

TABLE A.11: Input variables for the high-m_{HH} ggF BDT training in the $\tau_{\text{lep}}\tau_{\text{had}}$ LTT channel.

Variable	**Description**
m_{HH}	Invariant mass of the HH system, reconstructed from the τ-lepton pair (using the MMC) and b-tagged jet pair
m_{bb}	Invariant mass of the b-tagged jet pair system
$m_{\tau\tau}^{\text{MMC}}$	Invariant mass of the τ-lepton pair system, calculated using the MMC
$\Delta R(\tau\ \text{lep}\ )$	The ΔR between the two τ-lepton pair system
$\Delta p_T(\tau\ \text{lep}\ )$	$p_T(\text{lep}) - p_T(\tau)$
$\Delta\phi\left(\text{lep}, E_T^{\text{miss}}\right)$	The $\Delta\phi$ between lepton and missing transverse energy
H_T	Total hadronic transverse energy in the event, perpendicular to the beamline
$\Delta\phi\left(\tau\tau, E_T^{\text{miss}}\right)$	The $\Delta\phi$ between the τ-lepton pair system and missing transverse energy
m_{HH}^*	Reduced 4-object invariant mass, defined as $m_{HH}^* = m_{HH} - m_{bb} - m_{\tau\tau}^{\text{MMC}} + 250\text{GeV}$
T_1	Topness, as defined in Ref. [120]
T_2	Topness, as defined in Ref. [120]
mHHscaled	Scaled m_{HH} variable, computed from the four-momenta of the two Higgs candidates as mHHscaled $= \left(\alpha p_{H1}^{\mu} + \beta p_{H2}^{\mu}\right)^2$, where $\alpha = 125\text{GeV}/m_{H1}$ and $\beta = 125\text{GeV}/m_{H2}$
$\text{mEff}(b\bar{b}\tau\tau)$	Effective mass, taking into account only the HH decay products
$m\left(b_0\tau\right)$	Invariant mass of the leading b-jet and τ
$p_T(\tau\text{lep})$	Transverse momentum of the τ-lepton pair system
$m\left(b_1\tau\right)$	Invariant mass of the sub-leading b-jet and τ
$p_T(b\bar{b})$	Transverse momentum of the b-tagged jet pair system
$p_T\left(b_0\right)$	Transverse momentum of the leading b-tagged jet
$\Delta\phi(b\bar{b}, \tau\ \text{lep}\ )$	The $\Delta\phi$ between the b-tagged jet pair and τ-lepton pair systems

A.6.3 LTT ggF VBFSR optimised variables

TABLE A.12: Input variables for the VBF BDT training in the $\tau_{\text{lep}}\tau_{\text{had}}$ LTT channel.

Variable	**Description**
m_{HH}	Invariant mass of the HH system, reconstructed from the τ-lepton pair (using the MMC) and b-tagged jet pair
m_{bb}	Invariant mass of the b-tagged jet pair system
$m_{\tau\tau}^{\text{MMC}}$	Invariant mass of the τ-lepton pair system, calculated using the MMC
m_{jj}^{VBF}	Invariant mass of the VBF jet system
VBF $\eta_0 \times \eta_1$	Product of the pseudorapidities of the leading and sub-leading VBF jets
n_jets	Number of jets in the event
T_2	Topness, as defined in Ref. [120]
S_T	Total transverse energy in the event, summed over all jets, $\tau_{\text{had-vis}}$ and leptons in the event and E_T^{miss}
$p_T(HH)$	Transverse momentum of the HH system
$p_T(\tau)$	Transverse momentum of the τ's
$\cos\theta^*$	Tau decay angle
$p_T(\tau$ lep $)$	Transverse momentum of the τ-lepton pair system
$p_T\,(b_0)$	Transverse momentum of the leading b-tagged jet
m_{HH}^*	Reduced 4-object invariant mass, defined as $m_{HH}^* = m_{HH} - m_{bb} - m_{\tau\tau}^{\text{MMC}} + 250\text{GeV}$
mTW	The transverse mass of the reconstructed W boson
$\cos(\theta)_{\tau\tau}^{\text{helicity}}$	The angle of the τ-lepton pair with respect to the Higgs rest frame
mHHscaled	Scaled m_{HH} variable, computed from the four-momenta of the two Higgs candidates as mHHscaled $= (\alpha p_{H1}^{\mu} + \beta p_{H2}^{\mu})^2$, where $\alpha = 125\text{GeV}/m_{H1}$ and $\beta = 125\text{GeV}/m_{H2}$
$\Delta R\,(b_0, \tau_0)$	The ΔR between the leading b-tagged jet and τ

Bibliography

[1] "Observation of a new boson at a mass of 125 GeV with the CMS experiment at the LHC". In: (). https://www.sciencedirect.com/science/article/pii/S0370269312008581. DOI: https://doi.org/10.1016/j.physletb.2012.08.021. URL: https://www.sciencedirect.com/science/article/pii/S0370269312008581.

[2] "Observation of a new particle in the search for the Standard Model Higgs boson with the ATLAS detector at the LHC". In: (). https://www.sciencedirect.com/science/article/pii/S037026931200857X. DOI: https://doi.org/10.1016/j.physletb.2012.08.020. URL: https://www.sciencedirect.com/science/article/pii/S037026931200857X.

[3] F. Englert and R. Brout. "Broken Symmetry and the Mass of Gauge Vector Mesons". In: Phys. Rev. Lett. 13 (9 1964). https://link.aps.org/doi/10.1103/PhysRevLett.13.321, pp. 321–323. DOI: 10.1103/PhysRevLett.13.321. URL: https://link.aps.org/doi/10.1103/PhysRevLett.13.321.

[4] Peter W. Higgs. "Broken Symmetries and the Masses of Gauge Bosons". In: Phys. Rev. Lett. 13 (16 1964). https://link.aps.org/doi/10.1103/PhysRevLett.13.508, pp. 508–509. DOI: 10.1103/PhysRevLett.13.508. URL: https://link.aps.org/doi/10.1103/PhysRevLett.13.508.

[5] Peter W. Higgs. "Spontaneous Symmetry Breakdown without Massless Bosons". In: Phys. Rev. 145 (4 1966), pp. 1156–1163. DOI: 10.1103/PhysRev.145.1156. URL: https://link.aps.org/doi/10.1103/PhysRev.145.1156.

[6] G.C. Branco, P.M. Ferreira, and L. Lavoura .. "Theory and phenomenology of two-Higgs-doublet models". In: Physics Reports 516.1 (2012). https://www.sciencedirect.com/science/article/pii/S0370157312000695, pp. 1–102. ISSN: 0370-1573. DOI: https://doi.org/10.1016/j.physrep.2012.02.002. URL: https://www.sciencedirect.com/science/article/pii/S0370157312000695.

[7] Lisa Randall and Raman Sundrum. "Large Mass Hierarchy from a Small Extra Dimension". In: Phys. Rev. Lett. 83 (17 1999). https://link.aps.org/doi/10.1103/PhysRevLett.83.3370, pp. 3370–3373. DOI: 10.1103/PhysRevLett.83.3370. URL: https://link.aps.org/doi/10.1103/PhysRevLett.83.3370.

[8] "Technical Design Report for the ATLAS Inner Tracker Strip Detector". In: (Apr. 2017). URL: https://cds.cern.ch/record/2257755. URL: https://cds.cern.ch/record/2257755.

[9] O Brüning and L Rossi. "The High Luminosity Large Hadron Collider: The New Machine for Illuminating the Mysteries of Universe". In: World Scientific Publishing Company Pte Limited. Advanced Series on Directions in High Energy Physics (2015). URL: https://books.google.com/books?id=8pJEDwAAQBAJ.

[10] C. Agapopoulou et al. "Performance in beam tests of irradiated Low Gain Avalanche Detectors for the ATLAS High Granularity Timing Detector". In: JINST (). URL: https://iopscience.iop.org/article/10.1088/1748-0221/17/09/P09026. DOI: 10.1088/1748-0221/17/09/P09026.

[11] ATLAS Collaboration. "Search for resonant and non-resonant Higgs boson pair production in the $b\bar{b}\tau^+\tau^-$decay channel using 13 TeV pp collision data from the ATLAS detector". In: JHEP (). URL: https://link.springer.com/article/10.1007/JHEP07(2023)040. URL: https://link.springer.com/article/10.1007/JHEP07(2023)040.

[12] "Review of Particle Physics". In: PhysRevD.98.030001 (). URL: https://link.aps.org/doi/10.1103. URL: https://link.aps.org/doi/10.1103.

[13] Jeffrey Goldstone, Abdus Salam, and Steven Weinberg. "Broken Symmetries". In: Physical Review 127 (3 1962), pp. 965–970. DOI: 10.1103/PhysRev.127.965. URL: https://link.aps.org/doi/10.1103/PhysRev.127.965.

[14] W. Bentz et al. "Reassessment of the NuTeV determination of the weak mixing angle". In: https://doi.org/10.1016/j.physletb.2010.09.001 693 (2010), pp. 462–466. DOI: 10.1016/j.physletb.2010.09.001. arXiv: 0908.3198 [nucl-th].

[15] D de Florian et al. "Handbook of LHC Higgs Cross Sections: 4. Deciphering the Nature of the Higgs Sector". In: (2016). arXiv: 1610.07922 [hep-ph].

[16] Public plots. "LHC Higgs Cross Section Working Group". In: (). URL: https://twiki.cern.ch/twiki/bin/view/LHCPhysics/HiggsXSBR. URL: https://twiki.cern.ch/twiki/bin/view/LHCPhysics/HiggsXSBR.

[17] CERN. "Handbook of LHC Higgs Cross Sections: 4. Deciphering the Nature of the Higgs Sector". In: CERN Yellow Reports: Monographs (). URL: https://e-publishing.cern.ch/index.php/CYRM/issue/view/32.

[18] LHC Higgs Cross Section Working Group. "LHC Higgs Cross Section Working Group". In: LHC Physics Analysis Summary (). URL: https://twiki.cern.ch/twiki/bin/view/LHCPhysics/LHCHXSWGHH.

[19] J. Baglio et al. "$gg \to HH$: Combined Uncertainties". In: Physics Letters B (Aug. 2020), 056002 (2020). URL: https://cds.cern.ch/record/2729029.

[20] G. W. Bennett et al. (Muon g 2 Collaboration). E821 muon anomalous magnetic moment. 2006. URL: https://journals.aps.org/prd/abstract/10.1103/PhysRevD.73.072003.

[21] BaBar Collaboration. "Evidence for an excess of $\bar{B}\to D^{(*)}\tau^-\bar{\nu_\tau}$ Decays. arXiv:1205.5442v2 [hep-ex]". In: Physical Review Letters 108 (2012), p. 211801. DOI: 10.1103/PhysRevLett.108.211801. URL: https://arxiv.org/abs/1205.5442v2.

[22] BaBar Collaboration. "Measurement of an excess of $\bar{B}\to D^{(*)}\tau^-\bar{\nu_\tau}$ decays and implications for charged Higgs bosons. Phys. Rev. D 88, 072012". In: Physical Review D 88 (2013), p. 072012. DOI: 10.1103/PhysRevD.88.072012. URL: https://journals.aps.org/prd/abstract/10.1103/PhysRevD.88.072012.

[23] Belle Collaboration. "Measurement of the branching ratio of $\bar{B}\to D^{(*)}\tau^-\bar{\nu_\tau}$ relative to $\bar{B}\to D^{(*)}l^-\bar{\nu_l}$ decays with hadronic tagging at Belle Phys. Rev. D 92, 072014". In: Physical Review D 92 (2014), p. 072014. DOI: 10.1103/PhysRevD.92.072014. URL: https://journals.aps.org/prd/abstract/10.1103/PhysRevD.92.072014.

[24] Belle Collaboration. "Measurement of the branching ratio of $\bar{B}^0\to D^{(*+)}\tau^-\bar{\nu_\tau}$ relative to $\bar{B}^0\to D^{(*+)}l^-\bar{\nu_l}$ decays with a semileptonic tagging method. Phys. Rev. D 94, 072007". In: Physical Review D 94 (2016), p. 072007. DOI: 10.1103/PhysRevD.94.072007. URL: https://journals.aps.org/prd/abstract/10.1103/PhysRevD.94.072007.

[25] LHCb Collaboration. "Measurement of the Ratio of Branching Fractions $\mathcal{B}(\overline{B}^0 \to D^{*+}\tau^-\overline{\nu}_\tau)/\mathcal{B}(\overline{B}^0 \to D^{*+}\mu^-\overline{\nu}_\mu)$". In: Phys. Rev. Lett. 115 (2015), p. 111803. DOI: 10.1103/PhysRevLett.115.111803. URL: https://journals.aps.org/prl/abstract/10.1103/PhysRevLett.115.111803.

[26] LHCb Collaboration. "Measurement of CP-Averaged Observables in the $\overline{B^0}{\to}K^{0*}\mu^+\mu^-$ Decay". In: Phys. Rev. Lett. 125 (2020), p. 011802. DOI: 10.1103/PhysRevLett.125.011802. URL: https://journals.aps.org/prl/abstract/10.1103/PhysRevLett.125.011802.

[27] C. Bambi and A. D. Dolgov. "Introduction to Particle Cosmology - The Standard Model of Cosmology and its Open Problems". In: (2016). ISBN 978-3-662-48078-6.

[28] ATLAS Collaboration. "ATLAS detector and physics performance: Technical Design Report, 1". In: CERN Report (1999). URL: https://cds.cern.ch/record/391176.

[29] ATLAS Collaboration. "ATLAS detector and physics performance: Technical Design Report, 2". In: CERN Report (1999). URL: https://cds.cern.ch/record/391177.

[30] ATLAS Collaboration. "The ATLAS Experiment at the CERN Large Hadron Collider". In: JINST 3 (2008), S08003. DOI: 10.1088/1748-0221/3/08/S08003. URL: https://iopscience.iop.org/article/10.1088/1748-0221/3/08/S08003.

[31] Lyndon Evans and Philip Bryant. "LHC Machine". In: JINST 3 (2008), S08001. DOI: 10.1088/1748-0221/3/08/S08001. URL: https://iopscience.iop.org/article/10.1088/1748-0221/3/08/S08001.

[32] The CMS Collaboration. "The CMS experiment at the CERN LHC". In: JINST 3 (2008), S08004. DOI: 10.1088/1748-0221/3/08/S08004. URL: https://iopscience.iop.org/article/10.1088/1748-0221/3/08/S08004.

[33] The ALICE Collaboration. "The ALICE experiment at the CERN LHC". In: JINST 3 (2008), S08002. DOI: 10.1088/1748-0221/3/08/S08002. URL: https://iopscience.iop.org/article/10.1088/1748-0221/3/08/S08002.

[34] The LHCb Collaboration. "The LHCb experiment at the CERN LHC". In: JINST 3 (2008), S08005. DOI: 10.1088/1748-0221/3/08/S08005. URL: https://iopscience.iop.org/article/10.1088/1748-0221/3/08/S08005.

[35] The TOTEM Collaboration. "The TOTEM experiment at the CERN LHC". In: JINST 3 (2008), S08007. DOI: 10.1088/1748-0221/3/08/S08007. URL: https://iopscience.iop.org/article/10.1088/1748-0221/3/08/S08007.

[36] MoEDAL Collaboration. "Technical Design Report of the MoEDAL Experiment". In: CERN Report (). DOI: https://cds.cern.ch/record/1181486. URL: https://cds.cern.ch/record/1181486.

[37] The LHCf Collaboration. "The LHCf experiment at the CERN LHC". In: JINST 3 (2008), S08006. DOI: 10.1088/1748-0221/3/08/S08006. URL: https://iopscience.iop.org/article/10.1088/1748-0221/3/08/S08006.

[38] ATLAS Collaboration. "ATLAS Luminosity Results for Run-2 of the LHC". In: ATLAS Public Results (Available online). URL: https://twiki.cern.ch/twiki/bin/view/AtlasPublic/LuminosityPublicResultsRun2.

[39] John C. Collins and Davison E. Soper. "Parton distribution and decay functions". In: Nuclear Physics B 194.3 (1982), pp. 445–492. ISSN: 0550-3213. DOI: 10.1016/0550-3213(82)90021-9. URL: https://www.sciencedirect.com/science/article/pii/0550321382900219.

[40] A. D. Martin et al. "Parton distributions for the LHC". In: European Physical Journal C 63.2 (2009), pp. 189–285. DOI: 10.1140/epjc/s10052-009-1072-5. URL: https://link.springer.com/article/10.1140/epjc/s10052-009-1072-5.

[41] G. Altarelli and G. Parisi. "Asymptotic freedom in parton language". In: Nuclear Physics B 126.2 (1977), pp. 298–318. ISSN: 0550-3213. DOI: 10.1016/0550-3213(77)90384-4. URL: https://www.sciencedirect.com/science/article/pii/0550321377903844.

[42] Joao Pequenao. "Computer generated image of the whole ATLAS detector". In: CERN Document Server (Available online). URL: https://cds.cern.ch/record/1095924.

[43] ATLAS Collaboration. "ATLAS central solenoid: Technical Design Report". In: CERN Document Server (1997). URL: https://cds.cern.ch/record/331067.

[44] ATLAS Collaboration. "ATLAS inner detector: Technical Design Report, 1". In: CERN Document Server (1997). URL: https://cds.cern.ch/record/331063.

[45] Joao Pequenao. “Computer generated image of the ATLAS inner detector”. In: CERN Document Server (). URL: https://cds.cern.ch/record/1095926.

[46] ATLAS Collaboration. “ATLAS Insertable B-Layer: Technical Design Report”. In: CERN Document Server (2010). URL: https://cds.cern.ch/record/331069.

[47] Joao Pequenao. “Computer Generated image of the ATLAS calorimeter”. In: CERN Document Server (). URL: https://cds.cern.ch/record/1095927.

[48] ATLAS Collaboration. “ATLAS muon spectrometer: Technical Design Report, 2”. In: CERN Document Server (1997). URL: https://cds.cern.ch/record/331068.

[49] ATLAS Collaboration. Performance of the ATLAS Trigger System in 2015. 2015. URL: https://cds.cern.ch/record/2235584.

[50] Joao Pequenao. “How ATLAS detects particles: diagram of particle paths in the detector”. In: CERN Document Server (). URL: https://cds.cern.ch/record/1505342.

[51] ATLAS Collaboration. “Performance of the ATLAS track reconstruction algorithms in dense environments in LHC Run 2”. In: European Physical Journal C 77.5 (2017), p. 285. URL: https://link.springer.com/article/10.1140/epjc/s10052-017-5225-7.

[52] E. Belau, R. Klanner, and M. Riebesell. “Charge collection in silicon strip detectors”. In: Nuclear Instruments 223.2-3 (1984), pp. 358–361. ISSN: 0167-5087. DOI: https://doi.org/10.1016/0167-5087(84)90279-5. URL: https://www.sciencedirect.com/science/article/pii/0167508783905914.

[53] R. Frühwirth. “Application of Kalman filtering to track and vertex fitting”. In: Nuclear Instruments 262.2 (1987), pp. 444–450. ISSN: 0168-9002. DOI: https://doi.org/10.1016/0168-9002(87)90887-4. URL: https://www.sciencedirect.com/science/article/pii/0168900287908874.

[54] ATLAS Collaboration. “The new ATLAS track reconstruction (NEWT)”. In: Journal of Physics: Conference Series, Volume 119, 032014 (2019). URL: https://iopscience.iop.org/article/10.1088/1742-6596/119/3/032014.

[55] ATLAS Collaboration. “Performance of primary vertex reconstruction in proton-proton collisions at $\sqrt{s} = 7$ TeV in the ATLAS experiment”. In: ATLAS-CONF-2010-069 (2010). URL: https://cds.cern.ch/record/1281344.

[56] ATLAS Collaboration. "Reconstruction of primary vertices at the ATLAS experiment in Run 1 proton–proton collisions at the LHC". In: European Physical Journal C, Volume 77, Article 332 (2017). URL: https://link.springer.com/article/10.1140/epjc/s10052-017-4887-5.

[57] ATLAS Collaboration. "Electron reconstruction and identification in the ATLAS experiment using the 2015 and 2016 LHC proton-proton collision data at $\sqrt{s} = 13$ TeV". In: European Physical Journal C, Volume 79, Article 639 (2019). URL: https://arxiv.org/abs/1902.04655.

[58] ATLAS Collaboration. "Electron and photon energy calibration with the ATLAS detector using LHC Run 1 data". In: European Physical Journal C, Volume 74, Article 3071 (2014). URL: https://arxiv.org/abs/1407.5063.

[59] ATLAS Collaboration. "Electron and photon energy calibration with the ATLAS detector using 2015-2016 LHC proton-proton collision data". In: European Physical Journal C, Volume 74, Article 3071 (2018). URL: https://arxiv.org/abs/1812.03848.

[60] ATLAS Collaboration. "Muon reconstruction performance of the ATLAS detector in proton-proton collision data at $\sqrt{s} = 13$ TeV". In: Eur. Phys. J. C 76 (2016), p. 292. DOI: 10.1140/epjc/s10052-016-4120-y. arXiv: 1603.05598 [hep-ex]. URL: https://link.springer.com/article/10.1140/epjc/s10052-016-4120-y.

[61] ATLAS Collaboration. "Measurement of the muon reconstruction performance of the ATLAS detector using 2011 and 2012 LHC proton-proton collision data". In: Eur. Phys. J. C 74 (2014), p. 3130. DOI: 10.1140/epjc/s10052-014-3130-x. arXiv: 1407.3935 [hep-ex]. URL: https://link.springer.com/article/10.1140/epjc/s10052-014-3130-x.

[62] Gavin P. Salam. "Towards Jetography". In: Eur. Phys. J. C 67 (2010), pp. 637–686. DOI: 10.1140/epjc/s10052-010-1314-6. arXiv: 0906.1833 [hep-ph].

[63] T. Carli, K. Rabbertz, and S. Schumann. "Studies of Quantum Chromodynamics at the LHC". In: Springer, Cham (2015). URL: https://link.springer.com/chapter/10.1007/978-3-319-15001-7_5.

[64] Georges Aad et al. "Topological cell clustering in the ATLAS calorimeters and its performance in LHC Run 1". In: Eur. Phys. J. C 77 (2017), p. 490. DOI: 10.1140/epjc/s10052-017-5004-5. arXiv: 1603.02934 [hep-ex].

[65] M. Cacciari, G. P. Salam, and G. Soyez. “The anti-kt jet clustering algorithm”. In: JHEP 04 (2008), p. 063. URL: https://iopscience.iop.org/article/10.1088/1126-6708/2008/04/063.

[66] Morad Aaboud et al. “Determination of jet calibration and energy resolution in proton-proton collisions at $\sqrt{s} = 8$ TeV using the ATLAS detector”. In: Eur. Phys. J. C 80.12 (2020), p. 1104. DOI: 10.1140/epjc/s10052-020-08477-8. arXiv: 1910.04482 [hep-ex].

[67] ATLAS Collaboration. “Jet energy scale measurements and their systematic uncertainties in proton-proton collisions at $\sqrt{s} = 13$ TeV with the ATLAS detector”. In: Phys. Rev. D 96 (7 2017), p. 072002. DOI: 10.1103/PhysRevD.96.072002. URL: https://journals.aps.org/prd/abstract/10.1103/PhysRevD.96.072002.

[68] Matteo Cacciari and Gavin P. Salam. “Pileup subtraction using jet areas”. In: Physics Letters B 659.1 (2008), pp. 119–126. ISSN: 0370-2693. DOI: 10.1016/j.physletb.2007.09.077. URL: https://www.sciencedirect.com/science/article/pii/S0370269307011094.

[69] ATLAS Collaboration. “Tagging and suppression of pileup jets”. In: ATLAS-CONF-2014-018 (2014). URL: https://cds.cern.ch/record/1700870.

[70] ATLAS Collaboration. “ATLAS b-jet identification performance and efficiency measurement with $t\bar{t}$ events in pp collisions at $\sqrt{s} = 13\,\text{TeV}$”. In: Eur. Phys. J. C 79 (2019), p. 970. DOI: 10.1140/epjc/s10052-019-7450-8. arXiv: 1907.05120 [hep-ex]. URL: https://link.springer.com/article/10.1140/epjc/s10052-019-7450-8.

[71] ATLAS Collaboration. “Optimization and performance studies of the ATLAS b-tagging algorithms for the 2017-18 LHC run”. In: ATL-PHYS-PUB-2017-013 (2017). URL: https://cds.cern.ch/record/2273281.

[72] ATLAS Collaboration. “Identification of Jets Containing b-Hadrons with Recurrent Neural Networks at the ATLAS Experiment”. In: (2017). URL: https://cds.cern.ch/record/2255226.

[73] ATLAS Collaboration. “Evidence for the $H \to b\bar{b}$ decay with the ATLAS detector”. In: JHEP 12 (2017), p. 024. DOI: 10.1007/JHEP12(2017)024. URL: https://link.springer.com/article/10.1007/JHEP12(2017)024.

[74] Morad Aaboud et al. "Performance of missing transverse momentum reconstruction with the ATLAS detector using proton-proton collisions at $\sqrt{s}$ = 13 TeV". In: Eur. Phys. J. C 78.11 (2018), p. 903. DOI: 10.1140/epjc/s10052-018-6288-9. arXiv: 1802.08168 [hep-ex]. URL: https://link.springer.com/article/10.1140/epjc/s10052-018-6288-9.

[75] ATLAS Collaboration. "Reconstruction, Energy Calibration, and Identification of Hadronically Decaying Tau Leptons in the ATLAS Experiment for Run-2 of the LHC". In: ATL-PHYS-PUB-2015-045 (2015). URL: https://cds.cern.ch/record/2064383.

[76] ATLAS Collaboration. "Identification of hadronic tau lepton decays using neural networks in the ATLAS experiment". In: ATL-PHYS-PUB-2019-033 (2019). URL: https://cds.cern.ch/record/2688062.

[77] A. Elagin et al. "A new mass reconstruction technique for resonances decaying to $\tau\tau$". In: Nuclear Instruments and Methods in Physics Research Section A 654.1 (2011), pp. 481–489. ISSN: 0168-9002. DOI: 10.1016/j.nima.2011.07.009. URL: https://doi.org/10.1016/j.nima.2011.07.009.

[78] ATLAS Collaboration. "Search for non-resonant Higgs boson pair production in the $2b + 2\ell + E_{\mathrm{T}}^{\mathrm{miss}}$ final state in pp collisions at $\sqrt{s} = 13\mathrm{TeV}$ with the ATLAS detector, ATLAS-CONF-2023-064". In: ATLAS-CONF-2023-064 (). URL: https://cds.cern.ch/record/2873518.

[79] ATLAS Collaboration. "Search for resonant and non-resonant Higgs boson pair production in the $b\bar{b}\tau^+\tau^-$ decay channel using 13 TeV pp collision data from the ATLAS detector". In: arXiv:2209.10910 [hep-ex] (2022). arXiv: 2209.10910 [hep-ex]. URL: https://arxiv.org/abs/2209.10910.

[80] ATLAS Collaboration. "Combination of searches for non-resonant and resonant Higgs boson pair production in the $b\bar{b}\gamma\gamma$, $b\bar{b}\tau^+\tau^-$, and $b\bar{b}b\bar{b}$ decay channels using pp collisions at $\sqrt{s} = 13$ TeV with the ATLAS detector". In: ATLAS-CONF-2021-052 (2021). URL: https://cds.cern.ch/record/2786865.

[81] ATLAS Collaboration. "Constraining the Higgs boson self-coupling from single- and double-Higgs production with the ATLAS detector using pp collisions at $\sqrt{s} = 13$ TeV". In: ATLAS-CONF-2022-050 (2022). URL: https://cds.cern.ch/record/2816332.

[82] ATLAS Collaboration. "Luminosity determination in pp collisions at $\sqrt{s} = 13\,\text{TeV}$ using the ATLAS detector at the LHC". In: arXiv:2212.09379 [hep-ex] (2022). arXiv: 2212.09379 [hep-ex].

[83] GEANT4 Collaboration, S. Agostinelli, et al. "GEANT4 – a simulation toolkit". In: Nucl. Instrum. Meth. A 506 (2003), p. 250. DOI: 10.1016/S0168-9002(03)01368-8.

[84] T. Sjöstrand, S. Mrenna, and P. Skands. "A brief introduction to PYTHIA 8.1". In: Comput. Phys. Commun. 178 (2008), pp. 852–867. DOI: 10.1016/j.cpc.2008.01.036. arXiv: 0710.3820 [hep-ph].

[85] ATLAS Collaboration. The Pythia-8 A3 tune description of ATLAS minimum bias and inelastic ATL-PHYS-PUB-2016-017. 2016. URL: https://cds.cern.ch/record/2206965.

[86] Richard D. Ball et al. "Parton distributions with LHC data". In: Nucl. Phys. B 867 (2013), p. 244. DOI: 10.1016/j.nuclphysb.2012.10.003. arXiv: 1207.1303 [hep-ph].

[87] D. J. Lange. "The EvtGen particle decay simulation package". In: Nucl. Instrum. Meth. A 462 (2001), p. 152. DOI: 10.1016/S0168-9002(01)00089-4.

[88] Enrico Bothmann et al. "Event generation with Sherpa 2.2". In: SciPost Phys. 7.3 (2019), p. 034. DOI: 10.21468/SciPostPhys.7.3.034. arXiv: 1905.09127 [hep-ph].

[89] ATLAS Collaboration. "The ATLAS Simulation Infrastructure". In: The European Physical Journal C 70 (2010). DOI: 10.1140/epjc/s10052-010-1429-9. arXiv: 1005.4568 [physics.ins-det]. URL: https://link.springer.com/article/10.1140/epjc/s10052-010-1429-9.

[90] Simone Alioli et al. "A general framework for implementing NLO calculations in shower Monte Carlo programs: the POWHEG BOX". In: Journal of High Energy Physics 06 (2010), p. 043. DOI: 10.1007/JHEP06(2010)043. arXiv: 1002.2581 [hep-ph]. URL: https://link.springer.com/article/10.1007/JHEP06(2010)043.

[91] J. Alwall et al. "The automated computation of tree-level and next-to-leading order differential cross sections, and their matching to parton shower simulations". In: Journal of High Energy Physics 07 (2014), p. 079. DOI: 10.1007/JHEP07(2014)079. arXiv: 1405.0301 [hep-ph].

[92] Richard D. Ball et al. "Parton distributions for the LHC run II". In: 04 (2015), p. 040. DOI: 10.1007/JHEP04(2015)040. arXiv: 1410.8849 [hep-ph].

[93] P. Nason. "A New method for combining NLO QCD with shower Monte Carlo algorithms". In: JHEP 11 (2004), p. 040. DOI: 10.1088/1126-6708/2004/11/040. arXiv: hep-ph/0409146 [hep-ph].

[94] S. Frixione, P. Nason and C. Oleari. "Matching NLO QCD computations with parton shower simulations: the POWHEG method". In: JHEP 11 (2007), p. 070. DOI: 10.1088/1126-6708/2007/11/070. arXiv: 0709.2092 [hep-ph].

[95] Simone Alioli et al. "A general framework for implementing NLO calculations in shower Monte Carlo programs: the POWHEG BOX". In: JHEP 06 (2010), p. 043. DOI: 10.1007/JHEP06(2010)043. arXiv: 1002.2581 [hep-ph].

[96] NNPDF Collaboration. "Parton distributions for the LHC Run II". In: (2014). arXiv: 1410.8849 [hep-ph].

[97] Torbjorn Sjostrand et al. "An Introduction to PYTHIA 8.2". In: Comput. Phys. Commun. 191 (2015), pp. 159–177. arXiv: 1410.3012 [hep-ph].

[98] ATLAS Collaboration. ATLAS Pythia 8 tunes to 7 TeV data. ATL-PHYS-PUB-2014-021. 2014. URL: https://cds.cern.ch/record/1966419.

[99] ATLAS Collaboration. Summary of ATLAS Pythia 8 tunes. ATL-PHYS-PUB-2012-003. 2012. URL: https://cds.cern.ch/record/1474107.

[100] Richard D. Ball et al. "Parton distributions with LHC data". In: Nuclear Physics B 867.2 (2013), pp. 244 –289. ISSN: 0550-3213. DOI: https://doi.org/10.1016/j.nuclphysb.2012.10.003. URL: http://www.sciencedirect.com/science/article/pii/S0550321312005500.

[101] D. J. Lange. "The EvtGen particle decay simulation package". In: Nucl. Instrum. Meth. A 462 (2001), p. 152. DOI: 10.1016/S0168-9002(01)00089-4.

[102] Pierre Artoisenet et al. "Automatic spin-entangled decays of heavy resonances in Monte Carlo simulations". In: JHEP 03 (2013), p. 015. DOI: 10.1007/JHEP03(2013)015. arXiv: 1212.3460 [hep-ph].

[103] Tanju Gleisberg and Stefan Höche. "Comix, a new matrix element generator". In: JHEP 12 (2008), p. 039. DOI: 10.1088/1126-6708/2008/12/039. arXiv: 0808.3674 [hep-ph].

[104] Federico Buccioni et al. "OpenLoops 2". In: Eur. Phys. J. C 79.10 (2019), p. 866. DOI: 10.1140/epjc/s10052-019-7306-2. arXiv: 1907.13071 [hep-ph].

[105] Fabio Cascioli, Philipp Maierhöfer, and Stefano Pozzorini. "Scattering Amplitudes with Open Loops". In: Phys. Rev. Lett. 108 (2012), p. 111601. DOI: `10.1103/PhysRevLett.108.111601`. arXiv: `1111.5206 [hep-ph]`.

[106] Ansgar Denner, Stefan Dittmaier, and Lars Hofer. "COLLIER: A fortran-based complex one-loop library in extended regularizations". In: Comput. Phys. Commun. 212 (2017), pp. 220–238. DOI: `10.1016/j.cpc.2016.10.013`. arXiv: `1604.06792 [hep-ph]`.

[107] Stefan Höche et al. "A critical appraisal of NLO+PS matching methods". In: JHEP 09 (2012), p. 049. DOI: `10.1007/JHEP09(2012)049`. arXiv: `1111.1220 [hep-ph]`.

[108] Stefan Höche et al. "QCD matrix elements + parton showers. The NLO case". In: JHEP 04 (2013), p. 027. DOI: `10.1007/JHEP04(2013)027`. arXiv: `1207.5030 [hep-ph]`.

[109] S. Catani et al. "QCD Matrix Elements + Parton Showers". In: JHEP 11 (2001), p. 063. DOI: `10.1088/1126-6708/2001/11/063`. arXiv: `hep-ph/0109231`.

[110] Stefan Höche et al. "QCD matrix elements and truncated showers". In: JHEP 05 (2009), p. 053. DOI: `10.1088/1126-6708/2009/05/053`. arXiv: `0903.1219 [hep-ph]`.

[111] ATLAS Collaboration. "Modelling and computational improvements to the simulation of single vector-boson plus jet processes for the ATLAS experiment". In: JHEP 08 (2021), p. 089. DOI: `10.1007/JHEP08(2022)089`. arXiv: `2112.09588 [hep-ex]`.

[112] ATLAS Collaboration. "Measurement of the Z/γ^* boson transverse momentum distribution in pp collisions at $\sqrt{s}$ = 7 TeV with the ATLAS detector". In: JHEP 09 (2014), p. 145. DOI: `10.1007/JHEP09(2014)145`. arXiv: `1406.3660 [hep-ex]`.

[113] J. Pumplin et al. "New generation of parton distributions with uncertainties from global QCD analysis". In: JHEP 07 (2002), p. 012. DOI: `10.1088/1126-6708/2002/07/012`. arXiv: `hep-ph/0201195 [hep-ph]`.

[114] Morad Aaboud et al. "Jet reconstruction and performance using particle flow with the ATLAS Detector". In: Eur. Phys. J. C77.7 (2017), p. 466. DOI: `10.1140/epjc/s10052-017-5031-2`. arXiv: `1703.10485 [hep-ex]`.

[115] ATLAS Collaboration. “ATLAS Overlap Removal Tool: AssociationUtils”. In: (). URL: https://gitlab.cern.ch/atlas/athena/tree/21.2/PhysicsAnalysis/AnalysisCommon/AssociationUtils/.

[116] ATLAS Collaboration. “Recommended Overlap Removal Working Points”. In: (). URL: https://indico.cern.ch/event/631313/contributions/2683959/attachments/1518878/2373377/Farrell_ORTools_ftaghbb.pdf.

[117] ATLAS Collaboration. “Search for Resonant and Nonresonant Higgs Boson Pair Production in the $b\bar{b}\tau^+\tau^-$ Decay Channel in pp Collisions at $\sqrt{s} = 13$ TeV with the ATLAS Detector”. In: Phys. Rev. Lett. 121 (19 2018), p. 191801. DOI: 10.1103/PhysRevLett.121.191801. URL: https://link.aps.org/doi/10.1103/PhysRevLett.121.191801.

[118] A. Hoecker et al. “TMVA - Toolkit for Multivariate Data Analysis”. In: arXiv:physics/0703039 (). URL: https://arxiv.org/abs/physics/0703039v5.

[119] Catherine Bernaciak et al. “Fox-Wolfram moments in Higgs physics,” in: Physical Review D 87.7 (2013). DOI: 10.1103/physrevd.87.073014. URL: https://doi.org/10.1103\%2Fphysrevd.87.073014.

[120] Jeong Han Kim et al. “Probing the Triple Higgs Self-Interaction at the Large Hadron Collider”. In: Phys. Rev. Lett. 122.9 (2019), p. 091801. DOI: 10.1103/PhysRevLett.122.091801. arXiv: 1807.11498 [hep-ph].

[121] G. Aad et al. “Luminosity determination in pp collisions at $\sqrt{s} = 13$ TeV using the ATLAS detector at the LHC”. In: Eur. Phys. J. C 83.10 (2023), p. 982. DOI: 10.1140/epjc/s10052-023-11747-w. arXiv: 2212.09379 [hep-ex]. URL: https://link.springer.com/article/10.1140/epjc/s10052-023-11747-w.

[122] “Jet energy resolution in proton-proton collisions $\sqrt{s} = 7$ TeV recorded in 2010 with the ATLAS detector”. In: Eur. Phys. J. C 73 (2013). URL: https://cds.cern.ch/record/1489592.

[123] ATLAS Collaboration. “Performance of b-jet identification in the ATLAS experiment”. In: JINST 11.04 (2016), P04008. URL: http://stacks.iop.org/1748-0221/11/i=04/a=P04008.

[124] Georges Aad et al. “Measurements of WH and ZH production in the $H \to b\bar{b}$ decay channel in pp collisions at 13 TeV with the ATLAS detector”. In: Eur. Phys. J. C 81.2 (2021), p. 178. DOI: 10.1140/epjc/s10052-020-08677-2. arXiv: 2007.02873 [hep-ex]. URL: https:

//link.springer.com/article/10.1140/epjc/s10052-020-08677-2.

[125] R. Frederix and S. Frixione. “Merging meets matching in MC@NLO”. In: JHEP 12 (2012) 061 (). URL: https://link.springer.com/article/10.1007/JHEP12(2012)061.

[126] ATLAS Collaboration. “Object-based missing transverse momentum significance in the ATLAS detector”. In: ATLAS-CONF-2018-038 (2018). URL: https://inspirehep.net/literature/1682356.

[127] Glen Cowan et al. “Asymptotic formulae for likelihood-based tests of new physics”. In: Eur. Phys. J. C 10.1140/epjc/s10052-011-1554-0 71 (2011). [Erratum: Eur.Phys.J.C 73, 2501 (2013)], p. 1554. DOI: 10.1140/epjc/s10052-011-1554-0. arXiv: 1007.1727 [physics.data-an].

[128] A. L. Read. “Presentation of search results: the CL_s technique”. In: J. Phys. G: Nucl. Part. Phys. 28, 2693 (2002) (). URL: https://iopscience.iop.org/article/10.1088/0954-3899/28/10/313.

[129] "ATLAS Collaboration". “Constraints on the Higgs boson self-coupling from single- and double-Higgs production with the ATLAS detector using pp collisions at s=13 TeV”. In: Physics Letters B 843 (2023), p. 137745. ISSN: 0370-2693. DOI: https://doi.org/10.1016/j.physletb.2023.137745. URL: https://www.sciencedirect.com/science/article/pii/S0370269323000795.

[130] Jonathan Shlomi, Peter Battaglia, and Jean-Roch Vlimant. “Graph Neural Networks in Particle Physics”. In: (). Related DOI: https://doi.org/10.1088/2632-2153/abbf9a. DOI: 10.48550/arXiv.2007.13681. arXiv: 2007.13681 [hep-ex]. URL: https://doi.org/10.48550/arXiv.2007.13681.

[131] “Projected sensitivity of Higgs boson pair production in the $bb\tau\tau$ final state using proton-proton collisions at HL-LHC with the ATLAS detector”. In: (2021). URL: https://cds.cern.ch/record/2798448/files/ATL-PHYS-PUB-2021-044.pdf. URL: https://cds.cern.ch/record/2798448/files/ATL-PHYS-PUB-2021-044.pdf.

[132] “Simulated HL-LHC collision event in the ATLAS detector. General Photo:” in: (2019). URL: https://cds.cern.ch/record/2674770. URL: https://cds.cern.ch/record/2674770.

[133] "Technical Design Report for the ATLAS Inner Tracker Pixel Detector". In: (2017). URL: https://cds.cern.ch/record/2285585. DOI: {10.17181/CERN.FOZZ.ZP3Q}. URL: https://cds.cern.ch/record/2285585.

[134] "ATLAS Liquid Argon Calorimeter Phase-II Upgrade : Technical Design Report". In: (). URL: https://cds.cern.ch/record/2285582. DOI: 10.17181/CERN.6QIO.YGHO. URL: https://cds.cern.ch/record/2285582.

[135] "Technical Design Report for the Phase-II Upgrade of the ATLAS Tile Calorimeter". In: (). URL: https://cds.cern.ch/record/2285583. URL: https://cds.cern.ch/record/2285583.

[136] "A High-Granularity Timing Detector for the ATLAS Phase-II Upgrade: Technical Design Report". In: (). URL: https://cds.cern.ch/record/2719855. URL: https://cds.cern.ch/record/2719855.

[137] "Technical Design Report for the Phase-II Upgrade of the ATLAS Muon Spectrometer". In: (). URL: https://cds.cern.ch/record/2285580. URL: https://cds.cern.ch/record/2285580.

[138] "Technical Design Report for the Phase-II Upgrade of the ATLAS TDAQ System". In: (). URL: https://cds.cern.ch/record/2285584. DOI: 10.17181/CERN.2LBB.4IAL. URL: https://cds.cern.ch/record/2285584.

[139] "Technical Proposal: A High-Granularity Timing Detector for the ATLAS Phase-II Upgrade". In: ().

[140] G. Pellegrini et al. "Technology developments and first measurements of Low Gain Avalanche Detectors (LGAD) for high energy physics applications". In: Nuclear Instruments 765 (2014). HSTD-9 2013 - Proceedings of the 9th International "Hiroshima" Symposium on Development and Application of Semiconductor Tracking Detectors, pp. 12–16. ISSN: 0168-9002. DOI: https://doi.org/10.1016/j.nima.2014.06.008. URL: https://www.sciencedirect.com/science/article/pii/S0168900214007128.

[141] Christophe De La Taille et al. ""ALTIROC0, a 20 pico-second time resolution ASIC for the ATLAS High Granularity Timing Detector (HGTD)"". In: PoS https://pos.sissa.it/313/006 TWEPP-17 (2018), p. 006. DOI: 10.22323/1.313.0006.

[142] "CERN SPS North Area". In: (). Accessed on October 25, 2023. URL: http://sba.web.cern.ch/sba/BeamsAndAreas/H6/H6_presentation.html.

[143] Diener, R. and others. “The DESY II Test Beam Facility”. In: 922 (2019). URL: https://arxiv.org/abs/1807.09328, p. 265.

[144] M. Carulla et al. “First 50 μm thick LGAD fabrication at CNM”. In: (2016). URL: https://agenda.infn.it/getFile.py/access?contribId=20&sessionId=8&resId=0&materialId=slides&confId=11109. URL: https://agenda.infn.it/getFile.py/access?contribId=20&sessionId=8&resId=0&materialId=slides&confId=11109.

[145] RD50. “ — Radiation hard semiconductor devices for very high luminosity colliders”. In: (). Accessed: October 25, 2023. URL: http://rd50.web.cern.ch/rd50/.

[146] S. Hidalgo et al. “CNM activities on LGADs for ATLAS/CMS Timing Layers, talk given at the 32nd RD50 Workshop, Hamburg, Germany”. In: (2018). URL: https://indico.cern.ch/event/719814/contributions/3022492/. URL: https://indico.cern.ch/event/719814/contributions/3022492/.

[147] RD50. “Radiation hard semiconductor devices for very high luminosity colliders”. In: https://rd50.web.cern.ch ().

[148] G. Kramberger and all. “Radiation hardness of thin Low Gain Avalanche Detectors”. In: Nuclear Instruments 891 (2018), pp. 68–77. ISSN: 0168-9002. DOI: https://doi.org/10.1016/j.nima.2018.02.018. URL: https://www.sciencedirect.com/science/article/pii/S0168900218301682.

[149] C. Allaire et al. “Beam test measurements of Low Gain Avalanche Detector single pads and arrays for the ATLAS High Granularity Timing Detector”. In: (). DOI: 10.1088/1748-0221/13/06/P06017. arXiv: 1804.00622 [physics.ins-det].

[150] L. Castillo Garcia. “A High-Granularity Timing Detector for the Phase-II upgrade of the ATLAS Calorimeter system: detector concept, description, R&D and beam test results”. In: JINST (). URL: https://iopscience.iop.org/article/10.1088/1748-0221/15/09/C09047.

[151] H. Jansen et al. “Performance of the EUDET-type beam telescopes”. In: EPJ Tech. Instrum. 3 (2016) 7 (). URL: https://epjtechniquesandinstrumentation.springeropen.com/articles/10.1140/epjti/s40485-016-0033-2. URL: https://epjtechniquesandinstrumentation.springeropen.com/articles/10.1140/epjti/s40485-016-0033-2.

[152] V. Gkougkousis O.V. Posopkina and L. Castillo Garcia. “Design and integration of a SiPM based Timing Reference for ATLAS HGTD test beam”. In: (). URL: https://cds.cern.ch/record/2635107. URL: https://cds.cern.ch/record/2635107.

[153] I. Rubinskiy, EUTelescope. Offline track reconstruction and DUT analysis software, Tech. Rep., EUDET-Memo-2010-12, EUDET (2010), in: (). URL: https://www.eudet.org/e26/e28/e86887/e107460/EUDET-Memo-2010-12.pdf. URL: https://www.eudet.org/e26/e28/e86887/e107460/EUDET-Memo-2010-12.pdf.

[154] L. Castillo García et al. “Characterization of Irradiated Boron, Carbon-Enriched and Gallium Si-on-Si Wafer Low Gain Avalanche Detectors”. In: Instruments 6 (2022). Instruments 6 (2022) 2., p. 2.

[155] S. Ali et al. “Performance in beam tests of carbon-enriched irradiated Low Gain Avalanche Detectors for the ATLAS High Granularity Timing Detector”. In: Journal of Instrumentation 18 (2023). URL: https://iopscience.iop.org/article/10.1088/1748-0221/18/05/P05005, P05005. DOI: 10.1088/1748-0221/18/05/P05005. URL: https://iopscience.iop.org/article/10.1088/1748-0221/18/05/P05005.

[156] Dale Abbott et al. Supporting Document: The Search for Non-Resonant ggF and VBF Tech. rep. Geneva: CERN, 2021. URL: https://cds.cern.ch/record/2780536.

[157] “Measuring masses of semi-invisibly decaying particle pairs produced at hadron colliders”. In: Physics Letters B (). URL: https://inspirehep.net/literature/501707. URL: https://inspirehep.net/literature/501707.